ALMA MATER STUDIORUM
UNIVERSITÀ DI BOLOGNA

DOTTORATO DI RICERCA IN
DATA SCIENCE AND COMPUTATION
CICLO XXXVI

Settore Concorsuale: 02/A2
Settore Scientifico Disciplinare: PHYS-02/A (FIS/02)

Quantum Fisher Information for simulation of many-body systems and new Quantum Cellular Automata protocols for computation

Presentata da:
Federico Dell'Anna

Supervisore:
Prof.ssa Elisa Ercolessi

Coordinatore Dottorato:
Prof. Daniele Bonacorsi

Co-supervisore:
Prof. Antonio Zoccoli

Esame Finale Anno 2025

To my sweet nephew Tommaso.

Abstract

This work is divided into two parts. The first part focuses on Quantum Fisher Information (QFI), exploring its properties and its crucial role in the geometry of quantum mechanics, phase estimation theory, and its connection to multipartite entanglement. Specifically, we study ground state QFI in one-dimensional spin-1 models, using it as a tool to witness multipartite entanglement. The models examined include the *Bilinear-Biquadratic* model and the XXZ spin-1 chain, all with nearest-neighbor interactions and open boundary conditions. We demonstrate that the scaling of QFI with strictly non-local observables can characterize phase diagrams, particularly in the study of topological phases, where it exhibits maximal scaling.

To conclude this part, we demonstrate how QFI can be effectively utilized as a hybrid quantum-classical optimizer within variational algorithms in the NISQ era. Specifically, we evaluate the performance of the Quantum Approximate Optimization Algorithm (QAOA) by leveraging the Quantum Natural Gradient as the optimizer, showing that even with the noise, typically present in quantum devices, the QFI-based Natural Gradient allows the algorithm to converge more efficiently, reaching the cost function's minimum in fewer iterations compared to its classical counterpart.

In the second part, we introduce the concept of Quantum Cellular Automata (QCA) as an alternative paradigm to quantum computation, highlighting their versatility and applications across various fields of theoretical physics. Finally, we discuss how non-unitary QCA can solve the density classification task, which maps global density information to local density. Two approaches are considered: one that preserves number density and one that performs majority voting. For the number-preserving case, two QCAs are proposed that reach a fixed-point solution with a time complexity that scales almost quadratically with system size, both of which can be generated through continuous-time Lindblad dynamics. Additionally, a third QCA, a hybrid rule combining discrete-time and continuous-time three-body interactions, is introduced to solve the majority voting problem in a time that scales linearly with system size.

Contents

Abstract **5**

Introduction **11**

I **15**

1 Quantum Fisher Information **17**
1.1 Definition and properties . . . 17
1.2 Methods for computing the QFIm . . . 19
1.3 QFI and geometry of quantum mechanics . . . 21
1.3.1 Fubini-Study metric . . . 21
1.3.2 Fidelity and Bures metric . . . 22
1.3.3 Quantum Geometric Tensor . . . 22
1.4 QFI and phase estimation . . . 23
1.4.1 QFI and the Cramér-Rao lower bound . . . 23
1.5 QFI and multipartite entanglement . . . 26
1.5.1 From Shot Noise to the Heisenberg Limit . . . 27
1.5.2 k-particle entangled states . . . 28

2 QFI and multipartite entanglement in spin-1 chains **31**
2.1 Bilinear-Biquadratic model . . . 32
2.1.1 Phase diagram . . . 32
2.1.2 Numerical results . . . 35
2.2 XXZ spin-1 model . . . 38
2.2.1 Phase diagram . . . 38
2.2.2 Numerical results . . . 40
2.3 Conclusions and outlooks . . . 42

3 QAOA and Natural Gradient in a noisy Rydberg atoms device **45**
3.1 Quantum Approximate Optimization Algorithm and Natural Gradient . . . 46
3.1.1 QAOA Circuit . . . 46
3.1.2 Application to the Transverse Field Ising Model . . . 47
3.1.3 Quantum Natural Gradient . . . 48

3.2 Rydberg atoms implementation . . . 50
3.3 Numerical results . . . 52
3.3.1 Ground state preparation accuracy . . . 52
3.3.2 Comparison of QNG vs. Vanilla gradient descent . . . 53
3.4 Conclusions and outlook . . . 54

II **57**

4 From Classical to Quantum Cellular Automata **59**
4.1 Cellular Automata . . . 59
4.1.1 Rule 110: A Turing-Complete Cellular Automaton . . . 60
4.2 The density classification task . . . 62
4.2.1 Fukś density classifier . . . 64
4.2.2 Fatès density classifier . . . 66
4.3 Quantum Cellular Automata . . . 67
4.3.1 Definition and dynamics . . . 68
4.3.2 Partitioning schemes . . . 70
4.3.3 Rydberg atoms implementation . . . 72

5 Density Classification with non-unitary Quantum Cellular Automata **75**
5.1 Introduction . . . 75
5.2 State of the Art . . . 75
5.3 Problem . . . 77
5.4 Model . . . 78
5.4.1 Fukś QCA . . . 79
5.4.2 Dephasing QCA . . . 82
5.4.3 Majority Voting QCA . . . 83
5.5 Results . . . 85
5.5.1 Fukś QCA . . . 85
5.5.2 Dephasing QCA . . . 86
5.5.3 Majority Voting QCA . . . 87
5.6 Conclusion . . . 88

Conclusions **91**

Appendices **109**

A The AKLT model **111**

B Derivation of the Lindbladian describing the Fukś QCA **115**
B.0.1 $|00\rangle$ neighborhood . . . 115
B.0.2 $|01\rangle$ neighborhood . . . 117

C Proof of the conservation of the number density in the Fukś QCA **119**

D Steady states of the Lindbladian describing the Fukś QCA **123**
D.0.1 The set of steady states . . . 123
D.0.2 States that are not steady states . . . 126

E Proof that Dephasing QCA solves the DC task **131**

F Fatès QCA **133**

G Proof of the properties of $\hat{\mathbb{A}}$ and the dynamics of the Majority Voting Lindbladian **135**
G.1 Proof of the properties of $\hat{\mathbb{A}}$ . . . 135
G.2 Majority Voting Lindbladian $\hat{\mathbb{L}}^{(\mathrm{ML})}$ by using a Machine Learning approach . . . 136

H Proof of the scaling of τ with system size N in discrete-time evolution **139**

Acknowledgements **143**

Introduction

This thesis explores the intricate realms of *entanglement*, *quantum computing* and *quantum cellular automata*. To understand the connections and motivations behind these topics, it is essential to consider the revolutionary impact of quantum mechanics on modern physics.

Quantum mechanics has revolutionized modern physics. Its inherently probabilistic nature, the principle of superposition, and its properties of entanglement make it one of the most fascinating and complex theories in science. *Entanglement*, in particular, stands out as one of the most intriguing aspects of quantum mechanics. This phenomenon occurs when pairs or groups of particles become interconnected in such a way that the state of one particle is dependent on the state of the other(s), no matter the distance separating them. Einstein famously referred to this phenomenon as "spooky action at a distance", expressing his skepticism about the non-locality implied by quantum mechanics. In his 1935 paper with Podolsky and Rosen, Einstein challenged the completeness of quantum mechanics, proposing that there must be hidden variables that govern the behavior of entangled particles [1]. Later, John Bell introduced inequalities to test the validity of such hidden variable theories, and Alain Aspect's experiments subsequently demonstrated the violation of these inequalities, confirming the predictions of quantum mechanics [2].

However, the implications of entanglement extend beyond theoretical debates. Its practical applications in quantum computing and quantum cryptography make the exploration of this phenomenon, particularly its role within quantum many-body systems, not only a quest for understanding but also a frontier for technological advancement [3, 4]. Effectively addressing and solving the *many-body quantum problem* would be invaluable, with impacts extending both directly and indirectly across virtually every field of natural science. It would pave the way for technological innovations that could profoundly affect everyday life.

The complexity of the many-body quantum problem becomes evident when considering that the dimension of the space of possible configurations for a system with N primary constituents (such as quantum particles) increases exponentially with N. If each constituent is characterized by d possible states (e.g. spin configurations or electronic orbitals), the total number of possible configurations for the entire system is d^N. Typically, the goal is to find the eigenvector corresponding to the ground state of the system. To date, only a few exactly solvable models have been identified, and exact diagonalization techniques are limited to systems with very few constituents. Thus, the large-N limit, which is often the most interesting case, remains out of reach for many systems.

To tackle these challenges, researchers have developed a variety of theoretical and numerical methods, drawing from different disciplines to gain new insights into quantum many-body systems. Chief among them are numerical simulations based on Tensor Network (TN) techniques [5, 6].

These techniques originated from the density matrix renormalization group (DMRG) algorithm introduced by S. White more than three decades ago [7]. For a long time, the DMRG method was primarily applied to condensed matter physics. However, since the early 2000s, TN methods have been extended to a growing range of research areas, including quantum information, quantum chemistry, and lattice gauge theory. The TN approach leverages the tensor structure of the Hilbert space, enabling a more efficient representation of the wave function, significantly reducing the computational resources required for simulations [5, 6].

While classical computational methods have provided valuable tools, a revolutionary shift came with the idea of using quantum systems to simulate other quantum systems. Over forty years ago, Richard Feynman proposed a groundbreaking approach to solving the many-body problem in his seminal paper [8]. He suggested developing a dedicated *quantum computer* to address the quantum many-body problem, exploiting the fact that the exponential growth of the Hilbert space could naturally be mirrored by another many-body quantum system. However, it is only in the last decade that advancements in quantum information science and experimental techniques have allowed platforms (such as cold atoms, trapped ions, and superconducting qubits) to perform quantum simulations of various simple many-body phenomena with unprecedented control. Today, we are experiencing what is often referred to as the second quantum revolution [9]. Many algorithms developed over the years for quantum computers are now becoming practically realizable on quantum devices. These advancements hold the potential to revolutionize our understanding of complex systems and unlock new applications across a variety of fields, ranging from materials science to cryptography.

Quantum computing can be traced back to the need for a quantum version of the Turing machine, transitioning from classical bits and gates to quantum bits and quantum gates. However, beginning in the 1940s, an alternative computational paradigm emerged: cellular automata (CAs) [10]. Cellular automata are discrete models consisting of a grid of cells, each of which can exist in a finite number of states. The state of each cell is updated simultaneously according to a set of rules determined by the states of neighboring cells. Interest in this simple framework expanded beyond academia in the late 1970s, largely due to John Conway's *Game of Life*, a two-dimensional cellular automaton [11]. This model proved to be highly effective in exploring complex systems and phenomena, such as patterns and emergent behaviors in computational settings [12]. In the 1980s, Stephen Wolfram systematically classified elementary cellular automata [13], and Matthew Cook was able to prove that they can be Turing complete [14]. Cellular automata have since found numerous practical applications, including traffic modeling [15], fluid dynamics [16], biological pattern formation [17], and reaction-diffusion systems [16].

This natural evolution of computational paradigms has inspired the development of quantum analogs to classical models, leading to the concept of *Quantum Cellular Automata* (QCAs) which are the quantum counterpart of classical CAs. Specific models for QCAs were introduced in several works, such as [18–20], where they were proposed as an alternative paradigm for quantum computation and were shown to be universal, meaning they could efficiently simulate a quantum Turing machine. The transition from classical CAs to QCAs, however, was not straightforward. Various challenges arose, and naive approaches – such as extending classical evolution linearly to create a quantum version – proved inadequate. Only later was an axiomatic definition of QCAs established,

which captured the essence of classical CAs while ensuring that the evolution followed quantum principles [21]. One ambitious application of QCAs is in modeling discrete physics. QCAs have been considered as discretized quantum field theories, providing an alternative regularization of quantum field theory [22]. More recently, in condensed matter physics, QCAs have been proposed as models for quantum lattice systems evolving under time-dependent periodic Hamiltonians (i.e. Floquet systems) [23]. QCAs also offer intriguing applications in the study and classification of topological phases of matter [24, 25].

To provide a clear roadmap for the reader, the structure of this thesis is organized as follows.

We begin by introducing Quantum Fisher Information (QFI), along with its properties and applications in various areas of quantum mechanics (Chapter 1). In particular, we demonstrate its utility as a witness of multipartite entanglement (ME) in spin-1 chains (Chapter 2, based on [26]), utilizing Tensor Network (TN) techniques and the Density Matrix Renormalization Group (DMRG) algorithm for this analysis. A key challenge in this context is the detection of ME in topological quantum phases, where standard methods fail. In this chapter, we focus on two paradigmatic spin-1 models with local interactions: the *Bilinear-Biquadratic* (BLBQ) model and the XXZ model. The BLBQ model, in particular, represents the most general SU(2)-invariant spin-1 model and exhibits a rich phase diagram, including the topological Haldane phase. Our contribution involves extending QFI to non-local observables, allowing us to successfully classify quantum phases, including topological ones, and calculate critical exponents at phase transitions. This represents an advancement over previous approaches that only consider local observables (and for other spin models) and is part of a broader line of research emphasizing the importance of non-local observables in the detection of ME in such systems [27, 28].

In Chapter 3, we explore how this same quantity (QFI) can be used within variational algorithms, particularly the Quantum Approximate Optimization Algorithm (QAOA), to define a new type of optimizer known as the Quantum Natural Gradient (QNG) that outperforms its classical counterpart even in noisy devices. Here, a major challenge lies in dealing with noise and barren plateaus, which hinder optimization in noisy intermediate-scale quantum (NISQ) devices. Our contribution consists in implementing the QNG on a real quantum platform – Rydberg atoms – and demonstrating its robustness to noise in this quantum platform. We also employ an approximate version of QFI for mixed states, showing that this method remains effective. We find that the diagonal approximation of the QFI offers a favorable trade-off between computational cost and optimization performance, nearly matching the effectiveness of the full Quantum Natural Gradient method. Notably, our simulations show that while additional QAOA layers can improve the algorithm's performance in idealized settings, they also increase susceptibility to noise, indicating that an optimal depth should be carefully chosen based on the specific hardware and noise conditions.

In the second part of this thesis, we provide a brief overview of Cellular Automata and Quantum Cellular Automata (Chapter 4), introducing a well-studied problem in this context known as the density classification task. In Chapter 5, following [29], we present our proposal for solving the quantum version of this problem, along with potential applications and realizations. The main challenge addressed is the design of a Quantum Cellular Automaton (QCA) capable of solving the density classification problem with efficiency comparable to or better than classical probabilistic

CAs. Our original contribution includes developing a non-unitary QCA that leverages two-body interactions, improving convergence times over existing classical and quantum models. Furthermore, we introduce a QCA-based solution to the majority voting problem, with potential applications in measurement-free quantum error correction (MFQEC). A quantum solution to the majority problem is advantageous as it eliminates the need for measurements on the ancillae, a process that is both slow and prone to noise. Additionally, using QCA solutions instead of circuit-based approaches offers the benefit of avoiding single-qubit addressability, a requirement that is often difficult to achieve in practical implementations.

Part I

Chapter 1

Quantum Fisher Information

The Quantum Fisher Information matrix (QFIm) plays a central role in theoretical quantum metrology, particularly due to its connection with the quantum Cramér-Rao bound in quantum parameter estimation. However, recent studies have revealed deep ties between QFIm and other key areas of quantum mechanics, including quantum thermodynamics, quantum phase transitions, entanglement detection, quantum speed limits, and non-Markovian dynamics [30]. These discoveries indicate that QFIm is not merely a tool for quantum metrology, but rather a fundamental quantity in the broader framework of quantum mechanics.

In this chapter, we present an overview of the properties of QFIm and the methods available for its calculation across various contexts. We also trace the its role in the geometry of quantum mechanics and in the theory of phase estimation. Finally, we investigate its relationship with *multipartite entanglement*, formulating a criterion for its detection. This chapter is based on two of the major reviews on this topic, namely [30] and [31].

1.1 Definition and properties

Consider a parameter vector $\boldsymbol{\theta} = (\theta_0, \theta_1, \dots, \theta_a, \dots)^T$, where θ_a denotes the a-th parameter encoded in the density matrix $\rho = \rho(\boldsymbol{\theta})$. In this chapter, we refer to the Quantum Fisher Information matrix (QFIm) as F, with its elements defined as follows [32, 33]:

$$F_{ab} := \frac{1}{2}\mathrm{Tr}\left(\rho\{L_a, L_b\}\right), \tag{1.1}$$

where $\{\cdot,\cdot\}$ represents the anti-commutator, and L_a (L_b) is the Symmetric Logarithmic Derivative (SLD) corresponding to the parameter x_a (x_b). The SLD satisfies the equation:

$$\partial_a \rho = \frac{1}{2}(\rho L_a + L_a \rho), \tag{1.2}$$

and is a Hermitian operator, with its expected value given by $\mathrm{Tr}(\rho L_a) = 0$. Using this property, the matrix element F_{ab} can also be expressed as [34]:

$$F_{ab} = \mathrm{Tr}\left(L_b \partial_a \rho\right) = -\mathrm{Tr}\left(\rho \partial_a L_b\right). \tag{1.3}$$

From equation (1.1), the diagonal element of the QFIm is:

$$F_{aa} = \mathrm{Tr}\left(\rho L_a^2\right), \tag{1.4}$$

which corresponds to the Quantum Fisher Information (QFI) for the parameter θ_a.

The classical concept of the Fisher Information matrix (CFIm) originates from statistics. Given a probability distributions $\{p(\mu|\boldsymbol{\theta})\}$, where $p(\mu|\boldsymbol{\theta})$ is the conditional probability of obtaining outcome μ, the elements of the CFIm are defined as:

$$I_{ab} := \sum_{\mu} \frac{[\partial_a p(\mu|\boldsymbol{\theta})][\partial_b p(\mu|\boldsymbol{\theta})]}{p(\mu|\boldsymbol{\theta})}. \tag{1.5}$$

As quantum metrology has developed, the (CFIm) has been distinguished from its quantum counterpart. In quantum mechanics, the choice of measurement affects the resulting probability distribution, leading to variations in the CFIm. Thus, the CFIm depends on the specific measurement performed. As will be explained further in the chapter, the QFI is obtained by optimizing over all possible measurements [35], such that $F_{aa} = \max_{\{\mu\}} I_{aa}(\rho, \{\mu\})$, where $\{\mu\}$ represents a Positive-Operator Valued Measure (POVM). In many cases, no single measurement can fully realize the QFIm.

The QFIm derived from SLD is not the only quantum generalization of the CFIm. Another commonly used version is based on right and left logarithmic derivatives [33, 36], defined by $\partial_a \rho = \rho R_a$ and $\partial_a \rho = R_a^\dagger \rho$, which leads to:

$$F_{ab} = \mathrm{Tr}(\rho R_a R_b^\dagger). \tag{1.6}$$

Unlike the SLD-based QFIm, which is real and symmetric, the QFIm based on right and left logarithmic derivatives is complex and Hermitian. These various forms of the QFIm fit within the broader framework of Riemannian monotone metrics introduced by Petz in 1996 [37, 38]. Each variation offers a quantum generalization of the Cramér-Rao bound with differing levels of attainability. For pure quantum states, Fujiwara and Nagaoka [39] extended the SLD to a broader class of derivatives, defined by $\partial_a \rho = \frac{1}{2}(\rho L_a + L_a^\dagger \rho)$, where L_a need not be Hermitian. When L_a is Hermitian, this reduces to the standard SLD. One notable case is the anti-symmetric logarithmic derivative, where $L_a^\dagger = -L_a$. In this chapter, we primarily focus on the SLD-based QFIm, unless otherwise noted.

While the properties of QFI have been thoroughly explored by G. Tóth et al. [40], the QFIm itself possesses several powerful properties, widely applicable in practice. These properties are summarized below:

- F is real and symmetric, i.e., $F_{ab} = F_{ba} \in \mathbb{R}$.
- F is positive semi-definite, i.e., $F \geq 0$. If $F > 0$, then $[F^{-1}]_{aa} \geq \frac{1}{F_{aa}}$ for any a.
- $F(\rho(\boldsymbol{\theta})) = F(U\rho(\boldsymbol{\theta})U^\dagger)$ for any unitary operation U that does not depend on $\boldsymbol{\theta}$.
- If $\rho = \bigotimes_i \rho_i(\boldsymbol{\theta})$, then $F(\rho) = \sum_i F(\rho_i)$.
- If $\rho = \bigoplus_i \lambda_i \rho_i(\boldsymbol{\theta})$, where λ_i are weights independent of $\boldsymbol{\theta}$, then $F(\rho) = \sum_i \lambda_i F(\rho_i)$.

- $F(p\rho_1 + (1-p)\rho_2) \leq pF(\rho_1) + (1-p)F(\rho_2)$ for any $p \in [0,1]$ (convexity).
- F is monotonic under completely positive and trace-preserving maps Φ, i.e., $F(\Phi(\rho)) \leq F(\rho)$.
- If $\mathbf{y}$ is a function of $\boldsymbol{\theta}$, the QFIm with respect to $\mathbf{y}$ and $\boldsymbol{\theta}$ are related by $F(\rho(\boldsymbol{\theta})) = J^T F(\rho(\mathbf{y}))J$, where J is the Jacobian matrix with elements $J_{ij} = \frac{\partial y_i}{\partial \theta_j}$.

1.2 Methods for computing the QFIm

In this section, we review the methods for calculating the QFIm and present analytical results for specific cases. Traditional approaches to deriving the QFIm often assume that the density matrix is full-rank, meaning all its eigenvalues are strictly positive. Specifically, the density matrix can be expressed as $\rho = \sum_{i=0}^{\dim(\rho)-1} \lambda_i |\psi_i\rangle\langle\psi_i|$, where λ_i and $|\psi_i\rangle$ represent the eigenvalues and their corresponding eigenstates. Under the assumption that $\lambda_i > 0$ for all i, the QFIm is computed as follows.

For a full-rank density matrix $\rho = \sum_{i=0}^{d-1} \lambda_i |\psi_i\rangle\langle\psi_i|$, where d is the dimension of ρ, the QFIm is given by:

$$F_{ab} = \sum_{i,j=0}^{d-1} \frac{2\,\mathrm{Re}\left(\langle\psi_i|\partial_a\rho|\psi_j\rangle\langle\psi_j|\partial_b\rho|\psi_i\rangle\right)}{\lambda_i + \lambda_j}. \tag{1.7}$$

However, if the density matrix is not full-rank, this formula may lead to divergent terms. To handle these cases, it is possible to modify this expression to exclude such terms by summing over $\lambda_i + \lambda_j \neq 0$. By substituting the spectral decomposition of ρ into this formula, we obtain:

$$F_{ab} = \sum_{i=0}^{d-1} \frac{(\partial_a\lambda_i)(\partial_b\lambda_i)}{\lambda_i} + \sum_{\substack{i\neq j \\ \lambda_i+\lambda_j\neq 0}} \frac{2(\lambda_i-\lambda_j)^2}{\lambda_i+\lambda_j}\,\mathrm{Re}\left(\langle\psi_i|\partial_a\psi_j\rangle\langle\partial_b\psi_j|\psi_i\rangle\right). \tag{1.8}$$

Recent studies have rigorously demonstrated that the QFIm for a finite-dimensional density matrix can be expressed in terms of the support of the density matrix. The support, denoted by S, is the set of non-zero eigenvalues: $S := \{\lambda_i \neq 0 \mid \lambda_i \in \text{eigenvalues of } \rho\}$. The spectral decomposition then becomes $\rho = \sum_{\lambda_i\in S} \lambda_i |\psi_i\rangle\langle\psi_i|$, and the QFIm can be written as:

$$F_{ab} = \sum_{\lambda_i\in S} \frac{(\partial_a\lambda_i)(\partial_b\lambda_i)}{\lambda_i} + \sum_{\lambda_i\in S} 4\lambda_i\,\mathrm{Re}\left(\langle\partial_a\psi_i|\partial_b\psi_i\rangle\right) - \sum_{\lambda_i,\lambda_j\in S} \frac{8\lambda_i\lambda_j}{\lambda_i+\lambda_j}\,\mathrm{Re}\left(\langle\partial_a\psi_i|\psi_j\rangle\langle\psi_j|\partial_b\psi_i\rangle\right). \tag{1.9}$$

A detailed derivation of this equation can be found in [30]. This expression is the most general form of the QFIm for a finite-dimensional density matrix of arbitrary rank.

Since the QFIm is closely related to the QFI, the following corollary holds: given the spectral decomposition $\rho = \sum_{\lambda_i\in S} \lambda_i |\psi_i\rangle\langle\psi_i|$, the QFI for a parameter θ_a is given by

$$F_{aa} = \sum_{\lambda_i\in S} \frac{(\partial_a\lambda_i)^2}{\lambda_i} + \sum_{\lambda_i\in S} 4\lambda_i\langle\partial_a\psi_i|\partial_a\psi_i\rangle - \sum_{\lambda_i,\lambda_j\in S} \frac{8\lambda_i\lambda_j}{\lambda_i+\lambda_j}|\langle\partial_a\psi_i|\psi_j\rangle|^2. \tag{1.10}$$

The first term corresponds to the classical Fisher Information, as it depends solely on the eigenvalue derivatives. The other terms, involving the derivatives of the eigenstates, capture quantum effects and describe the local geometry of the eigenspace with respect to the parameter $\boldsymbol{\theta}$.

SLD operator plays a central role not only in calculating the QFIm but also in determining optimal measurements and assessing the attainability of the quantum Cramér-Rao bound. For the eigenspace of ρ, the elements of the SLD operator are given by:

$$\langle\psi_i|L_a|\psi_j\rangle = \delta_{ij}\frac{\partial_a\lambda_i}{\lambda_i} + \frac{2(\lambda_j-\lambda_i)}{\lambda_i+\lambda_j}\langle\psi_i|\partial_a\psi_j\rangle. \tag{1.11}$$

For $\lambda_i, \lambda_j \notin S$, the matrix elements $\langle\psi_i|L_a|\psi_j\rangle$ may assume arbitrary values. Nevertheless, Fujiwara and Nagaoka [39, 41] demonstrated that such uncertainties in the SLD do not influence the Quantum Fisher Information (QFI), thus these values are often set to zero for simplicity in practical calculations.

The Bloch representation is a widely used tool in quantum information theory. For a d-dimensional density matrix, it can be expressed as:

$$\rho = \frac{1}{d}\left(\mathbb{I}_d + \frac{d(d-1)}{2}\mathbf{r}\cdot\boldsymbol{\kappa}\right), \tag{1.12}$$

where $\mathbf{r} = (r_1, r_2, \ldots, r_m, \ldots)^T$ is the Bloch vector, satisfying $|\mathbf{r}|^2 \leq 1$, and $\boldsymbol{\kappa}$ is a (d^2-1)-dimensional vector of $\mathfrak{su}(d)$ generators, with $\mathrm{Tr}(\kappa_i) = 0$. The anti-commutation relation for these generators is $\{\kappa_i, \kappa_j\} = \frac{4}{d}\delta_{ij}\mathbb{I}_d + \sum_{m=1}^{d^2-1}\mu_{ijm}\kappa_m$, while the commutation relation is $[\kappa_i, \kappa_j] = i\sum_{m=1}^{d^2-1}\varepsilon_{ijm}\kappa_m$, where μ_{ijm} and ε_{ijm} are the symmetric and antisymmetric structure constants, respectively. Recently, Watanabe et al. [42–44] derived the formula for the QFIm for a general Bloch vector by treating the Bloch vector itself as the parameter to be estimated. In the Bloch representation of a d-dimensional density matrix, the QFIM can be written as:

$$F_{ab} = (\partial_b\mathbf{r})^T\left[\frac{d}{2(d-1)}G - \mathbf{r}\cdot\mathbf{r}^T\right]^{-1}\partial_a\mathbf{r}, \tag{1.13}$$

where G is a real symmetric matrix with entries:

$$G_{ij} = \frac{1}{2}\mathrm{Tr}(\rho\{\kappa_i, \kappa_j\}) = \frac{2}{d}\delta_{ij} + \frac{r}{d-1}\sum_m \mu_{ijm}r_m. \tag{1.14}$$

The most common application of this result is in single-qubit systems, where $\rho = \frac{1}{2}(\mathbb{I}_2 + \mathbf{r}\cdot\boldsymbol{\sigma})$, with $\boldsymbol{\sigma} = (\sigma_x, \sigma_y, \sigma_z)$ being the vector of Pauli matrices. For a single-qubit mixed state, the QFIm in the Bloch representation can be written as:

$$F_{ab} = (\partial_a\boldsymbol{r})\cdot(\partial_b\boldsymbol{r}) + \frac{(\boldsymbol{r}\cdot\partial_a\boldsymbol{r})(\boldsymbol{r}\cdot\partial_b\boldsymbol{r})}{1-|\boldsymbol{r}|^2}, \tag{1.15}$$

where $|\boldsymbol{r}|$ is the norm of the Bloch vector. For a single-qubit pure state [45], this simplifies to:

$$F_{ab} = (\partial_a\boldsymbol{r})\cdot(\partial_b\boldsymbol{r}). \tag{1.16}$$

For a pure state $|\psi\rangle$, the support of the density matrix has dimension 1, meaning there is only one non-zero eigenvalue (equal to 1), with the corresponding eigenstate being $|\psi\rangle$. The QFIm elements for a pure parameterized state $|\psi(\boldsymbol{\theta})\rangle$ are given by:

$$F_{ab} = 4\,\mathrm{Re}\left(\langle\partial_a\psi|\partial_b\psi\rangle - \langle\partial_a\psi|\psi\rangle\langle\psi|\partial_b\psi\rangle\right). \tag{1.17}$$

The QFI for the parameter θ_a is simply the diagonal component of the QFIm:

$$F_{aa} = 4\left(\langle\partial_a\psi|\partial_a\psi\rangle - |\langle\partial_a\psi|\psi\rangle|^2\right). \tag{1.18}$$

and the SLD operator for θ_a in a pure state is given by $L_a = 2\left(|\psi\rangle\langle\partial_a\psi| + |\partial_a\psi\rangle\langle\psi|\right)$.

An important example involves the parameterized pure state $|\psi\rangle = e^{-it\sum_j H_j\theta_j}|\psi_0\rangle$, where $[H_a, H_b] = 0$, and $|\psi_0\rangle$ is the initial probe state. In this case, the QFIm becomes:

$$F_{ab} = 4t^2\,\Delta(H_a, H_b)^2_{|\psi_0\rangle}, \tag{1.19}$$

where $\Delta(H_a, H_b)^2_{|\psi_0\rangle}$ is the covariance of the Hamiltonians H_a and H_b in the state $|\psi_0\rangle$ defined as $\Delta(H_a, H_b)^2_{|\psi_0\rangle} := \frac{1}{2}\langle\varphi|\{H_a, H_b\}|\varphi\rangle - \langle\varphi|H_a|\varphi\rangle\langle\varphi|H_b|\varphi\rangle$.

1.3 QFI and geometry of quantum mechanics

In the context of quantum mechanics, the states of quantum systems are described by wave functions or density matrices. While wave functions represent state vectors in Hilbert space, density matrices describe statistical mixtures of quantum states. The difference between quantum states can be expressed as a distance between these vectors or matrices. To define such a distance, it is necessary to introduce a metric in the space of states. An important extension of this concept arises from classical information theory, where the Fisher information metric is used to characterize distances between probability distributions. In quantum information theory, there is a quantum generalization of this metric, known as the Quantum Fisher Information metric. This metric provides a powerful geometric tool for studying the state space of quantum systems, allowing a deeper analysis of the structure and dynamics of quantum systems.

1.3.1 Fubini-Study metric

In quantum mechanics, pure states are represented as normalized vectors, adhering to the fundamental principle that the square of the vector's norm reflects the probability. These pure states can be represented as rays in projective Hilbert space, where the Fubini-Study metric is a Kähler metric [46–48]. The squared infinitesimal distance in this space is typically given by:

$$ds^2 = \langle d\psi|d\psi\rangle - \frac{|\langle d\psi|\psi\rangle|^2}{\langle\psi|\psi\rangle^2}. \tag{1.20}$$

For the case where $\langle\psi|\psi\rangle = 1$ and $d\psi = \sum_j \partial_j\psi d\theta^j$, this can be simplified to:

$$ds^2 = \frac{1}{4}\sum_{j,k} F_{jk}d\theta^j d\theta^k, \tag{1.21}$$

where F_{jk} is the jk-th element of the QFIm. This indicates that the Fubini-Study metric is a quarter of the QFI for pure states. This relationship is intrinsic to why the QFIm can determine the precision limit. Intuitively, the precision limit relates to the maximum distinguishability between states, which is naturally associated with the distance between them. For mixed states, the Fubini-Study metric's counterpart is the Bures metric, which is well-known in quantum information theory and closely related to quantum fidelity, as discussed below.

1.3.2 Fidelity and Bures metric

In quantum information theory, the fidelity $f(\rho_1, \rho_2)$ quantifies the similarity between two quantum states ρ_1 and ρ_2, defined as:

$$f(\rho_1, \rho_2) := \mathrm{Tr}\left(\sqrt{\sqrt{\rho_1}\rho_2\sqrt{\rho_1}}\right). \tag{1.22}$$

Fidelity ranges from 0 to 1, where $f = 1$ if and only if $\rho_1 = \rho_2$. While fidelity itself is not a distance measure, it can be used to construct the Bures distance D_B, defined as:

$$D_B^2(\rho_1, \rho_2) = 2\left(1 - f(\rho_1, \rho_2)\right). \tag{1.23}$$

The relationship between fidelity and the QFIm is well-established in the literature. When the rank of $\rho(\boldsymbol{\theta})$ remains constant as $\boldsymbol{\theta}$ varies, the QFIm is related to the infinitesimal Bures distance in a manner analogous to how it relates to the Fubini-Study metric:

$$D_B^2(\rho(\boldsymbol{\theta}), \rho(\boldsymbol{\theta} + d\boldsymbol{\theta})) = \frac{1}{4}\sum_{jk} F_{jk} d\theta^j d\theta^k. \tag{1.24}$$

Recently, it has been discovered that fidelity susceptibility, which captures the second-order variation of fidelity, can serve as an indicator of quantum phase transitions [49]. Due to the deep connection between the Bures metric and the QFIm, it is not surprising that the QFIm can be used similarly. Moreover, an increase in the QFIm at the critical point suggests that the precision limit of parameter estimation improves near a phase transition [50, 51]. However, if the rank of $\rho(\boldsymbol{\theta})$ differs from that of $\rho(\boldsymbol{\theta} + d\boldsymbol{\theta})$, Safranek recently [52] demonstrated that the QFIm does not precisely equal fidelity susceptibility. Seveso et al. [53] further proposed that the quantum Cramér-Rao bound might also fail in such cases.

In addition to the Fubini-Study and Bures metrics, the QFIm is closely related to the Riemannian metric because the state space of a quantum system forms a Riemannian manifold. Specifically, the QFIm belongs to a family of contractive Riemannian metrics [34, 37, 54]. In this context, the infinitesimal distance in state space is given by:

$$ds^2 = \sum_{jk} g_{jk} d\theta^j d\theta^k, \tag{1.25}$$

where g_{jk} represents the contractive Riemannian metric. In the eigenbasis of the density matrix ρ, g_{jk} is expressed as:

$$g_{\mu\nu} = \frac{1}{4}\sum_i \frac{\langle\lambda_i|d\rho|\lambda_i\rangle^2}{\lambda_i} + \frac{1}{2}\sum_{i<j} \frac{|\langle\lambda_i|d\rho|\lambda_j\rangle|^2}{\lambda_j h(\lambda_i/\lambda_j)}, \tag{1.26}$$

where $h(x)$ is the Morozova-Cencov function, which is operator monotone, self-inverse, and normalized. For $h(x) = \frac{1+x}{2}$, this metric reduces to the QFIm based on the SLD.

1.3.3 Quantum Geometric Tensor

The Quantum Geometric Tensor (QGT) emerges from a complex metric in projective Hilbert space and is a crucial tool in quantum information science, unifying the QFIm and the Berry connection. For a pure state $|\psi(\boldsymbol{\theta})\rangle$, the QGT is defined as:

$$Q_{jk} = \langle\partial_j\psi|\partial_k\psi\rangle - \langle\partial_j\psi|\psi\rangle\langle\psi|\partial_k\psi\rangle. \tag{1.27}$$

The real part of Q_{jk} (i.e. the Fubini-Studi metric) corresponds to the QFIm up to a constant factor:

$$\mathrm{Re}(Q_{jk}) = \frac{1}{4}F_{jk}. \tag{1.28}$$

Meanwhile, the imaginary part of Q_{jk} is related to the Berry connection $A_j = i\langle\psi|\partial_j\psi\rangle$ and Berry curvature $\Omega_{jk} = \partial_j A_k - \partial_k A_j$:

$$\mathrm{Im}(Q_{jk}) = -\frac{1}{2}(\partial_j A_k - \partial_k A_j). \tag{1.29}$$

The geometric phase can be computed as:

$$\gamma = \oint A_j d\theta^j, \tag{1.30}$$

where the integral is taken over a closed path in parameter space. Guo et al. [55] have connected the QFIm and Berry curvature via the Robertson uncertainty relation. Indeed, for a unitary process with two parameters, the determinant of the QFIm and Berry curvature should satisfy:

$$\det(F) + 4\det(\Omega) \geq 0. \tag{1.31}$$

1.4 QFI and phase estimation

What is the extent of precision achievable in statistical estimation? Is there an inherent limit to this precision? These inquiries lie at the core of statistical inference theory. Initial insights into these questions emerged in the 1940s, thanks to the contributions of Rao [56], Cramér [57], and Fréchet [58], who independently discovered a lower bound on the variance of any estimator. This limit, widely referred to as the Cramér-Rao lower bound, is closely associated with the Fisher information, a concept introduced by Fisher in the 1920s [59]. The Fisher information plays a pivotal role in the theory of phase estimation. By optimizing the Fisher information across all possible quantum measurements, we derive the quantum Fisher information [35], which establishes a quantum-specific lower limit to the Cramér-Rao bound [32, 60].

In this section, we will outline and clarify the Cramér-Rao lower bound and its significance for various estimation techniques. We begin with an input (probe) state denoted as ρ. An interferometer, in our framework, refers to any transformation applied to the probe that can be parameterized by an unknown real number θ. The process of estimating θ involves examining the outcomes of measurements conducted on the output state $\rho(\theta)$. These measurement results can be discrete, such as the particle counts at the output modes of a Mach-Zehnder interferometer, or continuous, like the spatial intensity distribution observed in a double-slit experiment [61, 62].

1.4.1 QFI and the Cramér-Rao lower bound

The most general form of measurement in quantum theory is described by a positive-operator valued measure (POVM), which consists of a set of Hermitian operators $\hat{E}(\boldsymbol{\mu})$ that are non-negative to ensure non-negative probabilities and sum to the identity operator to ensure normalization. A standard projective measurement is a specific type of POVM where the operators $\hat{E}(\boldsymbol{\mu})$ are orthogonal

projectors. For correlated subsystems described by ρ and performing m correlated measurements described by $\hat{E}(\boldsymbol{\mu})$, where $\boldsymbol{\mu} = \{\mu_1, \mu_2, \ldots, \mu_m\}$, the conditional probability of observing the result $\boldsymbol{\mu}$ for a given θ, also referred to as the likelihood, is given by

$$P(\boldsymbol{\mu}|\theta) = \mathrm{Tr}\left[\hat{E}(\boldsymbol{\mu})\rho(\theta)\right]. \tag{1.32}$$

If the probe state consists of m independent, uncorrelated subsystems,

$$\rho = \rho^{(1)} \otimes \rho^{(2)} \otimes \cdots \otimes \rho^{(m)}, \tag{1.33}$$

and we perform local operations and statistically independent measurements, then the likelihood function simplifies to the product of individual measurement probabilities:

$$P(\boldsymbol{\mu}|\theta) = \prod_{i=1}^{m} P_i(\mu_i|\theta), \tag{1.34}$$

where $P_i(\mu_i|\theta) = \mathrm{Tr}\left[\hat{E}^{(i)}(\mu_i)\rho^{(i)}(\theta)\right]$. For analytical purposes, the log-likelihood function is often used:

$$L(\boldsymbol{\mu}|\theta) := \ln P(\boldsymbol{\mu}|\theta) = \sum_{i=1}^{m} \ln P_i(\mu_i|\theta). \tag{1.35}$$

An estimator, denoted as $\Theta(\mu)$, functions as a mapping from the outcomes μ to the parameter space. Essentially, it links each set of measurement results to an estimate Θ of the parameter θ. A well-known example of an estimator is the maximum likelihood estimator. The goal in selecting an estimator is to minimize the discrepancy between Θ and the true value of θ. Since the estimator is derived from random outcomes, it itself is a random variable, characterized by its mean value, which depends on θ, represented as

$$\langle\Theta\rangle_\theta = \sum_{\mu} P(\mu|\theta)\Theta(\mu), \tag{1.36}$$

and its variance, given by

$$(\Delta\Theta)^2_\theta = \sum_{\mu} P(\mu|\theta)\left[\Theta(\mu) - \langle\Theta\rangle_\theta\right]^2. \tag{1.37}$$

A good estimator is characterized by being unbiased, meaning its statistical average equals the true parameter value, and providing minimal uncertainty, often measured by the square root of the variance. An estimator is deemed unbiased if its expected value aligns with the true parameter value for all θ:

$$\langle\Theta(\mu)\rangle_\theta = \theta, \quad \forall\theta. \tag{1.38}$$

On the other hand, an estimator $\Theta(\mu)$ is consistent if, as the number of measurements m increases, the sequence of estimates converges in probability to θ:

$$\lim_{m\to\infty} \Pr\left[|\Theta(\mu) - \theta| > \varepsilon\right] = 0, \quad \forall\theta, \tag{1.39}$$

where ε is an arbitrarily small number. A consistent estimator is also asymptotically unbiased, expressed as

$$\lim_{m\to\infty} \langle\Theta(\mu)\rangle_\theta = \theta, \quad \forall\theta. \tag{1.40}$$

Turning to classical Fisher information (CFI) and the Cramér-Rao lower bound, the Cramér-Rao bound is a fundamental theorem in phase estimation, providing a lower limit on the variance of any estimator:

$$(\Delta\Theta)^2_\theta \geq \Delta\Theta^2_{\mathrm{CR}} \equiv \frac{\left(\frac{\partial\langle\Theta\rangle_\theta}{\partial\theta}\right)^2}{I(\theta)}, \tag{1.41}$$

where $I(\theta)$ denotes the CFI, defined as

$$I(\theta) \equiv \left(\frac{\partial L(\boldsymbol{\mu}|\theta)}{\partial\theta}\right)^2_\theta = \sum_\varepsilon \frac{1}{P(\boldsymbol{\mu}|\theta)}\left(\frac{\partial P(\boldsymbol{\mu}|\theta)}{\partial\theta}\right)^2. \tag{1.42}$$

The Eq. (1.41) represents the most general form of the Cramér-Rao lower bound, but it becomes especially useful for unbiased estimators where $\frac{\partial\langle\Theta\rangle_\theta}{\partial\theta} = 1$: in this case, the bound simplifies to the inverse of the Fisher information. An estimator that reaches this bound is referred to as efficient. Although efficient estimators don't always exist in every scenario, when the number of measurements is large enough, at least one efficient estimator, such as the maximum likelihood estimator, is typically available.

To illustrate the Cramér-Rao lower bound, we start with the relation:

$$\frac{\partial\langle\Theta\rangle_\theta}{\partial\theta} = \sum_{\boldsymbol{\mu}} P(\boldsymbol{\mu}|\theta)\Theta(\boldsymbol{\mu})\frac{\partial L(\boldsymbol{\mu}|\theta)}{\partial\theta} = \left\langle \Theta\frac{\partial L(\boldsymbol{\mu}|\theta)}{\partial\theta}\right\rangle_\theta, \tag{1.43}$$

and

$$\frac{\partial}{\partial\theta}\sum_{\boldsymbol{\mu}} P(\boldsymbol{\mu}|\theta) = \sum_{\boldsymbol{\mu}} P(\boldsymbol{\mu}|\theta)\frac{\partial L(\boldsymbol{\mu}|\theta)}{\partial\theta} = \left\langle \frac{\partial L(\boldsymbol{\mu}|\theta}{\partial\theta}\right\rangle_\theta = 0. \tag{1.44}$$

By applying the Cauchy-Schwarz inequality,

$$\langle A^2\rangle_\theta\langle B^2\rangle_\theta \geq \langle AB\rangle^2_\theta, \tag{1.45}$$

with $A = \Theta - \langle\Theta\rangle_\theta$ and $B = \frac{\partial L(\boldsymbol{\mu}|\theta)}{\partial\theta}$, we find:

$$\left\langle(\Theta - \langle\Theta\rangle_\theta)^2\right\rangle_\theta \left\langle\left(\frac{\partial L(\boldsymbol{\mu}|\theta)}{\partial\theta}\right)^2\right\rangle_\theta \geq \left\langle(\Theta - \langle\Theta\rangle_\theta)\left(\frac{\partial L(\boldsymbol{\mu}|\theta)}{\partial\theta}\right)\right\rangle^2_\theta. \tag{1.46}$$

Notably,

$$\left\langle(\Theta - \langle\Theta\rangle_\theta)\frac{\partial L(\boldsymbol{\mu}|\theta)}{\partial\theta}\right\rangle_\theta = \frac{\partial\langle\Theta\rangle_\theta}{\partial\theta}, \tag{1.47}$$

leading to the conclusion that

$$(\Delta\Theta)^2_\theta \geq \frac{\left(\frac{\partial\langle\Theta\rangle_\theta}{\partial\theta}\right)^2}{\left\langle\left(\frac{\partial L(\boldsymbol{\mu}|\theta)}{\partial\theta}\right)^2\right\rangle_\theta} = \frac{1}{I(\theta)}, \tag{1.48}$$

which is the Cramér-Rao lower bound for an unbiased estimator.

When we switch to quantum, it is possilbe to derive an upper bound for CFI. This is achieved by maximizing it over all possible POVMs,

$$F(\rho(\theta)) := \max_{\{\hat{E}\}} I(\rho(\theta), \{\hat{E}(\boldsymbol{\mu})\}), \tag{1.49}$$

which is equivalently used as an alternative definition of the QFI. Indeed, in [31], it is possible to find the proof that this definition coincides with the one introduced in the previous section (1.4), specifically:

$$F(\rho(\theta)) = \mathrm{Tr}[\rho(\theta)\hat{L}_\theta^2], \tag{1.50}$$

where the Hermitian operator $\hat{L}_\theta$, is the symmetric logarithmic derivative, defined as usual. From eqs. (1.48) and (1.49), we obtain the following chain of inequalities:

$$\Delta\Theta_\theta^2 \geq \Delta\Theta_{\mathrm{CR},\theta}^2 \geq \Delta\Theta_{\mathrm{QCR},\theta}^2, \tag{1.51}$$

where

$$(\Delta\Theta_{\mathrm{QCR}})_\theta^2 \equiv \frac{\left(\frac{\partial\langle\Theta\rangle}{\partial\theta}\right)^2}{F(\rho(\theta))}. \tag{1.52}$$

Since the probe state consists of m independent, uncorrelated subsystems, and due to the additivity of the QFI, $F(\rho(\theta)) = mF(\rho^{(m)}(\theta))$. From now on, we will omit the index $^{(m)}$ to simplify the notation. In principle, this bound can be saturated through optimal measurements, such as those based on the symmetric logarithmic derivative. In practice, the Fisher information depends on the specific measurement chosen, and various strategies can be applied to maximize the information extracted. Since quantum systems can encode intricate information within their quantum states, the quantum Fisher information becomes essential in determining the ultimate precision limits in tasks like phase estimation.

1.5 QFI and multipartite entanglement

Let us examine two distinct, non-interacting systems, A and B, each associated with its own Hilbert space: $\mathcal{H}_A$ for system A and $\mathcal{H}_B$ for system B. The total state space of the combined system is described by the tensor product $\mathcal{H}_{AB} = \mathcal{H}_A \otimes \mathcal{H}_B$. If system A is in the pure state $|\psi_A\rangle$ and system B is in the pure state $|\psi_B\rangle$, the state of the composite system is represented as:

$$|\psi_{\mathrm{sep}}\rangle = |\psi_A\rangle \otimes |\psi_B\rangle. \tag{1.53}$$

States that can be written in this form are referred to as product or separable states. In such cases, any local operation applied to system A does not affect system B, and vice versa. Consequently, the expectation value of any joint measurement $\hat{M}_{AB} = \hat{M}_A \otimes \hat{M}_B$ on the composite system $\mathcal{H}_{AB}$ equals the product of the individual expectation values for each subsystem:

$$\langle\psi_{AB}|\hat{M}_{AB}|\psi_{AB}\rangle = \langle\psi_A|\hat{M}_A|\psi_A\rangle \times \langle\psi_B|\hat{M}_B|\psi_B\rangle. \tag{1.54}$$

Although systems A and B are independent, they can still exhibit classical correlations via communication. In such a scenario, the composite system might be found in a state like $|\psi_A^{(k)}\rangle \otimes |\psi_B^{(k)}\rangle$

with a probability p_k, where $p_k > 0$ and $\sum_k p_k = 1$. A mixed state of a composite quantum system is referred to as classically correlated (or separable) if it can be expressed as a weighted sum of density matrices corresponding to separable pure states [63, 64]:

$$\rho_{\text{sep}} = \sum_k p_k \left(|\psi_A^{(k)}\rangle\langle\psi_A^{(k)}| \otimes |\psi_B^{(k)}\rangle\langle\psi_B^{(k)}| \right). \tag{1.55}$$

States that cannot be described in this manner are classified as entangled. It is crucial to emphasize that local operations and classical communication are incapable of generating or eliminating entanglement which means this non-local property is preserved.

The notions of separability and entanglement can be extended to systems involving more than two subsystems. For a composite system consisting of N parts, with the total Hilbert space represented by $\mathcal{H}_1 \otimes \mathcal{H}_2 \otimes \cdots \otimes \mathcal{H}_N$, the system is separable if its state can be expressed as:

$$\rho_{\text{sep}} = \sum_k p_k \left(|\psi_1^{(k)}\rangle\langle\psi_1^{(k)}| \otimes |\psi_2^{(k)}\rangle\langle\psi_2^{(k)}| \otimes \cdots \otimes |\psi_N^{(k)}\rangle\langle\psi_N^{(k)}| \right). \tag{1.56}$$

Any state that cannot be written in the form of Eq. (1.56) is classified as entangled.

1.5.1 From Shot Noise to the Heisenberg Limit

Let us now considering a particularly relevant case of N subsystems. For each subsystem, we apply a local and unitary phase shift operation, represented as $e^{-i\theta\hat{h}_i}$, where $\hat{h}_i$ serves as the generator of the phase shift for the i^{th} subsystem. It is essential to note that the same phase shift, θ, is applied uniformly across all N subsystems. Consequently, the overall transformation affecting these N particles can be expressed as

$$\bigotimes_{i=1}^{N} e^{-i\hat{h}_i\theta} = e^{-i\hat{H}\theta}, \tag{1.57}$$

To simplify our analysis, we will assume that all N subsystems share the same dimension of Hilbert space and that each generator $\hat{h}_i$ is identical across subsystems, denoted as $\hat{h}$. We define $h_{\max}$ and $h_{\min}$ as the maximum and minimum eigenvalues of $\hat{h}$, respectively, with corresponding eigenvectors represented as $|h_{\max}\rangle$ and $|h_{\min}\rangle$.

In this section, we demonstrate that for the separable, QFI is strictly bounded [65]. The following chain of inequalities can be established:

$$F(\rho_{\text{sep}}) \leq \sum_k p_k F(|\psi_{\text{sep}}^{(k)}\rangle) = \sum_{i,k} p_k F(|\psi_i^{(k)}\rangle) \leq N \frac{(h_{\max} - h_{\min})^2}{4}. \tag{1.58}$$

The first inequality arises from the convexity of the QFI, while the equality follows from the additive property of the QFI. The final inequality is based on the result $F(|\psi_i^{(k)}\rangle) = 4(\Delta\hat{h}_i)^2$, (see Eq. (1.19) for $t = 1$ and $H_a = H_b$) and that $4(\Delta\hat{h}_i)^2 \leq (h_{\max} - h_{\min})^2$. This leads us to a significant conclusion: the optimal phase sensitivity, i.e. the quantum Cramér-Rao bound (see Eq. (1.52)), for separable states involving N particles and m independent measurements, is given by

$$\Delta\theta_{SN} = \frac{1}{\sqrt{Nm}|h_{\max} - h_{\min}|}, \tag{1.59}$$

which holds true regardless of the specific measurement or estimator employed. This expression is commonly referred to as the Shot Noise (SN) limit, or standard quantum limit. In this context, the number of particles acts as a statistical enhancement, akin to the effect of conducting multiple independent measurements. Furthermore, as we transition from qubits (where $h_{\max} - h_{\min} = 1$) to more complex multimode systems, the shot noise limit improves by a factor that is directly proportional to the number of modes involved.

From the results discussed, we can conclude that the condition

$$F(\rho) > \frac{N(h_{\max} - h_{\min})^2}{4} \tag{1.60}$$

is a sufficient criterion for establishing entanglement. This indicates that if the state ρ is separable, the inequality cannot hold. More specifically, this inequality represents the requirement for useful entanglement: it is both necessary and sufficient for a state to effectively estimate a phase shift θ with a sensitivity that surpasses the limitations defined for separable states.

A key point to emphasize is that not every entangled state is practically useful; those that are can be identified through their QFI [66]. We then delve into the optimal sensitivity achievable with an entangled probe state [65]. By employing the convexity of the QFI, we can express the relationship as follows:

$$F(\rho) \leq \max_{|\psi\rangle} F(|\psi\rangle) \leq N^2(h_{\max} - h_{\min})^2. \tag{1.61}$$

The final part of this inequality arises from the observation that

$$\max_{|\psi\rangle} F(|\psi\rangle) = 4 \max_{|\psi\rangle} (\Delta \hat{H})^2_{|\psi\rangle}, \tag{1.62}$$

where the maximum variance is dictated by the difference between the largest eigenvalue, $H_{\max}$, and the smallest eigenvalue, $H_{\min}$, of the collective Hamiltonian $\hat{H}$, satisfying the condition $(\Delta \hat{H})^2 \leq \frac{(H_{\max} - H_{\min})^2}{4}$. Since the Hamiltonian $\hat{H}$ is linear, we can express $H_{\max} = N h_{\max}$ and $H_{\min} = N h_{\min}$. This brings us to another significant conclusion: the maximum phase sensitivity allowed by quantum mechanics, referred to as the Heisenberg Limit (HL), is given by

$$\Delta\theta_{HL} = \frac{1}{N\sqrt{m}|h_{\max} - h_{\min}|}. \tag{1.63}$$

The primary distinction between the equations (1.59) and (1.63) lies in the enhanced scaling of phase sensitivity with the number of particles, a capability unattainable through classical means. The Heisenberg limit can be achieved using the state

$$|\psi_{\text{GHZ}}\rangle = \frac{1}{\sqrt{2}} \left(|h_{\max}\rangle^{\otimes N} + |h_{\min}\rangle^{\otimes N} \right), \tag{1.64}$$

which represents a maximally entangled state in the eigenstate basis of $\hat{h}$.

1.5.2 k-particle entangled states

In the previous sections, we explored two extreme scenarios: the fully separable state and the maximally entangled state, which correspond to the shot noise limit and the Heisenberg limit,

respectively. When examining many-particle systems, it is fascinating to investigate intermediate cases where only a subset of the N subsystems shows entanglement.

To clarify this concept, we introduce the definition of a k-producible state. A pure state involving $N \geq 2$ particles is classified as k-producible if it can be represented as a tensor product in the following manner:

$$|\psi_{k-\text{prod}}\rangle = |\psi_1\rangle \otimes |\psi_2\rangle \otimes \ldots \otimes |\psi_M\rangle, \tag{1.65}$$

where $|\psi_l\rangle$ denotes a state comprising $N_l \leq k$ particles, and the total particle count satisfies $\sum_{l=1}^{M} N_l = N$. This definition extends to mixed states: a mixed state is termed k-producible if it can be represented as a mixture of k_l-producible pure states:

$$\rho_{k-\text{prod}} = \sum_l p_l |\psi_{k_l-\text{prod}}\rangle\langle\psi_{k_l-\text{prod}}|, \quad \text{with } k_l \leq k, \tag{1.66}$$

where $p_l > 0$ and $\sum_l p_l = 1$. A state, either pure or mixed, is considered k-particle entangled if it is k-producible but not $(k-1)$-producible. This means a pure k-particle (or k-partite) entangled state can be expressed as:

$$|\psi_{k-\text{ent}}\rangle = \bigotimes_{l=1}^{M} |\psi_l\rangle, \tag{1.67}$$

where the product contains at least one state $|\psi_l\rangle$ involving $N_l = k$ particles that cannot be factorized [67]. Alternatively, we can state that a k-particle entangled state possesses an entanglement depth greater than $k-1$ [68].

In this section, we aim to establish the criteria for identifying useful multiparticle (or multipartite) entanglement [69, 70]. By utilizing the convexity of the quantum Fisher information (QFI), we derive the following result:

$$F(\rho_{k-\text{prod}}) \leq \sum_l p_l F(|\psi_{k_l-\text{prod}}\rangle) \leq \sum_l p_l 4(\Delta \hat{H})^2_{|\psi_{k_l-\text{prod}}\rangle}. \tag{1.68}$$

Given that the operator $\hat{H}$ is linear and that $|\psi_{k_l-\text{prod}}\rangle$ can be expressed in the product form shown in Eq. (1.65), we can derive the following relationship:

$$4\Delta \hat{H}^2_{|\psi_{kl-\text{prod}}\rangle} = \sum_{l=1}^{M} 4\Delta \hat{H}^2 |\psi_l\rangle \leq \sum_{l=1}^{M} \left(H^{(l)}_{\max} - H^{(l)}_{\min}\right)^2, \tag{1.69}$$

where $H^{(l)}_{\max}$ and $H^{(l)}_{\min}$ denote the maximum and minimum eigenvalues of $\hat{H}^{(l)} = \otimes_i^{N_l} \hat{h}_i$. This leads us to find:

$$\max_{\rho_{k-\text{prod}}} F_{\rho_{k-\text{prod}}} \leq (h_{\max} - h_{\min})^2 \max_{\{N_l\}} \left[\sum_{l=1}^{M} N_l^2\right], \tag{1.70}$$

where the maximum on the right side of this equation is calculated over all possible partitions $\{N_l\}$ of the system according to $\sum_{l=1}^{M} N_l = N$. Notably, since $(N_1+1)^2 + (N_2-1)^2 \geq N_1^2 + N_2^2$ when $N_1 \geq N_2$, the right-hand side of the equation above increases by maximizing the N_l values.

For a k-producible state, with $N_l \leq k$, we find:

$$\max_{\{N_l\}} \left[\sum_{l=1}^{M} N_l^2\right] = sk^2 + r^2, \tag{1.71}$$

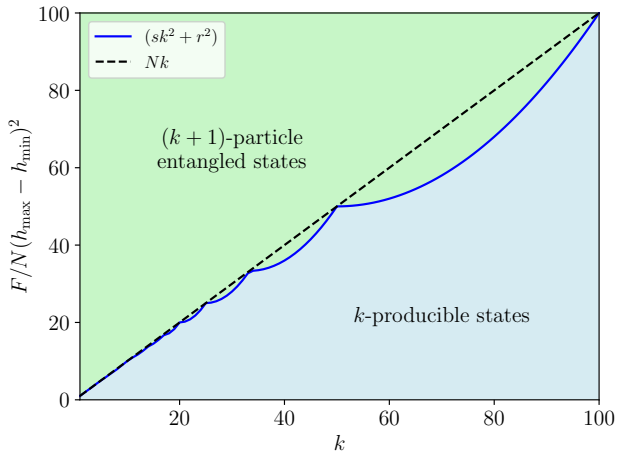

Figure 1.1: **Quantum Fisher Information Criterion for multipartite entanglement:** The solid line represents the bound given by $\frac{F}{(h_{\max}-h_{\min})^2} = (sk^2+r^2)$. This line effectively distinguishes k-producible states, which lie below it, from states that exhibit $(k+1)$-particle entanglement, found above the line. The dashed line illustrates the linear relationship $\frac{F}{(h_{\max}-h_{\min})^2} = Nk$, with N set to 100.

where $s = \lfloor \frac{N}{k} \rfloor$ is the largest integer less than or equal to $\frac{N}{k}$, and $r = N - sk$. The maximum QFI is thus achieved by the product of s GHZ states of k particles and a GHZ state with the remaining r particles:

$$|\psi\rangle = \bigotimes_{i=1}^{s} \left(\frac{|h_{\max}\rangle^{\otimes k} + |h_{\min}\rangle^{\otimes k}}{\sqrt{2}} \right) \otimes \left(\frac{|h_{\max}\rangle^{\otimes r} + |h_{\min}\rangle^{\otimes r}}{\sqrt{2}} \right). \tag{1.72}$$

Consequently, for k-producible states, we establish the bound:

$$F_{\rho_{k-\text{prod}}} \leq (h_{\max} - h_{\min})^2 (sk^2 + r^2). \tag{1.73}$$

Considering the linear operator $\hat{H}$ and the generic probe state $\hat{\rho}$, this criterion has a clear operational significance. If the bound is exceeded, then the probe state possesses useful $(k+1)$-particle entanglement: when used as the input state for the interferometer defined by the transformation $e^{-i\theta\hat{H}}$, $\hat{\rho}$ enables phase sensitivity that surpasses any k-producible state. A plot of the bound is illustrated in Fig. 1.1 as a function of k. Since the bound increases monotonically with k, the maximum achievable phase sensitivity also increases with the number of entangled particles. For $k = 1$, we recover the bound applicable to separable states. For $k = N - 1$, the bound is given by:

$$F[\rho_{(N-1)-\text{prod}}]/(h_{\max} - h_{\min})^2 \leq (N-1)^2 + 1, \tag{1.74}$$

where a QFI exceeding this value indicates that the state is fully N-particle entangled. The maximum value of the bound occurs for $k = N$ (hence $s = 1$ and $r = 0$), yielding:

$$F[\rho_{N-\text{ent}}]/(h_{\max} - h_{\min})^2 = N^2, \tag{1.75}$$

thus recovering equation (1.61).

Chapter 2

QFI and multipartite entanglement in spin-1 chains

In addition to be a crucial resource for quantum-enhanced metrology [31] and quantum computation [71], entanglement has been used to characterize quantum phases and quantum phase transitions (QPTs) in many-body models, particularly for low-dimensional systems, and has been important also to uncover exotic states of matter like topological spin liquids [72] or to describe many-body localization [73].

Bipartite entanglement has been the primary focus in the literature [74], with the area law [75] serving as a benchmark for relating the amount of entanglement between two partitions of a quantum many-body system to the surface area between the blocks [76, 77]. It has been proved [67] that the ground state of some spin chains should exhibit *Multipartite Entanglement* (ME), but somehow this topic has received less attention [67], despite the fact that many-body quantum states are far more complex than what can be captured with bipartite entanglement only.

A possible estimator of multipartite entanglement is *Quantum Fisher Information* (QFI), a quantity which is introduced in the context of the problem of phase estimation in metrology [65] and is of use in the study of the sensitivity of atomic interferometers beyond the shot-noise limit [78]. The QFI associated to local operators has recently been used to observe ME in models exhibiting Ginzburg-Landau-type quantum phase transitions [79] and in spin systems such as the Ising, XY, and Heisenberg models [79–81] also at finite temperature [82], where ME is expected to diverge at criticality. It has been pointed out, however, that the use of local operators in this method fails to detect ME at topological quantum phases and transitions. To address this issue, QFI-based methods need to be extended to include also non-local operators, as first outlined in [27, 28].

In this Chapter, we are going to study the ME in two paradigmatic spin-1 systems with nearest-neighbor interactions: the *Bilinear-Biquadratic (BLBQ) model* and the *XXZ model*, two models with a rich phase diagram which exhibit a topological Haldane phase. More specifically, we will show that QFI of non-local order parameters (such as string-order parameters [83]) gives indeed information about the ME of the ground state in the different phases of the models. Then, taking also in consideration QFI of local spin observables, we are able to classify all phases of the model as well as to calculate universal critical exponents at phase transitions.

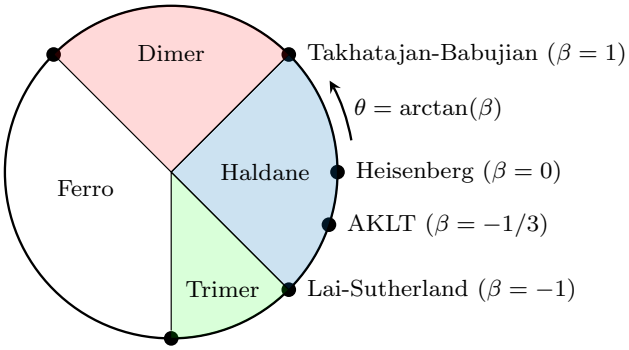

Figure 2.1: Phase diagram of BLBQ model on a circle, parametrized by θ, with some remarkable points: the AF Heisenberg model the AKLT point, and the critical points (Takhtajan-Babujian and Lai-Sutherland). In terms of β and J, the right half corresponds to a positive J and the left half to a negative J, while $\beta = \tan\theta$.

2.1 Bilinear-Biquadratic model

In this section we consider the *Bilinear-Biquadratic* (BLBQ) model on a chain of N sites:

$$H = J \sum_{i=1}^{N} \left[\boldsymbol{S}_i \cdot \boldsymbol{S}_{i+1} - \beta (\boldsymbol{S}_i \cdot \boldsymbol{S}_{i+1})^2 \right], \tag{2.1}$$

where $\boldsymbol{S}_i = (S_i^x, S_i^y, S_i^z)$ is the spin-1 operator for site i, J is the nearest-neighbor coupling and β is a real parameter expressing the ratio between the bilinear and biquadratic terms. This is the most general $SU(2)$-invariant isotropic spin-1 Hamiltonian with nearest-neighbor interactions only. Often in literature the Hamiltonian (2.1) is written as

$$H = J' \sum_{i=1}^{N} \left[\cos(\theta) \boldsymbol{S}_i \cdot \boldsymbol{S}_{i+1} - \sin(\theta) (\boldsymbol{S}_i \cdot \boldsymbol{S}_{i+1})^2 \right], \tag{2.2}$$

which can be obtained by setting $J = J' \cos(\theta)$ and $\beta = \tan(\theta)$, with the angular parameter $\theta \in [-\pi, \pi]$. By fixing $J' = 1$, the phase diagram can be drawn by varying the angular parameter θ, as shown in Fig. 2.1.

In the following we will describe the phases of the BLBQ model and some remarkable points.

2.1.1 Phase diagram

The *Haldane phase* corresponds to the region $-1 < \beta < 1$ and $J > 0$: here the system is massive, with a unique ground state and exponentially decaying correlation functions [84]. We recognize the antiferromagnetic Heisenberg model for $\beta = 0$ [85–87]. For $\beta = -1/3$ we recover the AKLT model, whose ground state is a Valence-Bond State (VBS), in which each spin-1 is thought of as made of two 1/2-spins that couple with the spins of neighboring sites in a singlet (entangled) state. A pictorial image of the AKLT state for a four sites chain is given in the upper panel of Fig. 2.2.

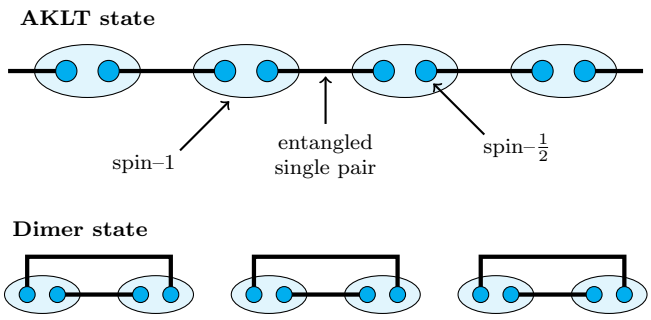

Figure 2.2: Example of states of the BLBQ model: every site (light blue oval) contains two spin-1/2 particles (blue dots) and each singlet state of spin-1/2 particles is represented with a thick black line. *Upper panel.* Entangled pair structure of the AKLT's ground state in the VBS representation. *Lower panel.* An example of spin-1 dimer state in the VBS representation with six sites.

The ground state has an exact description as a Matrix Product State, which is very useful for performing exact calculations. In particular, it can be shown that the local correlation functions have an exponential decay (see Appendix A).

The *Dimer phase* corresponds to $\beta > 1$ and $J > 0$, or $\beta < -1$ and $J < 0$: the system has a two-fold degenerate ground state and a small excitation gap [88]. The degeneracy is due to the broken translation symmetry, since neighboring spins tend to be coupled in pairs. A good approximation of the ground state in the whole phase is given by the dimer state [83]:

$$|d\rangle_{\pm} = \bigotimes_{i=1}^{L/2} \frac{1}{\sqrt{3}} \Big(|+\rangle_{2i} |-\rangle_{2i\pm1} + |-\rangle_{2i} |+\rangle_{2i\pm1} - |0\rangle_{2i} |0\rangle_{2i\pm1} \Big) \tag{2.3}$$

which is shown in the lower panel of Fig. 2.2. Haldane and Dimer phases are separated by the so-called *Takhtajan-Babujian critical point*, for $\beta = 1$ and $J > 0$. Here the Hamiltonian is integrable by means of Bethe Ansatz technique [89, 90] and its universality class is that of a $SU(2)_k$ Wess-Zummino-Witten conformal field theory with $k = 2$ and therefore with central charge $c = 3/2$ [91].

In the region $\beta < -1$ and $J > 0$ there is another antiferromagnetic phase, called the *Trimer Phase*, since the ground state tends to be invariant under translations of three sites. This is a gapless phase [92]. At $\beta = -1$, it is separated from the Haldane phase by a continuous phase transition. This point corresponds to the so-called *Lai-Sutherland model*, which has an enhanced symmetry to $SU(3)$, the Hamiltonian being equivalent to

$$\sum_{i=1}^{N-1} \boldsymbol{S}_i \cdot \boldsymbol{S}_{i+1} + (\boldsymbol{S}_i \cdot \boldsymbol{S}_{i+1})^2 = \frac{N}{3} + \frac{1}{2} \sum_{i=1}^{N-1} \sum_{a=1}^{8} \lambda_i^a \tag{2.4}$$

where λ^a are the Gell-Mann matrices, the eight generators of $SU(3)$ algebra. It is in the universality class of the $SU(3)_k$ Wess-Zummino-Witten conformal field theory with $k = 1$ [91, 93]. Here we will not consider the last phase present in Fig. 2.1, namely the ferromagnetic phase, which corresponds to an ordered and separable ground state.

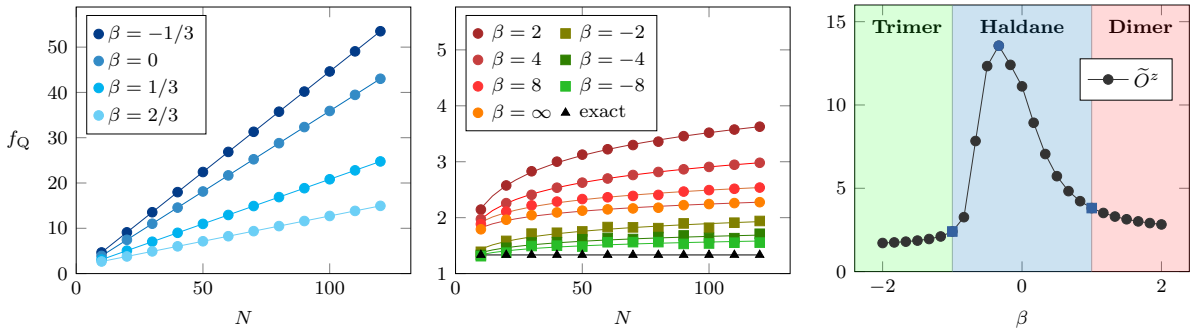

(a) Haldane phase. (b) Dimer and trimer phase. (c) QFI density at $N = 30$.

Figure 2.3: Scaling behaviors of the QFI density f_Q at different points of phase diagram using $\widetilde{O}^z$ in (2.6): (a) in the Haldane phase f_Q grows linearly, with the highest slope in correspondence of the AKLT point $\beta = -1/3$; (b) in the dimer and trimer phase f_Q grows logarithmically; (c) values of f_Q as a function of β with system size $N = 30$; the blue circle is the AKLT point where f_Q is maximal, while the two blue squares correspond to the phase-transition points.

The BLBQ model has a hidden symmetry (see Appendix A), that forces to introduce *non-local order parameters* (NLOPs) [83] to classify all phases. NLOPs, which are also called String Order Parameters, are defined as follows:

$$\widetilde{C}^\alpha = \lim_{r\to\infty} \left\langle S_1^\alpha \left(\prod_{k=2}^{r-1} e^{i\pi S_k^\alpha} \right) S_r^\alpha \right\rangle \tag{2.5}$$

where $\alpha = x, y, z$. The NLOPs $\widetilde{C}^\alpha$ have a non-zero expectation value only in the Haldane phase.

In the following, we will examine both the expectation value and the QFI of the non-local operator:

$$\widetilde{O}^z \equiv \sum_{j=1}^{N} \widetilde{S}_j^z \quad , \quad \widetilde{S}_j^z \equiv \left(e^{i\pi \sum_{l<j} S_l^z} S_j^z \right) \tag{2.6}$$

evaluated on the ground state $|\psi\rangle$ in the different phases of the BLBQ model. With some algebra one finds:

$$\langle \widetilde{O}^z \rangle = \sum_{l=1}^{N} \left\langle \left(\prod_{j=2}^{l-1} \Omega(j) \right) S_l^z \right\rangle \tag{2.7}$$

and

$$\langle (\widetilde{O}^z)^2 \rangle = \sum_{l=1}^{N} \langle (S_l^z)^2 \rangle - 2 \sum_{l<m} \left\langle S_l^z \left(\prod_{j=l+1}^{m-1} \Omega(j) \right) S_m^z \right\rangle, \tag{2.8}$$

where we have used

$$\Omega(l) = e^{i\pi S_l^z}, \quad \Omega^2(l) = \mathbb{I} \quad \text{and} \quad S_l^z \Omega(l) = -S_l^z. \tag{2.9}$$

These expressions are used to calculate the QFI

$$F_Q\left[|\psi\rangle, \widetilde{O}^z \right] = \left[\langle\psi| (\widetilde{O}^z)^2 |\psi\rangle - \langle\psi| \widetilde{O}^z |\psi\rangle^2 \right] \tag{2.10}$$

which coincides with what was discussed in the previous Chapter 1, up to a factor of 4 that we have neglected since we are dealing with a spin-1 operator with $\lambda_{\max} = -\lambda_{\min} = 1$.

2.1.2 Numerical results

To rewrite (2.8), it is useful to define the following $N \times N$ matrix:

$$M = \begin{pmatrix} \langle (S_1^z)^2 \rangle & \langle S_1^z S_2^z \rangle & \langle S_1^z \Omega(2) S_3^z \rangle & \cdots & \langle S_1^z \Omega(2) \cdots \Omega(N-1) S_N^z \rangle \\ 0 & \langle (S_2^z)^2 \rangle & \langle S_2^z S_3^z \rangle & \cdots & \langle S_2^z \Omega(3) \cdots \Omega(N-1) S_N^z \rangle \\ 0 & 0 & \langle (S_3^z)^2 \rangle & \cdots & \cdots \\ \cdots & \cdots & \cdots & \cdots & \cdots \\ 0 & 0 & 0 & \cdots & \langle S_{N-1}^z S_N^z \rangle \\ 0 & 0 & 0 & \cdots & \langle (S_N^z)^2 \rangle \end{pmatrix},$$

where each matrix element M_{ij} is given by

$$M_{ij} = \begin{cases} \langle S_i^z \, \Omega(i+1) \cdots \Omega(j-1) \, S_j^z \rangle & \text{if } i \leq j \\ 0 & \text{otherwise.} \end{cases} \tag{2.11}$$

Similarly, for the term (2.7) we can define the N-dimensional vector:

$$V = \left(\langle S_1^z \rangle, \langle \Omega(1) S_2^z \rangle, \ldots, \langle \Omega(1) \cdots \Omega(N-1)) S_N^z \rangle \right), \tag{2.12}$$

such that $\langle \widetilde{O}^z \rangle$ turns out to be the sum of all its elements.

In this way, the QFI can be written as

$$F_{\mathrm{Q}}\left[|\psi\rangle, \widetilde{O}^z \right] = \sum_{i=1}^{N} M_{ii} - 2 \sum_{i=1}^{N-1} \sum_{j>i}^{N} M_{ij} - \left(\sum_{i=1}^{N} V_i \right)^2, \tag{2.13}$$

Simulations to compute the elements of M and V can be easily implemented numerically. The states can be represented with Matrix Product States (MPSs) and the ground states can be obtained with the Density Matrix Renormalization Group (DMRG) algorithm. MPSs are Tensor Network (TN) techniques that are particularly effective in describing quantum states with short-range entanglement, making them ideal for representing ground states of local Hamiltonians in one dimension. These methods, although classical computation techniques, are considered quantum-inspired because they leverage the efficient representation of quantum states through matrices, significantly reducing computational complexity compared to a full state description. The DMRG algorithm is one of the most advanced methods for finding ground states, allowing for accurate solutions by using MPSs. A key parameter in MPS is the bond dimension, which controls the amount of entanglement the state can capture. While small bond dimensions are sufficient for systems with low entanglement, larger bond dimensions are required to accurately represent more entangled states, balancing between computational efficiency and accuracy. A comprehensive review on TNs and DMRG can be found in [94]. The numerical simulations have been done using the ITensor library [95, 96] and the DMRG computations have been performed with bond dimensions up to $\chi = 300$ and truncation error cutoff set to 10^{-12}, for a higher precision.

In order to investigate the scaling of the QFI density $f_{\mathrm{Q}} = F_{\mathrm{Q}}/N$, we have looked for a function of the form $q + bN^{\delta}$ (for the Haldane and critical points) or $q + b \ln N$ (for the dimer and trimer

phases), for system sizes up to $N = 120$. However, when the data showed a particularly flat trend, we have fitted f_Q against a constant function, in order to minimize the standard error on the parameters.

The results of the numerical calculations are summarized in Table 2.1 for the Haldane phase and in Table 2.2 for the Dimer and Trimer phases. The fit and their errors are computed using standard methods, like the one provided by Mathematica [97].

To analyze these results, let us start from the AKLT point, where the ground state is known exactly. To calculate the QFI analytically, we can exploit Lemma 2.6 of [84], extended to a string observable. Let O be an observable and N the system's size; then for any $l \leq N$ such that the support of O is contained in l, we have

$$\lim_{N\to\infty} \frac{\langle \Omega^N_{\alpha\beta}|O|\Omega^N_{\alpha\beta}\rangle}{\langle \Omega^N_{\alpha\beta}|\Omega^N_{\alpha\beta}\rangle} = \frac{\sum_{\alpha,\beta} \langle \Omega^l_{\alpha\beta}|O|\Omega^l_{\alpha\beta}\rangle}{\sum_{\alpha,\beta} \langle \Omega^l_{\alpha\beta}|\Omega^l_{\alpha\beta}\rangle} \tag{2.14}$$

where $|\Omega^N_{\alpha\beta}\rangle$ is one of the four ground states of the AKLT model (see Appendix A). This gives us an operational way to analytically calculate the terms of the QFI on the infinite volume ground state from (2.13) for a finite chain. It turns out that each diagonal term is equal to $2/3$ while each of the $N(N-1)/2$ off diagonal terms quickly approach to $-4/9$ (i.e. the value of NLOP (2.5) defined in the asymptotic limit) when N becomes larger. As the last addend in (2.13) is negligible, the QFI density for a system of N sites scales linearly as:

$$f_Q(|\psi_{\text{AKLT}}\rangle, \widetilde{O}^z) \simeq \frac{2}{9} + \frac{4}{9}N \tag{2.15}$$

as confirmed by numerical results in Table 2.1. The same argument holds for the Heisenberg point, where the asymptotic value of its NLOP is known to be $\simeq 0.36$ [98]. Furthermore, we observe that the QFI keeps a linear scaling in the whole Haldane phase, as shown in Fig. 2.3a. One can notice that the slope of the curves progressively decreases as we move away from the AKLT point.

When moving outside the Haldane phase, the linear scaling in the dimer and trimer phase becomes sublinear, as it can be seen in Fig. 2.3b. In the dimer phase, the numerical results can be compared with the analytical calculations performed on the dimer state (2.3) which can be considered a good approximation, as mentioned in Sec. 2.1. The resulting QFI density $f_Q(|d\rangle, \widetilde{O}^z)$ yields $4/3$, corresponding to a 2-partite entanglement structure, which is expected from the state (2.3) being a two-sites product state. Then, assuming that $\widetilde{O}^z$ is a good choice for the whole dimer phase, we can appreciate how good this approximation is in the different points of this phase, by comparing the various scaling with the exact value $4/3$. As we show in Table 2.2 and Fig. 2.3b, we get that a good function that fits the data is of the form $q + b \log N$, with b that progressively decreases when β goes to infinity.

We want to stress the crucial difference between the Haldane phase and the dimer and trimer ones. From the point of view of QFI criterion, the multipartite entanglement structure, in other words the k in (1.73), grows linearly with the system size in the Haldane phase while in the other two phases the k grows sublinearly. This may suggest that the ground state in the Haldane phase may not be factorizable in blocks of finite length in the thermodynamic limit, and this can be shown using only *non-local operators*. However, we cannot have direct information on the exact value of

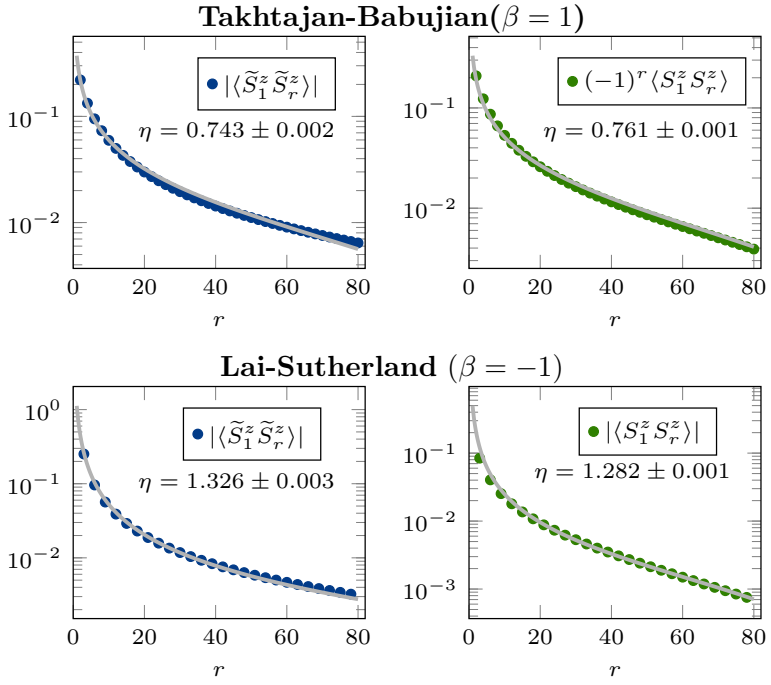

Figure 2.4: Power-law decay of correlation functions by using both string (in blue) and local (in green) operators in the Takhtajan-Babujian (upper panel) and Lai-Sutherland (lower panel) models. The dots are the computed value, while the gray line is obtained fit.

k using only $\widetilde{O}^z$, because we cannot be sure that this is the operator saturating the ground state QFI.

Let us now analyze the scaling behavior at the transition points $\beta = \pm 1$. The spin-spin correlations are asymptotically given by the fundamental WZW primary fields, leading to the prediction that, in an infinite system, the dominant antiferromagnetic correlations decay as a power law:

$$\langle S^\alpha_0 S^\alpha_r \rangle \sim \frac{(-1)^r}{|r|^\eta} \tag{2.16}$$

where $\eta = 2\Delta$ and the scaling dimension $\Delta = h + \bar{h}$ can be obtained from the primary field scaling dimension for a general $SU(n)$ level k WZW model [99]:

$$h = \bar{h} = \frac{n^2 - 1}{2n(n+k)} \tag{2.17}$$

As we said in the previous sections, $\beta = \pm 1$ are described by $SU(2)_2$ and $SU(3)_1$ conformal theories which means that their values of η are equal to $3/4$ and $4/3$ respectively. We recover this power-law scaling of correlators both for string and local operators, as we show in Fig. 2.4.

For $\beta = 1$, the numerical data display small oscillations between N even and odd, due to the double degeneracy that emerges in the dimer phase. To increase the accuracy of the fitting, we have decided to consider only the odd-numbered sites, this however does not modify the value of the exponents in the thermodynamic limit since these oscillations tend to zero as N increases.

As shown in [79], the QFI density of one-dimensional models at the critical point is supposed to scale as $f(O^\alpha) \sim N^{\delta_Q}$ (up to a non-universal pre-factor and sub-leading corrections) with $\delta_Q = 1 - 2\Delta^\alpha$, where Δ^α the scaling dimension of the operator O^α. We can recover this result from our approach and numerical data as well. Indeed, considering that the first sum in (2.13) goes as $\sim N$ (so it brings just a constant contribution in f) and neglecting V (because we are at the critical point), the only relevant contribution is given by the sum of the off-diagonal terms in the M matrix. Exploiting the (2.16) in the continuum limit, we get:

$$\sum_{r'=1}^{N-1} \sum_{r>r'}^{N} \langle S^\alpha_{r'} S^\alpha_r \rangle \longrightarrow \int_1^N dr' \int_{r'}^N \frac{dr}{r^\eta} \sim N^{2-\eta} \tag{2.18}$$

so that:

$$f_{\mathrm{Q}}(O^\alpha) \sim N^{1-2\Delta^\alpha} \tag{2.19}$$

The same holds for string operators up to a non-universal pre-factor and sub-leading corrections. It is evident now why we get the expected numerical value $\delta \simeq \delta_Q = 1 - 2\Delta = 1/4$ for the string magnetization, as reported in Table 2.1. A similar reasoning can be put forward for the calculation of $f_{\mathrm{Q}}(O^z_{\mathrm{st}})$ of the local staggered magnetization operator along z-axis, defined as

$$O^z_{\mathrm{st}} = \sum_{j=1}^{N} (-1)^j S^z_j. \tag{2.20}$$

Our numerical results for the calculation of the QFI density for O^z_{st} yield: $q = -3.770 \pm 0.002$, $b = 3.201 \pm 0.001$ and $\delta = 0.244 \pm 0.001$. Thus, we are able to read the critical exponent of the operator from its QFI.

At the Lai-Sutherland point $\beta = -1$, the numerical data display small oscillations with a periodicity of three sites, due to the trimer configuration that merges for $\beta < -1$. Unfortunately, from the data we observe what is mostly probable a flat trend, but we are not able to distinguish a linear fit from a one that decreases exponentially or, like it should be in this case, as a power law with a negative exponent. We believe that the pre-factors and sub-leading terms, that depend on N, might contribute to mask the predicted behavior at criticality.

2.2 XXZ spin-1 model

2.2.1 Phase diagram

The XXZ spin-1 chain is a well-studied quantum system that exhibits an interesting phase diagram as a function of the anisotropy parameter J_z. It has the following Hamiltonian:

$$H = \sum_{i=1}^{N-1} J_{xy}(S^x_i S^x_{i+1} + S^y_i S^y_{i+1}) + J_z(S^z_i S^z_{i+1}) \tag{2.21}$$

where we take $J_{xy} = 1$ and let J_z vary. It can also be considered as a particular case of the so-called $\lambda - D$ model [83], that includes also an isotropy term of the form $\sum_{i=1}^N D(S^z_i)^2$.

BLBQ model $f_{\mathrm{Q}}(\lvert\psi_\beta\rangle, \widetilde{O}^z) = q + bN^\delta$			
Haldane phase			
β	q	b	δ
$-1/3$	0.225±0.003	0.4441±0.0001	1.0002±0.0001
0	0.35 ±0.05	0.355 ±0.002	1.002 ±0.003
1/3	1.122±0.009	0.197 ±0.004	0.9999±0.0005
2/3	1.55 ±0.04	0.111 ±0.020	0.997 ±0.001
1	−3.632±0.004	3.132 ±0.002	0.252 ±0.001

Table 2.1: Numerical values of the fitting parameters in the Haldane phase.

BLBQ model $f(\lvert\psi_\beta\rangle, \widetilde{O}^z) = q + b\ln N$					
Dimer phase			Trimer phase		
β	q	b	β	q	b
2	0.81 ±0.04	0.58±0.01	−2	0.98±0.06	0.19±0.01
4	1.03 ±0.01	0.40±0.03	−4	1.08±0.06	0.12±0.01
8	1.34 ±0.05	0.24±0.01	−8	1.11±0.05	0.09±0.01
∞	1.39 ±0.04	0.18±0.01			

Table 2.2: Numerical values in the dimer and trimer phases.

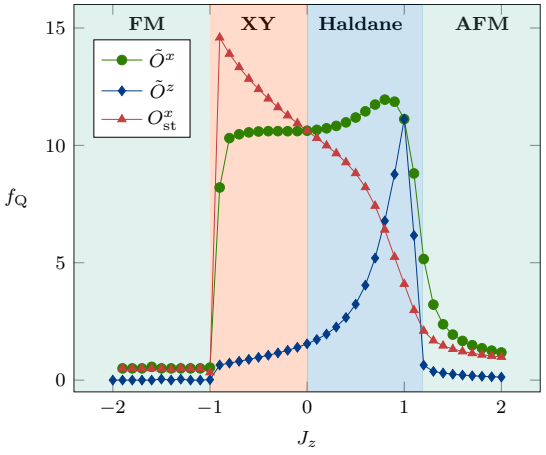

Figure 2.5: Trend of QFI densities in the phase diagram of the XXZ model of size $N = 30$, with the string magnetizations $\widetilde{O}^z$, $\widetilde{O}^x$, and the local magnetization O^x_{st}. From left to right: ferromagnetic (FM) phase, XY gapless phase, Haldane phase and antiferromagnetic (AFM) phase. The critical points are located at $J_z = -1$, $J_z^{(\mathrm{BKT})} = 0$ and $J_z^{(\mathrm{IS})} = 1.186$.

The quantum phase diagram of this Hamiltonian has been extensively studied [100]. It includes the *Haldane phase* for $0 < J_z \sim 1$. A second-order phase transition occurs from the Haldane phase to an antiferromagnetic (AFM) phase that belongs to the same universality class of the 2D Ising model with central charge $c = 1/2$. Various numerical techniques, including Monte-Carlo [101] and DMRG [102, 103], have determined the critical value: $J_z^{(\mathrm{IS})} = 1.186$. A *Berezinskii-Kosterlitz-Thouless* (BKT) transition occurs at $J_z^{(\mathrm{BKT})} = 0$ between the Haldane phase and a gapless disordered XY phase ($-1 < J_z < 0$). The value of $J_z^{(\mathrm{BKT})}$ is theoretically predicted to be exactly zero, using bosonization techniques [104]. Numerically, this has been verified via finite-size scaling [105, 106] and DMRG [102]. The entire XY phase (including the BKT transition point) is a critical phase, which has conformal symmetry with central charge $c = 1$. Finally, at $J_z = -1$, a first-order phase transition from the XY phase to a ferromagnetic (FM) phase takes place [100, 103, 107]. We will not examine in detail such ferromagnetic phase in the following.

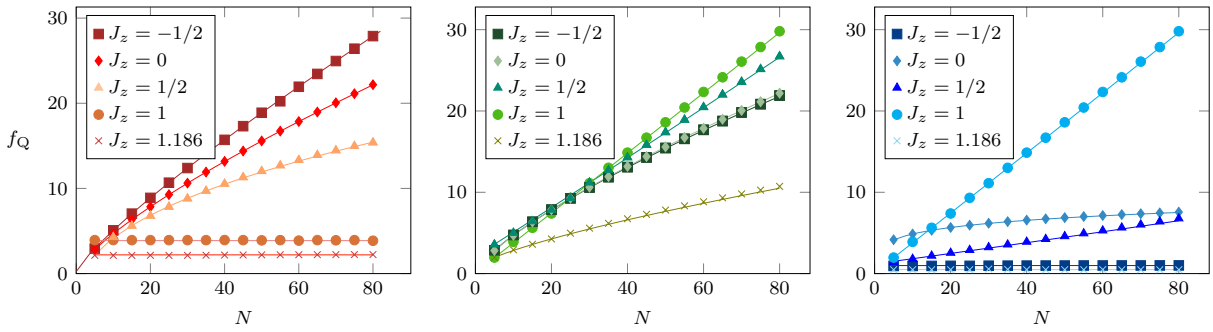

(a) Staggered magnetization O^x_{st} (b) String operator $\widetilde{O}^x$ (c) String operator $\widetilde{O}^z$

Figure 2.6: Scaling behaviors of the QFI density of different operators at some points of interest: (a) staggered magnetization O^x_{st} (shades of red); (b) x-string operator $\widetilde{O}^x$ (shades of green); (c) z-string operator $\widetilde{O}^z$ (shades of blue). Notice the abrupt change in behavior for the string operators $\widetilde{O}^x$ and $\widetilde{O}^z$ from $J = 1$ to $J = 1.186$, which can also be seen in Fig. 2.5.

2.2.2 Numerical results

Given the symmetries of the Hamiltonian, we consider the scaling behavior of the QFI density of local and string operators along the x and z axes, including the staggered ones. The ones that show an extensive scaling, at least in some phases of the model, are the following:

$$\widetilde{O}^z = \sum_{i=1}^{N} \widetilde{S}^z_i, \quad \widetilde{O}^x = \sum_{i=1}^{N} \widetilde{S}^x_i, \quad O^x_{\text{st}} = \sum_{i=1}^{N} (-1)^i S^x_i, \tag{2.22}$$

where, as usual, the operators with the tilde symbol are string operators. Similarly to the previous section, the numerically computed QFI density f_Q is fitted against the function $f_Q = q + bN^\delta$, or with a constant if the data presents an extremely flat trend.

In Fig. 2.5 we plot the shapes of the QFI densities of the operators (2.22) in the different phases of the model for a chain with $N = 30$ sites. The results of the fitting of the scaling with N are given in Tables 2.3, 2.4 and 2.5 and some details of the scaling are reported in Fig. 2.5. Let's analyze each operator below.

The operator O^x_{st} takes its maximal value close to the FM-XY transition point and then decreases progressively moving toward the Haldane phase. In particular, analyzing its scaling with N (see Fig. 2.6a and Table 2.3), f_Q reveals a power-law behavior in the XY phase with the coefficient $\delta = 0.8376 \pm 0.0001$ at $J_z = -1/2$ which gradually reduces (e.g. $\delta = 0.7574 \pm 0.0002$ at $J_z = 0$) until it vanishes for $J_z \gtrsim 1$.

Regarding the string operators (see Tables 2.4 and 2.5), it is possible to observe that $f_Q(\widetilde{O}^x)$ has a power-law scaling in the whole XY phase (including $J_z = 0$) where the $f_Q(\widetilde{O}^z)$ appears to be almost flat, ($\delta = 0.138 \pm 0.003$). In the Haldane phase, the QFI for both these operators shows a linear scaling ($\delta \simeq 1$) with a slope that increases with J_z, reaching the maximal values at $J_z = 0.8$ and $J_z = 1$ respectively. For $J_z = 1$ we recover the Heisenberg model where both have the same scaling coefficients as expected in an isotropic point.

The data on QFI can be used to extract information about the critical exponents of relevant operators at phase transition points and about correlation functions in general. At the critical point $J_z^{(\mathrm{IS})}$, we predict that the scaling dimension of the order parameter is $\Delta = 1/8$, in accordance with the universality of the 2D Ising model, since $\delta = 1 - 2\Delta \simeq 3/4$. This holds true for the string order operator $\widetilde{O}^x$, see Table 2.4, and the local staggered magnetization O^z_{st}. The latter is defined similarly to O^x_{st} in (2.22), for which we obtained $\delta = 0.76 \pm 0.01$.

More generally, we can consider the asymptotic behavior of local staggered and string correlation functions

$$\begin{aligned} C^\alpha_{\mathrm{st}}(r) &= (-1)^r \langle S^\alpha_1 S^\alpha_r \rangle \,, \\ \widetilde{C}^\alpha(r) &= \left\langle S^\alpha_1 \left(\prod_{k=2}^{r-1} e^{i\pi S^\alpha_k} \right) S^\alpha_r \right\rangle \end{aligned} \tag{2.23}$$

which are known to have the following behavior for large r in the (massive) Haldane phase [108]:

$$C^\alpha = a_0 \frac{e^{-\frac{r}{a_1}}}{\sqrt{r}}, \qquad \widetilde{C}^\alpha = a_2 + a_0 \frac{e^{-\frac{r}{a_1}}}{r^2} \tag{2.24}$$

where a_0, a_1 and a_2 are fitting parameters and $\alpha = x, z$ as usual, while at the transition point, they scale algebraically:

$$C^z = \widetilde{C}^x = \frac{a_0}{r^{1/4}}, \quad C^x = a_0 \frac{e^{-\frac{r}{a_1}}}{r^{1/4}}, \quad \widetilde{C}^z = a_2 + \frac{a_0}{r^2}. \tag{2.25}$$

The data reported in the Tables 2.3, 2.4 and 2.5 and Fig. 2.6 of the fitting parameters of f_{Q} are in agreement with these theoretical predictions. In order to understand the results, two comments are necessary.

The first one is that in the Haldane phase and at the critical points the only relevant contribution to the QFI density is due to (2.8), i.e. the M matrix made by the spin-spin correlators. The second one is that, as we said previously for the BLBQ, from our data it is not possible to distinguish the flat scaling of f_{Q} from an exponential or power-law decay with $\delta < 0$. Then, considering the correlations (2.24) and (2.25), we can understand that for string operators in the Haldane phase, the elements M_{ij} are going to approach a_2. This leads to a f_{Q} that scales linearly, with the slope $b \simeq a_2$. From our computations we get δ equal to 0.757 ± 0.001 and 0.727 ± 0.001 for O^z_{st} and $\widetilde{O}^x$, respectively, which is comparable to $1 - \eta$ as expected.

Finally, when $-1 < J_z < 0$, the system is in the XY phase. In this extended area of critically, also called "critical fan", the Hamiltonian can be replaced by the Hamiltonian of a Gaussian model [109], which admits two primary operators with conformal dimensions:

$$\Delta_1 = \frac{1}{8}, \qquad \Delta_2 = \frac{1}{4}\chi(J_z), \tag{2.26}$$

where χ is a function of the coupling J_z such that $\chi(0) = 1/2$ and $\chi(-1) = 0$. The explicit form of the function χ depends on the details about how the lattice model can be mapped to the Gaussian model at criticality. This means that there exists one operator for which the critical index δ of QFI densities will be constantly $3/4$ and one with varying between $3/4$ and 1, respectively. We identify such operators with $\widetilde{O}^x$ and O^x_{st}, respectively, as it suggested by the data of Tables 2.3 and

2.4: at $J_z = 0$ the values of their fitting parameters are extremely close to each other and close to 0.75; moving toward $J_z = -1/2$, $f_{\rm Q}(\widetilde{O}^x)$ remains fixed to a similar value ($\delta = 0.745 \pm 0.002$) while $f_{\rm Q}(O^x_{\rm st})$ has $\delta = 0.8376 \pm 0.0001$ and the latter continues to increase as suggested by Fig. 2.5.

XXZ model, staggered magnetization $f\big(\,\vert\psi_{(J_z)}\rangle\,, O^x_{\rm st}\big) = q + bN^\delta$			
J_z	q	b	δ
$-1/2$	0.231±0.003	0.7041±0.0002	0.8376±0.0001
0	0.138±0.003	0.797 ±0.001	0.7574±0.0002
1/2	−3.5 ±0.5	2.800 ±0.004	0.43 ±0.01
1	3.77 ±0.06		
1.186	2.199±0.009		

Table 2.3: Numerical values of the fitting parameters of the QFI density for the staggered magnetization $O^x_{\rm st}$ at different point of the XXZ model.

XXZ model, x-string operator $f(\vert\psi_{(J_z)}\rangle\,, \widetilde{O}^x) = q + bN^\delta$			
J_z	q	b	δ
$-1/2$	0.11 ±0.04	0.829 ±0.009	0.745 ±0.002
0	0.131±0.001	0.7992±0.0002	0.7570±0.0001
1/2	7.2 ±0.3	1.26 ±0.03	0.996 ±0.002
1	0.16 ±0.05	0.356 ±0.004	1.008 ±0.002
1.186	2.74 ±0.05	1.65 ±0.01	0.727 ±0.001

Table 2.4: Numerical values of the fitting parameters of the QFI density for the x-string operator $\widetilde{O}^x$ at different points of the XXZ model.

XXZ model, z-string operator $f(\vert\psi_{(J_z)}\rangle\,, \widetilde{O}^z) = q + bN^\delta$			
J_z	q	b	δ
$-1/2$	0.989 ±0.003		
0	−3.1 ±0.1	5.8 ±0.1	0.138 ±0.003
1/2	1.21 ±0.04	0.058 ±0.004	1.03 ±0.01
1	0.16 ±0.05	0.356 ±0.004	1.008 ±0.002
1.186	0.489 ±0.007		

Table 2.5: Numerical values of the fitting parameters of the QFI density for the z-string operator $\widetilde{O}^z$ at different points of the XXZ model.

2.3 Conclusions and outlooks

In this chapter, we have shown how QFI is able to detect multipartite entanglement (ME) in spin-1 chains with short range interactions. A key aspect in these calculations is the use of string operators whereas the QFI relative to local operators fails to detect ME, especially in the topological phases of these models, i.e. the Haldane phase. For the BLBQ model, given the symmetries of the Hamiltonian, we chose the string magnetization along z and obtained an extensive behavior in the topological phase, signaling the divergence of ME with the system size. The same applies to the Haldane phase of XXZ model as well.

In the dimer and trimer phases we found a sublinear behavior; in particular for the dimer phase, we also propose to use QFI density to estimate how well the 2-sites product state is approximating

the various ground states in this phase. Furthermore, we recover the expected power-law scaling of the QFI density for these 1D models in the critical phases. In fact, by knowing the critical exponent η of the correlators or the scaling dimension Δ of the operator with which the QFI is calculated, it is possible to predict how f_{Q} will scale at these critical points: $\delta = 1 - 2\Delta$.

From numerical simulation we obtained $\delta \simeq 0.25$ in the Takhtajan-Babujian point of BLBQ model and $\delta \simeq 0.75$ in the AFM-Haldane transition point of XXZ model as expected. Throughout the "critical fan" (XY phase) of the XXZ model, we observe a power-law behavior of f_{Q} with two different trends of δ: one fixed at the constant value of $3/4$ (string operator $\widetilde{O}^x$), the other varying between $3/4$ and 1 (staggered magnetization O^x_{st}) in analogy to what was done in [109].

We remark that QFI is useful for characterizing the different phases of a model, through its entanglement content. On the other hand, it is not the most appropriate tool for localizing the transition points, because it would require a tedious analysis of how the scaling of the QFI changes close to a critical point, having to include constant terms that often complicate the fitting procedures.

In the light of these promising results, it would be interesting to investigate whether it is feasible to use it for systems with more complicated degrees of freedom, such as models with higher symmetry groups [110] or with long range interactions [111].

Chapter 3

QAOA and Natural Gradient in a noisy Rydberg atoms device

Hybrid quantum-classical variational algorithms [112–114] are essential for exploring the potential of noisy intermediate-scale quantum (NISQ) devices [115]. These algorithms combine classical computation with quantum processing, where classical resources are used to optimize the parameters of quantum states. By employing heuristic techniques, they tackle variational problems, particularly combinatorial optimization tasks, which are both prevalent and critical in many real-world applications [116]. Consequently, these methods have garnered substantial interest from industries looking to leverage quantum computing, as solving such problems remains notoriously difficult for classical algorithms alone.

The Quantum Approximate Optimization Algorithm (QAOA) [117] stands out among hybrid variational algorithms for its promise in achieving quantum speedups on NISQ devices, drawing considerable interest [118]. QAOA has been successfully implemented across a variety of experimental platforms, such as Rydberg atom arrays [119], superconducting processors [120], and trapped-ion systems [121].

Similar to other hybrid algorithms, QAOA involves applying a series of parameterized quantum gates to a quantum state with the goal of minimizing the expectation value of an observable, typically the system's Hamiltonian. The classical part of the algorithm optimizes the gate parameters to achieve this minimization, requiring frequent evaluations of the Hamiltonian's expectation value [122]. The interplay between quantum execution and classical optimization demands repeated runs of the quantum circuit, making the process resource-intensive. This implies that finding the minimum of the cost function in just a few steps plays a crucial role.

A significant challenge in this approach is the occurrence of barren plateaus: large flat areas of the parameters landscape with exponentially small gradients as the number of qubits and circuit depth increase [123]. This problem can be exacerbated by noise [124] or by employing cost functions dependent on global observables [125].

This study will focus on a paradigmatic problem: finding the ground state preparation of the Transversal Field Ising Model (TFIM). In particular, we want to combine the QAOA algorithm with a Quantum-Natural-Gradient-based optimizer and test his performance on simulations of real noisy quantum devices. The initial exploration of applying the Quantum Natural Gradient (QNG)

to improve quantum variational algorithms was introduced by [126]. Several studies have since demonstrated the potential advantages of using natural gradient techniques in these algorithms [127, 128]. The main idea is to leverage information derived from the geometry of the Hilbert space. In particular, this involves equipping gradient descent with the real part of the quantum geometric tensor, i.e. the Fubini-Study metric, to accelerate the algorithm's convergence toward the solution. Building on this foundation, further research extended the natural gradient approach to tackle challenges such as noise and non-unitary evolutions in quantum systems [129], using their own noise models along with some procedure to compute the Fubini-Study metric.

In light of the existing work, our aim is to demonstrate the implementation of this protocol on a real quantum machine, such as a Rydberg atom array device, and evaluate the algorithm's robustness against the specific noise characteristic of these platforms. A key challenge lies in effectively applying QAOA evolutions by tuning laser parameters and leveraging the Rydberg blockade mechanism. These devices offer both digital and analog quantum computing, with the latter using global pulses to evolve the entire system. This avoids the need for local qubit addressing, which is often difficult to achieve in practice and more susceptible to noise.

3.1 Quantum Approximate Optimization Algorithm and Natural Gradient

The Quantum Approximate Optimization Algorithm (QAOA) is a hybrid quantum-classical algorithm designed to solve combinatorial optimization problems. It was first proposed by Edward Farhi and Jeffrey Goldstone in 2014 [117] and has since become one of the most promising quantum algorithms for near-term quantum devices. The algorithm consists of two main components: a classical optimizer and a quantum circuit that prepares a parameterized trial state on a quantum computer. The key idea is to iteratively adjust the parameters to minimize the expectation value of the cost Hamiltonian, thereby approaching the optimal solution.

3.1.1 QAOA Circuit

The QAOA circuit, as shown in Fig. 3.1, involves the following steps:

1. **Initialization**. The algorithm starts with an initial state, typically the uniform superposition state $|+\rangle^{\otimes N}$, where N is the number of qubits.

2. **Parameterized evolution**. The state is then evolved using two types of unitary operators:

   - *Cost Hamiltonian Unitary*: $U_c(\gamma) = e^{-i\gamma H_c}$
   - *Mixer Hamiltonian Unitary*: $U_m(\beta) = e^{-i\beta H_m}$

   Here, H_c is the cost Hamiltonian and H_m is the mixer Hamiltonian, usually chosen as $H_m = \sum_{i=1}^{N} \sigma_i^x$, where σ_i^x are Pauli-X operators acting on the i-th qubit.

3. **Layered structure**. The evolution is applied in layers, where each layer consists of a pair of unitaries $U_c(\gamma)$ and $U_m(\beta)$. The depth of the QAOA circuit is determined by the number of layers P, leading to a trial state:

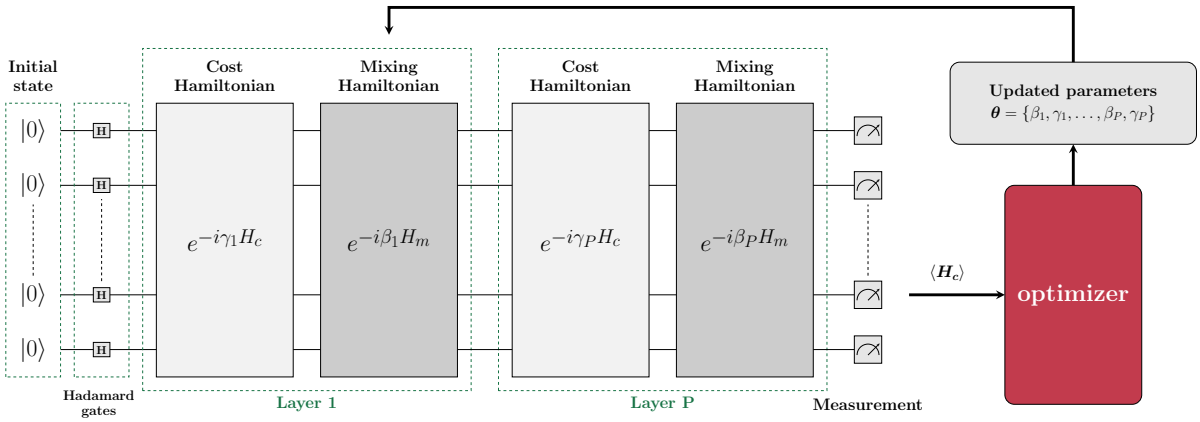

Figure 3.1: QAOA scheme: starting from an initial state, Hadamard gates prepare a superposition. Each layer alternates between the application of the Cost Hamiltonian $e^{-i\gamma H_c}$ and the Mixing Hamiltonian $e^{-i\beta H_m}$. The parameters γ and β are iteratively optimized to minimize the cost function $\langle H_c \rangle$ after the measurement phase.

$$|\psi(\vec{\gamma}, \vec{\beta})\rangle = U_m(\beta_P)U_c(\gamma_P) \cdots U_m(\beta_1)U_c(\gamma_1)|+\rangle^{\otimes N}$$

Here, $\vec{\gamma} = (\gamma_1, \gamma_2, \ldots, \gamma_p)$ and $\vec{\beta} = (\beta_1, \beta_2, \ldots, \beta_p)$ are the parameters to be optimized.

4. **Measurement and optimization**. The expectation value of the problem Hamiltonian is measured in the trial state:

$$E_c = \langle \psi(\vec{\gamma}, \vec{\beta}) | H_c | \psi(\vec{\gamma}, \vec{\beta}) \rangle \tag{3.1}$$

A classical optimizer adjusts the parameters $\vec{\gamma}$ and $\vec{\beta}$ to minimize this expectation value, iterating the process until convergence.

The QAOA merges the advantages of both quantum and classical computing. It harnesses quantum parallelism and entanglement to navigate the solution space, while relying on classical optimization methods to adjust the parameters.

3.1.2 Application to the Transverse Field Ising Model

In our study, we apply QAOA to the TFIM, a well-known model in quantum mechanics and statistical physics. The Hamiltonian for the 1D TFIM is given by:

$$H_c = -J \sum_{i=1}^{N} \sigma_i^z \sigma_{i+1}^z - h \sum_{i=1}^{N} \sigma_i^x \tag{3.2}$$

where σ_i^z and σ_i^x are Pauli-Z and Pauli-X operators acting on the i-th qubit, J is the interaction strengths between neighboring spins, and h is the transverse field strength. By optimizing the parameters of the QAOA circuit, we aim to find the ground state of this Hamiltonian, which corresponds to the solution of the optimization problem.

As previously mentioned, the QAOA algorithm follows a sequence of well-defined steps, though it permits flexibility in the choice of Hamiltonians used for evolving the system. The only constraint

is that the two Hamiltonians –the cost Hamiltonian and the mixer– must not commute with each other. Specifically, for the TFIM, it can be shown, by using exact diagonalization techniques provided by the `QuTiP` library [130], that selecting the cost Hamiltonian unitary as $U_{zz}(\gamma) = e^{-i\gamma H_{zz}}$ where $H_{zz} = \sum_i \sigma_i^z \sigma_{i+1}^z$, ensures that the ground state is reached at a depth of $P = \left\lfloor \frac{N}{2} \right\rfloor$. This implies that circuits with such a depth are sufficiently expressive to capture the ground state while maintaining the symmetries of the Hamiltonian. Hence, we adopt this parameterization for the algorithm's evolution, subject to validation during implementation on the selected platform, which inevitably includes certain approximations, both with and without noise.

The energy value obtained at the end of the optimization procedure E_c can be compered with the exact one E_0, allowing us to compute the accuracy:

$$\delta E := \frac{E_c - E_0}{|E_0|}. \tag{3.3}$$

The exact value of the energy, coming from the analytical solution of the TFIM, can be computed:

$$E_0 = -E_1 - 2\sum_{q=1}^{r} \frac{1}{1 + h^2 + 2h\cos\alpha_q}, \tag{3.4}$$

where:

$$r = \left\lfloor \frac{N}{2} \right\rfloor, \quad \alpha_q := \begin{cases} \frac{(2q-1)\pi}{N} & for\ N\ even \\ \frac{2q\pi}{N} & for\ N\ odd \end{cases} \quad \text{and} \quad E_1 := \begin{cases} 0 & for\ N\ even \\ 1+h & for\ N\ odd. \end{cases} \tag{3.5}$$

Our implementation of QAOA on a real quantum platform, i.e. such as Rydberg atoms, aims to demonstrate the algorithm's robustness and effectiveness even in the presence of different sources of noise.

3.1.3 Quantum Natural Gradient

Gradient descent is an optimization algorithm used to minimize a function by iteratively moving towards the steepest descent, as defined by the negative of the gradient. It is commonly used in machine learning and statistics to optimize models by adjusting parameters [131].

Here's a brief overview of the method: we start with an initial guess for the parameters, denoted as $\boldsymbol{\theta} = (\theta_1, \theta_2, \ldots, \theta_n)$. Next, we calculate the gradient of the loss function $C(\boldsymbol{\theta})$ parameter and update the parameters by moving in the opposite direction of the gradient. The update rule for each parameter θ_i is given by:

$$\boldsymbol{\theta}^{(t+1)} = \boldsymbol{\theta}^{(t)} - \eta \nabla C(\boldsymbol{\theta}^{(t)}), \tag{3.6}$$

where η is the learning rate, a small positive number that controls the step size. These steps are repeated until convergence that is typically defined by a condition such as:

$$\|C(\boldsymbol{\theta}^{t+1}) - C(\boldsymbol{\theta}^{t})\| < \varepsilon, \tag{3.7}$$

where ε is a small threshold indicating that the changes in the parameters are sufficiently small.

Classical natural gradient descent modifies the parameter update by multiplying the gradient with the inverse of Fisher Information matrix $I^{-1}(\boldsymbol{\theta})$, which captures the geometry of the statistical

model. Specifically, natural gradient descent scales the gradient to account for the local curvature of the space of probability distributions, making the update more efficient [132–135].

Classically, the Fisher information measures the sensitivity of a probability distribution to parameter changes. In quantum systems, the Quantum Fisher Information (QFI) extends this concept, as we described in Chapter 1.

Thus, the update rule for parameters with QAOA ansatz becomes:

$$\boldsymbol{\theta}^{(t+1)} = \boldsymbol{\theta}^{(t)} - \eta F(\boldsymbol{\theta}^{(t)})^{-1} \nabla E(\boldsymbol{\theta}^{(\boldsymbol{t})}). \tag{3.8}$$

where we denote $\boldsymbol{\theta} = (\gamma_1, \beta_1, \gamma_2, \beta_2, \cdots, \gamma_P, \beta_P)$, $\rho_i = |\psi\rangle\langle\psi|$ is the state obtained by evolving $|+\rangle$ through all the unitary operators, up to the one parameterized by θ_i such that $E(\boldsymbol{\theta}) := \mathrm{Tr}[\rho_{2P}(\boldsymbol{\theta}) H_c]$. A simple yet highly illustrative example, encapsulating the core message of this method, can be seen in Fig. 3.2.

Calculating F for arbitrary quantum states can be quite complex. For rank-r density matrices given by $\rho(\theta) = \sum_{n=1}^{r} \lambda_n |\psi_n\rangle\langle\psi_n|$, the entries are defined by the formula (1.9), provided below:

$$F_{ab} = \sum_{\lambda_i \in S} \frac{(\partial_a \lambda_i)(\partial_b \lambda_i)}{\lambda_i} + \sum_{\lambda_i \in S} 4\lambda_i \,\mathrm{Re}\left(\langle \partial_a \psi_i | \partial_b \psi_i \rangle\right) - \sum_{\lambda_i, \lambda_j \in S} \frac{8\lambda_i \lambda_j}{\lambda_i + \lambda_j} \,\mathrm{Re}\left(\langle \partial_a \psi_i | \psi_j \rangle \langle \psi_j | \partial_b \psi_i \rangle\right).$$

For pure states, this expression simplifies to the Fubini-Study metric tensor, up to a constant factor:

$$\begin{aligned} F_{ab} &= 4\mathrm{Re}\left[\langle \partial_a \psi | \partial_b \psi \rangle - \langle \partial_a \psi | \psi \rangle \langle \psi | \partial_b \psi \rangle\right] = \\ &= 4\left[\langle \psi_{a-1} | H_a \left(\prod_{k=a}^{b-1} e^{i\theta_k H_k} \right) H_b | \psi_{b-1} \rangle - \langle \psi_{a-1} | H_a | \psi_{a-1} \rangle \langle \psi_{b-1} | H_b | \psi_{b-1} \rangle \right]. \end{aligned} \tag{3.9}$$

The last equality arises because we are considering the unitary parameter embedding induced by the QAOA, where $H_a = H_{zz}$ if a is odd and $H_a = H_m$ otherwise. For the diagonal elements, this expression simplifies to:

$$F_{aa} = 4\left[\langle \psi_{a-1} | H_a^2 | \psi_{a-1} \rangle - \langle \psi_{a-1} | H_a | \psi_{a-1} \rangle^2\right] \tag{3.10}$$

In this study, we will also address mixed states arising from noisy circuits, so we choose to compute the Quantum Fisher Information matrix (QFIm) using the following approximation:

$$F_{ab} = 4\left[\mathrm{Tr}\left(\rho_{a-1} H_a \left(\prod_{k=a}^{b-1} e^{i\theta_k H_k} \right) H_b \rho_{b-1}\right) - \mathrm{Tr}\left(\rho_{a-1} H_a\right) \cdot \mathrm{Tr}\left(\rho_{b-1} H_b\right)\right] \tag{3.11}$$

and, for the diagonal elements:

$$F_{aa} = 4\left[\mathrm{Tr}\left(\rho_{a-1} H_a^2\right) - \left(\mathrm{Tr}\left(\rho_{a-1} H_a\right)\right)^2\right]. \tag{3.12}$$

Indeed, the resulting mixed state can be expressed in terms of its spectral decomposition as follows:

$$\rho = \lambda_0 |\psi\rangle\langle\psi| + \sum_{m=1}^{d} \lambda_m |\psi_m\rangle\langle\psi_m| \tag{3.13}$$

It has been shown that quantum hardware is expected to generate mixed quantum states, where the dominant eigenvector $|\psi\rangle$ closely approximates the ideal computational quantum state. This occurs due to the significant entropy of the error eigenvalues (probabilities) λ_m, which tends to increase with the system size (see [129, 136, 137]). Thus, in the limit where all λ_m are small, indicating that the noisy state is not far from a pure one, Eq. (3.11) provides a good approximation of the QFI.

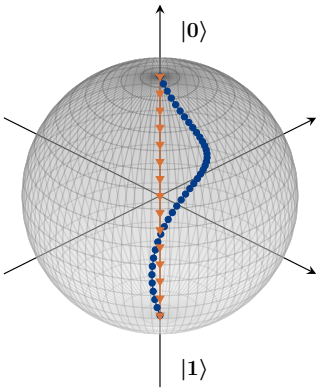

Figure 3.2: Comparison of the optimization paths on the Bloch sphere for minimizing σ_z (i.e., reaching $|1\rangle$) using vanilla gradient (blue) and Quantum Natural Gradient (QNG) (orange) descent. The QNG method outperforms Vanilla QAOA by reaching the target state in fewer steps while following the geodesic path on the Bloch sphere. This demonstrates the core advantage of the QNG descent in efficiently navigating quantum state space.

3.2 Rydberg atoms implementation

A quantum computer based on Rydberg atoms represents an ideal platform for testing the efficiency of our algorithm [138–140]. Analog quantum computing leverages the natural evolution of a quantum system to solve specific problems. Instead of programming discrete quantum gates (digital quantum computing), physical parameters, such as magnetic fields or laser intensities, are directly manipulated to induce a continuous-time dynamic evolution.

In the our case, we work with a *register* of Rydberg atoms, which serve as the qubits. Analog quantum computing is realized by evolving this atomic register according to a specific Hamiltonian, while continuously adjusting parameters like detuning or laser intensity. Indeed, by acting on all atoms with the same global pulse, one can evolve the entire system with the following Hamiltonian:

$$H(t) = \sum_i \left(\frac{\Omega(t)}{2} \sigma_i^x - \delta(t) n_i + \sum_{j<i} U_{ij} n_i n_j \right) \tag{3.14}$$

where $n_i = \frac{1}{2}(1 + \sigma_i^z)$. Here, $\Omega(t)$ is the Rabi frequency (which determines the strength of the interaction and it is proportional to the amplitude of the laser field), $\delta(t)$ (which denotes the discrepancy between the qubit resonance and the field frequencies) and U_{ij} denotes the blockade interaction parameter. This latter depends on the distance between qubits i and j: $U_{ij} = C_6/R_{ij}^6$, where C_6 is a constant. By the continuously manipulating $\Omega(t)$ and $\delta(t)$, one can achieve a significant level of control over the system's dynamics.

As introduced in the previous section, QAOA involves the evolution with two non-commuting Hamiltonians, namely:

$$H_{zz} = \sum_i \sigma_i^z \sigma_{i+1}^z \quad \text{and} \quad H_m = \sum_i \sigma_i^x. \tag{3.15}$$

The evolution operators of these two Hamiltonians can be easily implemented by fixing the qubit register (thus fixing the distance between individual atoms R_{ij}) and varying $\Omega(t)$ to enter and exit

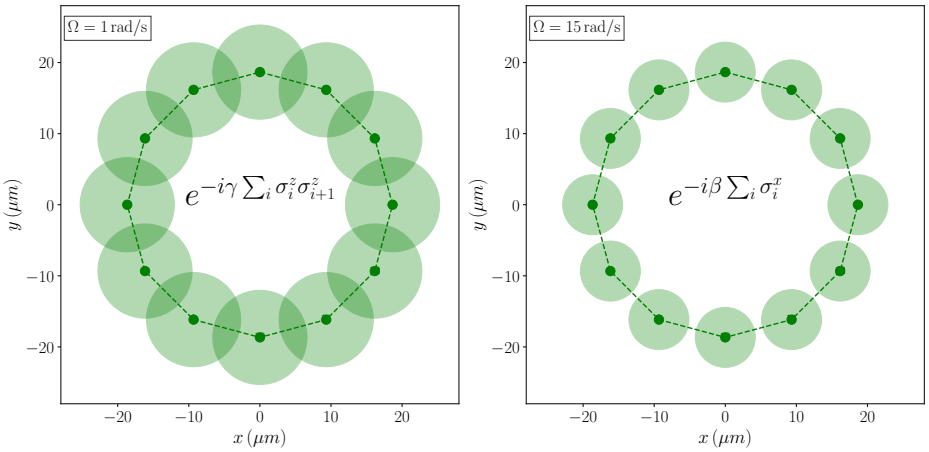

Figure 3.3: Effective implementation of the two time-evolution operators of the QAOA ansatz in a Rydberg atom register. In this example with $N = 12$, we demonstrate how these unitaries can be realized by transitioning in and out of the blockade regime, adjusting the value of Ω from 1 rad/sec to 15 rad/sec.

the blockade regime. Inside the blockade regime only the interaction terms $n_i n_{i+1}$ will be relevant, whereas outside σ_x will be the dominant factor. The blockade regime is determined by the Rydberg radius:

$$R_b = \left(\frac{C_6}{\Omega(t)} \right)^{1/6}. \tag{3.16}$$

In both regimes, we set the detuning value $\delta(t) = U_{i,i+1}$. In fact, expanding the interaction term $U_{i,i+1} n_i n_{i+1}$ reveals that it contains both $\sigma_i^z \sigma_{i+1}^z$ and σ_i^z terms. The latter can be canceled by this choice of detuning. An example of this implementation for $N = 12$ can be seen in Fig. 3.3.

This work focuses on the simulation of pulse sequences with noise and errors using the `pasqal-pulse` library [141]. These factors are intrinsic to real-world quantum systems and must be accurately replicated in simulations to ensure fidelity. A comprehensive explanation of these phenomena in Rydberg platforms is provided in [116]. Here, we will briefly outline the aspects considered in this study.

1. **SPAM (State Preparation And Measurement) Errors.**

   - **State Preparation Errors.** Initial attempts to prepare the state may occasionally fail to capture all atoms in the ground state. This is modeled using a probability, p, denoting the likelihood of an atom not being in the intended state during preparation.
   - **Measurement Errors.** Detection inaccuracies contribute to errors. These include falsely identifying an atom in the ground state as excited ("false positives") and vice versa ("false negatives").

2. **Laser Noises.** Laser properties such as frequency and amplitude fluctuations impact their efficacy in addressing atomic level transitions.

- **Doppler Effect.** Thermal motion of atoms causes Doppler shifts in the laser frequencies, altering the detuning frequency.
- **Laser Waist.** The Gaussian profile of laser amplitude means atoms at the edges of the beam experience slightly lower amplitudes compared to those at the focal point.
- **Amplitude Fluctuations.** Laser amplitude varies from pulse to pulse, influencing the consistency of laser operations.

3.3 Numerical results

In this study, we assessed the performance of the QAOA with QNG and vanilla gradient descent by analyzing their effectiveness in preparing the ground state of the TFIM. Our evaluation included comparisons of success rates in reaching the true ground state from multiple random initial points, both with and without noise, as well as the number of steps required to achieve this.

3.3.1 Ground state preparation accuracy

As explained in the previous sections, the QAOA algorithm adheres to a specific protocol, which in our case involves initializing the state in $|+\rangle^{\otimes N}$ and evolving it using the Hamiltonians in Eq. (3.15). By strictly following this procedure, it can be demonstrated that the ground state of is achieved with a depth of $P = \lfloor N/2 \rfloor$. However, as previously mentioned, it is not feasible to evolve precisely using those two Hamiltonians since the interaction term, even though it should be negligible outside the Blockade regime, remains present and might affect the accuracy and the number of layers required to reach the ground state. The same applies within the blockade regime, where $\Omega(t)$, although small, remains present.

We aimed to explore this aspect by plotting how fidelity varies with the number of layers P for different system sizes, both in the presence and absence of noise (see Fig. 3.4). We opted to present the fidelity trends because, in some cases, final states with nearly identical energies may still exhibit low fidelity values. As our primary goal is state preparation, our focus is on how closely the achieved state overlaps with the true ground state. The fidelity between a mixed state and a pure state is defined as $F = \langle \psi_g | \rho | \psi_g \rangle$, where ψ_g is the ground state vector determined through exact diagonalization. According to the simulation results, it is clear that in the noiseless scenario, the ground state is achieved with an accuracy of 10^{-8} when $P = \lfloor N/2 \rfloor + 1$. This accuracy is calculated as the difference between the energy value obtained by the algorithm at convergence and the true value (see Eq. (3.3)).

When two different sources of noise are introduced, we find that the optimal fidelity is consistently reached at $P = \lfloor N/2 \rfloor + 1$, with accuracy ranging from $[10^{-7}, 10^{-4}]$ as N changes. Additionally, the graph includes fidelity values for two extra layers to evaluate whether this might help the algorithm in achieving the desired ground state. However, the results indicate that adding layers does not provide any advantage: in the case of laser noise, the fidelity value stabilizes at the next layer after $P = \lfloor N/2 \rfloor + 1$ (though with increased variance), followed by a subsequent decrease. For spam errors, both the fidelity and its variance remain constant for $P \geq \lfloor N/2 \rfloor + 1$. This can be easily understood as adding parameters does not increase noise, unlike the situation with laser noise evolution.

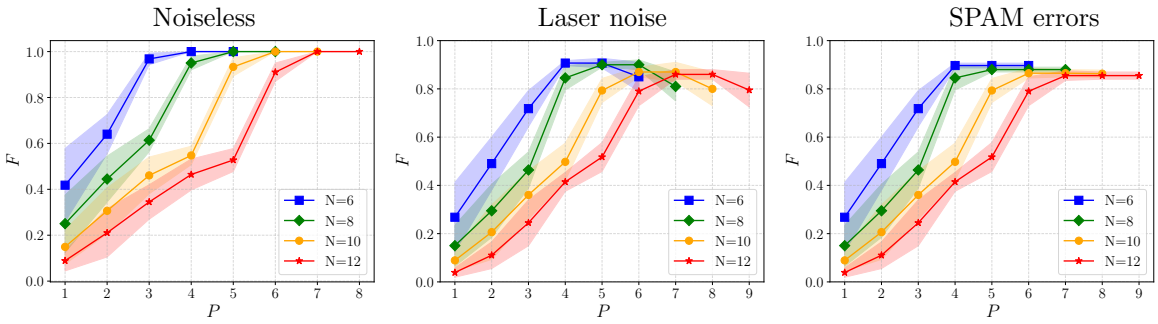

Figure 3.4: Growth of fidelity as a function of depth P for various system sizes ($N = [6, 8, 10, 12]$) and under three different scenarios: noiseless, laser noise, and SPAM errors. It is noteworthy that, in each case, the highest value of F is achieved when $P = \lfloor N/2 \rfloor + 1$.

3.3.2 Comparison of QNG vs. Vanilla gradient descent

We evaluated the performance of QNG and standard gradient descent in finding the true ground state of 1D TFIM by testing both methods across various system sizes, specifically in the range $N = [2, 12]$. The simulations were conducted under three different conditions: noiseless, with laser noise, and with SPAM errors. The value of magnetic field h was set to 0.5, $J = 1$ and the learning rate η was selected iteratively by conducting several trials with a fixed N, and choosing the best-performing values for both methods. The results are presented in Fig. 3.5. Notably, we observed two main comparison metrics: the *average number* of steps required to reach the ground state and the *convergence rate*, which indicates the percentage of successful algorithm completions in finding the ground state. A ground state is considered successfully reached when the accuracy is comparable to those values discussed in the previous section, which represent the best attainable outcomes across the three different scenarios. The *average number* of steps required to achieve the minimum was calculated by running the algorithm multiple times from random initial points and selecting the first 50 instances in which the ground state was successfully found. Conversely, the *convergence rate* was calculated by averaging the results from the first 50 runs.

Furthermore, the QNG was computed using both the full Quantum Fisher Information (QFI) and the diagonal approximation (which utilizes only the diagonal elements of the QFI matrix). This comparison is crucial for understanding the scenarios in which it is feasible to approximate the QNG while calculating fewer elements. This is significant because the QFI matrix must be inverted during the parameter update process, which incurs additional computational overhead, yet still offers potential advantages.

In all three scenarios, there is a clear advantage in employing QNG (both the full and diagonal approximations) compared to standard gradient descent. This advantage becomes more pronounced as the system size N increases. Furthermore, for the range of sizes we were able to simulate, there appears to be no significant benefit to using the full QNG over the diagonal approximation, as suggested in [126], with both methods displaying similar trends and occasionally overlapping performance (see Fig. 3.5, upper panel). Additionally, in terms of variance, the QNG outperforms the standard method, exhibiting lower variance, which indicates that the average number of steps needed to reach the minimum of the cost function is less dependent on the choice of the initial state.

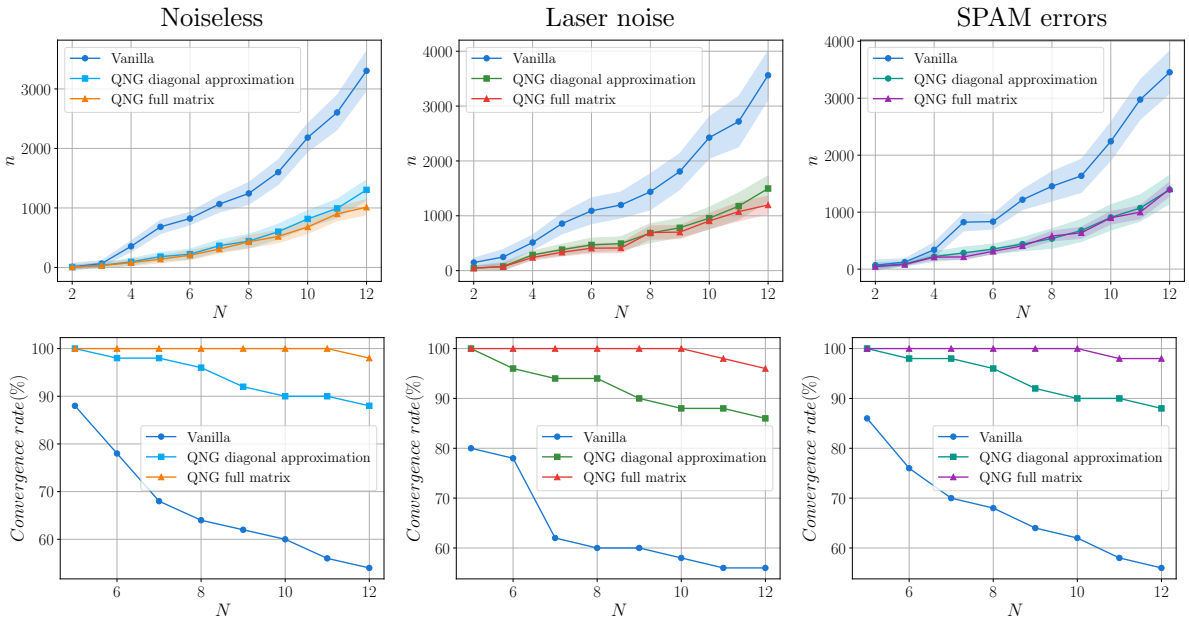

Figure 3.5: On the upper panels, the average number of steps n needed to reach the ground state as function of the systems size $N = [2, 12]$ with and without the different sources of noise. On the lower panels the convergence rate of QNG (full and with diagonal approximation) and vanilla with and without the different source of noise as function of the system size $N = [5, 12]$.

Next, let us analyze the convergence rate across the three scenarios as a function of system size (see Fig. 3.5, lower panel). Here, the range of N was chosen as $[5, 12]$, where we could observe the first significant discrepancies. It is evident that there continues to be a substantial and progressive gap in performance between the QNG methods and standard gradient descent as N increases. The former starts at a 100% convergence rate, tapering off to values greater than 86% at $N = 12$, while the standard method progressively declines to just above 56% across the different scenarios. Additionally, in this comparison, the difference between the two QNG approximations appears more pronounced, suggesting further improvement for larger sizes of N. This leads us to conclude that the advantages of using the full QNG over the diagonal approximation lie not so much in the "speed" of reaching the minimum, but rather in providing more effective directions for achieving the true one.

3.4 Conclusions and outlook

In this work, we have explored the implementation of the Quantum Approximate Optimization Algorithm (QAOA) using Rydberg atoms, a promising platform for quantum computation due to their highly tunable interactions and scalability. Our study focused on simulating pulse sequences under various noise conditions using the `pasqal-pulse` library, which allowed us to closely replicate real-world imperfections in quantum systems.

Our results demonstrate that the QAOA can effectively prepare the ground state of the transverse field Ising model (TFIM), with the number of layers $P = \lfloor N/2 \rfloor + 1$ being optimal in both

noiseless and noisy scenarios. However, the presence of laser noise and SPAM errors impacts the fidelity and convergence rates, particularly for larger system sizes. We observed that the addition of extra layers does not yield significant improvements in performance and may even degrade the results due to noise accumulation, particularly with laser fluctuations.

The comparison between Quantum Natural Gradient (QNG) methods and standard gradient descent showed a clear advantage for the QNG approach, particularly as the system size increases. The use of the diagonal approximation of the Quantum Fisher Information (QFI) was found to be almost as effective as the full QNG, offering a balance between computational cost and accuracy.

In our work, we utilized QAOA to find the ground state of the Ising model, which represents a "quantum" problem. However, QAOA can also be applied to solve classical computational problems where traditional methods, such as simulated annealing or branch-and-bound algorithms, become inefficient due to their poor scalability with increasing problem size.

The QNG approach involves computing each matrix element of the Quantum Fisher Information, requiring the evaluation of $4P^2$ elements and the subsequent inversion of this matrix classically. In principle, the evaluation of each element could be performed in parallel by replicating the system $4P^2$ times, evolving it accordingly, and measuring the expected value of the required observables. Given the effectiveness of the diagonal approximation, it may suffice to consider only the $2P$ diagonal elements to achieve a speed-up. However, this approach requires the capability of the Rydberg atom platform to replicate the initial register in different zones and evolve each independently through partial addressing of the total register. Unfortunately, this is not currently feasible with high efficiency on existing platforms but appears highly plausible and achievable in the near future.

Looking forward, several avenues of research could further improve the algorithm's efficiency and practical applicability. First, investigating advanced noise-mitigation techniques could help counteract the limitations posed by real-world imperfections. Second, optimizing pulse-shaping strategies could offer enhanced control over system dynamics, minimizing noise effects while maximizing the algorithm's fidelity. Finally, exploring the use of more complex quantum architectures or hybrid quantum-classical methods may provide further gains in both performance and scalability.

Overall, our work underscores the viability of Rydberg atom platforms for implementing QAOA and provides insights into the challenges and opportunities presented by noise and error in practical quantum computing systems.

Part II

Chapter 4

From Classical to Quantum Cellular Automata

In this chapter, we explore the transition from classical to quantum cellular automata (CAs and QCAs), with a focus on their computational models and applications. CAs are discrete computational systems that evolve based on local rules, and have a wide range of applications across various fields. We begin by examining classical CAs, highlighting key examples such as Conway's Game of Life and Rule 110. Following this, we introduce the density classification problem, an important challenge within this domain.

Next, we turn our attention to probabilistic CAs, discussing stochastic rules and their effectiveness in solving the density classification problem. Finally, we transition to QCAs, the quantum counterpart to CAs, exploring their definitions, dynamic behaviors, and potential applications. In particular, we discuss how QCAs can be used to model quantum systems and how they might be implemented using Rydberg atom devices. This section is not intended to be a comprehensive review of QCAs, but rather a brief introduction to the fundamental concepts and those essential for understanding the following chapter. For thorough reviews on the subject, excellent resources can be found in [142, 143].

4.1 Cellular Automata

A *cellular automaton* is a discrete computational model that has been extensively studied within the realm of automata theory. Also referred to as cellular spaces, tessellation automata, or iterative arrays, CAs are homogeneous systems that exhibit complex behavior through simple, local interactions. These models have found applications across diverse disciplines, including physics [144], theoretical biology [145], and the modeling of microstructures [146].

A cellular automaton consists of a grid of cells, each of which can be in one of a finite number of states. This grid can be of any dimensionality, allowing for flexibility in its spatial configuration. Each cell interacts with its neighboring cells, defined by a specific *neighborhood* structure that varies based on the model in use. Beginning from an initial configuration (at time $t = 0$), the system evolves over discrete time steps, where the state of each cell at the next step is determined by a set of *local rules*. These rules dictate the new state of each cell based on its current state

and the states of its neighboring cells. Typically, a *radius* is defined that limits the neighborhood to a fixed distance from the cell under consideration. In most models, the rules are homogeneous across the grid, applied synchronously at each time step, and remain unchanged over time. Variants such as stochastic or asynchronous cellular automata introduce additional complexity, allowing for probabilistic transitions or asynchronous updates.

The concept of cellular automata was first formulated in the 1940s by Stanislaw Ulam and John von Neumann, both of whom were conducting research at the Los Alamos National Laboratory [147]. Initially, the focus of their studies was on self-replicating systems. However, CA models only gained significant attention in the 1970s, when John Conway introduced the *Game of Life*, a two-dimensional cellular automaton that operates with binary states [148]. Popularized by Martin Gardner in his influential *Scientific American* column, the Game of Life is defined by a simple set of rules:

- any live cell with fewer than two live neighbors dies, as if by underpopulation;
- any live cell with two or three live neighbors survives to the next generation;
- any live cell with more than three live neighbors dies, as if by overpopulation;
- any dead cell with exactly three live neighbors becomes a live cell, as if by reproduction.

Despite the simplicity of these rules, the Game of Life exhibits a remarkable variety of behaviors, ranging from stable structures to chaotic, dynamic patterns. One of the most notable phenomena is the emergence of *gliders*, which are small configurations of cells that traverse the grid over time. By arranging gliders in specific ways, it is even possible to perform logical operations, making the Game of Life computationally equivalent to a universal Turing machine. This discovery underscored the potential of cellular automata to simulate any computation.

In the 1980s, Stephen Wolfram reignited interest in cellular automata through his comprehensive study of their behavior [149]. Driven by a curiosity to understand how complex patterns in nature emerge, seemingly defying the second law of thermodynamics, Wolfram investigated a broad range of CA models, most notably the one-dimensional Rule 30. His findings demonstrated that even simple rules could give rise to complex, seemingly random behavior. Wolfram also introduced the concept of *computational irreducibility*, arguing that the evolution of some systems cannot be simplified or predicted without actually performing each step of the computation. His research culminated in the identification of Rule 110 as a universal cellular automaton, a conjecture later proven by his research assistant Matthew Cook in [14].

4.1.1 Rule 110: A Turing-Complete Cellular Automaton

In an *elementary* cellular automaton, a one-dimensional sequence of 0s and 1s evolves according to a simple set of rules. The state of each cell in the next generation is determined by its current state and the states of its two neighboring cells. Rule 110 is one of the most significant elementary CA due to its computational power, including the ability to simulate a Turing machine.

The transition rules for Rule 110 are as follows:

Current pattern	111	110	101	100	011	010	001	000
New state for center cell	0	1	1	0	1	1	1	0

The sequence of current patterns is conventionally taken in the order shown above. The name "Rule 110" originates from the fact that the rule can be encoded as the binary sequence 01101110 (representing the new states of the center cell), which corresponds to the decimal number 110 when interpreted as a binary number. This naming convention applies to other elementary rules in the same manner.

Matthew Cook proved that Rule 110 is universal (or Turing complete) by demonstrating its ability to emulate a known universal computational model called the Cyclic Tag System (CTS) [14]. In his proof, Cook identified specific repeating structures, known as *spaceships*, which are localized patterns that propagate across the automaton's grid. He then showed how combinations of these spaceships could interact in ways that perform computation, thus establishing the universality of Rule 110.

The operation of this universal machine within Rule 110 relies on embedding a finite set of localized patterns within an infinitely repeating background pattern. This background, which is 14 cells wide, repeats every seven iterations and follows the sequence `00010011011111`.

Three critical localized patterns play a key role in the functioning of the Rule 110 universal machine. These patterns, embedded in the repeating background, are illustrated in Fig 4.1: the top row shows the initial state, while each subsequent row represents the system's state at the next time step.

- The first pattern, shown on the left, remains stationary and repeats every seven generations. It is formed by the sequence `111`, embedded within the repeating background.
- The second pattern, located in the center, shifts two cells to the right and repeats every three generations. It consists of the sequence `0001110111`, surrounded by the same background.
- The third pattern, on the right, shifts eight cells to the left and repeats every 30 generations. This pattern is composed of the sequence `1001111`, also embedded within the background.

These different patterns can interact in various ways when they encounter each other: they can either pass through one another without any interaction, maintaining their form and continuing their evolution as usual, or they can collide, producing a new pattern as a result of their interaction.

The CTS consists of three essential components:

1. a stationary *data string*;
2. a set of *production rules* that move from right to left in a cyclic and infinite pattern in time;
3. a series of *clock pulses* that move from left to right, also repeating infinitely.

The correct initialization of these components is crucial for the CTS to function properly. The cellular automaton must be set up so that the interactions between the localized structures occur in an orderly fashion, enabling the CTS to execute its operations seamlessly.

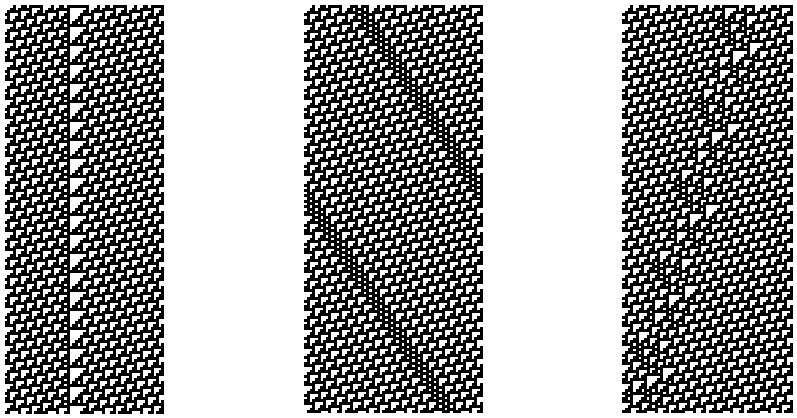

Figure 4.1: Three different types of patterns (from left to right, stationary, right-moving, and left-moving) generated by Rule 110.

In this system, the data string is represented by *stationary* repeating structures (like those discussed previously), with the spacing between these structures encoding the symbols 0 and 1. These symbols form the "word" on which the CTS operates. At each step, the first symbol of the string is removed. If the first symbol is a 1, new symbols are appended to the end of the string according to the production rules; if the first symbol is a 0, no new symbols are added.

From the right, a series of left-moving structures (representing the production rules) enters the system. These structures are arranged to encode the sequence of 0s and 1s that define the CTS's production rules. These rules are encoded as an infinitely repeating sequence, with each rule separated by a structure known as a *rule separator* (or block separator), which also moves leftward in sync with the production rules.

When a left-moving rule separator encounters the first symbol in the stationary data string, that symbol is destroyed. What follows depends on whether the symbol was a 0 or a 1. If the symbol was a 0, the rule separator transforms into a structure that blocks the incoming production rule, causing it to be destroyed upon meeting the next separator. If the symbol was a 1, the rule separator transforms into a different structure that allows the production rule to pass. This structure is eventually destroyed, but not before it permits the rule to continue leftward, adding new structures to the data string.

Finally, the right-moving clock pulses play a key role in the system by facilitating the transfer of information. These clock pulses continuously repeat a specific pattern, converting the 1s and 0s of the left-moving production rules into stationary symbols that extend the data string. This mechanism ensures the CTS continually updates its data string based on the applied production rules, thereby completing its computation.

4.2 The density classification task

The density classification problem, also known as majority problem, has a remarkably simple formulation: how can a dynamical system determine the majority state in its initial configuration? While the problem is trivial in most classical computing paradigms (e.g., Turing machines), the

challenge here lies in performing the task under the following constraints:

1. *Simplicity*: the cells' states are binary, allowing for a straightforward computational structure.
2. *Autonomy*:the system operates independently, with no external operator directing the computation. All changes occur internally, affecting only the states of its components, the cells.
3. *Spatial and temporal uniformity*: all cells follow the same rule, which remains fixed over time and space, ensuring consistency in their behavior.
4. *Locality*: each cell has a limited view of the system, typically interacting only with cells within a defined neighborhood.
5. *Consensus*: the computation is considered complete when the system reaches a stable consensus, where all cells agree on a specific state.

It is indeed possible to extend the density classification problem to other systems, such as higher-dimensional cellular automata (CA) [150] or networks [151, 152]. This inverse problem has attracted considerable attention since its original formulation by Packard [153]. The core challenge in solving this problem arises from the decentralized nature of information processing: unlike classical approaches, the system cannot rely on central control or straightforward counting mechanisms. Instead, the solution must emerge from local decisions, which may sometimes conflict with the global behavior of the system. Additionally, due to the homogeneity of CA systems in space and time, individual cells cannot be specialized for partial computations, further complicating the task.

Effectively solving this problem requires a delicate balance between making autonomous local decisions and following the influence of neighboring cells to achieve global consensus. In 1995, Land and Belew made an important discovery: they proved that no perfect (deterministic) density classifier can exist when using only two states [154]. Despite this, the search for highly efficient CA rules has continued, with genetic algorithms emerging as the primary tool for exploration (see, for example, [155] and references therein). Researchers have sought to determine how close a rule can come to a perfect solution.

In contrast, several modifications to the classical density classification problem have led to exact solutions. For instance, Capcarrère et al. introduced a variation to the output requirements of the problem, enabling perfect classification [156]. Similarly, Fukś showed that running two CA rules sequentially (the "traffic" and "majority" rules) can yield a viable solution [157].

Additionally, Martins and Oliveira found that specific pairs and triples of CA rules can solve the problem when applied sequentially for a predetermined number of steps, depending on the size of the lattice [158]. Some researchers have suggested enhancing the capabilities of CA rules by embedding memory into the cells themselves [150, 159].

However, all these approaches violate at least one of the initial problem constraints. Stochastic (or probabilistic) CA present a promising alternative that adhere to the original constraints while introducing an element of randomness. In such systems, the state transitions of individual cells are determined probabilistically rather than deterministically. The use of randomness in solving the density classification problem was first proposed by Fukś, who developed a rule where cells probabilistically "copy" the states of their neighbors [160]. However, this method lacked the necessary

driving force toward a unified system state. More recently, Schüle et al. proposed a stochastic rule based on local majority voting, which improved convergence but remained subject to certain intrinsic limitations [161]. Building on these ideas, Fatès introduced a novel stochastic rule capable of solving the density classification problem with arbitrarily high precision [162]. Specifically, for any given lattice size, the probability of correctly classifying the majority state can be made arbitrarily close to 1. In the next two sections, we will take a closer look at the solution proposed by Fukś and the one put forward by Fatès .

4.2.1 Fukś density classifier

In the following, we deal with a probabilistic cellular automaton introduced by Fukś that solves the density classification problem in a stochastic sense. Specifically, the probability that all sites eventually become occupied corresponds to the initial density of occupied sites in the system's starting configuration. We consider a one-dimensional lattice with periodic boundary conditions. Let $s_i(t)$ be the state of lattice site i at time t, where $i \in \mathbb{Z}$ and $t \in \mathbb{N}$. The spatial index i is treated modulo L, where L is the lattice length. Each site can take a value from the set $s_i(t) \in \{0, 1\}$, where $s_i(t) = 1$ indicates that site i is occupied at time t, and $s_i(t) = 0$ indicates that it is empty. The system evolves based on local interactions: empty sites become occupied with a probability proportional to the number of occupied neighbors, while occupied sites become empty with a probability proportional to the number of empty neighbors. All sites are updated simultaneously at each time step. More formally, let $P(s_i(t+1)|s_{i-1}(t), s_i(t), s_{i+1}(t))$ denote the probability that site i, with neighbors $s_{i-1}(t)$ and $s_{i+1}(t)$, changes to state $s_i(t+1)$ in the next time step. The transition probabilities for a central cell to change to state 1 (or remain in state 1 if it is already there), denoted as $P(1 \mid a, b, c)$ for all $a, b, c \in \{0, 1\}$, are provided in the table below:

Current pattern	111	110	101	100	011	010	001	000
Transition probability	1	$1-p$	$2p$	p	$1-p$	$1-2p$	p	0

where $p \in (0, 1/2]$. The transition probabilities for a cell to change to or remain in state 0 can be derived using the relation $P(0 \mid a, b, c) = 1 - P(1 \mid a, b, c)$ for all $a, b, c \in \{0, 1\}$.

To make the probabilistic CA defined by the rule above more explicit, we introduce a set of independent and identically distributed random variables $\{X_i\}_{i=0}^{L}$ with the probability distribution $P(X_i = 1) = p$ and $P(X_i = 0) = 1 - p$, along with another set $\{Y_i\}_{i=0}^{L}$ with the distribution $P(Y_i = 1) = 2p$ and $P(Y_i = 0) = 1 - 2p$. The dynamics of the rule can then be expressed by the following equation:

$$\begin{aligned} s_i(t+1) = {} & X_i(1-s_{i-1})(1-s_i)s_{i+1} + (1-Y_i)(1-s_{i-1})s_i(1-s_{i+1}) + \\ & + (1-X_i)(1-s_{i-1})s_i s_{i+1} + X_i s_{i-1}(1-s_i)(1-s_{i+1}) + \\ & + Y_i s_{i-1}(1-s_i)s_{i+1} + (1-X_i)s_{i-1}s_i(1-s_{i+1}) + s_{i-1}s_i s_{i+1}. \end{aligned} \tag{4.1}$$

For clarity, we have omitted the time argument in the above formula, denoting $s_i(t)$ simply by s_i. After simplifying and rearranging the terms, the final expression becomes:

$$s_i(t+1) = s_i - s_i Y_i + X_i s_{i-1} + X_i s_{i+1} + (s_{i-1}s_i + s_i s_{i+1} - 2s_{i-1}s_i s_{i+1})(Y_i - 2X_i). \tag{4.2}$$

At time t, the state of the system is determined by the states of all lattice sites and can be represented as the Boolean random field $\boldsymbol{s}(t) = \{s_i(t) : i = 0, \ldots, L\}$. The sequence $\{\boldsymbol{s}(t) : t = 0, 1, 2, \ldots\}$ forms a Markov stochastic process. Let $\mathbb{E}_{\boldsymbol{s}(0)}$ denote the expected value of this Markov process given the initial configuration $\boldsymbol{s}(0)$. The expected local density of occupied sites is defined as $\rho_i(t) = \mathbb{E}_{\boldsymbol{s}(0)}[s_i(t)]$. The expected global density is given by:

$$\rho(t) = \frac{1}{L} \sum_{i=0}^{L} \rho_i(t). \tag{4.3}$$

Although both $\rho_i(t)$ and $\rho(t)$ depend on the initial configuration $\boldsymbol{s}(0)$, we will omit this dependence for simplicity. Assuming the initial configuration is known and deterministic, we define the initial global density as:

$$\rho(0) = \frac{1}{L} \sum_{i=0}^{L} s_i(0), \tag{4.4}$$

which represents the fraction of initially occupied sites. Taking the expectation of both sides of equation (4.2) and using the fact that $\mathbb{E}_{\boldsymbol{s}(0)}[Y_i - 2X_i] = 0$, we derive the following expression for the expected local density:

$$\rho_i(t+1) = \rho_i(t) + p\left(\rho_{i+1}(t) + \rho_{i-1}(t) - 2\rho_i(t)\right). \tag{4.5}$$

By summing over all lattice sites and accounting for the periodic boundary conditions, this equation becomes:

$$\rho(t+1) = \rho(t), \tag{4.6}$$

which implies that the expected global density remains constant, independent of the parameter p and the initial configuration $\boldsymbol{s}(0)$. Thus, we conclude that this probabilistic cellular automaton preserves the number of occupied sites.

Let $N(t) = \sum_{i=1}^{L} s_i(t)$ represent the number of occupied sites at time t. If the initial condition is $N(0) = 0$, then $N(t) = 0$ for all $t > 0$. Similarly, if $N(0) = L$, then $N(t) = L$ for all $t > 0$. Therefore, the process has two absorbing states (i.e., states from which the system cannot escape once reached): one where all sites are empty (denoted as state $\mathbf{0}$) and one where all sites are fully occupied (denoted as state $\mathbf{1}$).

Now, define $P_N(t)$ as the probability that exactly N sites are occupied at time t. Since the Markov process $\{\boldsymbol{s}(t) : t = 0, 1, 2, \ldots\}$ is finite (meaning that only a limited number of configurations are reachable at each time, given that L is finite) and absorbing, regardless of the initial state, the probability that the process eventually reaches an absorbing state approaches 1 as $t \to \infty$. This leads to the following:

$$\lim_{t\to\infty} P_N(t) = 0 \quad \text{for} \quad N \neq 0, L, \quad \text{and} \quad \lim_{t\to\infty} \left(P_L(t) + P_0(t)\right) = 1. \tag{4.7}$$

The expected global density, does not change with t. Thus, we have:

$$\rho(0) = \frac{1}{L}\mathbb{E}_{s(0)}[N(t)] = \frac{1}{L} \sum_{N=1}^{L} N P_N(t). \tag{4.8}$$

Taking the limit as $t \to \infty$ on both sides of the above equation, and using Eq. (4.7), we obtain:

$$\lim_{t\to\infty} P_L(t) = \rho(0) \quad \text{and} \quad \lim_{t\to\infty} P_0(t) = 1 - \rho(0). \tag{4.9}$$

Thus, the probability that the dynamics reaches the absorbing state **1** equals the initial fraction of occupied sites, $\rho(0)$. Conversely, the probability of reaching the absorbing state **0** is $1 - \rho(0)$.

The result above can be interpreted as a probabilistic extension of the density classification problem. In the deterministic version, the goal is to find a cellular automaton rule that converges to state **1** (or **0**) if the initial fraction of occupied sites is greater (or less) than 1/2.

In contrast to the deterministic case, where the outcome is strictly defined, this process yields a probabilistic result. When the initial fraction of occupied sites exceeds 1/2, the system is more likely to reach state **1** than state **0**. Conversely, if the initial fraction is below 1/2, the system is more likely to converge to state **0**. Furthermore, this approach offers a method to estimate the initial concentration of occupied sites. By running the process multiple times with the same initial condition and observing the absorbing state, the frequency of reaching state 1 provides an increasingly accurate approximation of $N(0)/L$ as the number of runs increases.
This section has reviewed the key steps of the proof presented by FukśFor further details and numerical results, see the original reference [160].

4.2.2 Fatès density classifier

In this section, we examine a probabilistic CA introduced by Fatès [162], designed to solve the density classification task with arbitrary precision. The automaton's transition probabilities for a central cell are given in the table below:

Current pattern	111	110	101	100	011	010	001	000
Transition probability	1	η	1	$1-\eta$	1	0	0	0

where $\eta \in (0, 1)$. The rule works by applying rule 184 (also known as the "traffic" rule) with probability $1 - \eta$, and rule 232 (the "majority" rule) with probability η, at each cell and time step. This means that at every step, a random number in the range $(0, 1)$ determines whether to apply rule 184 or rule 232, and once a rule is selected, the entire chain evolves according to that rule. To prove the success of this rule, we introduce key definitions and supporting lemmas.

Definition 1 *For $q \in \{0, 1\}$, a configuration $\boldsymbol{s}(t)$ is called a q-archipelago if all cells in state q are isolated. In other words, $\boldsymbol{s}(t)$ does not contain two adjacent cells in state q.*

In a *q-archipelago*, each cell in state q is referred to as an "island." These islands of cells in state q are separated by at least one cell in the opposite state, ensuring no direct adjacency between cells in state q. The notion of islands is crucial for analyzing the convergence behavior of the cellular automaton, as the evolution of the system leads to the eventual disappearance of these states.

Lemma 1 *An archipelago is well-classified with probability 1. Specifically, a configuration $\boldsymbol{s}(t)$ that forms a q-archipelago with k cells in state q has an expected convergence time $E\{T(\boldsymbol{s}(t))\} \leq \frac{k}{\eta}$.*

Proof. The proof is straightforward and relies on two key observations. First, the successor of a *q-archipelago* is also a *q-archipelago*. Assume, without loss of generality, that $\boldsymbol{s}(t)$ is a *1-archipelago*. By applying the transition rule, all isolated 1s will eventually turn into 0s. As for 0s that turn into 1s, they must be preceded by a 1 (which has turned into a 0) and followed by either another 1 (also turning into a 0) or a 0 (remaining 0 because $000 \to 0$ and $001 \to 0$). This ensures that no two 1s become adjacent in $\boldsymbol{s}(t+1)$. Second, the number of 1s in $\boldsymbol{s}(t)$ is a non-increasing function of time. At each step, any isolated 1 has a non-zero probability $\eta > 0$ of disappearing. As a result, all 1s will eventually vanish, leading the system to converge to the fixed point $\mathbf{0}$, which represents a correct classification since the density $\rho(0) < 1/2$. Until the system reaches a fixed point, there is always a probability greater than η that the number of islands decreases by 1. If the archipelago initially contains k islands, the expected time for all islands to disappear is upper-bounded by k/η. □

Definition 2 *For a given configuration $\boldsymbol{s}$, we define an archipelago $\boldsymbol{a}$ as* appropriate *if it shares the same majority state as $\boldsymbol{s}$.*

Specifically, this means that either $\rho_{\boldsymbol{s}}(0) < \frac{1}{2}$ and $\rho_{\boldsymbol{a}}(0) < \frac{1}{2}$, or $\rho_{\boldsymbol{s}}(0) > \frac{1}{2}$ and $\rho_{\boldsymbol{a}}(0) > \frac{1}{2}$. Another key property of the rule is that any configuration is transformed into an appropriate archipelago with a probability that approaches 1 as $\eta \to 0$.

Lemma 2 *For every $p \in [0, 1)$, there exists a setting η such that every configuration $\boldsymbol{s}$ will evolve to an appropriate archipelago with a probability greater than p.*

Proof. First, we claim that starting from any configuration $\boldsymbol{s}$, if the system evolves with the *traffic* rule for $T = \lceil L/2 \rceil$ steps, the system reaches the appropriate archipelago corresponding to $\boldsymbol{s}$. This claim is based on two key facts: (1) the *traffic* rule is number-conserving, and (2) it always evolves to an archipelago in at most T steps (see [156]). To prove the lemma, it is sufficient to choose η such that the probability of a discrepancy between the two rules is less than p. By examining the transition tables for the rule 184 and Fatès rule, we observe that differences occur only when transitions of the form $100 \to 0$ or $110 \to 1$ happen, which occur with probability η. Furthermore, the number of such transitions can be upper-bounded by LT. Therefore, to ensure that the probability of a difference is lower than p, we require $\eta < p^{1/LT}$. □

Thus, our initial assertion regarding the attainment of the correct final state with arbitrary precision is validated by combining the results from the two preceding lemmas: for sufficiently small η, the system evolves into an appropriate archipelago (as stated in Lemma 2); it then gradually drifts toward the suitable fixed point (as outlined in Lemma 1). Therefore, the probability of reaching the correct final state approaches 1 as $\eta \to 0$.

4.3 Quantum Cellular Automata

Quantum cellular automata (QCAs) are the quantum counterpart to classical cellular automata (CAs). The early conceptual foundation of QCAs dates back to [163], where it was suggested that quantum computers, rather than classical ones, would be more suited to simulate quantum physics. In fact, it is widely believed that quantum simulations of physical systems will likely

be among the first practical applications of quantum computers [164]. This is because quantum systems are inherently difficult to simulate on classical computers, particularly when the complexity of the system grows. Specific QCA models were introduced in works such as [20, 165, 166]. In [20], QCAs were proposed as an alternative paradigm for quantum computation, demonstrating their universality, meaning they could efficiently simulate a quantum Turing machine. The significance of this result lies in the fact that universality is a key feature of any computation model that aims to be fully generalizable. An earlier paper [166] presented a model of quantum computation described as a classically controlled QCA, where a series of global, translationally invariant unitary operations are applied over discrete timesteps.

One advantage of this type of quantum computation is its reliance on homogeneous global operations on all qudits, unlike the circuit model that requires precise control over individual or small groups of qubits, which can be challenging, especially in systems like trapped ions. This advantage can potentially lead to simpler implementations of quantum algorithms, making QCAs attractive for practical uses.

However, the development of QCAs from classical CAs was not without difficulties. Various obstacles emerged, as naïve approaches, such as extending classical evolution linearly to create a quantum version, often failed. A significant issue is that while CAs allow all cells to be updated simultaneously, in QCAs, copying a cell's state (to update its neighbors later) is impossible due to the no-cloning theorem [167, 168]. This theorem is a fundamental principle in quantum mechanics that prohibits the exact copying of arbitrary quantum states. To address these challenges, several constructive methods were proposed, typically involving finite-depth circuit layers and shifting qudits to neighboring sites. It wasn't until later that an axiomatic definition of QCAs was formulated, capturing the essence of CAs while ensuring the evolution remained quantum [21]. This axiomatic approach not only resolved many of the initial issues but also provided a formal framework that could be extended to more complex quantum systems.

The axiomatic definition we will use describes a QCA as a spatial lattice with quantum systems at each site. The evolution occurs in discrete time steps, governed by an operator that preserves locality. Locality preservation is the discrete analogue of relativistic causality, meaning that local operators in the Heisenberg picture remain local over time. In other words, information cannot propagate faster than a certain speed, preserving the causal structure of the system. We will explore this in greater detail in Sec. 4.3.1.

A particularly ambitious application of QCAs is to model discrete physical systems. Once spacetime is considered discrete and a maximum speed of information propagation is assumed, the only remaining assumption needed is unitarity, which naturally leads to a QCA framework. In contrast, continuous-time dynamics on a lattice governed by a local Hamiltonian does not impose a strict upper bound on information propagation. This difference makes QCAs an appealing framework for exploring fundamental questions about the nature of spacetime and information transfer at the quantum level.

4.3.1 Definition and dynamics

QCAs are defined on quantum lattice systems, which means we have a discrete spatial lattice with quantum systems located at each lattice site (or cell). While some authors consider more general

graphs [169], we will focus on lattices in this work. This simplification will allow us to highlight the core aspects of QCA dynamics without getting into the complexities introduced by more general graph structures. The lattices, in general, can be either infinite, such as $\mathbb{Z}^d$, or finite, potentially with periodic boundary conditions. At each lattice site, we assume there are finite-dimensional quantum systems, i.e. qudits. QCAs for continuous variable systems have also been explored in [170], where a specific class of QCAs, known as Gaussian QCAs, was introduced. These evolve through Gaussian operations, which transform Gaussian states into other Gaussian states.

For finite lattice systems, the total Hilbert space is the tensor product of the Hilbert spaces corresponding to each lattice site. This structure allows us to consider localized observables and their interactions, which will be central to our discussion on the dynamics of QCAs.

To describe the dynamics of QCAs, it is often convenient to work in the Heisenberg picture, where the observables evolve over time. This approach simplifies understanding and defining a key feature of the dynamics: locality preservation. However, in some cases, switching to the Schrödinger picture is useful, as it provides a clearer connection to quantum computation. The choice between these two pictures depends on the specific problem we aim to solve, but both are mathematically equivalent and provide valuable insights into QCA behavior. In each discrete time step, the QCA usually evolves through a unitary operator.

We represent the QCA dynamics by $u : \hat{O} \to u(\hat{O})$, where $\hat{O}$ belongs to the algebra of observables $\mathcal{O}$ acting on the system. Importantly, we require that the evolution preserves locality (see Fig. 4.2). This means that local operators are mapped to operators localized in a nearby region. This property is sometimes referred to as "causality" [169], drawing an analogy with relativistic causality. More formally, we can define locality preservation as follows.

Definition 3 *The dynamics of a QCA u is locality preserving if there exists a range $l \geq 0$ such that, for any site $\vec{x}$ and any operator $\hat{O}$ localized at $\vec{x}$, the operator $u(\hat{O})$ is localized in a region consisting only of sites $\vec{y}$ where $|\vec{x} - \vec{y}| \leq l$.*

This means that the action of u does not spread information arbitrarily far, ensuring that the operator $u(\hat{O})$ only affects a bounded region around the initial site $\vec{x}$.

We can further introduce the concept of the neighborhood of a point $\vec{x}$, denoted by $J(\vec{x})$, which is the smallest region in which the algebra $u(\hat{O}_{\vec{x}})$ is localized after applying the QCA. This notion can naturally be extended to a larger region R, with its neighborhood denoted by $J(R)$, representing the smallest set of sites that can be influenced by the QCA dynamics acting on the region R. These neighborhood concepts are essential for understanding how information propagates in QCAs, as they impose strict limits on how far and how quickly influences can spread across the lattice.
Combining all these aspects, we can encapsulate the definition of a QCA as follows:

Definition 4 *A QCA consists of a discrete hypercubic lattice with a finite quantum system at each site (qudits and/or fermion modes). The evolution proceeds in discrete time steps via a locality-preserving unitary operator.*

We do not always assume that QCAs are translationally invariant (i.e. their dynamics commute with shifts along any lattice direction), although this assumption has been made in many works.

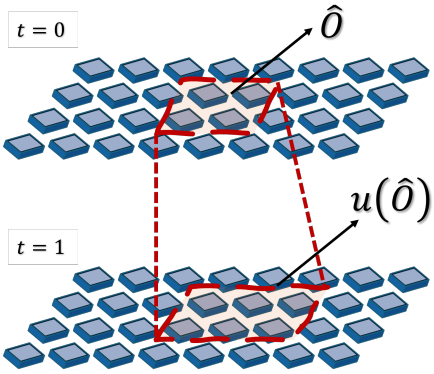

Figure 4.2: **Locality-preserving property of QCA:** at time $t = 0$, an operator $\hat{O}$ is localized across four sites. After a single time step, the updated operator $u(\hat{O})$ is found to be localized across six nearby sites.

While it would be more in the spirit of classical CAs to always consider translationally invariant dynamics, some of the most intriguing QCA structure theorems do not require any form of translational invariance. Thus, relaxing the translational invariance condition opens up the possibility of discovering novel QCA behaviors and structures that might not be apparent otherwise.

Finally, it would also be interesting to explore irreversible (i.e. non-unitary) QCAs, as discussed in [168, 171, 172], although relatively little research has been conducted in this direction. In these cases, unitary operators would be replaced by completely positive trace-preserving maps (CPTP), which represent the most general dynamics allowed by quantum theory [167]. These irreversible dynamics may offer insights into how quantum systems behave under dissipation or noise, which is important for practical applications like quantum error correction. An example of this is the investigation of how to solve the majority vote problem in a quantum setting, which we explore in Chapter 5.

4.3.2 Partitioning schemes

We consider partitioning the lattice into P distinct sets, with each set comprising supercells denoted by $C^p_{\vec{n}}$, where $\vec{n} \in \mathbb{Z}^d$ and $p \in \{1, \ldots, P\}$. Each site in the lattice belongs to exactly one supercell within each partition (see Fig. 4.3). The dynamics of the QCA are then described by the composition of unitary transformations:

$$u_1 \circ \cdots \circ u_P \tag{4.10}$$

In this context, each u_p represents a product of unitaries $U^p_{\vec{n}}$ that are localized on the supercells $C^p_{\vec{n}}$. Explicitly, this can be expressed as:

$$u_p(\cdot) = \left(\prod_{\vec{n}} U^{p\dagger}_{\vec{n}}\right) \cdot \left(\prod_{\vec{n}} U^p_{\vec{n}}\right), \tag{4.11}$$

where the order of multiplication is inconsequential, as the unitaries operate on non-overlapping regions and thus commute.

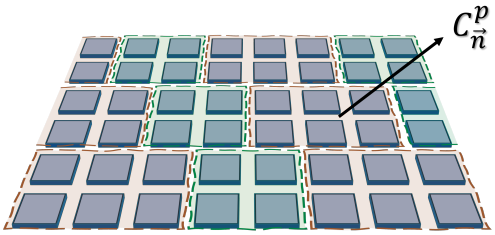

Figure 4.3: Partition of the lattice into finite supercells $C^p_{\vec{n}}$ of arbitrary shape. Unitary transformations, or more generally, CPTP transformations, are then applied to the systems within these supercells.

An illustrative example of a QCA constructed using this partitioning approach is the *block-partitioned* QCA discussed in [168], which employs layers of conditional unitaries. For the case of nearest-neighbor interactions in a one-dimensional lattice of qubits, we define an operator that acts non-trivially on sites $n-1$ with $|a\rangle\langle a|$, n with v^{ab}, and $n+1$ with $|b\rangle\langle b|$ as follows:

$$D_n^{ab} = |a\rangle\langle a|_{n-1} \otimes v_n^{ab} \otimes |b\rangle\langle b|_{n+1}, \quad a, b \in \{0, 1\}, \tag{4.12}$$

where v_n^{ab} is a unitary operator. The corresponding conditional unitary operator is defined as:

$$V_n = \sum_{a,b\in\{0,1\}} D_n^{ab}. \tag{4.13}$$

When the qubits at sites $n+1$ and $n-1$ are in the state $|0\rangle$, the unitary v_n^{00} is applied to the qubit at site n. The QCA dynamics are then modeled using a depth-three quantum circuit: first, apply V_n to all sites where $n \mod 3 = 0$, then to those where $n \mod 3 = 1$, and finally to those where $n \mod 3 = 2$. This scheduling ensures that unitaries are never applied simultaneously to overlapping supercells. The properties of such QCAs, including information transport and entanglement generation, were explored in [168]. This partitioning method also facilitates the construction of non-unitary QCAs, as demonstrated in the same reference, where local unitaries are replaced by local CPTP maps.

To implement the discrete-time evolution of the system, we define a quantum channel using the Kraus operator decomposition [167]:

$$\hat{S}[\hat{\rho}] = \sum_{a,b\in\{0,1\}} \hat{K}^{ab} \hat{\rho} \big(\hat{K}^{ab}\big)^\dagger \tag{4.14}$$

where $\hat{K}^{ab} = \prod_n \hat{D}_n^{ab}$, satisfying the trace-preserving condition:

$$\sum_{a,b} \big(\hat{K}^{ab}\big)^\dagger \hat{K}^{ab} = \hat{\mathbb{1}}. \tag{4.15}$$

Alternatively, in the context of continuous-time dynamics, we can introduce the Lindbladian:

$$\hat{\mathcal{L}}[\hat{\rho}] = -i\left[\hat{H}, \hat{\rho}\right] + \sum_{n=1}^{N} \sum_{a,b} \left(\hat{L}_n^{ab} \hat{\rho} (\hat{L}_n^{ab})^\dagger - \frac{1}{2} \left((\hat{L}_n^{ab})^\dagger \hat{L}_n^{ab} \hat{\rho} + \hat{\rho} (\hat{L}_n^{ab})^\dagger \hat{L}_n^{ab} \right) \right) \tag{4.16}$$

where $\hat{H}$ represents the Hamiltonian, and $\left\{\hat{L}_n^{ab}\right\}$ denotes the set of jump operators acting on lattice site n, which take the same form as in Eq. (4.12).

This framework leads to irreversible QCAs, such as the solutions to the quantum version of the density classification task explored in Chapter 5, or the quantum analog of the classical Rule 110 cellular automaton discussed in Sec. 4.1.1. In the latter case, since Rule 110 is inherently irreversible, a non-unitary QCA is necessary for its replication.

4.3.3 Rydberg atoms implementation

Unlike the quantum circuit model, where global unitary operations are built using single-qubit gates or small sets of qubit interactions, QCAs achieve global unitary dynamics without the need for addressing individual qubits directly. This is often seen as an advantage, since controlling individual sites can be challenging in practice [173]. A promising experimental proposal suggests using ultracold atoms excited to Rydberg states to implement QCAs [174]. This approach demonstrates the suitability of QCAs for tasks such as variational quantum optimization and quantum state engineering, where the system can be tuned to reach highly entangled steady states.

We consider a physical setup consisting of an array of three-level systems with a ground state $|g\rangle \equiv |0\rangle$, a strongly interacting Rydberg state $|r\rangle \equiv |1\rangle$, and a short-lived intermediate state $|e\rangle$, which mediates non-unitary interactions (see Fig. 4.4). This configuration can be realized using various technologies, such as single atoms [175–179], trapped ions [180, 181], or Rydberg-blockaded atomic ensembles [182–184]. For simplicity, we assume an equidistant 1D chain of trapped atoms with nearest-neighbor interactions. Two fields, each with several discrete frequency components, couple the $|g\rangle \leftrightarrow |r\rangle$ and $|r\rangle \leftrightarrow |e\rangle$ transitions.

Under the rotating wave approximation, the system's dynamics are governed by a time-dependent quantum master equation in Lindblad form (with $\hbar = 1$):

$$\frac{\partial \hat{\rho}}{\partial t} = \mathcal{L}[\hat{\rho}] = -i[\hat{H}, \hat{\rho}] + D[\hat{\rho}], \tag{4.17}$$

where the Hamiltonian $\hat{H}$ is given by:

$$\hat{H} = \sum_{j,k} \left(\frac{\theta_j^k}{2} e^{ikVt} \hat{\sigma}_j^{rg} + \frac{\phi_j^k}{2} e^{ikVt} \hat{\sigma}_j^{re} + \text{h.c.} \right) + V \hat{\sigma}_j^{rr} \hat{\sigma}_{(j+1)}^{rr}. \tag{4.18}$$

Here, $\hat{\sigma}_j^{ab} = |a\rangle\langle b|_j$ acts on site j, and V represents the nearest-neighbor interaction strength. The time-dependent phase factors describe the discrete components of the multifrequency fields, with detunings kV ($k = 0, 1, 2$), and coupling strengths θ_j^k and ϕ_j^k. These couplings may vary across the system (e.g., between even and odd sites) or remain uniform. Dissipation is described by:

$$D[\hat{\rho}] = \sum_j \hat{L}_j \hat{\rho} \hat{L}_j^\dagger - \frac{1}{2} \left(\hat{L}_j^\dagger \hat{L}_j \hat{\rho} + \hat{\rho} \hat{L}_j^\dagger \hat{L}_j \right), \tag{4.19}$$

where the jump operators $\hat{L}_j = \sqrt{\Gamma} \hat{\sigma}_j^{ge}$ describe spontaneous decay from the $|e\rangle$ state. The decay of the Rydberg state $\sqrt{\gamma} \hat{\sigma}_j^{gr}$ is assumed to be much slower and will be neglected.

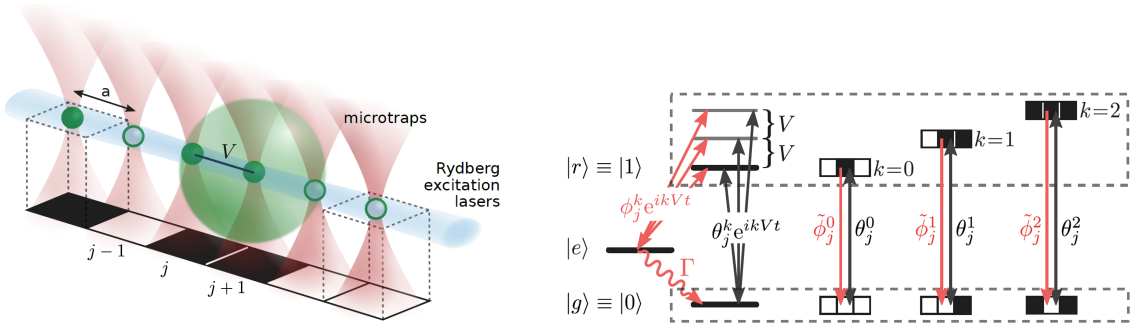

Figure 4.4: **Implementation of QCA using Rydberg atoms.** Left: A one-dimensional array of atoms in optical microtraps, separated by a distance a, with interactions limited to nearest neighbors with interaction strength V. Right: Transitions between states $|g\rangle \leftrightarrow |r\rangle$ and $|r\rangle \leftrightarrow |e\rangle$ are driven by fields with detunings kV and coupling strengths θ_j^k and ϕ_j^k. The system can be simplified to an effective two-state model, where the couplings θ_k^j and $\widetilde{\phi}_k^j$ enable unitary (reversible) and non-unitary (dissipative) conditional interactions, dependent on the number of excited neighbors k. Image taken from [174].

In the regime $V \gg \Gamma > \theta_j^k, \phi_j^k$, the full quantum master equation simplifies to an effective two-level system with time-independent three-body conditional interactions [174]. To achieve this, we first transform the Hamiltonian (4.18) into the interaction picture with respect to the nearest-neighbor Rydberg-Rydberg interactions [185] and adiabatically eliminate the time-dependent phase factors using a large-frequency expansion [186, 187]. Subsequently, we eliminate the rapidly decaying $|e\rangle$ states through the effective operator formalism [188], leading to a time-independent master equation described by the effective Hamiltonian:

$$\hat{H}_{\text{eff}} = \frac{1}{2} \sum_j \sum_{a,b} \theta_j^k \hat{P}_{j-1}^a \hat{X}_j \hat{P}_{j+1}^b, \tag{4.20}$$

and the effective Lindblad operator:

$$\hat{L}_{\text{eff}}^- = \frac{1}{2} \sum_j \sum_{a,b} \sqrt{\widetilde{\phi}_j^k} P_{j-1}^a \left(\hat{X}_j - i\hat{Y}_j \right) P_{j+1}^b, \tag{4.21}$$

where $\widetilde{\phi}_j^k = \phi_j^k / \sqrt{\Gamma}$, and we assume $\theta_j^k \in \mathbb{R}$. The double sum over a and b runs from 0 to 1, with $k = a + b$, $P_j^a = |\alpha\rangle\langle\alpha|_j$, and $\hat{X}_j, \hat{Y}_j, \hat{Z}_j$ are Pauli matrices.

Although this model is framed in a 1D geometry with nearest-neighbor interactions, it can be extended to higher dimensions or include additional neighbors by incorporating more frequency components in the driving fields.

Equations (4.20) and (4.21) describe an effective PXP model, commonly used to model Rydberg blockade and facilitation in atomic chains [185, 189–191]. This model generalizes the PXP approach by introducing a broader range of unitary and dissipative conditional operators, arising from multifrequency driving fields. Fig. 4.4 (left panel) illustrates the unitary and non-unitary conditional update rules for the central site j of a three-site neighborhood. Each field component θ_j^k induces transitions when there are exactly k Rydberg excitations in the neighborhood, controlled by the

projection operators P^a_{j-1}, P^b_{j+1}. For example, $a = b = 1$ means the state changes only if both left and right neighbors are in the $|1\rangle$ state. The special case $\theta^0_j \neq 0,\ \theta^{k>0}_j = 0$ corresponds to Rydberg blockade, while $\theta^{k>0}_j \neq 0,\ \theta^0_j = 0$ corresponds to facilitated excitation when k neighbors are already excited. Introducing strong dissipative couplings via the second multifrequency field ϕ^k adds irreversible interactions, returning atoms to the $|0\rangle$ state.

The missing jump operators,

$$\hat{L}^+_{\text{eff}} = \frac{1}{2} \sum_j \sum_{a,b} \sqrt{\widetilde{\phi}^k_j} P^a_{j-1} \left(\hat{X}_j + i\hat{Y}_j \right) P^b_{j+1}, \tag{4.22}$$

are required to implement incoherent excitation across all sites j, conditioned on the states of neighboring sites. The L^+ operators can be derived by conjugating the system with spin-flip operators and adjusting $\widetilde{\phi}^k_j$ to match the desired jump rates. When the time intervals between spin-flip pulses are sufficiently short, the actions of both L^+ and L^- operators can be considered simultaneous, as suggested by the Trotterization argument.

While QCAs offer certain advantages, particularly due to their reliance on global operations, most quantum computing research still focuses on other models, especially the circuit model. Consequently, a well-developed theory of error correction for QCAs remains lacking, unlike for the circuit model. Developing such a theory could be an exciting avenue of research, possibly avoiding the need for few-qubit operations altogether.

Chapter 5

Density Classification with non-unitary Quantum Cellular Automata

5.1 Introduction

In this chapter, three Quantum Cellular Automata (QCAs) are introduced to address the Density Classification (DC) task and the Majority Voting (MV) problem, which, in a quantum setting, are no longer completely equivalent. Two of these QCAs solve the DC task: one is inspired by the classical CA model by Fukś (2002) [192], and the other is a novel quantum model showcasing additional quantum characteristics, such as quantum coherences and correlations within the system, and is limited to two-body interactions only.

A third QCA is designed specifically for the MV problem and is implemented as a hybrid rule. Both discrete-time completely positive trace-preserving (CPTP) maps and corresponding continuous-time Lindblad dynamics are considered. The efficiency of the first two QCAs in solving the DC task is demonstrated by calculating the spectral gap of their respective Lindbladians, while the convergence time for the third QCA is established in the discrete case.

The definitions for the DC algorithm are presented in Sec. 5.3, followed by descriptions of the QCA models in Sec. 5.4. Their dynamics are then analyzed in Sec. 5.5, with conclusions provided in Sec. 5.6.

5.2 State of the Art

Cellular automata (CAs) are dynamical systems characterized by a spatial lattice of multistate cells, which are synchronously updated based on their own state and the states of neighboring cells within a certain radius. The dynamics of CAs are invariant under translations in both space and time, preserving locality and causality. A classic challenge for CAs is the DC task [193–195], which aims to map the global density of 1s in an arbitrary initial configuration of two-state 0/1 lattice cells to local density information.

It has been proven [154] that no one-dimensional, two-state, radius $r \geq 1$, deterministic CA with periodic boundary conditions can classify the density of all initial configurations. This proof has been extended to both deterministic and probabilistic CAs in any dimension [196]. However, by relaxing certain assumptions—such as incorporating boundary conditions [197] or allowing broken translational invariance in the output [156]—it is possible to design a two-state CA that performs the DC task with a convergence time τ_{conv} scaling linearly with the system size N.

Furthermore, Fukś investigated a sequence of two elementary CA rules, first applying traffic rule 184 for half the updates and then majority rule 232 for the remaining steps. This approach, detailed in [157], successfully solves the DC task with a convergence time $\tau_{\text{conv}} = N$. The traffic rule 184 eliminates all 00 blocks if the density is greater than 1/2, or all 11 blocks if the density is less than 1/2, while rule 232 then results in a homogeneous configuration of all 0s or all 1s. Later work by Fukś [198] examined a subset of ternary (three-state) CA rules with additive invariants, revealing that absolute DC is impossible using just a pair of ternary rules.

As outlined in the previous Chapter 4, introducing randomness can prove useful when updates are restricted to a single rule. In this context, Fukś [192] proposed a probabilistic CA with a non-deterministic local update rule that solves the DC task with a convergence time $\tau_{\text{conv}} = \mathcal{O}(N^2)$. Additionally, Fatès [162] demonstrated how a stochastic combination of two deterministic rules, traffic and majority rules, distinct from [157], achieves classification accuracy above 90%, with an experimentally confirmed (quasi-)linear scaling of $\tau_{\text{conv}} = \mathcal{O}(N)$.

Given these classical CA models for addressing the DC task, it naturally raises the question of whether quantum versions of these CA models can be developed as efficient density classifiers. This becomes particularly relevant when implementing CA-like dynamics on qubits, where the transition rules must comply with the principles of quantum mechanics. Direct translation of CA update rules to quantum cellular automata (QCAs) is often non-trivial, as classical CA rules typically involve synchronous updates on all cells, whereas QCAs require partitioning of the rule due to the inability to perform synchronous updates [199, 200]. In fact, directly applying local synchronous CA rules to partitioned QCA rules can lead to significantly different dynamics [201].

Some progress on QCAs for DC has recently been made. Guedes et al. [202] proposed two QCAs based on the classical elementary CA rule 232, each with density-classification capabilities. These include the local majority voting and the two-line voting, the latter of which extends rule 232 by adding a temporal dimension. Although not a perfect classifier, their method has been demonstrated to facilitate efficient measurement-free quantum error correction (MFQEC) in the context of bit-flip channels. This construction can be implemented using local gates in a quasi-1D lattice, while our work focuses on a single 1D lattice.

The majority voting problem, closely related to DC, involves mapping the majority to a binary-valued local density, rather than translating a global density into a real-valued local density. It is a widely studied problem in mathematics and computer science and has recently been explored using quantum computing algorithms. For instance, recent work has proposed quantum-accelerated voting algorithms [203], quantum logical veto and nomination rules [204], quantum parliaments [205], quantum voting protocols capable of selecting multiple winners [206], non-oracular quantum adaptive search methods [207], quantum majority votes that violate the quantum Arrow's impossibility theorem [208], and generalized quantum majority votes for determining the majority state from a

sequence of quantum states [209].

5.3 Problem

The DC task sets the question of finding an efficient algorithm that can extract information about the global density of the input state on a 1D lattice from a local measurement on any cell.

Definition 5 *Let N be a natural number and $\vec{b} = (b_1, \ldots, b_N)$ an N-bit string. Then the* majority function $\mathrm{maj} : \{0,1\}^N \to \{-1,+1\}$ *is defined so that*

$$\mathrm{maj}\,(b_1, \ldots, b_N) = \begin{cases} +1 & \text{if } \sum_{j=1}^{N} b_j > N/2, \\ -1 & \text{if } \sum_{j=1}^{N} b_j \leq N/2. \end{cases} \tag{5.1}$$

For the translation onto quantum systems, whose outcomes are probabilistic in nature, we propose an evaluation criterion that correlates the probabilities of measurements with the number density of the initial state. After mapping an N-bit string $\vec{b} = (b_1, ..., b_N)$ to an N-qubit system $|b_1 \cdots b_N\rangle$, a lattice site j is chosen at which the measurement will be performed.

Definition 6 *Let $\hat{S}$ be an N-cell QCA. We say that $\hat{S}$ is a* density classifier *at time t if for any location j the following procedure computes a function that solves the density classification task.*

1. *Encode the N-bit input string into an N-qubit quantum register.*
2. *Apply $\hat{S}$ to the quantum register t times.*
3. *Measure the j^{th} qubit of the quantum register in the computational basis.*

The result of the three steps in Def. 6 is a quantum version of the guessing function $g_{j,t} : \{0,1\}^N \to \{-1,+1\}$, in which the majority is defined within a certain error threshold δ:

$$g_{j,t}\left(\vec{b}\right) = \begin{cases} +1 & \text{if } \mathrm{Tr}\left[|1\rangle\langle 1|_j \otimes \hat{S}^t\left(\left|\vec{b}\right\rangle\left\langle\vec{b}\right|\right)\right] \geq 1/2 + \delta, \\ -1 & \text{if } \mathrm{Tr}\left[|1\rangle\langle 1|_j \otimes \hat{S}^t\left(\left|\vec{b}\right\rangle\left\langle\vec{b}\right|\right)\right] \leq 1/2 - \delta. \end{cases} \tag{5.2}$$

where the outcomes $\{+1, -1\}$ match those of the function maj in Def. 5. A QCA can thus solve the DC problem if it maps global densities to local densities, satisfying the aforementioned density classifier definition. On the other hand, if all cells of the system are evolved to the state that the initial majority of the cells were in, then the Majority Voting problem is solved as a sub-problem of the DC task. Therefore, although the terms "Density Classification task" and "Majority Voting problem" were previously used interchangeably in the classical version of the problem, we will henceforth distinguish between them and refer to each appropriately.

5.4 Model

Three non-unitary QCAs are proposed, two of which are density classifiers that conserve the number density of the system and one that outputs the string with all bits carrying the majority of the input string. The first QCA is inspired by a CA that has been shown to solve the DC task, namely the "Fukś CA" [192], that will be used as a framework to construct a corresponding quantum model, see Sec. 5.4.1. The second is a novel QCA, called "Dephasing QCA", that outperforms the Fukś QCA by only including two-cell interactions, see Sec. 5.4.2. The third QCA is introduced for solving the majority voting problem and is a hybrid rule defined by discrete-time three-body interactions, see Sec. 5.4.3. All QCAs are defined on a one-dimensional lattice with N lattice sites and periodic boundary conditions, see Fig. 5.1.

To establish the foundational mathematical framework on which this chapter is based, the description of the quantum channels is outlined in the following prelude. To start, a quantum channel $\hat{S}$ is in the Kraus decomposition given by

$$\hat{S}[\hat{\rho}] = \sum_{\mu} \hat{K}_{\mu}\, \hat{\rho} \left(\hat{K}_{\mu}\right)^{\dagger}, \tag{5.3}$$

where $\{\hat{K}_{\mu}\}$ labels the set of Kraus operators satisfying the trace-preserving condition $\sum_{\mu} \left(\hat{K}_{\mu}\right)^{\dagger} \hat{K}_{\mu} = \hat{\mathbb{1}}$, where $\hat{\mathbb{1}}$ is the identity operator. The quantum density matrices are vectorized using the Choi-isomorphism $|a\rangle\langle b| \to |a\rangle \otimes |b\rangle$, such that a density matrix $\hat{\rho}(t) = \sum_{a,b} \hat{\rho}_{a,b}(t)\, |a\rangle\langle b|$ becomes a vector in a doubled space $\sum_{a,b} \hat{\rho}_{a,b}(t)\, |a\rangle \otimes |b\rangle$, where the states at each individual site are vectorized first before the tensor product over all sites is applied [210]. Under this mapping, the Kraus decomposition (5.3) becomes,

$$\hat{\mathbb{S}} = \sum_{\mu} \hat{K}_{\mu} \otimes \left(\hat{K}_{\mu}\right)^{*}, \tag{5.4}$$

which acts on the doubled Hilbert space $\mathcal{H} = \prod_j \mathcal{H}_j \otimes \mathcal{H}_j^*$, where $\mathcal{H}_j^*$ denotes the dual Hilbert space on site j. Furthermore, for considering continuous-time dynamics, the Lindblad evolution

$$\hat{\mathcal{L}}[\hat{\rho}] = -i\Big[\hat{H}, \hat{\rho}\Big] + \sum_{j=1}^{N} \sum_{k} \left(\hat{L}_{k_j} \hat{\rho} \hat{L}_{k_j}^{\dagger} - \frac{1}{2}\Big(\hat{L}_{k_j}^{\dagger} \hat{L}_{k_j} \hat{\rho} + \hat{\rho} \hat{L}_{k_j}^{\dagger} \hat{L}_{k_j}\Big)\right) \tag{5.5}$$

is utilized, where i labels the imaginary unit, $\hat{H}$ represents the Hamiltonian, and $\{\hat{L}_{k_j}\}$ is the set of jump operators acting on lattice site j (henceforth we set $\hbar \equiv 1$). In the vectorized form, Eq. (5.5) becomes

$$\hat{\mathbb{L}} = -i\Big(\hat{H} \otimes \hat{\mathbb{1}} - \hat{\mathbb{1}} \otimes \hat{H}^{T}\Big) + \sum_{j=1}^{N} \sum_{k} \left(\hat{L}_{k_j} \otimes \hat{L}_{k_j}^{*} - \frac{1}{2}\Big(\hat{L}_{k_j}^{\dagger} \hat{L}_{k_j} \otimes \hat{\mathbb{1}} + \hat{\mathbb{1}} \otimes \hat{L}_{k_j}^{\dagger} \hat{L}_{k_j}\Big)\right). \tag{5.6}$$

Given this framework, the theoretical description of the proposed QCA models is outlined next.

5.4.1 Fukś QCA

The Fukś rule [192] is a radius-one probabilistic CA given by the transition probabilities presented in Tab. 5.1. A cell in state one with two neighboring zero states becomes zero with probability $2p$, and, analogously, a cell in the zero state surrounded by two one states is becomes a one state with the same probability $2p$. If the neighboring sites are in two different states, then the state at the center site is flipped with probability p. Zero(one) states are mapped to one (zero) states with a probability proportional to the number of ones (zeroes) in the neighborhood. It was shown that the dynamics of the local density can be approximated by the standard diffusion equation implying that the convergence time scales quadratically with the system size N, $\tau_{\text{conv}} = \mathcal{O}(N^2)$. Deriving quantum

neighborhood	transition	probability	Kraus operators
00	$000 \to 010$	$p_{000} = 0$	amplitude damping
	$010 \to 010$	$p_{010} = 1 - 2p$	$\left\{\hat{P}_0 + \sqrt{1-2p}\,\hat{P}_1, \sqrt{2p}\,\hat{\sigma}^-\right\}$
01	$001 \to 011$	$p_{001} = p$	
	$011 \to 011$	$p_{011} = 1 - p$	stochastic bit-flip
10	$100 \to 110$	$p_{100} = p$	$\left\{\sqrt{1-p}\,\hat{\mathbb{1}}, \sqrt{p}\,\hat{X}\right\}$
	$110 \to 110$	$p_{110} = 1 - p$	
11	$101 \to 111$	$p_{101} = 2p$	amplitude pumping
	$111 \to 111$	$p_{111} = 1$	$\left\{\sqrt{1-2p}\,\hat{P}_0 + \hat{P}_1, \sqrt{2p}\,\hat{\sigma}^+\right\}$

Table 5.1: Fukś QCA. The transition probabilities p_{acb} represent the likelihood of the state transition $|acb\rangle \to |a1b\rangle$, with $a, b, c \in \{0, 1\}\ \forall\ p \in \left(0, \frac{1}{2}\right]$. Note that the associate input/output states are two-on-one with the output center site set to be in the one state; the transition from the same input state to the corresponding output state with the center site in the zero state is, correspondingly, one minus the associate transition probability (for example, the transition $110 \to 100$ occurs with probability $1 - p_{110} = 1 - (1 - p) = p$). Fourth column: set of Kraus operators of the associated quantum channels acting on the center site j, where $\hat{P}_0 = |0\rangle\langle 0|$, $\hat{P}_1 = |1\rangle\langle 1|$, $\hat{\mathbb{1}} = |0\rangle\langle 0| + |1\rangle\langle 1|$, $\hat{\sigma}^- = |0\rangle\langle 1|$, and $\hat{\sigma}^+ = |1\rangle\langle 0|$.

dynamics inspired by the *non-partitioned* Fukś CA faces the challenge that CAs are implemented by making a copy of the whole state at each time step — because only then could all cells, at both even and odd lattice sites, be updated simultaneously based on the neighboring states at the previous time step. This copy operation, as a fundamental part of classical CAs, can however not be performed on a quantum state due to the no-cloning theorem [211]. Only specifically *partitioned* CAs that update all even and all odd sites one after the other in consecutive time steps and do not involve the implementation of a copy process, can be directly translated into a corresponding QCA. One example of a partitioned CA is the Domany-Kinzel CA model, as originally proposed in [212], whose associate quantum version has been intensively investigated in [191, 213–216]. On the

other hand, CAs that are not partitioned (and do include the copy process) could not be directly translated into a quantum map. This is why the definitions of the quantum channel are in this work merely inspired by the basic framework of the considered non-partitioned CAs.

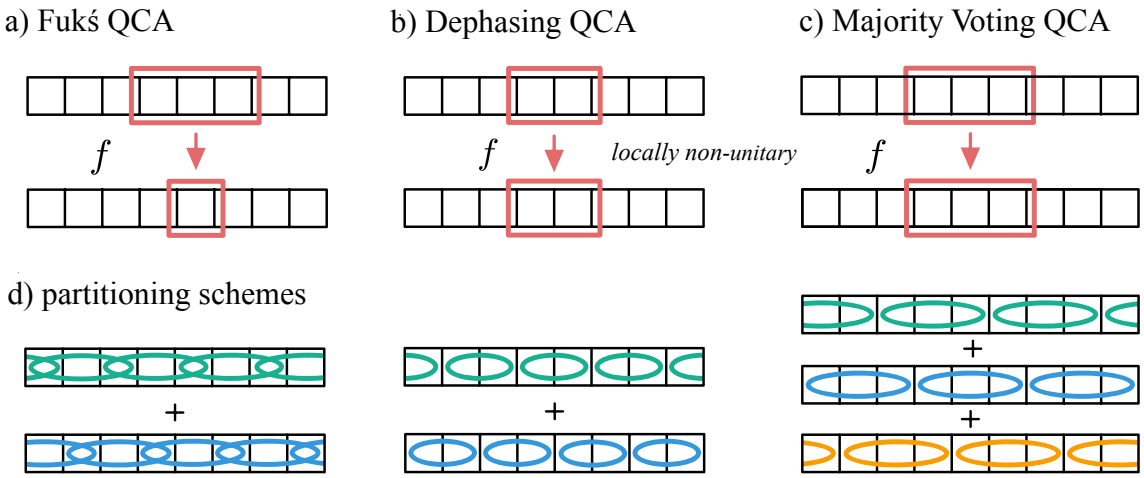

Figure 5.1: Illustration of the dynamics of a) the Fukś QCA, b) the Dephasing QCA, c) the Majority Voting QCA, and d) their partitioning schemes with periodic boundaries, where f represents the respective local transition function. While the Fukś QCA is defined by three-body operations where only the center site is updated, all cells of the two-body neighborhoods are updated for the Dephasing QCA and likewise all three cells are updated for the Majority Voting QCA. d) For the Fukś QCA, the three-body operations are applied subsequently onto all even and then all odd lattice sites of the system, whereas in case of the Dephasing QCA and the Majority Voting QCA, only all neighboring non-overlapping neighborhoods can be updated simultaneously.

A quantum version based on the Fukś CA is defined by

$$\hat{\mathbb{S}}^{(\text{Fukś})} = \prod_j \left(\hat{\mathbb{S}}_j^{(00)} + \hat{\mathbb{S}}_j^{(01)} + \hat{\mathbb{S}}_j^{(10)} + \hat{\mathbb{S}}_j^{(11)} \right), \tag{5.7}$$

where

$$\hat{\mathbb{S}}_j^{(ab)} = |aa\rangle\langle aa|_{j-1} \otimes \hat{\mathbb{K}}^{(ab)} \otimes |bb\rangle\langle bb|_{j+1}\,, \tag{5.8}$$

and

$$\hat{\mathbb{K}}^{(ab)} = \sum_\mu \hat{K}_\mu^{(ab)} \otimes \left(\hat{K}_\mu^{(ab)} \right)^* \quad \forall\ a, b \in \{0, 1\}. \tag{5.9}$$

Note that each local operator of the superoperator (5.7) acts non-trivially only on the three-cell neighborhood $(j-1, j, j+1)$ of the lattice, thereby preserving locality as well as spatial and temporal invariance by performing the same operation on all sites during each QCA update. The projectors $|aa\rangle\langle aa|$ and $|bb\rangle\langle bb|$ that act on the left $(j-1)$ and the right $(j+1)$ sites determine the neighborhood of the qubit at the center site j, on which the superoperator acts on. The definition of the four sets

of Kraus operators $\{\hat{K}_\mu^{(ab)}\}$ thus fully defines the quantum channel. For the Fukś QCA, these are given by

$$\hat{K}_0^{(00)} = \hat{P}_0 + \sqrt{1-2p}\,\hat{P}_1, \qquad \hat{K}_1^{(00)} = \sqrt{2p}\,\hat{\sigma}^-, \tag{5.10a}$$

$$\hat{K}_0^{(01)} = \sqrt{1-p}\,\hat{\mathbb{1}}, \qquad \hat{K}_1^{(01)} = \sqrt{p}\,\hat{X}, \tag{5.10b}$$

$$\hat{K}_0^{(10)} = \sqrt{1-p}\,\hat{\mathbb{1}}, \qquad \hat{K}_1^{(10)} = \sqrt{p}\,\hat{X}, \tag{5.10c}$$

$$\hat{K}_0^{(11)} = \hat{P}_1 + \sqrt{1-2p}\,\hat{P}_0, \qquad \hat{K}_1^{(11)} = \sqrt{2p}\,\hat{\sigma}^+, \tag{5.10d}$$

which satisfy the trace-preserving condition $\sum_{\mu=0,1}\left(\hat{K}_\mu^{(ab)}\right)^\dagger \hat{K}_\mu^{(ab)} = \hat{\mathbb{1}}$, where $p \in \left(0, \frac{1}{2}\right]$, $\hat{P}_0 = |0\rangle\langle 0|$, $\hat{P}_1 = |1\rangle\langle 1|$ $\hat{\sigma}^- = |0\rangle\langle 1|$, $\hat{\sigma}^+ = |1\rangle\langle 0|$ and $\hat{X}$ is the Pauli-X operator. [1] Associate continuous-time dynamics are described by the Lindbladian

$$\hat{\mathbb{L}}^{(\text{Fukś})} = \sum_{j=1}^{N}\sum_{k=1}^{6}\left(\hat{L}_{k_j}\otimes\hat{L}_{k_j}^* - \frac{1}{2}\left(\hat{L}_{k_j}^\dagger\hat{L}_{k_j}\otimes\hat{\mathbb{1}} + \hat{\mathbb{1}}\otimes\hat{L}_{k_j}^\dagger\hat{L}_{k_j}\right)\right), \tag{5.12}$$

with the six jump operators

$$\hat{L}_{1_j} = \sqrt{\gamma}\,|0\rangle\langle 0|_{j-1}\otimes\hat{\sigma}_j^-\otimes|0\rangle\langle 0|_{j+1}\,, \tag{5.13a}$$

$$\hat{L}_{2_j} = \sqrt{\frac{\gamma}{2}}\,|0\rangle\langle 0|_{j-1}\otimes\hat{\sigma}_j^-\otimes|1\rangle\langle 1|_{j+1}\,, \tag{5.13b}$$

$$\hat{L}_{3_j} = \sqrt{\frac{\gamma}{2}}\,|0\rangle\langle 0|_{j-1}\otimes\hat{\sigma}_j^+\otimes|1\rangle\langle 1|_{j+1}\,, \tag{5.13c}$$

$$\hat{L}_{4_j} = \sqrt{\frac{\gamma}{2}}\,|1\rangle\langle 1|_{j-1}\otimes\hat{\sigma}_j^-\otimes|0\rangle\langle 0|_{j+1}\,, \tag{5.13d}$$

$$\hat{L}_{5_j} = \sqrt{\frac{\gamma}{2}}\,|1\rangle\langle 1|_{j-1}\otimes\hat{\sigma}_j^+\otimes|0\rangle\langle 0|_{j+1}\,, \tag{5.13e}$$

$$\hat{L}_{6_j} = \sqrt{\gamma}\,|1\rangle\langle 1|_{j-1}\otimes\hat{\sigma}_j^+\otimes|1\rangle\langle 1|_{j+1}\,. \tag{5.13f}$$

The jump operators $\hat{L}_{1_j}$ and $\hat{L}_{6_j}$ ensure the amplitude damping/pumping transitions $010 \to 000$ and $101 \to 111$ for long-time evolution $\tau \gg 1/\gamma$. The other jump operators $\hat{L}_{2_j}$ to $\hat{L}_{5_j}$ simulate the bit-flip channel in case of the 01 and 10 neighborhoods, where the overall scaling factor $\frac{1}{\sqrt{2}}$ ensures that the bit-flip operation is implemented with half the probability compared to the amplitude damping/pumping operations — this is analogous to the classical Fukś CA that implements the bit-flip with probability p and the amplitude damping/pumping with probability $2p$, see Tab. 5.1 and derivation in Appendix B. Note that by setting the decay rate $\gamma \equiv 1$ in all calculations, the convergence time of the system can thus be determined as multiples of the time steps τ.

[1] Another way to describe the CA is by applying, for each cell j independently, the elementary CA rule 170 with probability p, rule 240 with the same probability p, and the identity operation with probability $1-2p$; see p. 230 in [162]:

$$\hat{\mathbb{S}}^{(\text{Fukś})} = p\,\hat{\mathbb{S}}^{(170)} + p\,\hat{\mathbb{S}}^{(240)} + (1-2p)\,\hat{\mathbb{1}}. \tag{5.11}$$

Furthermore, as illustrated on the left in Fig. 5.1d), the Fukś QCA is approximated by a partitioning scheme which is enhanced by repeatedly updating all even and then all odd lattice sites with infinitesimal time updates τ:

$$e^{\hat{\mathbb{L}}^{(\text{even})}\tau}e^{\hat{\mathbb{L}}^{(\text{odd})}\tau} \approx e^{\left(\hat{\mathbb{L}}^{(\text{even})}+\hat{\mathbb{L}}^{(\text{even})}\right)\tau}, \tag{5.14}$$

where $\hat{\mathbb{L}}^{(\text{even/odd})}$ describes the Fukś Lindbladian (5.12) acting on all even/odd lattice sites simultaneously.

5.4.2 Dephasing QCA

While the Fukś QCA is inspired by a classical CA, the here introduced quantum model, dubbed the Dephasing QCA, is more efficiently constructed since the local map requires only two-body interactions. This rule preserves the number density of the input state and maps the system's global number density to the local density information. The Dephasing QCA is given by the Lindblad evolution

$$\begin{aligned}\hat{\mathbb{L}}^{(\text{Dephasing})} =& -i\Big(\hat{H}\otimes\hat{\mathbb{1}}-\hat{\mathbb{1}}\otimes\hat{H}^T\Big)+\\ &+\sum_{j=1}^{N}\sum_{k=1}^{4}\left(\hat{L}_{k_{j,j+1}}\otimes\hat{L}^*_{k_{j,j+1}}-\frac{1}{2}\Big(\hat{L}^\dagger_{k_{j,j+1}}\hat{L}_{k_{j,j+1}}\otimes\hat{\mathbb{1}}+\hat{\mathbb{1}}\otimes\hat{L}^\dagger_{k_{j,j+1}}\hat{L}_{k_{j,j+1}}\Big)\right)\end{aligned} \tag{5.15}$$

with Hamiltonian

$$\hat{H} = \Omega\sum_{j=1}^{N}\Big(\hat{X}_j\hat{X}_{j+1}+\hat{Y}_j\hat{Y}_{j+1}\Big), \tag{5.16}$$

where $\Omega\in\mathbb{R}$, $\hat{X}$ and $\hat{Y}$ represent the associated Pauli operators, and the jump operators $\hat{L}_{k_{j,j+1}}$ act each on the two neighboring sites, j and $j+1$, where $j+1\equiv 1$ if $j=N$ considering periodic boundary conditions. The latter are given by the four projectors

$$\hat{L}_{1_{j,j+1}} = |00\rangle\langle 00|_{j,j+1}\,, \tag{5.17a}$$
$$\hat{L}_{2_{j,j+1}} = |\psi^+\rangle\langle\psi^+|_{j,j+1}\,, \tag{5.17b}$$
$$\hat{L}_{3_{j,j+1}} = |\psi^-\rangle\langle\psi^-|_{j,j+1}\,, \tag{5.17c}$$
$$\hat{L}_{4_{j,j+1}} = |11\rangle\langle 11|_{j,j+1}\,, \tag{5.17d}$$

with the Bell states $|\psi^\pm\rangle = \frac{1}{\sqrt{2}}(|01\rangle\pm|10\rangle)$. Note that the QCA acts in the same way on the left and on the right site of each two-cell neighborhood and that the dissipator is parity-symmetric. The projectors are eigenstates of the Hamiltonian and are designed to remove coherences between different eigenspaces of $\hat{S}_z$, but also within the same eigenspace of $\hat{S}_z$.

The corresponding partitioning scheme of the QCA is illustrated and described in Fig. 5.1d), where the two sets of two-body updates are, analogous to the Fukś QCA, approximated by infinitesimal time updates generated by Lindbladians according to Eq. (5.14), where the even (odd) updates are here defined to be those where the left cells of the two-body neighborhoods are located at the even (odd) lattice sites, and the neighborhoods do not overlap in one partial time step.

5.4.3 Majority Voting QCA

For the task of majority voting, analogously to what was done for the Fukś rule above, one might try to use a quantum version of the Fatès CA [162] rule. However, a direct construction is ineffective, as it fails to yield the desired steady states as described in Appendix F.
Therefore, a new solution is proposed. This solution requires relaxing the strict definition of CA in which only the central cell is updated. Furthermore, since our goal is to classify the initial state based on whether its initial density is greater or less than $N/2$, the idea is to structure what differentiates these two sectors. Let n be the expectation value of $\hat{n} = \sum_j |1\rangle\langle 1|_j$. It is easy to observe that if $n \leq N/2$, it will always be possible to distribute the ones along the chain in such a way as to avoid them being neighboring. For $n > N/2$, this is no longer possible. The idea is to define a transformation $\hat{\mathbb{A}}$ such that

- its repeated action on a state $|\hat{\rho}\rangle$ spreads the $|1\rangle$ states out along the chain, so that the final state obtained does not exhibit two neighboring $|1\rangle$ states
- it satisfies $\left[\hat{\mathbb{S}}_z, \hat{\mathbb{A}}\right] = 0$, where $\hat{S}_z = \frac{1}{2}\sum_j \hat{Z}_j$ with Pauli operator $\hat{Z}_j$, which will preserve the number density in the system.

Thus, we define this transformation as:

$$\hat{\mathbb{A}} = \prod_j \sum_{\mu=0,1} \left(\hat{K}_{\mu_j} \otimes \hat{K}^*_{\mu_j}\right), \tag{5.18}$$

where

$$\hat{K}_{0_j} = |1\rangle\langle 1|_{j-1} \otimes |0\rangle\langle 1|_j \otimes |1\rangle\langle 0|_{j+1}\,, \tag{5.19a}$$
$$\hat{K}_{1_j} = \hat{\mathbb{1}} - |1\rangle\langle 1|_{j-1} \otimes |1\rangle\langle 1|_j \otimes |0\rangle\langle 0|_{j+1}\,, \tag{5.19b}$$

that satisfy the trace-preserving condition $\sum_{\mu=0,1} \hat{K}^\dagger_\mu \hat{K}_\mu = \hat{\mathbb{1}}$.The proof for $\hat{\mathbb{A}}$ satisfying the two aforementioned properties can be found in Appendix G.1. In Eq. (5.18), each factor in the product does not commute with its nearest neighbors nor with its next-to-nearest neighbors, but rather with every third site. This implies that different orders of these factors lead to different versions of $\hat{\mathbb{A}}$. However, each of them satisfies the aforementioned requirements, such that it is convenient to choose the one that maximizes the number of operations in a single time step:

$$\hat{\mathbb{A}} \longrightarrow \hat{\mathbb{A}}^{(1)}\hat{\mathbb{A}}^{(2)}\hat{\mathbb{A}}^{(3)} \tag{5.20}$$

where $\hat{\mathbb{A}}^{(x)}$ with $x \in \{1,2,3\}$ describes the action on the associate sets of neighboring, non-overlapping three-cell neighborhoods, see illustration in Fig. 5.1d).

Once transformation $\hat{\mathbb{A}}$ is applied, the resulting state must be brought to $|0\rangle^{\otimes N}$ if it doesn't contain any cluster of $|1\rangle$s. Otherwise, such a cluster must be progressively expanded until it covers the entire chain and reaches the state $|1\rangle^{\otimes N}$. This can be obtained by applying repeatedly:

$$\hat{\mathbb{B}} = \prod_j \sum_{\mu=0,1,2,3} \left(\hat{K}_{\mu_j} \otimes \hat{K}^*_{\mu_j}\right), \tag{5.21}$$

where

$$\hat{K}_{0_j} = |0\rangle\langle 0|_{j-1} \otimes |0\rangle\langle 1|_j \otimes |0\rangle\langle 0|_{j+1}\,, \tag{5.22a}$$

$$\hat{K}_{1_j} = |1\rangle\langle 1|_{j-1} \otimes |1\rangle\langle 1|_j \otimes |1\rangle\langle 0|_{j+1}\,, \tag{5.22b}$$

$$\hat{K}_{2_j} = |1\rangle\langle 0|_{j-1} \otimes |1\rangle\langle 1|_j \otimes |1\rangle\langle 1|_{j+1}\,, \tag{5.22c}$$

$$\begin{aligned}\hat{K}_{3_j} =& \hat{\mathbb{1}} - (|0\rangle\langle 0|_{j-1} \otimes |1\rangle\langle 1|_j \otimes |0\rangle\langle 0|_{j+1} + \\ &+ |1\rangle\langle 1|_{j-1} \otimes |1\rangle\langle 1|_j \otimes |0\rangle\langle 0|_{j+1} + |0\rangle\langle 0|_{j-1} \otimes |1\rangle\langle 1|_j \otimes |1\rangle\langle 1|_{j+1}),\end{aligned} \tag{5.22d}$$

that satisfy the trace-preserving condition $\sum_{\mu=0,1,2,3} \hat{K}_\mu^\dagger\, \hat{K}_\mu = \hat{\mathbb{1}}$. Similar to $\hat{\mathbb{A}}$, we adopt a non-overlapping three-cell partition pattern for $\hat{\mathbb{B}}$. The minimum number of times $\hat{\mathbb{A}}$ and $\hat{\mathbb{B}}$ need to be applied (m_a and m_b) depends on the specific partition scheme chosen as well as the initial state. In Appendix H, we derive the minimum number of layers with respect to our partition scheme capable of classifying every initial state.

In summary, our proposal to solve the majority voting problem is:

$$\begin{aligned}\hat{\mathbb{B}}^{m_b}\hat{\mathbb{A}}^{m_a}\,|\hat{\rho}\rangle = &\underbrace{\hat{\mathbb{B}}^{(1)}\hat{\mathbb{B}}^{(2)}\hat{\mathbb{B}}^{(3)}}_{m_b}\ \underbrace{\hat{\mathbb{B}}^{(1)}\hat{\mathbb{B}}^{(2)}\hat{\mathbb{B}}^{(3)}}_{m_b-1}\ \cdots\ \underbrace{\hat{\mathbb{B}}^{(1)}\hat{\mathbb{B}}^{(2)}\hat{\mathbb{B}}^{(3)}}_{2}\ \underbrace{\hat{\mathbb{B}}^{(1)}\hat{\mathbb{B}}^{(2)}\hat{\mathbb{B}}^{(3)}}_{1} \\ &\times \underbrace{\hat{\mathbb{A}}^{(1)}\hat{\mathbb{A}}^{(2)}\hat{\mathbb{A}}^{(3)}}_{m_a}\ \underbrace{\hat{\mathbb{A}}^{(1)}\hat{\mathbb{A}}^{(2)}\hat{\mathbb{A}}^{(3)}}_{m_a-1}\ \cdots\ \underbrace{\hat{\mathbb{A}}^{(1)}\hat{\mathbb{A}}^{(2)}\hat{\mathbb{A}}^{(3)}}_{2}\ \underbrace{\hat{\mathbb{A}}^{(1)}\hat{\mathbb{A}}^{(2)}\hat{\mathbb{A}}^{(3)}}_{1}\,|\hat{\rho}\rangle\,.\end{aligned} \tag{5.23a}$$

In addition, it is possible to define two Lindbladian operators $\mathcal{L}_A$ and $\mathcal{L}_B$ capable of implementing the continuous-time evolution of transformations $\hat{\mathbb{A}}$ and $\hat{\mathbb{B}}$, which, in the vectorized form, are:

$$\hat{\mathbb{L}}^{\mathrm{A}} = \sum_{j=1}^{N}\left(\hat{L}^a_{0_j}\otimes\hat{L}^a_{0_j} - \frac{1}{2}\left(\hat{L}^{a\dagger}_{0_j}\hat{L}^a_{0_j}\otimes\hat{\mathbb{1}} + \hat{\mathbb{1}}\otimes\hat{L}^{a\dagger}_{0_j}\hat{L}^a_{0_j}\right)\right), \tag{5.24}$$

$$\hat{\mathbb{L}}^{\mathrm{B}} = \sum_{j=1}^{N}\sum_{k=0}^{2}\left(\hat{L}^b_{k_j}\otimes\hat{L}^b_{k_j} - \frac{1}{2}\left(\hat{L}^{b\dagger}_{k_j}\hat{L}^b_{k_j}\otimes\hat{\mathbb{1}} + \hat{\mathbb{1}}\otimes\hat{L}^{b\dagger}_{k_j}\hat{L}^b_{k_j}\right)\right) \tag{5.25}$$

where

$$\hat{L}^a_{0_j} = |1\rangle\langle 1|_{j-1} \otimes |0\rangle\langle 1|_j \otimes |1\rangle\langle 0|_{j+1} \tag{5.26a}$$

$$\hat{L}^b_{0_j} = |0\rangle\langle 0|_{j-1} \otimes |0\rangle\langle 1|_j \otimes |0\rangle\langle 0|_{j+1}\,, \tag{5.26b}$$

$$\hat{L}^b_{1_j} = |1\rangle\langle 1|_{j-1} \otimes |1\rangle\langle 1|_j \otimes |1\rangle\langle 0|_{j+1}\,, \tag{5.26c}$$

$$\hat{L}^b_{2_j} = |1\rangle\langle 0|_{j-1} \otimes |1\rangle\langle 1|_j \otimes |1\rangle\langle 1|_{j+1}\,. \tag{5.26d}$$

Then, our proposal to solve the majority voting problem, by using the continuous-time evolution, is:

$$e^{\hat{\mathbb{L}}^{\mathrm{B}}\tau_B}e^{\hat{\mathbb{L}}^{\mathrm{A}}\tau_A}\,|\hat{\rho}\rangle \tag{5.27}$$

where τ_A represents the time needed to reach a state without two adjacent $|1\rangle$s, and τ_B represents the time to expand a cluster of $|1\rangle$s along the entire chain, both in the worst-case scenario.

Note the jump operators in Eqs. 5.25 differ from corresponding jump operators in Eqs. 5.12 in that they don't restrict to projectors on the left and right cells, and hence have discrete evolution

that is less parallelizable. An attempt was made to find jump operators like in the Fukś rule here by using a supervised machine learning approach. However, this method yielded only a partial solution with extremely long convergence times, and it was not further explored. Nevertheless, a detailed description of this approach and its results can be found in Appendix G.2.

5.5 Results

Next, the research results on the three QCA models are presented: the Fukś QCA in Sec. 5.5.1, the Dephasing QCA in Sec. 5.5.2, and the Majority Voting QCA in Sec. 5.5.3.

5.5.1 Fukś QCA

The dynamics of the Fukś QCA are elaborated in the following, see definition in Sec. 5.4.1. It is shown that $\hat{\mathbb{L}}^{(\text{Fukś})}[\hat{\rho}]$ conserves the number density of the initial state $\hat{\rho}$ in analogy to the associate classical CA rule. The number density can be quantified by the operator $\hat{S}_z = \frac{1}{2}\sum_j \hat{Z}_j$, whose expectation value is conserved as

$$\frac{\mathrm{d}}{\mathrm{d}t}\left\langle \hat{S}_z(t)\right\rangle = 0, \tag{5.28}$$

see proof in Appendix. C. Furthermore, the Fukś Lindbladian in Eq. (5.12) exhibits four zero eigenvalues that correspond to the set of steady states

$$\hat{\rho}_{\text{ss}}^{(\text{Fukś})} = (1-\alpha)\,|0...0\rangle\langle 0...0| + \beta\,|0...0\rangle\langle 1...1| + \beta^*\,|1...1\rangle\langle 0...0| + \alpha\,|1...1\rangle\langle 1...1|\,, \tag{5.29}$$

where $\alpha \in [0,1]$ represents the global (and local) number density of the state, and $\beta, \beta^* \in \mathbb{C}$ are the amplitudes of the off-diagonal coherence terms; see proof in Appendix D. Note that the pure states $|0...0\rangle$ and $|1...1\rangle$, as well as the GHZ state are included in this set corresponding to the parameter sets $\{\alpha = 0, \beta = 0\}$, $\{\alpha = 1, \beta = 0\}$, and $\{\alpha = \frac{1}{2}, \beta = \frac{1}{2}\}$, respectively. All off-diagonal elements unequal to $|0...0\rangle\langle 1...1|$ or $|1...1\rangle\langle 0...0|$ are shown to decohere under the action of this map as derived in Appendix D.0.2. As an example for the dynamics of this QCA, the initial states $|001\rangle$ and $|011\rangle$ are considered that would in the long-time limit $t \gg 1$ evolve to the following steady states:

$$|001\rangle\langle 001| \to \frac{2}{3}\,|000\rangle\langle 000| + \frac{1}{3}\,|111\rangle\langle 111|\,, \tag{5.30a}$$

$$|011\rangle\langle 011| \to \frac{1}{3}\,|000\rangle\langle 000| + \frac{2}{3}\,|111\rangle\langle 111|\,, \tag{5.30b}$$

where the global number densities of $\frac{1}{3}$ and $\frac{2}{3}$, respectively, are conserved.

For quantifying the convergence time τ_{conv}, i.e. the maximum time to reach the steady state of the system, the spectral gap $\Delta\lambda$ is determined. The latter is the energy difference between the ground state and the first excited state, and is given by the smallest non-zero absolute value of the eigenvalues of the Lindbladian. Note that all non-zero eigenvalues are negative, such that the spectral gap corresponds to the negative of largest non-zero eigenvalue. A logarithmic plot of the spectral gap versus the system size is shown in Fig. 5.2.

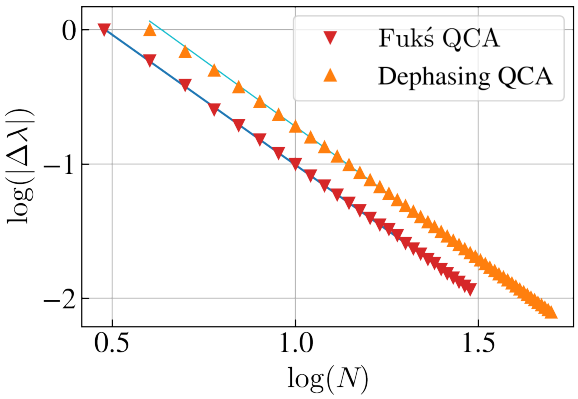

Figure 5.2: Logarithmic plot of the spectral gap $\Delta\lambda$ versus the system size N for the Lindbladians $\hat{\mathcal{L}}^{(\text{Fukś})}$ and $\hat{\mathcal{L}}^{(\text{Dephasing})}$, see Eqs. (5.12) and (5.15), respectively. For the Dephasing QCA the Hamiltonian is turned off ($\Omega = 0$). Using the DMRG algorithm [217], the spectral gap was computed for system sizes $N \in [3, 30]$ for the Fukś QCA, and $N \in [4, 50]$ for the Dephasing QCA. The subjacent blue and cyan lines represent the corresponding linear regression fits $\log(|\Delta\lambda|) = c \cdot \log(N) + d$ with parameters $c = -1.937 \pm 5 \cdot 10^{-3}$ and $d = 0.931 \pm 6 \cdot 10^{-3}$ for the Fukś QCA, and $c = -1.972 \pm 3 \cdot 10^{-3}$ and $d = 1.252 \pm 4 \cdot 10^{-3}$ for the Dephasing QCA. For the latter, the first two points of the spectral gap corresponding to $N = 4, 5$ are excluded from the calculation of the linear regression, which has halved the associate standard deviation of the slope.

An almost quadratic inverse scaling of the spectral gap with the system size is observed, $\Delta\lambda \propto N^{-1.942\pm0.005}$, such that the convergence time scales almost quadratically with the system size:

$$\tau_{\text{conv}} \propto \mathcal{O}\left(\frac{1}{\Delta\lambda}\right) \approx \mathcal{O}\left(N^2\right). \tag{5.31}$$

5.5.2 Dephasing QCA

Next, the results of the Dephasing QCA are outlined, see definition in Sec. 5.4.2. It is derived that the number density of the system is conserved with

$$\frac{\mathrm{d}}{\mathrm{d}t}\left\langle \hat{S}_z(t) \right\rangle = 0, \tag{5.32}$$

and that the Dephasing QCA indeed solves the DC task, see proof in Appendix E. To exemplify the dynamics of this QCA, the initial states $|001\rangle$ and $|011\rangle$ are considered that would in the long-time limit $t \gg 1$ evolve to the following mixed steady states:

$$|001\rangle\langle 001| \to \frac{1}{3}(|001\rangle\langle 001| + |010\rangle\langle 010| + |100\rangle\langle 100|), \tag{5.33a}$$

$$|011\rangle\langle 011| \to \frac{1}{3}(|011\rangle\langle 011| + |101\rangle\langle 101| + |110\rangle\langle 110|). \tag{5.33b}$$

For determining the convergence time τ_{conv}, the spectral gap $\Delta\lambda$ is computed, mirroring the approach taken for the Fukś QCA in the previous subsection. The result is presented in Fig. 5.2, where the slope of the linear regression fit shows that $\Delta\lambda \propto N^{-1.972\pm0.003}$, such that the convergence

time τ_{conv} scales almost quadratically with the system size N similar to the Fukś QCA, see Eq. (5.31). However, the spectral gap is by a constant factor of $0.321 \pm 9 \cdot 10^{-3}$ larger than the spectral gap of the Fukś QCA, which implies that τ_{conv} is reduced (i.e. improved) by this factor in comparison to the Fukś QCA. When including the Hamiltonian (5.16), numerical simulations indicate that the scaling of the convergence time τ_{conv} with N remains unaltered.

5.5.3 Majority Voting QCA

In the following, the dynamics of the Majority Voting QCA are discussed, see Sec. 5.4.3. Our discrete-time-evolution proposal consists of a repeated application of $\hat{\mathbb{A}}$ and, subsequently, $\hat{\mathbb{B}}$ (see Eq. (5.23)) with a non-overlapping three-cell partition pattern as shown in Fig. 5.1d), allowing for the correct classification of every initial state. We consider the application of a single layer per unit time, so the time required to reach the final state, in the worst-case scenario and with $N\text{mod}(3) = 0$, scales in the following way with the system size:

$$\tau = \tau_A + \tau_B = 4 \left\lfloor \frac{N}{2} \right\rfloor + \frac{2}{3}N - 5. \tag{5.34}$$

The proof of this equation can be found in Appendix H.

If $N\text{mod}(3) = 1$ (or 2), the partition scheme will have 1 (or 2) non-updated cell(s) at each layer. To prevent the same cells from remaining non-updated each time, one could periodically shift the partition scheme so that these cells change over time, traversing through the chain. However, in these cases, it is challenging to establish the worst-case scenario to provide a sufficient value of τ valid for all initial states. Additionally, we have observed that starting from certain initial states, delays due to the lack of updating some cells scale linearly with N. This is sufficient to propose a more efficient solution: if $N\text{mod}(3) = 1$, one can simply add two extra qubits (one in $|0\rangle$ and the other in $|1\rangle$) and evolve the entire system; if $N\text{mod}(3) = 2$, one can add four extra qubits (two in $|0\rangle$ and two in $|1\rangle$) and evolve the entire system. This approach enables us to achieve systems with $N\text{mod}(3) = 0$ without altering the initial majority of $|0\rangle$s or $|1\rangle$s.

As outlined in Sec. 5.4.3, a continuous-time evolution proposal is possible (see Eq. (5.27)). To showcase different scenarios, two initial states, belonging to two different sectors of n (with n the expectation value of $\hat{n} = \sum_j P_{1j}$), were chosen in Fig. 5.3. These states having a size $N = 30$ and containing 15 and 16 $|1\rangle$s respectively are evolved by using both discrete-time and continuous-time evolutions. These numerical simulations of the continuous-time evolutions have been obtained by exploiting the Time-Dependent Variational Principle (TDVP) [218, 219], implemented in the ITensor library [96] in `C++`. It is noticeable in Fig. 5.3 how the action of $\hat{\mathbb{A}}$ separates and disperses the $|1\rangle$s along the chain, resulting in a state where there are no neighboring $|1\rangle$s (the same can be appreciated in the continuous case under the action of $\mathbb{L}^{\text{A}}$). When $n/N \leq 1/2$, $\hat{\mathbb{A}}$ successfully achieves its goal, and the subsequent action of $\hat{\mathbb{B}}$ enables the attainment of the state $|0\rangle^{\otimes N}$. However, when $n/N > 1/2$, at least one small cluster of $|1\rangle$s survives, providing $\hat{\mathbb{B}}$ with the opportunity to propagate it along the entire chain. This dual action of $\hat{\mathbb{B}}$ is evident in in Fig. 5.3 (bottom panel, left plot), where it is thus responsible for the momentary decrease in n/N. Such evidence is no longer clearly observable in the corresponding continuous case because, after applying $\mathbb{L}^{\text{A}}$, $\mathbb{L}^{\text{B}}$ evolves

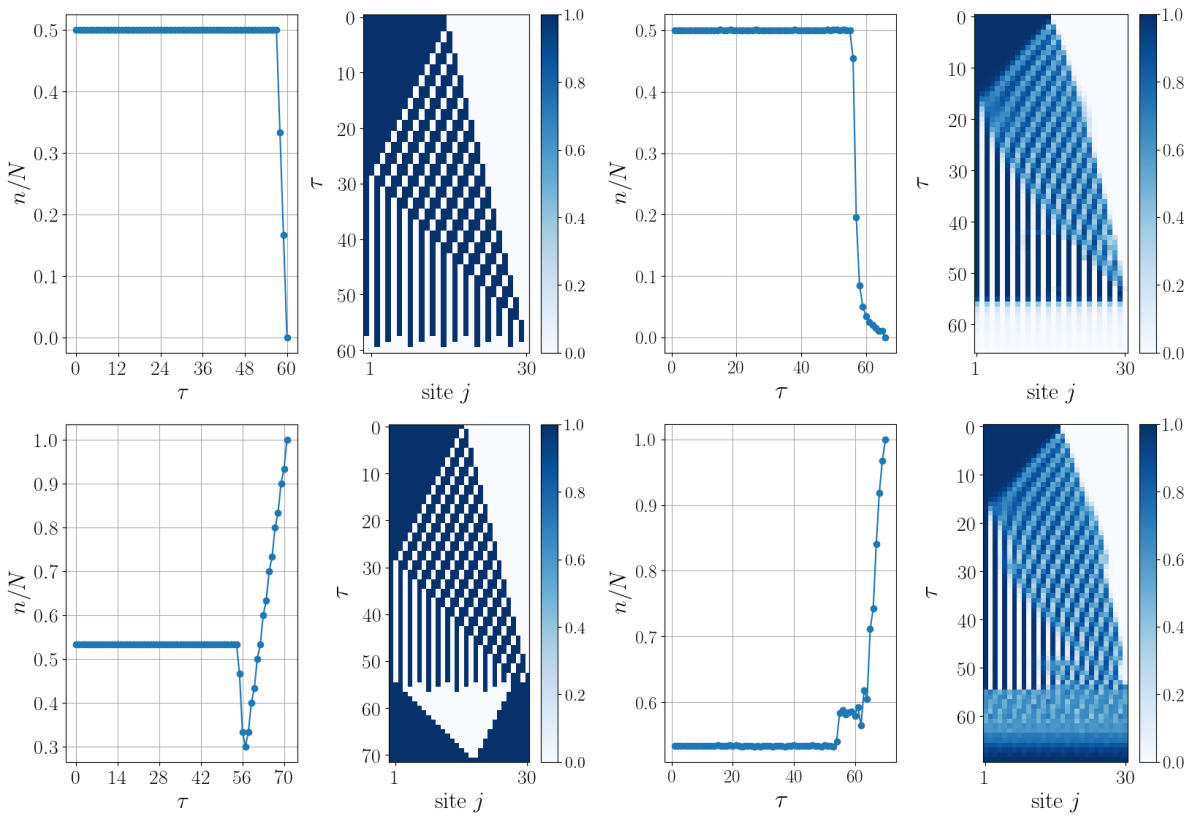

Figure 5.3: Two examples of how our proposed solution successfully solves the majority voting problem both with discrete (left plots) and continuous (right plots) time evolution, starting from an initial states with $N = 30$ and consisting of 15 $|1\rangle$s (top panel) and 16 $|1\rangle$s (bottom panel), respectively. In each plot, the variation of n/N as a function of τ and the QCA evolution are shown.

a state that is no longer classical. If it was, then we could observe its dual action even in the continuous case (as shown in a simple example in Fig. 5.4) and one can appreciate how the two evolutions are truly similar.

Lastly, we present a comparison of how $\tau = \tau_A + \tau_B$ scales with system size N in the discrete and continuous cases (see Fig. 5.5). In the former, we simply plotted Eq. (5.34). Similarly, in the continuous case, we computed τ_A and τ_B in the worst-case scenario: for τ_A, we considered the desired state achieved when n/N (whose sum, in this case, is only over odd sites) exceeds $0.99/2$; for τ_B, when n/N exceeds 0.99.

5.6 Conclusion

The DC task has been studied using one-dimensional non-unitary QCAs which perform a computation that maps global information to local information. Two approaches are considered: one that preserves the number density and one that performs majority voting. For the DC, two QCAs have been introduced that have been shown to solve the task by reaching the fixed point with

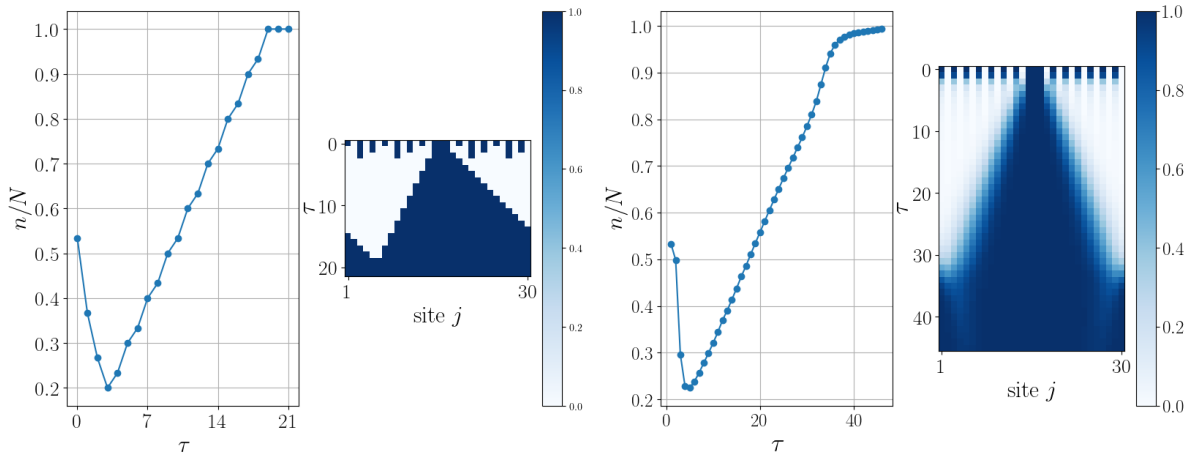

Figure 5.4: Comparison between $\hat{\mathbb{B}}$ and $\hat{\mathbb{L}}^{\mathrm{B}}$ evolution of the state $|10101010101010111010101010101010\rangle$ without applying $\hat{\mathbb{A}}$ and $\hat{\mathbb{L}}^{\mathrm{A}}$ first, respectively. It is possible to notice how, in both evolutions, the only cluster present in the chain is enlarged until recover the whole chain while the other parts of the chain are brought to zero. It is due to the latter action the momentary decrease in n/N.

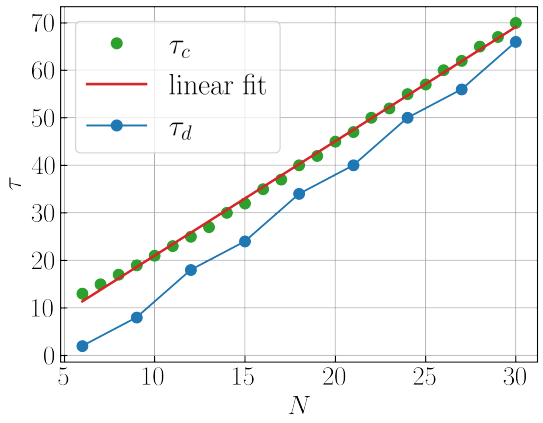

Figure 5.5: Comparison between the time required to reach the final state of Majority Voting (MV) with discrete-time (τ_d) and continuous-time (τ_c) evolutions, as a function of the system size $N \in [6, 30]$. The τ_c data were computed using the Time-Dependent Variational Principle (TDVP) [218, 219] implemented in the ITensor library [96] in `C++`, whereas the τ_d data represent the plot of the function (5.34) by selecting $N \mathrm{mod}(3) = 0$. The linear regression fit corresponds to the τ_c data, yielding $\tau_c(N) = b \cdot N + q$ with parameters $b = 2.40 \pm 0.02$ and $q = -3.0 \pm 0.4$.

an approximately quadratical time scaling with the system size. One of them is inspired by the Fukś CA [192] and the other one is a new quantum model which is restricted to only two-body interactions and has been shown to solve the DC task faster than the Fukś QCA. A third QCA model is introduced which has been shown to solve the majority voting problem within a time that scales linearly with the system size N. Both, discrete-time CPTP maps as well as corresponding

continuous-time Lindblad dynamics have been considered.

A potential application of our majority voting QCA is for MFQEC mentioned in the Sec. 5.2 for more general noise channels. MFQEC is an alternative to measurement-based QEC suited to architectures where measurements are particularly noisy and slow. The basic approach to MFQEC with stabilizer codes is to map stabilizer outcomes to freshly prepared ancillae using transversal gates, and then to coherently apply correction operations on the data register based on the information contained in the ancillae. For Shor-type MFQEC [220], in order to make it fault tolerant several repetitions are made of the mapping of stabilizer outcomes to d ancillae, where d is the code distance, and then a majority vote is made on the ancillary register followed by a coherent correction on the data register. Since the ancilla register is in fact quantum, classically processing by a majority voting circuit using boolean logic is not possible without first translating it into classical data via measurement, which was to be avoided in the first place. The Majority Voting QCA would obviate this by efficiently computing the majority voting in place on the ancilla. Note other approaches to MFQEC have been proposed including unitary Steane type stabilizer mappings [221] and unitary majority voting gadgets [222] but using this QCA approach could simplify some implementations as it does not require addressability of the ancillary register.

In [202], a method is also developed to perform the density classification task in the context of error correction, and the algorithm appears to scale linearly with the system size. However, the implementation of decoherence may require the addition of extra qubits, and the approach remains based on local qubit addressing.

Conversely, the QCA-based solutions proposed here are designed for implementation on platforms that enable the global evolution of the system according to a specific Lindbladian, such as Rydberg atom devices, as discussed at the end of Chapter 4. When considering different types of platforms, it is necessary to take into account the possible qubit topologies that can be implemented, which means assessing whether all required local operations can be efficiently performed. Furthermore, single-atom addressing could result in an increased quantum circuit depth, as individual gates in each layer would need to be decomposed into the fundamental ones executable by the machine.

Conclusions

This thesis has investigated several pivotal aspects of quantum information theory and quantum computation, with a particular focus on quantum entanglement, quantum variational algorithms, and quantum cellular automata.

We began by exploring Quantum Fisher Information (QFI) as a powerful tool to detect and quantify multipartite entanglement in complex quantum systems, such as spin-1 chains. In Chapter 2, we demonstrated that QFI, when computed using non-local string operators, is highly effective at distinguishing various quantum phases, including the symmetry-protected topological (STP) phase. This approach was particularly successful in detecting extensive entanglement in the Haldane phase, while traditional methods relying on local operators struggled.

Our analysis focused on two specific spin-1 models: the *Bilinear Biquadratic* (BLBQ) model and the XXZ model. In both cases, we observed that QFI was a robust indicator of quantum phase transitions and entanglement properties. The BLBQ model, known for exhibiting rich quantum phase diagrams, revealed that QFI could effectively identify the Haldane phase as well as critical points associated with quantum phase transitions. Similarly, in the XXZ model, QFI captured the intricate interplay between topological and critical phases.

We also observed critical behavior in certain phases, where the QFI followed a power-law scaling characterized by specific critical exponents [109]. However, the QFI was found to be less effective at precisely locating phase transition points, where a detailed analysis of its scaling behavior near criticality would be required. These results provide strong evidence of the versatility of QFI as an entanglement witness, with potential for application in a broad range of quantum systems, particularly those with topological order and long-range interactions.

In the second part of this thesis, Chapter 3 focused on quantum optimization algorithms, specifically the Quantum Approximate Optimization Algorithm (QAOA). We introduced the Quantum Natural Gradient (QNG), which uses the structure of the QFI to optimize the variational parameters of QAOA more efficiently than classical gradient-based methods. Through detailed simulations of QAOA implemented on a system of Rydberg atoms [111], we demonstrated that QNG consistently outperformed classical gradient descent, particularly in systems of increasing size, even in the presence of realistic noise sources such as SPAM errors and laser fluctuations. We found that the diagonal approximation of the QFI offered a favorable trade-off between computational cost and optimization performance, nearly matching the effectiveness of the full QNG method. Notably, our simulations showed that while additional QAOA layers can improve the algorithm's performance in idealized settings, they also increase susceptibility to noise, indicating that an optimal depth should be carefully chosen based on the specific hardware and noise conditions. These findings emphasize

the practical utility of QAOA and QNG for near-term quantum devices, offering a pathway for achieving more efficient quantum optimization even on noisy intermediate-scale quantum (NISQ) devices.

In the final part of this thesis, Chapters 4 and 5 expanded the discussion to Quantum Cellular Automata (QCA) and their application to the Density Classification (DC) task, a well-known challenge in classical cellular automata. We proposed and analyzed novel QCA models designed to solve the DC. One model is inspired by Fukś classical CA [160], while the other is a quantum model limited to two-body interactions, demonstrating an improvement in solving the DC task compared to Fukś QCA. Furthermore, we introduced a new QCA model restricted to two-body interactions that solved the DC task with quadratic time scaling in system size, providing a significant improvement in efficiency. Finally, we explored a third QCA model that was tailored for majority voting, solving this task with a linear time scaling. These results illustrate the power of QCA in performing complex computational tasks with significant speedups over classical cellular automata. Moreover, our majority voting QCA model offers potential applications in fault-tolerant quantum computation, particularly in Measurement Free Quantum Error Correction (MFQEC) protocols. In this context, our model provides a practical solution to the challenge of coherently processing ancilla information without requiring noisy and slow measurements, a key limitation in many quantum error correction schemes [220–222].

The results presented here not only advance our understanding of these topics but also introduce practical tools and models for real-world quantum computing applications. The QFI has proven to be an insightful tool for detecting and quantifying entanglement, especially in STP phases, while the introduction of QNG paves the way for more efficient optimization algorithms in noisy quantum environments. Moreover, our work on QCA opens new ways and possibilities for using QCA in computational tasks, with immediate implications for quantum error correction protocols. Future research could explore the application of these techniques to higher-dimensional systems, more complex quantum architectures, and further refinements of noise mitigation strategies in variational algorithms. Together, these contributions underscore the potential of quantum systems and algorithms to revolutionize the field of computation, as we move closer to practical, large-scale quantum computing.

Bibliography

[1] A. Einstein, B. Podolsky, and N. Rosen. "Can quantum-mechanical description of physical reality be considered complete?" In: *Phys. Rev.* 47.10 (1935), pp. 777–780.

[2] A. Aspect, J. Dalibard, and G. Roger. "Experimental test of Bell's inequalities using time-varying analyzers". In: *Phys. Rev. Lett.* 49.25 (1982), pp. 1804–1807.

[3] D. J. Thouless. *The quantum mechanics of many-body systems*. Courier Corporation, 2013.

[4] J. P. Dowling and G. J. Milburn. "Quantum technology: the second quantum revolution". In: *Philosophical Transactions of the Royal Society of London. Series A: Mathematical, Physical and Engineering Sciences* 361.1809 (2003), pp. 1655–1674.

[5] F. Verstraete, D. Porras, and J. I. Cirac. "Density Matrix Renormalization Group and Periodic Boundary Conditions: A Quantum Information Perspective". In: *Physical review letters* 93.22 (2004), p. 227205.

[6] U. Schollwøck. "The density-matrix renormalization group in the age of matrix product states". In: *Annals of physics* 326.1 (2011), pp. 96–192.

[7] S. R. White. "Density matrix formulation for quantum renormalization groups". In: *Physical review letters* 69.19 (1992), p. 2863.

[8] R. P. Feynman. "Simulating physics with computers". In: *Feynman and computation*. CRC Press, 2018, pp. 133–153.

[9] M. Riedel et al. "Europe's quantum flagship initiative". In: *Quantum Science and Technology* 4.2 (2019), p. 020501.

[10] J. Von Neumann. "The general and logical theory of automata". In: *Systems research for behavioral science*. Routledge, 2017, pp. 97–107.

[11] M Gardner. *Mathematical Games: The fantastic combinations of John Conway's new solitaire game'life'Scientific American*. 1970.

[12] P. Rendell. "A Turing machine in Conway's Game of Life, extendable to a universal Turing machine". In: *Collision-Based Computing* (2002).

[13] S. Wolfram. "Computation theory of cellular automata". In: *Communications in Mathematical Physics* 96.1 (1984), pp. 15–57.

[14] M. Cook. "Universality in elementary cellular automata". In: *Complex Systems* 15.1 (2004), pp. 1–40.

[15] K. Nagel and M. Schreckenberg. "A cellular automaton model for freeway traffic". In: *Journal de Physique I* 2.12 (1992), pp. 2221–2229.

[16] B. Chopard and M. Droz. *Cellular Automata Modeling of Physical Systems*. Cambridge University Press, 1998.

[17] P. Hogeweg. "Cellular automata as a paradigm for ecological modeling". In: *BioSystems* 31.2-3 (1993), pp. 107–125.

[18] N. Margolus. "Quantum computation". In: *Ann. New York Acad. Sci* 480 (1986), pp. 487–497.

[19] S. Lloyd. "A potentially realizable quantum computer". In: *Science* 261.5128 (1993), pp. 1569–1571.

[20] J. Watrous. "On one-dimensional quantum cellular automata". In: *Proceedings of IEEE 36th annual foundations of computer science*. IEEE. 1995, pp. 528–537.

[21] B. Schumacher and R. F. Werner. "Reversible quantum cellular automata". In: *arXiv preprint quant-ph/0405174* (2004).

[22] T. Farrelly and J. Streich. "Discretizing quantum field theories for quantum simulation". In: *arXiv preprint arXiv:2002.02643* (2020).

[23] S. Lloyd. "Quantum cellular automata: Theory and experiment". In: *Journal of Statistical Physics* 103.5-6 (2001), pp. 1069–1085.

[24] D. Gross et al. "Index theory of one dimensional quantum walks and cellular automata". In: *Communications in Mathematical Physics* 310.2 (2012), pp. 419–454.

[25] R. Raussendorf. "Quantum cellular automata for topological phases". In: *Annals of Physics* 321.9 (2006), pp. 2242–2260.

[26] Federico Dell'Anna et al. "Quantum Fisher information and multipartite entanglement in spin-1 chains". In: *Physical Review B* 108.14 (2023), p. 144414.

[27] L. Pezzè et al. "Multipartite Entanglement in Topological Quantum Phases". In: *Physical review letters* 119 25 (2017), p. 250401. DOI: 10.1103/PhysRevLett.119.250401.

[28] L. Pezzè et al. "Witnessing entanglement without entanglement witness operators". In: *Proceedings of the National Academy of Sciences* 113.41 (2016), pp. 11459–11464. DOI: 10.1073/pnas.1603346113.

[29] Elisabeth Wagner et al. "Density Classification with Non-Unitary Quantum Cellular Automata". In: *Entropy* 27.1 (2024), p. 26.

[30] J. Liu et al. "Quantum Fisher information matrix and multiparameter estimation". In: *J. Phys. A: Math. Theor.* 53.2 (2020), p. 023001.

[31] L. Pezzé and A. Smerzi. *Quantum theory of phase estimation*. 2014. arXiv: 1411.5164 [quant-ph].

[32] C. W. Helstrom. "Quantum detection and estimation theory". In: *Journal of Statistical Physics* 1 (1969), pp. 231–252.

[33] A. S. Holevo. *Probabilistic and statistical aspects of quantum theory*. Vol. 1. Springer Science & Business Media, 2011.

[34] S. Amari and H. Nagaoka. *Methods of information geometry*. Vol. 191. American Mathematical Soc., 2000.

[35] S. L. Braunstein and C. M. Caves. "Statistical distance and the geometry of quantum states". In: *Physical Review Letters* 72.22 (1994), p. 3439.

[36] H. Yuen and M. Lax. "Multiple-parameter quantum estimation and measurement of nonselfadjoint observables". In: *IEEE Transactions on Information Theory* 19.6 (1973), pp. 740–750.

[37] D. Petz. "Monotone metrics on matrix spaces". In: *Linear algebra and its applications* 244 (1996), pp. 81–96.

[38] D. Petz. *Quantum information theory and quantum statistics*. Springer Science & Business Media, 2007.

[39] A. Fujiwara and H. Nagaoka. "Quantum Fisher metric and estimation for pure state models". In: *Physics Letters A* 201.2-3 (1995), pp. 119–124.

[40] G. Tóth and I. Apellaniz. "Quantum metrology from a quantum information science perspective". In: *Journal of Physics A: Mathematical and Theoretical* 47.42 (2014), p. 424006.

[41] A. Fujiwara and H. Nagaoka. "An estimation theoretical characterization of coherent states". In: *Journal of Mathematical Physics* 40.9 (1999), pp. 4227–4239.

[42] Y. Watanabe, T. Sagawa, and M. Ueda. "Optimal Measurement on Noisy Quantum Systems". In: *Phys. Rev. Lett.* 104 (2010), p. 020401. DOI: 10.1103/PhysRevLett.104.020401.

[43] Y. Watanabe, T. Sagawa, and M. Ueda. "Uncertainty relation revisited from quantum estimation theory". In: *Phys. Rev. A* 84 (2011), p. 042121. DOI: 10.1103/PhysRevA.84.042121.

[44] Y. Watanabe. *Formulation of Uncertainty Relation Between Error and Disturbance in Quantum Measurement by Using Quantum Estimation Theory*. Springer Berlin Heidelberg, 2014. DOI: 10.1007/978-3-642-42081-1.

[45] W. Zhong et al. "Fisher information under decoherence in Bloch representation". In: *Physical Review A—Atomic, Molecular, and Optical Physics* 87.2 (2013), p. 022337.

[46] I. Bengtsson and K. Życzkowski. *Geometry of quantum states: an introduction to quantum entanglement*. Cambridge University Press, 2017.

[47] I. Contreras, E. Ercolessi, and M. Schiavina. "On the geometry of mixed states and the Fisher information tensor". In: *Journal of Mathematical Physics* 57.6 (2016).

[48] E. Ercolessi and M Schiavina. "Geometry of mixed states for a q-bit and the quantum Fisher information tensor". In: *Journal of Physics A: Mathematical and Theoretical* 45.36 (2012), p. 365303.

[49] S. Gu. "Fidelity approach to quantum phase transitions". In: *International Journal of Modern Physics B* 24.23 (2010), pp. 4371–4458.

[50] I. Frérot and T. Roscilde. "Quantum critical metrology". In: *Physical review letters* 121.2 (2018), p. 020402.

[51] M. M. Rams et al. "At the limits of criticality-based quantum metrology: apparent super-Heisenberg scaling revisited". In: *Physical Review X* 8.2 (2018), p. 021022.

[52] D. Šafránek. "Discontinuities of the quantum Fisher information and the Bures metric". In: *Physical Review A* 95.5 (2017), p. 052320.

[53] L. Seveso et al. "On the discontinuity of the quantum Fisher information for quantum statistical models with parameter dependent rank". In: *Journal of Physics A: Mathematical and Theoretical* 53.2 (2019), 02LT01.

[54] M. Hayashi. *Asymptotic theory of quantum statistical inference: selected papers*. World Scientific, 2005.

[55] W. Guo et al. "Berry curvature as a lower bound for multiparameter estimation". In: *Physical Review A* 93.4 (2016), p. 042115.

[56] C. R. Rao. "Information and accuracy attainable in the estimation of statistical parameters". In: *Bulletin of the Calcutta Mathematical Society* 37.3 (1945), pp. 81–91.

[57] H. Cramer. "Mathematical methods of statistics". In: *Math Rev (Math-SciNet) MR16588 Zentralblatt MATH* 63 (1946), p. 300.

[58] M. Fréchet. "L'Invariance des Intégrales Multidimensionnelles dans le Calcul des Probabilités". In: *Rev. Internat. Stat. Inst.* 11 (1943), p. 182.

[59] R. A. Fisher. "Theory of statistical estimation". In: *Mathematical proceedings of the Cambridge philosophical society*. Vol. 22. 5. Cambridge University Press. 1925, pp. 700–725.

[60] S. P. Gudder. "Review: A. S. Holevo, Probabilistic and statistical aspects of quantum theory". In: *Bulletin of the American Mathematical Society (New Series)* 13.1 (1985), pp. 80–85.

[61] J. Chwedeńczuk, F. Piazza, and A. Smerzi. "Phase estimation from atom position measurements". In: *New Journal of Physics* 13.6 (2011), p. 065023.

[62] J. Chwedeńczuk et al. "Sub-shot-noise interferometry from measurements of the one-body density". In: *New Journal of Physics* 14.9 (2012), p. 093001.

[63] D. Bruss. "Quantum Information and the Structure of the Classical Phase Space". In: *Journal of Mathematical Physics* 43.10 (2002), p. 4233. DOI: 10.1063/1.1497927.

[64] R. F. Werner. "Quantum States with Nonlocal Properties". In: *Physical Review A* 40.8 (1989), pp. 4277–4281. DOI: 10.1103/PhysRevA.40.4277.

[65] V. Giovannetti, S. Lloyd, and L. Maccone. "Quantum metrology". In: *Physical Review Letters* 96.1 (2006), p. 010401. DOI: 10.1103/PhysRevLett.96.010401.

[66] L. Pezzé and A. Smerzi. "Entanglement, nonlinear dynamics, and the Heisenberg limit". In: *Physical Review Letters* 102.10 (2009), p. 100401. DOI: 10.1103/PhysRevLett.102.100401.

[67] O. Gühne, G. Tóth, and H. J Briegel. "Multipartite entanglement in spin chains". In: *New Journal of Physics* 7.1 (2005), p. 229. DOI: 10.1088/1367-2630/7/1/229.

[68] A. S. Sørensen and K. Mølmer. "Entanglement and extreme spin squeezing". In: *Physical Review Letters* 86.20 (2001), p. 4431.

[69] P. Hyllus et al. "Fisher information and multiparticle entanglement". In: *Physical Review A* 85.2 (2012), p. 022321. DOI: 10.1103/PhysRevA.85.022321.

[70] G. Tóth. "Multipartite entanglement and high-precision metrology". In: *Physical Review A—Atomic, Molecular, and Optical Physics* 85.2 (2012), p. 022322.

[71] J. I. Cirac and P. Zoller. "Goals and opportunities in quantum simulation". In: *Nature physics* 8.4 (2012), pp. 264–266. DOI: 10.1038/nphys2275.

[72] L. Savary and L. Balents. "Quantum spin liquids: a review". In: *Reports on Progress in Physics* 80.1 (2016), p. 016502. DOI: 10.1088/0034-4885/80/1/016502.

[73] P. Ponte et al. "Many-Body Localization in Periodically Driven Systems". In: *Phys. Rev. Lett.* 114 (14 Apr. 2015), p. 140401. DOI: 10.1103/PhysRevLett.114.140401. URL: https://link.aps.org/doi/10.1103/PhysRevLett.114.140401.

[74] L. Amico et al. "Entanglement in many-body systems". In: *Rev. Mod. Phys.* 80 (2 May 2008), pp. 517–576. DOI: 10.1103/RevModPhys.80.517. URL: http://link.aps.org/doi/10.1103/RevModPhys.80.517.

[75] J. Eisert, M. Cramer, and M. B. Plenio. "*Colloquium*: Area laws for the entanglement entropy". In: *Rev. Mod. Phys.* 82 (1 Feb. 2010), pp. 277–306. DOI: 10.1103/RevModPhys.82.277. URL: http://link.aps.org/doi/10.1103/RevModPhys.82.277.

[76] J. Latorre and A. Riera. "A short review on entanglement in quantum spin systems". In: *Journal of Physics A: Mathematical and Theoretical* 42.50 (2009), p. 504002. DOI: 10.1088/1751-8113/42/50/504002.

[77] G. Vidal et al. "Entanglement in Quantum Critical Phenomena". In: *Phys. Rev. Lett.* 90 (22 June 2003), p. 227902. DOI: 10.1103/PhysRevLett.90.227902. URL: http://link.aps.org/doi/10.1103/PhysRevLett.90.227902.

[78] V. Giovannetti, S. Lloyd, and L. Maccone. "Quantum-enhanced measurements: beating the standard quantum limit". In: *Science* 306.5700 (2004), pp. 1330–1336. DOI: 10.1126/science.1104149.

[79] P. Hauke et al. "Measuring multipartite entanglement through dynamic susceptibilities". In: *Nature Physics* 12.8 (2016), pp. 778–782. DOI: 10.1038/nphys3700.

[80] W.-F. Liu, J. Ma, and X. Wang. "Quantum Fisher information and spin squeezing in the ground state of the XY model". In: *Journal of Physics A: Mathematical and Theoretical* 46.4 (2013), p. 045302. DOI: 10.1088/1751-8113/46/4/045302.

[81] J. Lambert and E. S. Sørensen. "State space geometry of the spin-1 antiferromagnetic Heisenberg chain". In: *Phys. Rev. B* 107 (17 May 2023), p. 174427. DOI: 10.1103/PhysRevB.107.174427. URL: https://link.aps.org/doi/10.1103/PhysRevB.107.174427.

[82] J. Lambert and E. S. Sørensen. "Estimates of the quantum Fisher information in the $S = 1$ antiferromagnetic Heisenberg spin chain with uniaxial anisotropy". In: *Phys. Rev. B* 99 (4 Jan. 2019), p. 045117. DOI: 10.1103/PhysRevB.99.045117. URL: https://link.aps.org/doi/10.1103/PhysRevB.99.045117.

[83] T. Kennedy and H. Tasaki. "Hidden symmetry breaking and the Haldane phase in $S = 1$ quantum spin chains". In: *Communications in mathematical physics* 147 (1992), pp. 431–484. DOI: 10.1007/BF02097239.

[84] I. Affleck et al. "Valence bond ground states in isotropic quantum antiferromagnets". In: *Communications in Mathematical Physics* 115.3 (1988), pp. 477–528. DOI: 10.1007/BF01218021.

[85] F. D. M. Haldane. "Continuum dynamics of the 1-D Heisenberg antiferromagnet: Identification with the $O(3)$ nonlinear sigma model". In: *Physics Letters A* 93.9 (Feb. 1983), pp. 464–468. DOI: 10.1016/0375-9601(83)90631-x. URL: https://doi.org/10.1016%2F0375-9601%2883%2990631-x.

[86] F. D. M. Haldane. "Nonlinear Field Theory of Large-Spin Heisenberg Antiferromagnets: Semiclassically Quantized Solitons of the One-Dimensional Easy-Axis Néel State". In: *Physical Review Letters* 50.15 (Apr. 1983), pp. 1153–1156. DOI: 10.1103/physrevlett.50.1153. URL: https://doi.org/10.1103%2Fphysrevlett.50.1153.

[87] M. P. Nightingale and H. W. J. Blöte. "Gap of the linear spin-1 Heisenberg antiferromagnet: A Monte Carlo calculation". In: *Physical Review B* 33.1 (1986), p. 659. DOI: 10.1103/PhysRevB.33.659.

[88] M. N. Barber and M. T. Batchelor. "Spectrum of the biquadratic spin-1 antiferromagnetic chain". In: *Physical Review B* 40.7 (1989), p. 4621. DOI: 10.1103/PhysRevB.40.4621.

[89] L. Takhtajan. "The picture of low-lying excitations in the isotropic Heisenberg chain of arbitrary spins". In: *Physics Letters A* 87.9 (1982), pp. 479–482. DOI: 10.1016/0375-9601(82)90764-2.

[90] H. Babujian. "Exact solution of the one-dimensional isotropic Heisenberg chain with arbitrary spins S". In: *Physics Letters A* 90.9 (1982), pp. 479–482. DOI: 10.1016/0375-9601(82)90403-0.

[91] P. Di Francesco, P. Mathieu, and D. Sénéchal. *Conformal Field Theory*. Springer, New York, 1997.

[92] J. Sólyom. "Competing bilinear and biquadratic exchange couplings in spin-1 Heisenberg chains". In: *Physical Review B* 36.16 (1987), p. 8642. DOI: 10.1103/PhysRevB.36.8642.

[93] B. Sutherland. "Model for a multicomponent quantum system". In: *Physical Review B* 12.9 (1975), p. 3795. DOI: 10.1103/PhysRevB.12.3795.

[94] J. C. Bridgeman and C. T. Chubb. "Hand-waving and Interpretive Dance: An Introductory Course on Tensor Networks". In: *J. Phys. A: Math. Theor.* 50 (2017), p. 223001. DOI: 10.1088/1751-8121/aa6dc3. arXiv: 1603.03039 [cond-mat.str-el]. URL: https://arxiv.org/abs/1603.03039.

[95] M. Fishman, S. R. White, and E. Miles Stoudenmire. "The ITensor Software Library for Tensor Network Calculations". In: *SciPost Phys. Codebases* (2022), p. 4. DOI: 10.21468/SciPostPhysCodeb.4. URL: https://scipost.org/10.21468/SciPostPhysCodeb.4.

[96] M. Fishman, S. R. White, and E. Miles Stoudenmire. "Codebase release 0.3 for ITensor". In: *SciPost Phys. Codebases* (2022), 4–r0.3. DOI: 10.21468/SciPostPhysCodeb.4-r0.3. URL: https://scipost.org/10.21468/SciPostPhysCodeb.4-r0.3.

[97] Wolfram Research Inc. *Mathematica, Version 13.2*. Champaign, IL, 2022. 2022. URL: https://www.wolfram.com/mathematica.

[98] C. Degli Esposti Boschi, E. Ercolessi, and G. Morandi. "Low-Dimensional Spin Systems: Hidden Symmetries, Conformal Field Theories and Numerical Checks". In: *Symmetries in Science XI*. Springer. 2005, pp. 145–173.

[99] V. G. Knizhnik and A. B. Zamolodchikov. "Current algebra and Wess-Zumino model in two dimensions". In: *Nuclear Physics B* 247.1 (1984), pp. 83–103. DOI: 10.1016/0550-3213(84)90374-2.

[100] A. Kitazawa, K. Nomura, and K. Okamoto. "Phase diagram of $S = 1$ bond-alternating XXZ chains". In: *Physical review letters* 76.21 (1996), p. 4038. DOI: 10.1103/PhysRevLett.76.4038.

[101] Kiyohide Nomura. "Spin-correlation functions of the $S = 1$ Heisenberg-Ising chain by the large-cluster-decomposition Monte Carlo method". In: *Physical Review B* 40.13 (1989), p. 9142. DOI: 10.1103/PhysRevB.40.9142.

[102] Y. Heng Su et al. "Non-local correlations in the Haldane phase for an XXZ spin-1 chain: A perspective from infinite matrix product state representation". In: *Journal of the Physical Society of Japan* 81.7 (2012), p. 074003. DOI: 10.1143/JPSJ.81.074003.

[103] G.-H. Liu et al. "Entanglement spectrum and quantum phase transitions in one-dimensional $S = 1$ XXZ model with uniaxial single-ion anisotropy". In: *Physica B: Condensed Matter* 443 (2014), pp. 63–69. DOI: 10.1016/j.physb.2014.03.007.

[104] H. Schulz. "Phase diagrams and correlation exponents for quantum spin chains of arbitrary spin quantum number". In: *Physical Review B* 34.9 (1986), p. 6372. DOI: 10.1103/PhysRevB.34.6372.

[105] H. Ueda, H. Nakano, and K. Kusakabe. "Finite-size scaling of string order parameters characterizing the Haldane phase". In: *Physical Review B* 78.22 (2008), p. 224402. DOI: 10.1103/PhysRevB.78.224402.

[106] R. Botet and R. Jullien. "Ground-state properties of a spin-1 antiferromagnetic chain". In: *Physical Review B* 27.1 (1983), p. 613. DOI: 10.1103/PhysRevB.27.613.

[107] W. Chen, K. Hida, and B. Sanctuary. "Ground-state phase diagram of $S = 1$ XXZ chains with uniaxial single-ion-type anisotropy". In: *Physical Review B* 67.10 (2003), p. 104401. DOI: 10.1103/PhysRevB.67.104401.

[108] C. Degli Esposti Boschi et al. "Effective mapping of spin-1 chains onto integrable fermionic models. A study of string and Néel correlation functions". In: *Journal of Physics A: Mathematical and Theoretical* 42.5 (2009), p. 055002. DOI: 10.1088/1751-8113/42/5/055002.

[109] M. Kohmoto, M. den Nijs, and L. P. Kadanoff. "Hamiltonian studies of the $d = 2$ Ashkin-Teller model". In: *Physical Review B* 24.9 (1981), p. 5229. DOI: 10.1103/PhysRevB.24.5229.

[110] M. Aguado et al. "Density-Matrix Renormalization-Group simulation of the $SU(3)$ antiferromagnetic Heisenberg model". In: *Phys. Rev. B* 79 (1 Jan. 2009), p. 012408. DOI: 10.1103/PhysRevB.79.012408. URL: https://link.aps.org/doi/10.1103/PhysRevB.79.012408.

[111] Z.-X. Gong et al. "Kaleidoscope of quantum phases in a long-range interacting spin-1 chain". In: *Phys. Rev. B* 93 (20 May 2016), p. 205115. DOI: 10.1103/PhysRevB.93.205115. URL: http://link.aps.org/doi/10.1103/PhysRevB.93.205115.

[112] J. R. McClean et al. "The theory of variational hybrid quantum-classical algorithms". In: *New Journal of Physics* 18.2 (2016), p. 023023.

[113] A. Peruzzo et al. "A variational eigenvalue solver on a photonic quantum processor". In: *Nature Communications* 5.1 (2014), p. 4213.

[114] N. Moll et al. "Quantum optimization using variational algorithms on near-term quantum devices". In: *Quantum Science and Technology* 3.3 (2018), p. 030503.

[115] J. Preskill. "Quantum computing in the NISQ era and beyond". In: *Quantum* 2 (2018), p. 79.

[116] S. De Léséleuc et al. "Analysis of imperfections in the coherent optical excitation of single atoms to Rydberg states". In: *Physical Review A* 97.5 (2018), p. 053803.

[117] E. Farhi, J. Goldstone, and S. Gutmann. "A quantum approximate optimization algorithm". In: *arXiv preprint arXiv:1411.4028* (2014).

[118] L. Zhou et al. "Quantum approximate optimization algorithm: Performance, mechanism, and implementation on near-term devices". In: *Physical Review X* 10.2 (2020), p. 021067.

[119] S. Ebadi et al. "Quantum optimization of maximum independent set using Rydberg atom arrays". In: *Science* 376.6598 (2022), pp. 1209–1215.

[120] M. P. Harrigan et al. "Quantum approximate optimization of non-planar graph problems on a planar superconducting processor". In: *Nature Physics* 17.3 (2021), pp. 332–336.

[121] G. Pagano et al. "Quantum approximate optimization of the long-range Ising model with a trapped-ion quantum simulator". In: *Proceedings of the National Academy of Sciences* 117.41 (2020), pp. 25396–25401.

[122] H.-Y. Huang, R. Kueng, and J. Preskill. "Predicting many properties of a quantum system from very few measurements". In: *Nature Physics* 16.10 (2020), pp. 1050–1057.

[123] J. R. McClean et al. "Barren plateaus in quantum neural network training landscapes". In: *Nature Communications* 9.1 (2018), p. 4812.

[124] G. Wang et al. "Minimizing estimation runtime on noisy quantum computers". In: *PRX Quantum* 2.1 (2021), p. 010346.

[125] M. Cerezo et al. “Cost function dependent barren plateaus in shallow parametrized quantum circuits”. In: *Nature Communications* 12.1 (2021), p. 1791.

[126] J. Stokes et al. “Quantum natural gradient”. In: *Quantum* 4 (2020), p. 269.

[127] D. Wierichs, C. Gogolin, and M. Kastoryano. “Avoiding local minima in variational quantum eigensolvers with the natural gradient optimizer”. In: *Physical Review Research* 2.4 (2020), p. 043246.

[128] A. Lopatnikova and M.-N. Tran. “Quantum natural gradient for variational Bayes”. In: *arXiv preprint arXiv:2106.05807* (2021).

[129] B. Koczor and S. C. Benjamin. “Quantum natural gradient generalized to noisy and nonunitary circuits”. In: *Physical Review A* 106.6 (2022), p. 062416.

[130] J. R. Johansson, P. D. Nation, and F. Nori. “QuTiP 2: A Python framework for the dynamics of open quantum systems”. In: *Computer Physics Communications* 184.4 (2013), pp. 1234–1240.

[131] S. Ruder. “An overview of gradient descent optimization algorithms”. In: *arXiv preprint arXiv:1609.04747* (2016).

[132] S. Amari, R. Karakida, and M. Oizumi. “Fisher information and natural gradient learning in random deep networks”. In: *The 22nd International Conference on Artificial Intelligence and Statistics*. PMLR. 2019, pp. 694–702.

[133] S. Amari. “Neural learning in structured parameter spaces-natural Riemannian gradient”. In: *Advances in Neural Information Processing Systems* 9 (1996).

[134] I. Goodfellow, Y. Bengio, and A. Courville. “Regularization for deep learning”. In: *Deep Learning* (2016), pp. 216–261.

[135] S. Amari, H. Park, and K. Fukumizu. “Adaptive method of realizing natural gradient learning for multilayer perceptrons”. In: *Neural Computation* 12.6 (2000), pp. 1399–1409.

[136] B. Koczor. “Exponential error suppression for near-term quantum devices”. In: *Phys. Rev. X* 11 (2021), p. 031057.

[137] W. J. Huggins et al. “Virtual distillation for quantum error mitigation”. In: *arXiv preprint* (2020). eprint: arXiv:2011.07064.

[138] A. Browaeys and T. Lahaye. “Many-body physics with individually controlled Rydberg atoms”. In: *Nature Physics* 16.2 (2020), pp. 132–142.

[139] L. Henriet et al. “Quantum computing with neutral atoms”. In: *Quantum* 4 (2020), p. 327.

[140] M. Saffman. “Quantum computing with atomic qubits and Rydberg interactions: progress and challenges”. In: *Journal of Physics B: Atomic, Molecular and Optical Physics* 49.20 (2016), p. 202001.

[141] H. Silvério et al. “Pulser: An open-source package for the design of pulse sequences in programmable neutral-atom arrays”. In: *Quantum* 6 (2022), p. 629.

[142] T. Farrelly. “A review of quantum cellular automata”. In: *Quantum* 4 (2020), p. 368.

[143] Pablo Arrighi. "An overview of quantum cellular automata". In: *Natural Computing* 18.4 (2019), pp. 885–899.

[144] T. Toffoli and N. Margolus. *Cellular Automata Machines: A New Environment for Modeling*. Cambridge, MA: MIT Press, 1987.

[145] S. Wolfram. *A New Kind of Science*. Champaign, IL: Wolfram Media, 2002.

[146] M. Hohnisch et al. "Modeling Microstructures in Cellular Automata: A Review". In: *Journal of Cellular Automata* 1.3 (2005), pp. 209–229.

[147] J. von Neumann. *Theory of Self-Reproducing Automata*. Ed. by Arthur W. Burks. Urbana, IL: University of Illinois Press, 1966.

[148] M. Gardner. "The Fantastic Combinations of John Conway's New Solitaire Game Life". In: *Scientific American* 223.4 (1970), pp. 120–123.

[149] S. Wolfram. "Statistical mechanics of cellular automata". In: *Reviews of Modern Physics* 55.3 (1983), pp. 601–644.

[150] R. Alonso-Sanz and L. Bull. "A very effective density classifier two-dimensional cellular automaton with memory". In: *Journal of Physics A: Mathematical and Theoretical* 42.48 (2009), p. 485101. DOI: 10.1088/1751-8113/42/48/485101.

[151] F. Bénézit. "Distributed average consensus for wireless sensor networks". PhD thesis. École Polytechnique Fédérale de Lausanne (EPFL), 2009. DOI: 10.5075/epfl-thesis-4509.

[152] C. Darabos, M. Giacobini, and M. Tomassini. "Scale-free automata networks are not robust in a collective computational task". In: *Cellular Automata*. Ed. by S. El Yacoubi, B. Chopard, and S. Bandini. Vol. 4173. Lecture Notes in Computer Science. Berlin: Springer, 2006, pp. 512–521. DOI: 10.1007/11861201_64.

[153] N. H. Packard. "Adaptation toward the edge of chaos". In: *Dynamic Patterns in Complex Systems*. Singapore: World Scientific, 1988, pp. 293–301.

[154] M. Land and R.K. Belew. "No perfect two-state cellular automata for density classification exists". In: *Physical Review Letters* 74.25 (1995), pp. 5148–5150. DOI: 10.1103/PhysRevLett.74.5148.

[155] G. M. B. Oliveira et al. "Some investigations about synchronization and density classification tasks in one-dimensional and two-dimensional cellular automata rule spaces". In: *Electronic Notes in Theoretical Computer Science* 252 (2009), pp. 121–142. DOI: 10.1016/j.entcs.2009.09.029.

[156] M. S. Capcarrere, M. Sipper, and M. Tomassini. "Two-state, $r = 1$ Cellular Automaton that Classifies Density". In: *Phys. Rev. Lett.* 77 (24 Dec. 1996), pp. 4969–4971. DOI: 10.1103/PhysRevLett.77.4969. URL: https://doi.org/10.1103/PhysRevLett.77.4969.

[157] H. Fukś. "Solution of the density classification problem with two cellular automata rules". In: *Phys. Rev. E* 55 (3 Mar. 1997), R2081–R2084. DOI: 10.1103/PhysRevE.55.R2081. URL: https://doi.org/10.1103/PhysRevE.55.R2081.

[158] C. L. Martins and P. P. de Oliveira. "Evolving sequential combinations of elementary cellular automata rules". In: *Advances in Artificial Life*. Ed. by M.S. Capcarrere et al. Vol. 3630. Lecture Notes in Computer Science. Berlin: Springer, 2005, pp. 461–470. DOI: 10.1007/11553090_47.

[159] C. Stone and L. Bull. "Evolution of cellular automata with memory: The density classification task". In: *Biosystems* 97.2 (2009), pp. 108–116. DOI: 10.1016/j.biosystems.2009.03.004.

[160] H. Fukś. "Nondeterministic Density Classification with Diffusive Probabilistic Cellular Automata". In: *Physical Review E* 66.6 (2002), p. 066106. DOI: 10.1103/PhysRevE.66.066106.

[161] M. Schüle, T. Ott, and R. Stoop. "Computing with probabilistic cellular automata". In: *Proceedings of the 19th International Conference on Artificial Neural Networks (ICANN'09)*. Berlin: Springer, 2009, pp. 525–533. DOI: 10.1007/978-3-642-04274-4_54.

[162] N. Fatès. "Stochastic Cellular Automata Solutions to the Density Classification Problem: When Randomness Helps Computing". In: *Theory of Computing Systems* 53 (2013), pp. 223–242.

[163] R. P. Feynman. "Simulating physics with computers". In: *International Journal of Theoretical Physics* 21 (1982), pp. 467–488. DOI: 10.1007/bf02650179.

[164] A. Trabesinger. "Quantum simulation". In: *Nature Physics* 8 (2012), p. 263. DOI: 10.1038/nphys2258.

[165] N. Margolus. "Quantum computation". In: *Annals of the New York Academy of Sciences* 480.1 (1986), pp. 487–497. DOI: 10.1111/j.1749-6632.1986.tb12451.x.

[166] S. Lloyd. "A potentially realizable quantum computer". In: *Science* 261.5128 (1993), pp. 1569–1571. DOI: 10.1126/science.261.5128.1569.

[167] M. A. Nielsen and I. L. Chuang. *Quantum Computation and Quantum Information*. Cambridge: Cambridge University Press, 2000. DOI: 10.1017/cbo9780511976667.

[168] G. K. Brennen and J. E. Williams. "Entanglement dynamics in one-dimensional quantum cellular automata". In: *Phys. Rev. A* 68 (2003), p. 042311. DOI: 10.1103/PhysRevA.68.042311.

[169] P. Arrighi, V. Nesme, and R. F. Werner. "Unitarity plus causality implies localizability". In: *Journal of Computer and System Sciences* 77.2 (2011), pp. 372–378. DOI: 10.1016/j.jcss.2010.05.004.

[170] O. Krüger and R. F. Werner. "Gaussian quantum cellular automata". In: *Quantum Information with Continuous Variables of Atoms and Light*. Ed. by N. Cerf, G. Leuchs, and E. S. Polzik. London: Imperial College Press, 2007. DOI: 10.1142/9781860948169_0005.

[171] S. Richter and R. F. Werner. "Ergodicity of quantum cellular automata". In: *Journal of Statistical Physics* 82.3 (1996), pp. 963–998. DOI: 10.1007/BF02179798.

[172] L. Piroli and J. I. Cirac. "Quantum cellular automata, tensor networks, and area laws". In: (2020).

[173] S. C. Benjamin. "Schemes for parallel quantum computation without local control of qubits". In: *Physical Review A* 61.2 (2000), p. 020301.

[174] T. M Wintermantel et al. “Unitary and nonunitary quantum cellular automata with Rydberg arrays”. In: *Physical Review Letters* 124.7 (2020), p. 070503.

[175] P. Schauß et al. “Observation of spatially ordered structures in a two-dimensional Rydberg gas”. In: *Nature* 491 (2012), pp. 87–91. DOI: 10.1038/nature11596.

[176] H. Labuhn et al. “Tunable two-dimensional arrays of single Rydberg atoms for realizing quantum Ising models”. In: *Nature* 534 (2016), p. 667. DOI: 10.1038/nature18274.

[177] H. Bernien et al. “Probing many-body dynamics on a 51-atom quantum simulator”. In: *Nature* 551 (2017), p. 579. DOI: 10.1038/nature24622.

[178] E. Guardado-Sanchez et al. “Probing the quench dynamics of antiferromagnetic correlations in a 2D quantum Ising spin system”. In: *Phys. Rev. X* 8 (2018), p. 021069. DOI: 10.1103/PhysRevX.8.021069.

[179] V. Lienhard et al. “Observing the space- and time-dependent growth of correlations in dynamically tuned synthetic Ising models with antiferromagnetic interactions”. In: *Phys. Rev. X* 8 (2018), p. 021070. DOI: 10.1103/PhysRevX.8.021070.

[180] M. Müller et al. “Trapped Rydberg ions: from spin chains to fast quantum gates”. In: *New J. Phys.* 10 (2008), p. 093009. DOI: 10.1088/1367-2630/10/9/093009.

[181] C. Zhang et al. “Sub-microsecond entangling gate between trapped ions via Rydberg interaction”. In: *arXiv* (2019). arXiv: 1908.11284 [quant-ph].

[182] M. Ebert et al. “Coherence and Rydberg blockade of atomic ensemble qubits”. In: *Phys. Rev. Lett.* 115 (2015), p. 093601. DOI: 10.1103/PhysRevLett.115.093601.

[183] S. Whitlock, A. W. Glaetzle, and P. Hannaford. “Simulating quantum spin models using Rydberg-excited atomic ensembles in magnetic microtrap arrays”. In: *J. Phys. B* 50 (2017), p. 074001. DOI: 10.1088/1361-6455/aa6145.

[184] F. Letscher, D. Petrosyan, and M. Fleischhauer. “Many-body dynamics of holes in a driven, dissipative spin chain of Rydberg superatoms”. In: *New J. Phys.* 19 (2017), p. 113014. DOI: 10.1088/1367-2630/aa93a6.

[185] I. Lesanovsky. “Many-body Spin Interactions and the Ground State of a Dense Rydberg Lattice Gas”. In: *Physical Review Letters* 106.2 (2011), p. 025301.

[186] M. Sanz, E. Solano, and I.L. Egusquiza. “Beyond Adiabatic Elimination: Effective Hamiltonians and Singular Perturbation”. In: *Applications + Practical Conceptualization + Mathematics = fruitful Innovation*. Springer Japan, 2016, pp. 127–142.

[187] D. F. V. James and J. Jerke. “Effective Hamiltonian Theory and Its Applications in Quantum Information”. In: *Canadian Journal of Physics* 85.6 (2007), pp. 625–632.

[188] F. Reiter and A. S. Sørensen. “Effective Operator Formalism for Open Quantum Systems”. In: *Physical Review A* 85.3 (2012), p. 032111.

[189] M. Roghani and H. Weimer. “Dissipative preparation of entangled many-body states with Rydberg atoms”. In: *Quantum Science and Technology* 3.3 (2018), p. 035002.

[190] B. Olmos, I. Lesanovsky, and J. P. Garrahan. "Facilitated spin models of dissipative quantum glasses". In: *Phys. Rev. Lett.* 109 (2012), p. 020403. DOI: 10.1103/PhysRevLett.109.020403.

[191] I. Lesanovsky, K. Macieszczak, and J. P. Garrahan. "Non-equilibrium absorbing state phase transitions in discrete-time quantum cellular automaton dynamics on spin lattices". In: *Quantum Science and Technology* 4.2 (2019), 02LT02.

[192] H. Fukś. "Nondeterministic density classification with diffusive probabilistic cellular automata". In: *Phys. Rev. E* 66 (6 Dec. 2002), p. 066106. DOI: 10.1103/PhysRevE.66.066106. URL: https://doi.org/10.1103/PhysRevE.66.066106.

[193] M. Vispoel, A. J. Daly, and J. M. Baetens. "Progress, gaps and obstacles in the classification of cellular automata". In: *Physica D: Nonlinear Phenomena* 432 (2022), p. 133074. DOI: 10.1016/j.physd.2021.133074. URL: https://doi.org/10.1016/j.physd.2021.133074.

[194] Z. Laboudi. "An Effective Approach for Solving the Density Classification Task by Cellular Automata". In: *2019 4th World Conference on Complex Systems (WCCS)*. 2019, pp. 1–8. DOI: 10.1109/ICoCS.2019.8930805.

[195] Z. Laboudi. "Efficient Solutions of the Density Classification Task in One-Dimensional Cellular Automata: Where Can They Be Found?" In: *Complex Systems* 29 (Sept. 2020), pp. 669–688. DOI: 10.25088/ComplexSystems.29.3.669.

[196] A. Bušić et al. "Density classification on infinite lattices and trees". In: *Electronic Journal of Probability* 18 (2013), pp. 1–22. DOI: 10.1214/EJP.v18-2325. URL: https://doi.org/10.1214/EJP.v18-2325.

[197] M. Sipper, M. S. Capcarrere, and E. Ronald. "A Simple Cellular Automaton that Solves the Density and Ordering Problems". In: *International Journal of Modern Physics C* 9.7 (1998), pp. 899–902. DOI: 10.1142/S0129183198000868. URL: https://doi.org/10.1142/S0129183198000868.

[198] H. Fukś and R. Procyk. "Explorations of Ternary Cellular Automata and Ternary Density Classification Problems". In: *Acta Physica Polonica B Proceedings Supplement* 12.1 (2019), p. 75. DOI: 10.5506/aphyspolbsupp.12.75. URL: https://doi.org/10.5506/aphyspolbsupp.12.75.

[199] B. Schumacher and R. F. Werner. *Reversible quantum cellular automata*. 2004. DOI: 10.48550/arXiv.quant-ph/0405174. arXiv: quant-ph/0405174 [quant-ph]. URL: https://doi.org/10.48550/arXiv.quant-ph/0405174.

[200] G. K. Brennen and J. E. Williams. "Entanglement dynamics in one-dimensional quantum cellular automata". In: *Phys. Rev. A* 68 (4 Oct. 2003), p. 042311. DOI: 10.1103/PhysRevA.68.042311. URL: https://doi.org/10.1103/PhysRevA.68.042311.

[201] T. M. Wintermantel et al. "Unitary and Nonunitary Quantum Cellular Automata with Rydberg Arrays". In: *Phys. Rev. Lett.* 124 (7 Feb. 2020), p. 070503. DOI: 10.1103/PhysRevLett.124.070503. URL: https://doi.org/10.1103/PhysRevLett.124.070503.

[202] T. L. M. Guedes, D. Winter, and M. Müller. *Quantum cellular automata for quantum error correction and density classification*. 2023. DOI: 10.48550/arXiv.2309.03608. arXiv: 2309.03608 [quant-ph]. URL: https://doi.org/10.48550/arXiv.2309.03608.

[203] A. Liu et al. *Accelerating Voting by Quantum Computation*. 2023. DOI: 10.48550/arXiv.2301.02995. arXiv: 2301.02995 [cs.CY]. URL: https://doi.org/10.48550/arXiv.2301.02995.

[204] X. Sun, X. Su, and X. Bian. "Quantum Vote Based on Quantum Logical Operators". In: *Available at SSRN 4686153* (2023). DOI: 10.2139/ssrn.4686153. URL: https://doi.org/10.2139/ssrn.4686153.

[205] T. Andronikos and M. Stefanidakis. "A Two-Party Quantum Parliament". In: *Algorithms* 15.2 (2022). DOI: 10.3390/a15020062. URL: https://doi.org/10.3390/a15020062.

[206] Y.-R. Li et al. "A quantum voting protocol using single-particle states". In: *Quantum Information Processing* 20.3 (2021), p. 110. DOI: 10.1007/s11128-021-03048-6. URL: https://doi.org/10.1007/s11128-021-03048-6.

[207] W. Zhong et al. *Best Subset Selection: Statistical Computing Meets Quantum Computing*. 2021. arXiv: 2107.08359 [stat.ME].

[208] N. Bao and N. Yunger Halpern. "Quantum voting and violation of Arrow's impossibility theorem". In: *Phys. Rev. A* 95 (6 June 2017), p. 062306. DOI: 10.1103/PhysRevA.95.062306. URL: https://doi.org/10.1103/PhysRevA.95.062306.

[209] H. Buhrman et al. *Quantum majority vote*. 2022. arXiv: 2211.11729 [quant-ph].

[210] A. Gilchrist, D. R. Terno, and C. J. Wood. *Vectorization of quantum operations and its use*. 2011. arXiv: 0911.2539 [quant-ph].

[211] W. K. Wootters and W. H. Zurek. "A single quantum cannot be cloned". In: *Nature* 299.5886 (1982), pp. 802–803. DOI: 10.1038/299802a0. URL: https://doi.org/10.1038/299802a0.

[212] E. Domany and W. Kinzel. "Equivalence of Cellular Automata to Ising Models and Directed Percolation". In: *Phys. Rev. Lett.* 53 (4 July 1984), pp. 311–314. DOI: 10.1103/PhysRevLett.53.311. URL: https://doi.org/10.1103/PhysRevLett.53.311.

[213] E. Gillman, F. Carollo, and I. Lesanovsky. "Nonequilibrium Phase Transitions in $(1+1)$-Dimensional Quantum Cellular Automata with Controllable Quantum Correlations". In: *Phys. Rev. Lett.* 125 (10 Sept. 2020), p. 100403. DOI: 10.1103/PhysRevLett.125.100403. URL: https://doi.org/10.1103/PhysRevLett.125.100403.

[214] E. Gillman, F. Carollo, and I. Lesanovsky. "Quantum and Classical Temporal Correlations in $(1+1)$D Quantum Cellular Automata". In: *Phys. Rev. Lett.* 127 (23 Dec. 2021), p. 230502. DOI: 10.1103/PhysRevLett.127.230502. URL: https://doi.org/10.1103/PhysRevLett.127.230502.

[215] E. Gillman, F. Carollo, and I. Lesanovsky. "Numerical simulation of quantum nonequilibrium phase transitions without finite-size effects". In: *Phys. Rev. A* 103 (4 Apr. 2021), p. L040201. DOI: 10.1103/PhysRevA.103.L040201. URL: https://doi.org/10.1103/PhysRevA.103.L040201.

[216] R. Nigmatullin, E. Wagner, and G. K. Brennen. "Directed percolation in non-unitary quantum cellular automata". In: *Phys. Rev. Res.* 3 (4 Dec. 2021), p. 043167. DOI: 10.1103/PhysRevResearch.3.043167. URL: https://doi.org/10.1103/PhysRevResearch.3.043167.

[217] S. R. White. "Density matrix formulation for quantum renormalization groups". In: *Phys. Rev. Lett.* 69 (19 Nov. 1992), pp. 2863–2866. DOI: 10.1103/PhysRevLett.69.2863. URL: https://doi.org/10.1103/PhysRevLett.69.2863.

[218] J. Haegeman et al. "Time-dependent variational principle for quantum lattices". In: *Physical Review Letters* 107.7 (2011), p. 070601.

[219] J. Haegeman et al. "Unifying time evolution and optimization with matrix product states". In: *Physical Review B* 94.16 (2016), p. 165116.

[220] P. O. Boykin et al. "Fault tolerant computation on ensemble quantum computers". In: *International Conference on Dependable Systems and Networks, 2004.* 2004, pp. 157–166. DOI: 10.1109/DSN.2004.1311886.

[221] S. Heußen, D. F. Locher, and M. Müller. "Measurement-Free Fault-Tolerant Quantum Error Correction in Near-Term Devices". In: *PRX Quantum* 5 (1 Feb. 2024), p. 010333. DOI: 10.1103/PRXQuantum.5.010333. URL: https://doi.org/10.1103/PRXQuantum.5.010333.

[222] G. A. Paz-Silva, G. K. Brennen, and J. Twamley. "Fault Tolerance with Noisy and Slow Measurements and Preparation". In: *Phys. Rev. Lett.* 105 (10 Aug. 2010), p. 100501. DOI: 10.1103/PhysRevLett.105.100501. URL: https://doi.org/10.1103/PhysRevLett.105.100501.

[223] D. J. Wales. "Exploring Energy Landscapes". In: *Annual Review of Physical Chemistry* 69.1 (2018), pp. 401–425. DOI: 10.1146/annurev-physchem-050317-021219. URL: https://doi.org/10.1146/annurev-physchem-050317-021219.

[224] D. J. Wales and J. P. K. Doye. "Global Optimization by Basin-Hopping and the Lowest Energy Structures of Lennard-Jones Clusters Containing up to 110 Atoms". In: *The Journal of Physical Chemistry A* 101.28 (1997), pp. 5111–5116. ISSN: 1520-5215. DOI: 10.1021/jp970984n. URL: https://doi.org/10.1021/jp970984n.

[225] P. Virtanen et al. "SciPy 1.0: Fundamental Algorithms for Scientific Computing in Python". In: *Nature Methods* 17 (2020), pp. 261–272. DOI: 10.1038/s41592-019-0686-2. URL: https://doi.org/10.1038/s41592-019-0686-2.

[226] J. R. Johansson, P. D. Nation, and F. Nori. "QuTiP: An open-source Python framework for the dynamics of open quantum systems". In: *Computer Physics Communications* 183.8 (Aug. 2012), pp. 1760–1772. DOI: 10.1016/j.cpc.2012.02.021. URL: https://doi.org/10.1016/j.cpc.2012.02.021.

Appendices

Appendix A

The AKLT model

The AKLT model is the projection point at $\beta = -1/3$, where the Hamiltonian can be expressed as a sum over the projection operators $P_j(i, i+1)$. Each projector acts on a pair of interacting spins for a given value of the total spin $j = 0, 1, 2$. Thus, it can be written as:

$$H_{\text{AKLT}} = -\frac{2}{3}NJ + 2J\sum_{i=1}^{N} P_2(i, i+1) \tag{A.1}$$

where

$$P_2(i, i+1) = \frac{1}{3} + \frac{1}{2}\left(\boldsymbol{S}_i \cdot \boldsymbol{S}_{i+1} + \frac{1}{3}(\boldsymbol{S}_i \cdot \boldsymbol{S}_{i+1})^2\right). \tag{A.2}$$

As shown in [84], the system can be thought of as made up of two spin-1/2 variables for each site. By introducing the *valence bond basis*, it is possible to build the ground state, called a *valence bond solid* (VBS), so that in the chain there is always a bond between two neighboring spins (see upper panel of Fig. 2.2).

The VBS state $|\text{VBS}\rangle$ satisfies

$$P_2(i, i+1)\,|\text{VBS}\rangle = 0 \qquad \forall i. \tag{A.3}$$

In the spin-1/2's computational basis $\psi_1 = |0\rangle$, $\psi_2 = |1\rangle$, we can construct an orthogonal basis for the $s = 1$ state space, by taking the symmetrized tensor products:

$$\psi_{\alpha\beta} = \frac{1}{\sqrt{2}}(\psi_\alpha \otimes \psi_\beta + \psi_\beta \otimes \psi_\alpha) \tag{A.4}$$

Then, in order to contract a pair of spin-1/2's to form a singlet, we use the Levi-Civita tensor of rank two:

$$\Omega_{\alpha\beta} = \varepsilon^{\gamma\delta}\psi_{\alpha\gamma} \otimes \psi_{\delta\beta}, \tag{A.5}$$

where the indices α and β refer to the outer spin-1/2's. It is now easy to generalize the construction for a chain of length N:

$$\Omega_{\alpha\beta} = \varepsilon^{\beta_1\alpha_2} \cdots \varepsilon^{\beta_{N-1}\alpha_N}\psi_{\alpha\beta_1} \otimes \psi_{\alpha_2\beta_2} \otimes \cdots \otimes \psi_{\alpha_N\beta}. \tag{A.6}$$

The AKLT model has exponentially decaying correlations, and this applies to the whole Haldane phase. In fact, this can be shown by computing the two-point correlation function in the limit $N \to \infty$, which yields:

$$\lim_{N\to\infty} \langle\Omega|\, S_1^a S_r^b \,|\Omega\rangle = \delta^{ab}(-1)^r \,\frac{4}{3}\, 3^{-r}. \tag{A.7}$$

showing, as anticipated, an exponentially decaying correlation function with correlation length $\xi = \ln(3)^{-1}$. Therefore, one may conclude that there is no order in this phase but, as we will see, a different kind of hidden order is actually there. We are going to show this fact on the valence bond state.

As it can be easily understood from Fig. 2.2, in a finite chain the ground state of AKLT model is four-fold degenerate due to the effective free spin-1/2's at the boundaries. Let us write the ground state of AKLT as Φ_σ, where σ is a string of +'s, −'s and 0's so that Φ_σ can be expressed as a tensor product of a single site states $|+\rangle$, $|-\rangle$ and $|0\rangle$. If the first spin-1/2 of the chain is in the $|\uparrow\rangle$ state, then for the first site we cannot have a $|-\rangle$ state but only $|+\rangle$ or $|0\rangle$. In the latter case, we still must have the first non-zero character to be a + in σ in order to satisfy the construction of the valence bond state. It can be verified that there has to be the same number of +'s and −'s alternating all along the σ string, with no further restrictions on the number of 0's between them.

Therefore, a typical allowed state Φ_σ in the AKLT model could look like this:

$$\Phi_\sigma = |000+-0+-+0-+0-+-0\rangle \tag{A.8}$$

A look at (A.8) reveals that is a sort of Néel order (antiferromagnetic order) if we ignore the 0's. Still, we cannot predict what two spins in two distant sites will be, as we have no control on the number of the 0's. Indeed, there is no *local* order parameter that can be found to be non-zero in the Haldane phase and that can be used to distinguish this phase from the others. But, there is actually a *non-local* order parameter, the string order parameter, that is able to reveal the hidden order of the Haldane phase.

In order to see how we can arrive at its definition, let us introduce the non-local unitary transformation

$$U = \prod_{k=1}^{N} \prod_{j=2}^{k-1} \exp\left(i\pi S_j^z S_k^x\right), \tag{A.9}$$

where N is the number of sites, such that Consider a typical AKLT state Φ_σ, for example (A.8). On this state, the operator U acts as

$$U\Phi_\sigma = (-1)^{z(\sigma)}\Phi_{\bar{\sigma}}, \tag{A.10}$$

where $z(\sigma)$ is the number of 0 characters in odd sites and $\bar{\sigma}$ is the new transformed string. It is defined as follows:

- if $\sigma_i = +$ (or $-$) and the number of non-zero characters to the left of the site i is odd, then $\bar{\sigma}_i = -$ (or $+$).
- otherwise, $\sigma_i = \bar{\sigma}_i$

where σ_i is the i-th character of the string σ. In particular, if we apply this transformation on the allowed state (A.8), it becomes:

$$U\Phi_\sigma = |000++0+++0++0+++0\rangle\,. \tag{A.11}$$

Then this unitary transformation aligns all the non-zero spins i.e. if the first non-zero character is $+$ (or $-$) all the other non-zero characters become $+$ (or $-$). It is also evident that $U^{-1} = U$.

Under the action of U, the spin operators transform as follows:

$$\begin{aligned}
\widetilde{S}^x_j &= US^x_jU^\dagger = S^x_j\left(e^{i\pi\sum_{l>j}S^x_l}\right),\\
\widetilde{S}^y_j &= US^y_jU^\dagger = \left(e^{i\pi\sum_{l<j}S^z_l}\right)S^y_j\left(e^{i\pi\sum_{l>j}S^x_l}\right),\\
\widetilde{S}^z_j &= US^z_jU^\dagger = \left(e^{i\pi\sum_{l<j}S^z_l}S^z_j\right).
\end{aligned} \tag{A.12}$$

Notice that the local operators have been mapped onto non-local operators, as they contain a sum of spin operators acting on different sites. This is not surprising, given that U itself is a non-local unitary transformation.

It is reasonable to expect that also the local Hamiltonian H is mapped onto a non-local one $\widetilde{H} = UHU^{-1}$, but it turns out that $\widetilde{H}$ is still, in fact, local:

$$\widetilde{H} = J\sum_j\left[h_j + \beta(h_j)^2\right], \tag{A.13}$$

where

$$h_j = -S^x_jS^x_{j+1} + S^y_je^{i\pi\left(S^z_j+S^x_{j+1}\right)}S^y_{j+1} - S^z_jS^z_{j+1} \tag{A.14}$$

The transformed Hamiltonian $\widetilde{H}$ still has the same symmetries of H, but they may not be local anymore. Actually, the only local symmetry of H is related to its invariance under rotations of π about each coordinate axis. This symmetry group is equivalent to $\mathbb{Z}_2\times\mathbb{Z}_2$: indeed, the product of two π-rotations about two different axes produce a π- rotation about the third one.

It is possible to prove [84] that at the AKLT point the transformed Hamiltonian has four ground states, which are product states and break such symmetry. These four degenerate ground states of H_{AKLT} converge to a single ground state in the infinite volume limit. The same is not true for the ground states of $\widetilde{H}_{\text{AKLT}}$, as they converge to four distinct states in the infinite volume limit, even though the two Hamiltonians are related by a unitary transformation. In a sense, the non-locality of the transformation U does not guarantee a one-to-one correspondence between the ground states in the infinite volume limit.

Finally, we can understand the role of the string order parameter (A.12). In fact, it is straightforward to verify that

$$S^\alpha_1\left(\prod_{k=2}^{r-1}e^{i\pi S^\alpha_k}\right)S^\alpha_r = -U^{-1}S^\alpha_1S^\alpha_rU. \tag{A.15}$$

This shows that the NLOPs in (2.5) reveal the ferromagnetic order in the language of the non-local spins (A.12) or, equivalently, the breaking of the hidden symmetry in the original system. Such a symmetry breaking holds in the whole Haldane phase, not just the AKLT model. Indeed, in the dimer phase the symmetry is completely unbroken and the string order parameter (2.5) will vanish for every α.

Appendix B

Derivation of the Lindbladian describing the Fukś QCA

In this section, it is shown that the relative weightings of the jump operators describing the Fukś QCA are correct, see Eqs. (5.13), by establishing a relationship between the probabilities p and the product of the decay rate γ and the time duration τ of each QCA update. The derivation is based on the idea that the (continuous-time) Lindblad dynamics mimic the (discrete-time) superoperator in Eq. (5.8) with the Kraus operators in Eq. (5.10) — i.e. the Lindbladian is determined in such a way that it results in the same dynamics as the superoperator for a given time step τ. Hereby, γ is found to have an explicit relation to the probability p of the probabilistic QCA; or in other words, γ is found to be tuned in such a way that it implements the QCA for different values of $p \in (0, 1/2]$.

The relationship between γ and p can be derived by setting the state undergoing the time evolution according to the Lindblad dynamics in Eq. (5.12) equal to the state that is being updated by the discrete-time transfer matrix in Eq. (5.7):

$$e^{\hat{\mathcal{L}}^{(\text{Fukś})}\tau}[\hat{\rho}] = \hat{S}^{(\text{Fukś})}[\hat{\rho}]. \tag{B.1}$$

B.0.1 $|00\rangle$ neighborhood

For the scope of this proof, it is sufficient to take the evolution of only one qubit into account by fixing the nearest-neighboring qubits to, say at first, the $|0\rangle\langle 0|_{j-1} \otimes |0\rangle\langle 0|_{j+1}$ state. In such a way, only the first jump operator $\hat{L}_{1_j} = \sqrt{\gamma}\,|0\rangle\langle 0|_{j-1} \otimes \hat{\sigma}_j^- \otimes |0\rangle\langle 0|_{j+1}$, see Eq. (5.13a), acts non-trivially on the qubit at site j, and the neighboring sites can be traced out for simplicity. Analogously, only the Kraus operators $\hat{K}_0^{(00)} = \begin{pmatrix} 1 & 0 \\ 0 & \sqrt{1-2p} \end{pmatrix}$, and $\hat{K}_1^{(00)} = \begin{pmatrix} 0 & \sqrt{2p} \\ 0 & 0 \end{pmatrix}$, see Eq. (5.10a), must be taken into account, because $\hat{\mathbb{S}}^{(00)}$ in Eq. (5.8) is the only transfer operator that acts on the state at the center site j given the $|0\rangle\langle 0|_{j-1} \otimes |0\rangle\langle 0|_{j+1}$ neighborhood.

The corresponding continuous-time evolution (5.12) of the quantum state $\hat{\rho} = \begin{pmatrix} \rho_{00} & \rho_{01} \\ \rho_{10} & \rho_{11} \end{pmatrix}$ at

site j is then given by

$$\begin{aligned}\hat{\mathcal{L}}^{(00)}[\hat{\rho}] &= \gamma\left[\hat{\sigma}^-\hat{\rho}\,\hat{\sigma}^+ - \frac{1}{2}\left(\hat{\sigma}^+\hat{\sigma}^-\hat{\rho} + \hat{\rho}\,\hat{\sigma}^+\hat{\sigma}^-\right)\right] \\ &= \gamma\left[\begin{pmatrix}0 & 1\\ 0 & 0\end{pmatrix}\begin{pmatrix}\rho_{00} & \rho_{01}\\ \rho_{10} & \rho_{11}\end{pmatrix}\begin{pmatrix}0 & 0\\ 1 & 0\end{pmatrix} - \right. \\ &\quad \left. -\frac{1}{2}\left(\begin{pmatrix}0 & 0\\ 1 & 0\end{pmatrix}\begin{pmatrix}0 & 1\\ 0 & 0\end{pmatrix}\begin{pmatrix}\rho_{00} & \rho_{01}\\ \rho_{10} & \rho_{11}\end{pmatrix} + \begin{pmatrix}\rho_{00} & \rho_{01}\\ \rho_{10} & \rho_{11}\end{pmatrix}\begin{pmatrix}0 & 0\\ 1 & 0\end{pmatrix}\begin{pmatrix}0 & 1\\ 0 & 0\end{pmatrix}\right)\right] \\ &= -\gamma\begin{pmatrix}-(1-\rho_{00}) & \rho_{01}/2\\ \rho_{10}/2 & \rho_{11}\end{pmatrix}. \end{aligned} \tag{B.2}$$

which leads with $\rho_{00} = 1 - \rho_{11}$ to the output state

$$e^{\hat{\mathcal{L}}^{(00)}\tau}[\hat{\rho}] = \begin{pmatrix}1 - e^{-\gamma\tau}(1-\rho_{00}) & e^{-\gamma\tau/2}\rho_{01}\\ e^{-\gamma\tau/2}\rho_{10} & e^{-\gamma\tau}\rho_{11}\end{pmatrix}. \tag{B.3}$$

On the other side, the discrete-time evolution (5.8) results in the state

$$\begin{aligned}\sum_{\mu=0,1}\hat{K}_\mu^{(00)}\,\hat{\rho}\,\left(\hat{K}_\mu^{(00)}\right)^\dagger &= \begin{pmatrix}1 & 0\\ 0 & \sqrt{1-2p}\end{pmatrix}\begin{pmatrix}\rho_{00} & \rho_{01}\\ \rho_{10} & \rho_{11}\end{pmatrix}\begin{pmatrix}1 & 0\\ 0 & \sqrt{1-2p}\end{pmatrix} \\ &\quad + \begin{pmatrix}0 & \sqrt{2p}\\ 0 & 0\end{pmatrix}\begin{pmatrix}\rho_{00} & \rho_{01}\\ \rho_{10} & \rho_{11}\end{pmatrix}\begin{pmatrix}0 & 0\\ \sqrt{2p} & 0\end{pmatrix} \\ &= \begin{pmatrix}(1-2p)\rho_{00} + 2p & \sqrt{1-2p}\,\rho_{01}\\ \sqrt{1-2p}\,\rho_{10} & (1-2p)\rho_{11}\end{pmatrix}. \end{aligned} \tag{B.4}$$

Setting the time-evolved density matrices in Eqs. (B.3) and (B.4) equal to each other according to Eq. (B.1), one can find the relationship between γ and p by equating the individual density operator components. For example, taking $\rho_{01}(\tau)$ into account:

$$e^{-\gamma\tau/2} = \sqrt{1-2p}, \tag{B.5}$$

which is equivalent to equating the $\rho_{11}(\tau)$ components and leads to the same result:

$$\begin{aligned} e^{-\gamma\tau} &= 1 - 2p \\ \Rightarrow \gamma\tau &= -\ln(1-2p). \end{aligned} \tag{B.6}$$

Note that the other two density matrix elements exhibit the same information as $\rho_{00}(\tau) = 1 - \rho_{11}(\tau)$ and $\rho_{10}(\tau) = (\rho_{01}(\tau))^*$.

B.0.2 $|01\rangle$ neighborhood

Next, fixing the nearest-neighboring qubits to the $|0\rangle\langle 0|_{j-1} \otimes |1\rangle\langle 1|_{j+1}$ state, only the two jump operators $\hat{L}_{2_j} = \sqrt{\gamma}\,|0\rangle\langle 0|_{j-1} \otimes \hat{\sigma}_j^- \otimes |1\rangle\langle 1|_{j+1}$ and $\hat{L}_{3_j} = \sqrt{\gamma}\,|0\rangle\langle 0|_{j-1} \otimes \hat{\sigma}_j^+ \otimes |1\rangle\langle 1|_{j+1}$ in Eqs. (5.13b) and (5.13c) as well as the Kraus operators $\hat{K}_0^{(01)} = \sqrt{1-p}\;\hat{\mathbb{1}}$ and $\hat{K}_1^{(01)} = \sqrt{p}\,\hat{X}$ from Eq. (5.10b), have to be taken into account. The corresponding Lindblad evolution (5.12) of the quantum state $\hat{\rho}$ at site j is then given by

$$
\begin{aligned}
\hat{\mathcal{L}}^{(01)}[\hat{\rho}] &= \frac{\gamma}{2}\left[\hat{\sigma}^-\hat{\rho}\,\hat{\sigma}^+ + \hat{\sigma}^+\hat{\rho}\,\hat{\sigma}^- - \frac{1}{2}(\hat{\sigma}^+\hat{\sigma}^-\hat{\rho} + \hat{\rho}\,\hat{\sigma}^+\hat{\sigma}^-) - \frac{1}{2}(\hat{\sigma}^-\hat{\sigma}^+\hat{\rho} + \hat{\rho}\,\hat{\sigma}^-\hat{\sigma}^+)\right] \\
&= \frac{\gamma}{2}\left[\begin{pmatrix}0&1\\0&0\end{pmatrix}\begin{pmatrix}\rho_{00}&\rho_{01}\\\rho_{10}&\rho_{11}\end{pmatrix}\begin{pmatrix}0&0\\1&0\end{pmatrix} + \begin{pmatrix}0&0\\1&0\end{pmatrix}\begin{pmatrix}\rho_{00}&\rho_{01}\\\rho_{10}&\rho_{11}\end{pmatrix}\begin{pmatrix}0&1\\0&0\end{pmatrix}\right. \\
&\quad - \frac{1}{2}\left(\begin{pmatrix}0&0\\1&0\end{pmatrix}\begin{pmatrix}0&1\\0&0\end{pmatrix}\begin{pmatrix}\rho_{00}&\rho_{01}\\\rho_{10}&\rho_{11}\end{pmatrix} + \begin{pmatrix}\rho_{00}&\rho_{01}\\\rho_{10}&\rho_{11}\end{pmatrix}\begin{pmatrix}0&0\\1&0\end{pmatrix}\begin{pmatrix}0&1\\0&0\end{pmatrix}\right) \\
&\quad \left. - \frac{1}{2}\left(\begin{pmatrix}0&1\\0&0\end{pmatrix}\begin{pmatrix}0&0\\1&0\end{pmatrix}\begin{pmatrix}\rho_{00}&\rho_{01}\\\rho_{10}&\rho_{11}\end{pmatrix} + \begin{pmatrix}\rho_{00}&\rho_{01}\\\rho_{10}&\rho_{11}\end{pmatrix}\begin{pmatrix}0&1\\0&0\end{pmatrix}\begin{pmatrix}0&0\\1&0\end{pmatrix}\right)\right] \\
&= \frac{\gamma}{2}\left[\begin{pmatrix}\rho_{11}&0\\0&0\end{pmatrix} + \begin{pmatrix}0&0\\0&\rho_{00}\end{pmatrix} - \frac{1}{2}\left(\begin{pmatrix}0&0\\\rho_{10}&\rho_{11}\end{pmatrix} + \begin{pmatrix}0&\rho_{01}\\0&\rho_{11}\end{pmatrix} + \begin{pmatrix}\rho_{00}&\rho_{01}\\0&0\end{pmatrix} + \begin{pmatrix}\rho_{00}&0\\\rho_{10}&0\end{pmatrix}\right)\right] \\
&= -\gamma\begin{pmatrix}\rho_{00}-\frac{1}{2}&\rho_{01}/2\\\rho_{10}/2&\rho_{11}-\frac{1}{2}\end{pmatrix},
\end{aligned}
\tag{B.7}
$$

where the index j is dropped for clarity, and $\rho_{00} = 1 - \rho_{11}$ is used in the last step. This result leads to the output state

$$
e^{\hat{\mathcal{L}}^{(01)}\tau}[\hat{\rho}] = \begin{pmatrix}e^{-\gamma\tau}\rho_{00} + \frac{1}{2}(1-e^{-\gamma\tau}) & e^{-\gamma\tau/2}\rho_{01}\\ e^{-\gamma\tau/2}\rho_{10} & e^{-\gamma\tau}\rho_{11} + \frac{1}{2}(1-e^{-\gamma\tau})\end{pmatrix}. \tag{B.8}
$$

On the other side, the discrete-time evolution (5.8) results in the state

$$
\begin{aligned}
\sum_{\mu=0,1}\hat{K}_\mu^{(01)}\,\hat{\rho}\,\left(\hat{K}_\mu^{(01)}\right)^\dagger &= (1-p)\;\hat{\mathbb{1}}\begin{pmatrix}\rho_{00}&\rho_{01}\\\rho_{10}&\rho_{11}\end{pmatrix}\hat{\mathbb{1}} + p\begin{pmatrix}0&1\\1&0\end{pmatrix}\begin{pmatrix}\rho_{00}&\rho_{01}\\\rho_{10}&\rho_{11}\end{pmatrix}\begin{pmatrix}0&1\\1&0\end{pmatrix} \\
&= (1-p)\begin{pmatrix}\rho_{00}&\rho_{01}\\\rho_{10}&\rho_{11}\end{pmatrix} + p\begin{pmatrix}\rho_{11}&\rho_{10}\\\rho_{01}&\rho_{00}\end{pmatrix} \\
&= \begin{pmatrix}(1-2p)\rho_{00}+p & (1-p)\,\rho_{01} + p\rho_{10}\\ (1-p)\,\rho_{10} + p\rho_{01} & (1-2p)\rho_{11}+p\end{pmatrix},
\end{aligned}
\tag{B.9}
$$

with (again) $\rho_{00} = 1 - \rho_{11}$ applied in the last step. Setting the time-evolved density operators in Eqs. (B.8) and (B.9) equal to each other according to Eq. (B.1), one can analogously to the previous subsection in Appendix B.0.1 find the relationship between γ and p by equating the individual density operator components. Taking $\rho_{01}(t)$ into account, one can find that

$$
e^{-\gamma\tau/2}\rho_{01} = (1-p)\,\rho_{01} + p\,\rho_{10} \tag{B.10}
$$

does not lead to a unique solution; however, equating the $\rho_{11}(t)$ components leads to the same result (B.6) derived using the 00 neighborhood in the previous subsection:

$$\begin{aligned} e^{-\gamma\tau}\rho_{00} + \frac{1}{2}(1 - e^{-\gamma\tau}) &= (1-2p)\rho_{00} + p \\ \Rightarrow e^{-\gamma\tau} &= 1 - 2p \\ \Rightarrow \gamma\tau &= -\ln(1-2p). \end{aligned} \tag{B.11}$$

Equivalent expressions hold for the density matrix components $\rho_{00}(t) = 1 - \rho_{11}(t)$ and $(\rho_{10}(t) = \rho_{01}(t))^*$, respectively. Furthermore, the same relationship between p and γ follows from an analogous inspection of the 10 and 11 neighborhoods.

Appendix C

Proof of the conservation of the number density in the Fukś QCA

In the following, it is derived that the global number density of the Fukś QCA is conserved. The proof arises from the conservation of the expectation value of $\hat{S}_z = \frac{1}{2}\sum_i \hat{Z}_i$, considering the corresponding Lindblad dynamics in Eq. (5.12). The time derivative of $\hat{S}_z(t)$, expressed as the trace of the product of $\hat{S}_z$ and the Lindbladian acting on the density matrix $\hat{\rho}(t)$, can be shown to be equal to the trace of the product of $\hat{\rho}(t)$ and the *adjoint* Lindbladian $\hat{\mathcal{L}}^\dagger$ acting on $\hat{S}_z$:

$$\frac{\mathrm{d}}{\mathrm{d}t}\left\langle \hat{S}_z(t)\right\rangle = \mathrm{Tr}\left[\hat{\mathcal{L}}[\hat{\rho}(t)]\cdot \hat{S}_z\right] = \mathrm{Tr}\left[\hat{\mathcal{L}}^\dagger\left[\hat{S}_z\right]\cdot\hat{\rho}(t)\right]. \tag{C.1}$$

Thus, the problem reduces to the calculation of

$$\hat{\mathcal{L}}^\dagger\left[\hat{S}_z\right] = \hat{\mathcal{L}}^\dagger\left[\frac{1}{2}\sum_i \hat{Z}_i\right] = \frac{1}{2}\sum_i \hat{\mathcal{L}}^\dagger\left[\hat{Z}_i\right] = \frac{1}{2}\sum_{i,j}\hat{\mathcal{L}}_j^\dagger\left[\hat{Z}_i\right], \tag{C.2}$$

where $\hat{\mathcal{L}}_j^\dagger$ represents the local adjoint Lindbladian that acts non-trivially on the neighborhood at sites $j-1$, j, and $j+1$ only, see definition of the associate jump operators in Eq. (5.13). This means, that

$$\hat{\mathcal{L}}_j^\dagger\left[\hat{Z}_i\right] = \sum_{k=1}^{6}\left(\hat{L}_{k_j}^\dagger\hat{Z}_i\hat{L}_{k_j} - \frac{1}{2}\left(\hat{Z}_i\hat{L}_{k_j}^\dagger\hat{L}_{k_j} + \hat{L}_{k_j}^\dagger\hat{L}_{k_j}\hat{Z}_i\right)\right) \tag{C.3}$$

is only non-zero iff $i \in \{j-1, j, j+1\}$, because for all other i $\hat{\mathcal{L}}_j^\dagger$ acts merely trivially on $\hat{Z}_i$ $\Big($as all jump operators are the identity operator in this case, $\hat{L}_{k_i} = \hat{\mathbb{1}}_i \;\forall\; k \in [1,6]$, such that $\hat{\mathcal{L}}_j^\dagger\left[\hat{Z}_{i\neq\{j-1,j,j+1\}}\right]$ only includes terms like $\hat{\mathbb{1}}_i^\dagger\hat{Z}_i\hat{\mathbb{1}}_i = \hat{Z}_i\Big)$, and, additionally, its action onto the identity operators at sites $\{j-1, j, j+1\}$ returns zero, $\hat{\mathcal{L}}_j^\dagger[\hat{\mathbb{1}}_{j-1}\otimes\hat{\mathbb{1}}_j\otimes\hat{\mathbb{1}}_{j+1}] = 0$, according to Eq. (C.3). (Another (potentially more intuitive) way to think about this derivation is to notice that the identity channel possesses a constant expectation value,

$$\frac{\mathrm{d}}{\mathrm{d}t}\left\langle\hat{O}(t)\right\rangle = \frac{\mathrm{d}}{\mathrm{d}t}\,\mathrm{Tr}\left[\hat{O}\,\hat{\rho}(t)\right] = 0 \text{ if } \hat{O} = \hat{\mathbb{1}}, \tag{C.4}$$

and does therefore not change the total time derivative of the expectation value of $\hat{S}_z$.)

As a result, Eq. (C.2) simplifies to

$$\hat{\mathcal{L}}^\dagger\left[\hat{S}_z\right] = \frac{1}{2}\sum_j \left(\hat{\mathcal{L}}_j^\dagger\left[\hat{Z}_{j-1}\right] + \hat{\mathcal{L}}_j^\dagger\left[\hat{Z}_j\right] + \hat{\mathcal{L}}_j^\dagger\left[\hat{Z}_{j+1}\right]\right), \tag{C.5}$$

where each summand is going to be inspected separately in the following.
To start, $\hat{\mathcal{L}}_j^\dagger\left[\hat{Z}_{j-1}\right]$ includes the terms $\sum_{k=1}^6 \hat{L}_{k_j}^\dagger \hat{Z}_{j-1}\hat{L}_{k_j}$, $\sum_{k=1}^6 \hat{Z}_{j-1}\hat{L}_{k_j}^\dagger\hat{L}_{k_j}$ and $\sum_{k=1}^6 \hat{L}_{k_j}^\dagger\hat{L}_{k_j}\hat{Z}_{j-1}$, see Eq. (C.3). The first sum comprises the terms according to the jump operators in Eq. (5.13), where $\gamma \equiv 1$ for clarity:

$$\begin{aligned}
\hat{L}_{1_j}^\dagger \hat{Z}_{j-1}\hat{L}_{1_j} &= |0\rangle\langle 0|\,\hat{Z}\,|0\rangle\langle 0| \otimes |1\rangle\langle 1| \otimes |0\rangle\langle 0| &&= |0\rangle\langle 0| \otimes |1\rangle\langle 1| \otimes |0\rangle\langle 0| \\
\hat{L}_{2_j}^\dagger \hat{Z}_{j-1}\hat{L}_{2_j} &= \frac{1}{2}|0\rangle\langle 0|\,\hat{Z}\,|0\rangle\langle 0| \otimes |1\rangle\langle 1| \otimes |1\rangle\langle 1| &&= \frac{1}{2}|0\rangle\langle 0| \otimes |1\rangle\langle 1| \otimes |1\rangle\langle 1| \\
\hat{L}_{3_j}^\dagger \hat{Z}_{j-1}\hat{L}_{3_j} &= \frac{1}{2}|0\rangle\langle 0|\,\hat{Z}\,|0\rangle\langle 0| \otimes |0\rangle\langle 0| \otimes |1\rangle\langle 1| &&= \frac{1}{2}|0\rangle\langle 0| \otimes |0\rangle\langle 0| \otimes |1\rangle\langle 1| \\
\hat{L}_{4_j}^\dagger \hat{Z}_{j-1}\hat{L}_{4_j} &= \frac{1}{2}|1\rangle\langle 1|\,\hat{Z}\,|1\rangle\langle 1| \otimes |1\rangle\langle 1| \otimes |0\rangle\langle 0| &&= -\frac{1}{2}|1\rangle\langle 1| \otimes |1\rangle\langle 1| \otimes |0\rangle\langle 0| \\
\hat{L}_{5_j}^\dagger \hat{Z}_{j-1}\hat{L}_{5_j} &= \frac{1}{2}|1\rangle\langle 1|\,\hat{Z}\,|1\rangle\langle 1| \otimes |0\rangle\langle 0| \otimes |0\rangle\langle 0| &&= -\frac{1}{2}|1\rangle\langle 1| \otimes |0\rangle\langle 0| \otimes |0\rangle\langle 0| \\
\hat{L}_{6_j}^\dagger \hat{Z}_{j-1}\hat{L}_{6_j} &= |1\rangle\langle 1|\,\hat{Z}\,|1\rangle\langle 1| \otimes |0\rangle\langle 0| \otimes |1\rangle\langle 1| &&= -\,|1\rangle\langle 1| \otimes |0\rangle\langle 0| \otimes |1\rangle\langle 1|\,,
\end{aligned} \tag{C.6}$$

which are the same as the terms in the second sum,

$$\begin{aligned}
\hat{Z}_{j-1}\hat{L}_{1_j}^\dagger \hat{L}_{1_j} &= \hat{Z}\,|0\rangle\langle 0|\,|0\rangle\langle 0| \otimes |1\rangle\langle 1| \otimes |0\rangle\langle 0| &&= |0\rangle\langle 0| \otimes |1\rangle\langle 1| \otimes |0\rangle\langle 0| \\
\hat{Z}_{j-1}\hat{L}_{2_j}^\dagger \hat{L}_{2_j} &= \frac{1}{2}\hat{Z}\,|0\rangle\langle 0|\,|0\rangle\langle 0| \otimes |1\rangle\langle 1| \otimes |1\rangle\langle 1| &&= \frac{1}{2}|0\rangle\langle 0| \otimes |1\rangle\langle 1| \otimes |1\rangle\langle 1| \\
\hat{Z}_{j-1}\hat{L}_{3_j}^\dagger \hat{L}_{3_j} &= \frac{1}{2}\hat{Z}\,|0\rangle\langle 0|\,|0\rangle\langle 0| \otimes |0\rangle\langle 0| \otimes |1\rangle\langle 1| &&= \frac{1}{2}|0\rangle\langle 0| \otimes |0\rangle\langle 0| \otimes |1\rangle\langle 1| \\
\hat{Z}_{j-1}\hat{L}_{4_j}^\dagger \hat{L}_{4_j} &= \frac{1}{2}\hat{Z}\,|1\rangle\langle 1|\,|1\rangle\langle 1| \otimes |1\rangle\langle 1| \otimes |0\rangle\langle 0| &&= -\frac{1}{2}|1\rangle\langle 1| \otimes |1\rangle\langle 1| \otimes |0\rangle\langle 0| \\
\hat{Z}_{j-1}\hat{L}_{5_j}^\dagger \hat{L}_{5_j} &= \frac{1}{2}\hat{Z}\,|1\rangle\langle 1|\,|1\rangle\langle 1| \otimes |0\rangle\langle 0| \otimes |0\rangle\langle 0| &&= -\frac{1}{2}|1\rangle\langle 1| \otimes |0\rangle\langle 0| \otimes |0\rangle\langle 0| \\
\hat{Z}_{j-1}\hat{L}_{6_j}^\dagger \hat{L}_{6_j} &= \hat{Z}\,|1\rangle\langle 1|\,|1\rangle\langle 1| \otimes |0\rangle\langle 0| \otimes |1\rangle\langle 1| &&= -\,|1\rangle\langle 1| \otimes |0\rangle\langle 0| \otimes |1\rangle\langle 1|\,,
\end{aligned} \tag{C.7}$$

and analogously the same as the third due to the symmetric action of the hermitian Pauli operator $\hat{Z} = \hat{Z}^\dagger$ onto the binary basis elements. In total, one can find that $\sum_{k=1}^6 \hat{L}_{k_j}\hat{Z}_{j-1}\hat{L}_{k_j}^\dagger = \sum_{k=1}^6 \hat{Z}_{j-1}\hat{L}_{k_j}^\dagger\hat{L}_{k_j} = \sum_{k=1}^6 \hat{L}_{k_j}^\dagger\hat{L}_{k_j}\hat{Z}_{j-1}$, such that $\hat{\mathcal{L}}_j^\dagger\left[\hat{Z}_{j-1}\right]$ is vanishing according to Eq. (C.3). In the same way, one can show that $\hat{\mathcal{L}}_j^\dagger\left[\hat{Z}_{j+1}\right] = 0$ by reflection symmetry around the center site j.

Hence, Eq. (C.5) becomes

$$\hat{\mathcal{L}}^\dagger\left[\hat{S}_z\right] = \frac{1}{2}\sum_j \hat{\mathcal{L}}_j^\dagger\left[\hat{Z}_j\right], \tag{C.8}$$

where $\hat{\mathcal{L}}_j^\dagger\left[\hat{Z}_j\right]$ includes the summands

$$
\begin{aligned}
\hat{L}_{1_j}^\dagger \hat{Z}_j \hat{L}_{1_j} &= |0\rangle\langle 0| \otimes |1\rangle\langle 0|\, Z\, |0\rangle\langle 1| \otimes |0\rangle\langle 0| && = |0\rangle\langle 0| \otimes |1\rangle\langle 1| \otimes |0\rangle\langle 0| \\
\hat{L}_{2_j}^\dagger \hat{Z}_j \hat{L}_{2_j} &= \frac{1}{2}\, |0\rangle\langle 0| \otimes |1\rangle\langle 0|\, Z\, |0\rangle\langle 1| \otimes |1\rangle\langle 1| && = \frac{1}{2}\, |0\rangle\langle 0| \otimes |1\rangle\langle 1| \otimes |1\rangle\langle 1| \\
\hat{L}_{3_j}^\dagger \hat{Z}_j \hat{L}_{3_j} &= \frac{1}{2}\, |0\rangle\langle 0| \otimes |0\rangle\langle 1|\, \hat{Z}\, |1\rangle\langle 0| \otimes |1\rangle\langle 1| && = -\frac{1}{2}\, |0\rangle\langle 0| \otimes |0\rangle\langle 0| \otimes |1\rangle\langle 1| \\
\hat{L}_{4_j}^\dagger \hat{Z}_j \hat{L}_{4_j} &= \frac{1}{2}\, |1\rangle\langle 1| \otimes |1\rangle\langle 0|\, Z\, |0\rangle\langle 1| \otimes |0\rangle\langle 0| && = \frac{1}{2}\, |1\rangle\langle 1| \otimes |1\rangle\langle 1| \otimes |0\rangle\langle 0| \\
\hat{L}_{5_j}^\dagger \hat{Z}_j \hat{L}_{5_j} &= \frac{1}{2}\, |1\rangle\langle 1| \otimes |0\rangle\langle 1|\, \hat{Z}\, |1\rangle\langle 0| \otimes |0\rangle\langle 0| && = -\frac{1}{2}\, |1\rangle\langle 1| \otimes |0\rangle\langle 0| \otimes |0\rangle\langle 0| \\
\hat{L}_{6_j}^\dagger \hat{Z}_j \hat{L}_{6_j} &= |1\rangle\langle 1| \otimes |0\rangle\langle 1|\, \hat{Z}\, |1\rangle\langle 0| \otimes |1\rangle\langle 1| && = -\,|1\rangle\langle 1| \otimes |0\rangle\langle 0| \otimes |1\rangle\langle 1|
\end{aligned}
\tag{C.9}
$$

and

$$
\begin{aligned}
\hat{Z}_j \hat{L}_{1_j}^\dagger \hat{L}_{1_j} &= \hat{L}_{1_j}^\dagger \hat{L}_{1_j} \hat{Z}_j = |0\rangle\langle 0| \otimes Z\, |1\rangle\langle 1| \otimes |0\rangle\langle 0| && = -\,|0\rangle\langle 0| \otimes |1\rangle\langle 1| \otimes |0\rangle\langle 0| \\
\hat{Z}_j \hat{L}_{2_j}^\dagger \hat{L}_{2_j} &= \hat{L}_{2_j}^\dagger \hat{L}_{2_j} \hat{Z}_j = \frac{1}{2}\, |0\rangle\langle 0| \otimes Z\, |1\rangle\langle 1| \otimes |1\rangle\langle 1| && = -\frac{1}{2}\, |0\rangle\langle 0| \otimes |1\rangle\langle 1| \otimes |1\rangle\langle 1| \\
\hat{Z}_j \hat{L}_{3_j}^\dagger \hat{L}_{3_j} &= \hat{L}_{3_j}^\dagger \hat{L}_{3_j} \hat{Z}_j = \frac{1}{2}\, |0\rangle\langle 0| \otimes Z\, |0\rangle\langle 0| \otimes |1\rangle\langle 1| && = \frac{1}{2}\, |0\rangle\langle 0| \otimes |0\rangle\langle 0| \otimes |1\rangle\langle 1| \\
\hat{Z}_j \hat{L}_{4_j}^\dagger \hat{L}_{4_j} &= \hat{L}_{4_j}^\dagger \hat{L}_{4_j} \hat{Z}_j = \frac{1}{2}\, |1\rangle\langle 1| \otimes Z\, |1\rangle\langle 1| \otimes |0\rangle\langle 0| && = -\frac{1}{2}\, |1\rangle\langle 1| \otimes |1\rangle\langle 1| \otimes |0\rangle\langle 0| \\
\hat{Z}_j \hat{L}_{5_j}^\dagger \hat{L}_{5_j} &= \hat{L}_{5_j}^\dagger \hat{L}_{5_j} \hat{Z}_j = \frac{1}{2}\, |1\rangle\langle 1| \otimes Z\, |0\rangle\langle 0| \otimes |0\rangle\langle 0| && = \frac{1}{2}\, |1\rangle\langle 1| \otimes |0\rangle\langle 0| \otimes |0\rangle\langle 0| \\
\hat{Z}_j \hat{L}_{6_j}^\dagger \hat{L}_{6_j} &= \hat{L}_{6_j}^\dagger \hat{L}_{6_j} \hat{Z}_j = |1\rangle\langle 1| \otimes Z\, |0\rangle\langle 0| \otimes |1\rangle\langle 1| && = |1\rangle\langle 1| \otimes |0\rangle\langle 0| \otimes |1\rangle\langle 1|\,.
\end{aligned}
\tag{C.10}
$$

One can see that $\sum_{k=1}^{6} \hat{L}_{k_j} \hat{Z}_j \hat{L}_{k_j}^\dagger = -\sum_{k=1}^{6} \hat{Z}_j \hat{L}_{k_j}^\dagger \hat{L}_{k_j}$ and $\sum_{k=1}^{6} \hat{Z}_j \hat{L}_{k_j}^\dagger \hat{L}_{k_j} = \sum_{k=1}^{6} \hat{L}_{k_j}^\dagger \hat{L}_{k_j} \hat{Z}_j$, such that $\hat{\mathcal{L}}_j^\dagger\left[\hat{Z}_j\right] = 2\sum_{k=1}^{6} \hat{L}_{k_j} \hat{Z}_j \hat{L}_{k_j}^\dagger$ according to the definition of the adjoint Lindbladian, see Eq. (C.3).

Summarizing, this leads with Eqs. (C.3) and (C.8) to

$$\begin{aligned}
\hat{\mathcal{L}}^{\dagger}\left[\hat{S}_z\right] &= \frac{1}{2}\sum_j \Big(2\,|0\rangle\langle 0|_{j-1} \otimes |1\rangle\langle 1|_j \otimes |0\rangle\langle 0|_{j+1} + |0\rangle\langle 0|_{j-1} \otimes |1\rangle\langle 1|_j \otimes |1\rangle\langle 1|_{j+1} + \\
&\quad + |1\rangle\langle 1|_{j-1} \otimes |1\rangle\langle 1|_j \otimes |0\rangle\langle 0|_{j+1} - |0\rangle\langle 0|_{j-1} \otimes |0\rangle\langle 0|_j \otimes |1\rangle\langle 1|_{j+1} - \\
&\quad - |1\rangle\langle 1|_{j-1} \otimes |0\rangle\langle 0|_j \otimes |0\rangle\langle 0|_{j+1} - 2\,|1\rangle\langle 1|_{j-1} \otimes |0\rangle\langle 0|_j \otimes |1\rangle\langle 1|_{j+1} \Big) \\
&= \frac{1}{2}\sum_j \Big(|0\rangle\langle 0|_{j-1} \otimes |1\rangle\langle 1|_j \otimes |0\rangle\langle 0|_{j+1} + |0\rangle\langle 0|_{j-1} \otimes |1\rangle\langle 1|_j \otimes |1\rangle\langle 1|_{j+1} + \\
&\quad + |1\rangle\langle 1|_{j-1} \otimes |1\rangle\langle 1|_j \otimes |0\rangle\langle 0|_{j+1} - |0\rangle\langle 0|_{j-1} \otimes |0\rangle\langle 0|_j \otimes |1\rangle\langle 1|_{j+1} - \\
&\quad - |1\rangle\langle 1|_{j-1} \otimes |0\rangle\langle 0|_j \otimes |0\rangle\langle 0|_{j+1} - |1\rangle\langle 1|_{j-1} \otimes |0\rangle\langle 0|_j \otimes |1\rangle\langle 1|_{j+1} \Big) \\
&= \frac{1}{2}\sum_j \Big(|0\rangle\langle 0|_{j-1} \otimes |1\rangle\langle 1|_j \otimes \hat{\mathbb{1}}_{j+1} + \hat{\mathbb{1}}_{j-1} \otimes |1\rangle\langle 1|_j \otimes |0\rangle\langle 0|_{j+1} - \\
&\quad - \hat{\mathbb{1}}_{j-1} \otimes |0\rangle\langle 0|_j \otimes |1\rangle\langle 1|_{j+1} - |1\rangle\langle 1|_{j-1} \otimes |0\rangle\langle 0|_j \otimes \hat{\mathbb{1}}_{j+1} \Big) \\
&= \frac{1}{2}\sum_j \Big(|0\rangle\langle 0|_j \otimes |1\rangle\langle 1|_{j+1} + |1\rangle\langle 1|_j \otimes |0\rangle\langle 0|_{j+1} - \\
&\quad - |0\rangle\langle 0|_j \otimes |1\rangle\langle 1|_{j+1} - |1\rangle\langle 1|_j \otimes |0\rangle\langle 0|_{j+1} \Big) \\
&= 0, \qquad \text{(C.11)}
\end{aligned}$$

where, in the first step, the first and the last projectors are each split into a sum of two identical summands; writing $2\,|0\rangle\langle 0|_{j-1} \otimes |1\rangle\langle 1|_j \otimes |0\rangle\langle 0|_{j+1} = |0\rangle\langle 0|_{j-1} \otimes |1\rangle\langle 1|_j \otimes |0\rangle\langle 0|_{j+1} + |0\rangle\langle 0|_{j-1} \otimes |1\rangle\langle 1|_j \otimes |0\rangle\langle 0|_{j+1}$, and analogously for $-2\,|1\rangle\langle 1|_{j-1} \otimes |0\rangle\langle 0|_j \otimes |1\rangle\langle 1|_{j+1}$. In the second step, all summands that are written next to each other are combined by identifying two identical projectors acting on the same site, while the sum of orthogonal projectors acting on the third site simplifies to $|0\rangle\langle 0| + |1\rangle\langle 1| = \hat{\mathbb{1}}$. Because of the space-invariance of lattice sites j, one can then in the fourth step shift the first and the last terms by one lattice site to the right, $j \to j+1$, and choose by convention to not write down the identity channels explicitly. The projectors thus cancel each other out in the last trivial step.

Plugging this result into the right-hand site of the initial Eq. (C.1), one can see that

$$\frac{\mathrm{d}}{\mathrm{d}t}\left\langle \hat{S}_z(t) \right\rangle = 0. \qquad \text{(C.12)}$$

The conservation of $\hat{S}_z$ for the Lindbladian describing the Fukś QCA has thus been proved.

Appendix D

Steady states of the Lindbladian describing the Fukś QCA

This section presents a derivation of the steady states of the continuous-time quantum dynamics describing the Fukś QCA. The corresponding Lindbladian is defined by Eqs. (5.12) and (5.13) in the main text. The steady states of this system are by definition invariant in time, i.e. they satisfy the equation

$$\hat{\mathcal{L}}^{(\text{Fukś})}[\hat{\rho}_{\text{ss}}] = \frac{\mathrm{d}}{\mathrm{d}t}\hat{\rho}_{\text{ss}} = 0, \tag{D.1}$$

whose solutions will be presented in the following Sec. D.0.1. Non-steady states that do not satisfy this equation are discussed in Sec. D.0.2.

D.0.1 The set of steady states

First, the trivial solutions, the pure states $|0...0\rangle\langle 0...0|$ and $|1...1\rangle\langle 1...1|$, are derived to be steady states by showing that they fulfill Eq. (D.1), i.e.

$$\hat{\mathcal{L}}^{(\text{Fukś})}[|0...0\rangle\langle 0...0|] = 0, \tag{D.2a}$$
$$\hat{\mathcal{L}}^{(\text{Fukś})}[|1...1\rangle\langle 1...1|] = 0. \tag{D.2b}$$

Inspecting the form of the Lindbladian in Eqs. (5.12) and (5.13), note that it only exhibits one jump operator that acts on the $|0\rangle\langle 0|_{j-1} \otimes |0\rangle\langle 0|_{j+1}$ ($|1\rangle\langle 1|_{j-1} \otimes |1\rangle\langle 1|_{j+1}$) neighborhood, $\hat{L}_1$ in Eq. (5.13a) ($\hat{L}_6$ in Eq. (5.13f)), that includes the amplitude damping (amplitude pumping) channel acting on the center site, $|0\rangle\langle 1|_j$ ($|1\rangle\langle 0|_j$). This annihilation (rising) operator destroys the state if, as in the case of the $|0...0\rangle\langle 0...0|$ ($|1...1\rangle\langle 1...1|$) state, the center qubit is in the same state as its neighboring qubits, writing $\sigma^- |0\rangle = |0\rangle\langle 1| |0\rangle = 0$ ($\sigma^+ |1\rangle = |1\rangle\langle 0| |1\rangle = 0$), which is the basic argument on which the following complete derivation of Eq. (D.2) is based on.

Dividing the Lindbladian into a sum of superoperators acting on a subset of a three qubit

neighborhood, $\hat{\mathcal{L}} = \sum_j \hat{\mathcal{L}}_j$, its action on the state $|0\rangle\langle 0|_{j-1} \otimes |0\rangle\langle 0|_j \otimes |0\rangle\langle 0|_{j+1} =: |000\rangle\langle 000|_j$ yields:

$$\begin{aligned}
\hat{\mathcal{L}}_j^{(\text{Fuks})}[|000\rangle\langle 000|_j] &= \sum_{k=1}^{6} \left(\hat{L}_{k_j} |000\rangle\langle 000|_j \, L_{k_j}^\dagger - \frac{1}{2}\Big(|000\rangle\langle 000|_j \, L_{k_j}^\dagger \hat{L}_{k_j} + \hat{L}_{k_j}^\dagger \hat{L}_{k_j} |000\rangle\langle 000|_j \Big) \right) \\
&= \hat{L}_{1_j} |000\rangle\langle 000|_j \, \hat{L}_{1_j}^\dagger - \frac{1}{2}\Big(|000\rangle\langle 000|_j \, \hat{L}_{1_j}^\dagger \hat{L}_{1_j} + \hat{L}_{1_j}^\dagger \hat{L}_{1_j} |000\rangle\langle 000|_j \Big) \\
&= \gamma \, (|0\rangle\langle 0| \, |0\rangle\langle 0| \, |0\rangle\langle 0| \otimes |0\rangle\langle 1| \, |0\rangle\langle 0| \, |1\rangle\langle 0| \otimes |0\rangle\langle 0| \, |0\rangle\langle 0| \, |0\rangle\langle 0| \\
&- \frac{1}{2}(|0\rangle\langle 0| \, |0\rangle\langle 0| \, |0\rangle\langle 0| \otimes (|0\rangle\langle 0| \, |1\rangle\langle 0| \, |0\rangle\langle 1| + |1\rangle\langle 0| \, |0\rangle\langle 1| \, |0\rangle\langle 0|) \otimes |0\rangle\langle 0| \, |0\rangle\langle 0| \, |0\rangle\langle 0|))_j \\
&= 0, \qquad \text{(D.3)}
\end{aligned}$$

and thus: $\hat{\mathcal{L}}[|0...0\rangle\langle 0...0|] = \sum_j \hat{\mathcal{L}}_j[|000\rangle\langle 000|_j] = 0$. Analogously, $\hat{\mathcal{L}}[|1...1\rangle\langle 1...1|] = 0$ can be shown by replacing $\hat{L}_1$ with $\hat{L}_6$ in the second step, and swapping the annihilation and creation operators $|0\rangle\langle 1|$ and $|1\rangle\langle 0|$ in the third step. As linear combinations of steady states are also steady states, all mixed states of the $|0...0\rangle\langle 0...0|$ and $|1...1\rangle\langle 1...1|$ states are steady states of the system as well.

Furthermore, it can be shown that the associate coherence terms remain invariant in this system,

$$\hat{\mathcal{L}}^{(\text{Fuks})}[|0...0\rangle\langle 1...1|] = 0, \qquad \text{(D.4a)}$$

$$\hat{\mathcal{L}}^{(\text{Fuks})}[|1...1\rangle\langle 0...0|] = 0, \qquad \text{(D.4b)}$$

because the projectors included in the jump operators that determine the states of the neighboring sites $j-1$ and $j+1$, see Eq. (5.13), annihilate all off-diagonal density matrix elements. For example, the action of the first and second jump operators onto the state $|0\rangle\langle 1|_{j-1} \otimes |0\rangle\langle 1|_j \otimes |0\rangle\langle 1|_{j+1} =: |000\rangle\langle 111|_j$ lead to:

$$\begin{aligned}
&\left(\hat{L}_{1_j} |000\rangle\langle 111|_j \, \hat{L}_{1_j}^\dagger - \frac{1}{2}\Big(|000\rangle\langle 111|_j \, \hat{L}_{1_j}^\dagger \hat{L}_{1_j} + \hat{L}_{1_j}^\dagger \hat{L}_{1_j} |000\rangle\langle 111|_j \Big) \right) \\
&= \gamma \, (|0\rangle\langle 0| \, |0\rangle\langle 1| \, |0\rangle\langle 0| \otimes |0\rangle\langle 1| \, |0\rangle\langle 1| \, |1\rangle\langle 0| \otimes |0\rangle\langle 0| \, |0\rangle\langle 1| \, |0\rangle\langle 0| - \\
&\quad - \frac{1}{2}(|0\rangle\langle 1| \, |0\rangle\langle 0| \otimes |0\rangle\langle 1| \, |1\rangle\langle 0| \, |0\rangle\langle 1| \otimes |0\rangle\langle 1| \, |0\rangle\langle 0| + \\
&\quad + |0\rangle\langle 0| \, |0\rangle\langle 1| \otimes |1\rangle\langle 0| \, |0\rangle\langle 1| \, |0\rangle\langle 1| \otimes |0\rangle\langle 0| \, |0\rangle\langle 1|)))_j = 0, \qquad \text{(D.5a)}
\end{aligned}$$

$$\begin{aligned}
&\left(\hat{L}_{2_j} |000\rangle\langle 111|_j \, \hat{L}_{2_j}^\dagger - \frac{1}{2}\Big(|000\rangle\langle 111|_j \, \hat{L}_{2_j}^\dagger \hat{L}_{2_j} + \hat{L}_{2_j}^\dagger \hat{L}_{2_j} |000\rangle\langle 111|_j \Big) \right) \\
&= \gamma \, (|0\rangle\langle 0| \, |0\rangle\langle 1| \, |0\rangle\langle 0| \otimes |0\rangle\langle 1| \, |0\rangle\langle 1| \, |1\rangle\langle 0| \otimes |1\rangle\langle 1| \, |0\rangle\langle 1| \, |1\rangle\langle 1| - \\
&\quad - \frac{1}{2}(|0\rangle\langle 1| \, |0\rangle\langle 0| \otimes |0\rangle\langle 1| \, |1\rangle\langle 0| \, |0\rangle\langle 1| \otimes |0\rangle\langle 1| \, |1\rangle\langle 1| + \\
&\quad + |0\rangle\langle 0| \, |0\rangle\langle 1| \otimes |1\rangle\langle 0| \, |0\rangle\langle 1| \, |0\rangle\langle 1| \otimes |1\rangle\langle 1| \, |0\rangle\langle 1|)))_j = 0. \qquad \text{(D.5b)}
\end{aligned}$$

Hence,

$$\hat{\rho}_{\text{ss}}^{(\text{Fuks})} = \alpha \, |0...0\rangle\langle 0...0| + \beta \, |0...0\rangle\langle 1...1| + \beta^* \, |1...1\rangle\langle 0...0| + (1-\alpha) \, |1...1\rangle\langle 1...1| \qquad \text{(D.6)}$$

has been shown to be a set of steady states. The set includes the GHZ state $\frac{1}{2}(|0...0\rangle\langle 0...0| + |0...0\rangle\langle 1...1| + |1...1\rangle\langle 0...0| + |1...1\rangle\langle 1...1|)$ with $\alpha = \beta = \frac{1}{2}$, as well as the pure states $|0...0\rangle\langle 0...0|$ and $|1...1\rangle\langle 1...1|$ with $\alpha = 1$ or $\alpha = 0$, respectively, and the mixed state $\alpha\,|0...0\rangle\langle 0...0| + (1-\alpha)\,|1...1\rangle\langle 1...1|)$ with $\beta = 0$ and $\alpha \in (0, 1)$; according to Eqs. (D.2) and (D.4).

Note that all steady states are translationally invariant, which means that the state exhibits the same *local* number density at every lattice site which is (thus) equal to the *global* number density of the whole state. This number density is the same as the global density of the input state $\hat{\rho}$ as shown in Appendix C.

Explicitly, the amplitude α that defines the number density of the steady state (D.6) is determined by the input state $\hat{\rho}$ as follows:

$$\alpha = \mathrm{Tr}\left[\hat{P}_0\,\hat{\rho}\right], \tag{D.7a}$$

$$1 - \alpha = \mathrm{Tr}\left[\hat{P}_1\,\hat{\rho}\right], \tag{D.7b}$$

where $\hat{P}_0 = \sum_j \frac{\hat{1}_j + \hat{Z}_j}{2}$ and $\hat{P}_1 = \sum_j \frac{\hat{1}_j - \hat{Z}_j}{2}$. As a simple example, the map evolves the input state $\hat{\rho} = |0001\rangle\langle 0001|$ to the steady state $\frac{3}{4}\,|0000\rangle\langle 0000| + \frac{1}{4}\,|1111\rangle\langle 1111|$, where $\alpha = \frac{3}{4}$ defines the normalized number of zero states and $1 - \alpha = \frac{1}{4}$ the normalized number of one states of the input state. The amplitudes β and β^* of the off-diagonal coherence terms in (D.6) are given by

$$\beta = \mathrm{Tr}\left[|0...0\rangle\langle 1...1|\;\hat{\rho}\right], \tag{D.8a}$$

$$\beta^* = \mathrm{Tr}\left[|1...1\rangle\langle 0...0|\;\hat{\rho}\right], \tag{D.8b}$$

with upper bound $|\beta| \leq \sqrt{\alpha(1-\alpha)}$.

For the proof of Eq. (D.8b), we are going to investigate whether a state $\hat{\rho}$ that does not exhibit the density matrix element $|0...0\rangle\langle 1...1|$ (or its complex-conjugate) would evolve into a state that does include the density matrix element $|0...0\rangle\langle 1...1|$ state (or its complex-conjugate) under long-time evolution; i.e. if that would be the case, then

$$\mathrm{Tr}\left[e^{\hat{\mathcal{L}}^{(\mathrm{Fuks\acute{})}}t}[\hat{\rho}]\;|1...1\rangle\langle 0...0|\right] = 0 \tag{D.9}$$

would be satisfied, which is going to be checked in the following. To start, it is sufficient to consider short-time evolution by taking into account that if the state decays in the long-term limit, it does so in the short-term limit too. The Lindblad evolution can then for $t \ll 1$ be approximated by

$$e^{\hat{\mathcal{L}}^{(\mathrm{Fuks\acute{})}}t}[\hat{\rho}] \approx \hat{\rho} + t\,\hat{\mathcal{L}}^{(\mathrm{Fuks\acute{})}}[\hat{\rho}], \tag{D.10}$$

where only the last term $\hat{\mathcal{L}}[\hat{\rho}]$ has the potential to include the $|0...0\rangle\langle 1...1|$ matrix element as $\hat{\rho}$ does not by definition. Considering the evolution of the density matrix element $|0...0\rangle\langle 1...1_{j-1}0_j1_{j+1}...1|$, where as the $|0...0\rangle\langle 0...0|$ and the $|1...1\rangle\langle 1...1|$ states have already been shown to vanish under the action the Lindbladian, see Eq. (D.2), only the remaining density matrix elements need to be inspected. Only those terms of the Lindbladian that act on the qubit at site j (i.e. the state that is not equal to the states of the surrounding qubits in the lattice) can be non-zero; writing with $|x\rangle\langle\widetilde{x}|_{j-1} \otimes |y\rangle\langle\widetilde{y}|_j \otimes |z\rangle\langle\widetilde{z}|_{j+1} =: |xyz\rangle\langle\widetilde{x}\widetilde{y}\widetilde{z}|_j \;\forall\, x, \widetilde{x}, y, \widetilde{y}, z, \widetilde{z} \in \{0, 1\}$:

$$\hat{\mathcal{L}}^{(\text{Fuks})}[|0...0\rangle\langle 1...1_{j-1}0_j1_{j+1}...1|] = \hat{\mathcal{L}}^{(\text{Fuks})}_{j-1}[|000\rangle\langle 110|_{j-1}] + \hat{\mathcal{L}}^{(\text{Fuks})}_{j}[|000\rangle\langle 101|_{j}] + \tag{D.11}$$

$$+ \hat{\mathcal{L}}^{(\text{Fuks})}_{j+1}[|000\rangle\langle 011|_{j+1}]. \tag{D.12}$$

As the local Lindbladians acting on the three-cell neighborhood are

$$\begin{aligned}
\hat{\mathcal{L}}_{j-1}\Big[|000\rangle\langle 110|_{j-1}\Big] &= \sum_{k=1}^{6}\Bigg(\underbrace{\hat{L}_{k_{j-1}}\,|000\rangle\langle 110|_{j-1}\,\hat{L}^{\dagger}_{k_{j-1}}}_{=0\ \forall k} - \\
&\quad - \frac{1}{2}\Bigg(\,|000\rangle\langle 110|_{j-1}\,\hat{L}^{\dagger}_{4_{j-1}}\hat{L}_{4_{j-1}} + \underbrace{L^{\dagger}_{1_{j-1}}\hat{L}_{1_{j-1}}\,|000\rangle\langle 110|_{j-1}}_{=0}\Bigg)\Bigg) \\
&= -\frac{\gamma}{4}\,|000\rangle\langle 110|_{j-1}\,, \qquad (D.13) \\
\hat{\mathcal{L}}_{j}\Big[|000\rangle\langle 101|_{j}\Big] &= \sum_{k=1}^{6}\Bigg(\underbrace{\hat{L}_{k_j}\,|000\rangle\langle 101|_{j}\,\hat{L}^{\dagger}_{k_j}}_{=0\ \forall k} - \frac{1}{2}\Bigg(\,|000\rangle\langle 101|_{j}\,\hat{L}^{\dagger}_{6_j}\hat{L}_{6_j} + \underbrace{L^{\dagger}_{1_j}\hat{L}_{1_j}\,|000\rangle\langle 101|_{j}}_{=0}\Bigg)\Bigg) \\
&= -\frac{\gamma}{4}\,|000\rangle\langle 101|_{j}\,, \qquad (D.14) \\
\hat{\mathcal{L}}_{j+1}\Big[|000\rangle\langle 011|_{j+1}\Big] &= \sum_{k=1}^{6}\Bigg(\underbrace{\hat{L}_{k_{j+1}}\,|000\rangle\langle 011|_{j+1}\,\hat{L}^{\dagger}_{k_{j+1}}}_{=0\ \forall k} - \\
&\quad - \frac{1}{2}\Bigg(\,|000\rangle\langle 011|_{j+1}\,\hat{L}^{\dagger}_{2_{j+1}}\hat{L}_{2_{j+1}} + \underbrace{L^{\dagger}_{1_{j+1}}\hat{L}_{1_{j+1}}\,|000\rangle\langle 011|_{j+1}}_{=0}\Bigg)\Bigg) \\
&= -\frac{\gamma}{4}\,|000\rangle\langle 011|_{j+1}\,. \qquad (D.15)
\end{aligned}$$

one can find that

$$\hat{\mathcal{L}}^{(\text{Fuks})}[|0...0\rangle\langle 1...1_{j-1}0_j1_{j+1}...1|] = -\frac{\gamma}{4}(|000\rangle\langle 110|_{j-1} + |000\rangle\langle 101|_{j} + |000\rangle\langle 101|_{j+1}). \tag{D.16}$$

Thus, the Lindbladian does not map the state $|0...0\rangle\langle 1...1_{j-1}0_j1_{j+1}...1|$ to the $|0...0\rangle\langle 1...1|$ state, where analogous derivations hold for all other off-diagonal elements of the initial state that do not equal the $|0...0\rangle\langle 1...1|$ state. It has hence been shown that β in Eq. (D.8b) does indeed represent the amplitude of the density matrix element $|0...0\rangle\langle 1...1|$ of the initial state, because there is no other density matrix element that evolves to this state.

D.0.2 States that are not steady states

How about density matrices that include neighboring sites exhibiting different quantum states — could those be also steady states of the explored system? For gleaning this, a superposition state is considered consisting of an arbitrary convex sum of projectors with all qubits except one (at an

arbitrary site j) occupying the same state:

$$\begin{aligned}\hat{\rho} = a\,|0...0\rangle\langle 0...0| + b\,|0...0_{j-1}1_j0_{j+1}...0\rangle\langle 0...0_{j-1}1_j0_{j+1}...0| \\ + c\,|1...1_{j-1}0_j1_{j+1}...1\rangle\langle 1...1_{j-1}0_j1_{j+1}...1| + d\,|1...1\rangle\langle 1...1| \\ + e\,|0...0\rangle\langle 0...0_{j-1}1_j0_{j+1}...0| + e^*\,|0...0_{j-1}1_j0_{j+1}...0\rangle\langle 0...0| \\ + f\,|1...1\rangle\langle 1...1_{j-1}0_j1_{j+1}...1| + f^*\,|1...1_{j-1}0_j1_{j+1}...1\rangle\langle 1...1|\,,\end{aligned} \tag{D.17}$$

where $d = 1 - a - b - c$ due to trace-preserving condition of quantum states.

As the $|0...0\rangle\langle 0...0|$ and the $|1...1\rangle\langle 1...1|$ states have already been shown to vanish under the action the Lindbladian, see Eq. (D.2), only the remaining density matrix elements need to be inspected in the following:

$$\begin{aligned}\hat{\mathcal{L}}^{(\text{Fukś})}[\hat{\rho}] = b\,\hat{\mathcal{L}}^{(\text{Fukś})}[|0...0_{j-1}1_j0_{j+1}...0\rangle\langle 0...0_{j-1}1_j0_{j+1}...0|] + \\ + c\,\hat{\mathcal{L}}^{(\text{Fukś})}[|1...1_{j-1}0_j1_{j+1}...1\rangle\langle 1...1_{j-1}0_j1_{j+1}...1|] \\ + e\,\hat{\mathcal{L}}^{(\text{Fukś})}[|0...0\rangle\langle 0...0_{j-1}1_j0_{j+1}...0|] + e^*\,\hat{\mathcal{L}}^{(\text{Fukś})}[|0...0_{j-1}1_j0_{j+1}...0\rangle\langle 0...0|] \\ + f\,\hat{\mathcal{L}}^{(\text{Fukś})}[|1...1\rangle\langle 1...1_{j-1}0_j1_{j+1}...1|] + f^*\,\hat{\mathcal{L}}^{(\text{Fukś})}[|1...1_{j-1}0_j1_{j+1}...1\rangle\langle 1...1|],\end{aligned} \tag{D.18}$$

where, by the similar argument that $\hat{\mathcal{L}}_j[|000\rangle\langle 000|_j] = 0$, see Eq. (D.3), only those terms of the Lindbladian that act on the qubit at site j (i.e. the state that is not equal to the states of the surrounding qubits in the lattice) are non-zero — for example, for the first term in Eq. (D.18) this means:

$$\begin{aligned}\hat{\mathcal{L}}[|0...0_{j-1}1_j0_{j+1}...0\rangle\langle 0...0_{j-1}1_j0_{j+1}...0|] = \hat{\mathcal{L}}_{j-1}[|001\rangle\langle 001|_{j-1}] + \hat{\mathcal{L}}_j[|010\rangle\langle 010|_j] + \\ + \hat{\mathcal{L}}_{j+1}[|100\rangle\langle 100|_{j+1}].\end{aligned} \tag{D.19}$$

For the derivation of these three terms, it is convenient to notice that only one of the six jump operators in Eq. (5.13) act on a given state: In the second term, $|010\rangle\langle 010|_j$, only the jump operator $\hat{L}_{1_j}$ acts on the state as the neighborhood is in the state $|0\rangle\langle 0|_{j-1} \otimes |0\rangle\langle 0|_{j+1}$, see Eq. (5.13a); whereas jump operators $\hat{L}_3$ and $\hat{L}_5$ each act on the states of the first and the third term, $|001\rangle\langle 001|_{j-1}$ and $|100\rangle\langle 100|_{j+1}$, due to the respective $|0\rangle\langle 0|_{j-2} \otimes |1\rangle\langle 1|_j$ and $|1\rangle\langle 1|_j \otimes |0\rangle\langle 0|_{j+2}$ neighborhoods, and the

center site being in the $|0\rangle\langle 0|$ state. In such a way, the summands in Eq. (D.19) yield:

$$\begin{aligned}\hat{\mathcal{L}}_{j-1}^{(\text{Fuks})}\Big[|001\rangle\langle 001|_{j-1}\Big] &= \hat{L}_{3_{j-1}}\,|001\rangle\langle 001|_{j-1}\,\hat{L}_{3_{j-1}}^{\dagger} - \frac{1}{2}\Big(|001\rangle\langle 001|_{j-1}\,\hat{L}_{3_{j-1}}^{\dagger}\hat{L}_{3_{j-1}} + \hat{L}_{3_{j-1}}^{\dagger}\hat{L}_{3_{j-1}}\,|001\rangle\langle 001|_{j-1}\Big) \\ &= \frac{\gamma}{2}\,|0\rangle\langle 0|_{j-2} \otimes \Big(|1\rangle\langle 0|\,|0\rangle\langle 0|\,|0\rangle\langle 1| - \frac{1}{2}(|0\rangle\langle 0|\,|0\rangle\langle 1|\,|1\rangle\langle 0| + |0\rangle\langle 1|\,|1\rangle\langle 0|\,|0\rangle\langle 0|)\Big)_{j-1} \otimes |1\rangle\langle 1|_{j} \\ &= -\frac{\gamma}{2}\,|0\rangle\langle 0|_{j-2} \otimes (|0\rangle\langle 0| - |1\rangle\langle 1|)_{j-1} \otimes |1\rangle\langle 1|_{j}\,, \end{aligned} \tag{D.20a}$$

$$\begin{aligned}\hat{\mathcal{L}}_{j}^{(\text{Fuks})}\Big[|010\rangle\langle 010|_{j}\Big] &= \hat{L}_{1_j}\,|010\rangle\langle 010|_{j}\,\hat{L}_{1_j}^{\dagger} - \frac{1}{2}\Big(|010\rangle\langle 010|_{j}\,\hat{L}_{1_j}^{\dagger}\hat{L}_{1_j} + \hat{L}_{1_j}^{\dagger}\hat{L}_{1_j}\,|010\rangle\langle 010|_{j}\Big) \\ &= \gamma\,|0\rangle\langle 0|_{j-1} \otimes \Big(|0\rangle\langle 1|\,|1\rangle\langle 1|\,|1\rangle\langle 0| - \frac{1}{2}(|1\rangle\langle 1|\,|1\rangle\langle 0|\,|0\rangle\langle 1| + |1\rangle\langle 0|\,|0\rangle\langle 1|\,|1\rangle\langle 1|)\Big)_{j} \otimes |0\rangle\langle 0|_{j+1} \\ &= \gamma\,|0\rangle\langle 0|_{j-1} \otimes (|0\rangle\langle 0| - |1\rangle\langle 1|)_{j} \otimes |0\rangle\langle 0|_{j+1}\,, \end{aligned} \tag{D.20b}$$

$$\begin{aligned}\hat{\mathcal{L}}_{j+1}^{(\text{Fuks})}\Big[|100\rangle\langle 100|_{j+1}\Big] &= \hat{L}_{5_{j+1}}\,|100\rangle\langle 100|_{j+1}\,\hat{L}_{5_{j+1}}^{\dagger} - \frac{1}{2}\Big(|100\rangle\langle 100|_{j+1}\,\hat{L}_{5_{j+1}}^{\dagger}\hat{L}_{5_{j+1}} + \hat{L}_{5_{j+1}}^{\dagger}\hat{L}_{5_{j+1}}\,|100\rangle\langle 100|_{j+1}\Big) \\ &= \frac{\gamma}{2}\,|1\rangle\langle 1|_{j} \otimes \Big(|1\rangle\langle 0|\,|0\rangle\langle 0|\,|0\rangle\langle 1| - \frac{1}{2}(|0\rangle\langle 0|\,|0\rangle\langle 1|\,|1\rangle\langle 0| + |0\rangle\langle 1|\,|1\rangle\langle 0|\,|0\rangle\langle 0|)\Big)_{j+1} \otimes |0\rangle\langle 0|_{j+2} \\ &= -\frac{\gamma}{2}\,|1\rangle\langle 1|_{j} \otimes (|0\rangle\langle 0| - |1\rangle\langle 1|)_{j+1} \otimes |0\rangle\langle 0|_{j+2}\,, \end{aligned} \tag{D.20c}$$

so that the overall sum of $\hat{\mathcal{L}}_{j-1}\Big[|001\rangle\langle 001|_{j-1}\Big]$, $\hat{\mathcal{L}}_{j}\Big[|010\rangle\langle 010|_{j}\Big]$ and $\hat{\mathcal{L}}_{j+1}\Big[|100\rangle\langle 100|_{j+1}\Big]$ is non-zero,

$$\begin{aligned}&\hat{\mathcal{L}}^{(\text{Fuks})}[|0...0_{j-1}1_j0_{j+1}...0\rangle\langle 0...0_{j-1}1_j0_{j+1}...0|] = \\ &= -\frac{\gamma}{2}\,|0\rangle\langle 0|_1 \otimes ... \otimes |0\rangle\langle 0|_{j-2} \otimes \Big((|0\rangle\langle 0| - |1\rangle\langle 1|)_{j-1} \otimes |1\rangle\langle 1|_j \otimes |0\rangle\langle 0|_{j+1} - \\ &\qquad - 2\,|0\rangle\langle 0|_{j-1} \otimes (|0\rangle\langle 0| - |1\rangle\langle 1|)_j \otimes |0\rangle\langle 0|_{j+1} + \\ &\qquad + |0\rangle\langle 0|_{j-1} \otimes |1\rangle\langle 1|_j \otimes (|0\rangle\langle 0| - |1\rangle\langle 1|)_{j+1}\Big) \otimes |0\rangle\langle 0|_{j+2} \otimes ... \otimes |0\rangle\langle 0|_N \\ &= -\frac{\gamma}{2}\,|0\rangle\langle 0|_1 \otimes ... \otimes |0\rangle\langle 0|_{j-2} \otimes \Big(-2\,|000\rangle\langle 000|_j + 4\,|010\rangle\langle 010|_j - \\ &\qquad - |011\rangle\langle 011|_j - |110\rangle\langle 110|_j\Big) \otimes |0\rangle\langle 0|_{j+2} \otimes ... \otimes |0\rangle\langle 0|_N = \\ &= \gamma\,|0\rangle\langle 0|_1 \otimes ... \otimes |0\rangle\langle 0|_{j-2} \otimes \Big(|000\rangle\langle 000|_j - 2\,|010\rangle\langle 010|_j + \\ &\qquad + \frac{1}{2}(|011\rangle\langle 011|_j + |110\rangle\langle 110|_j)\Big) \otimes |0\rangle\langle 0|_{j+2} \otimes ... \otimes |0\rangle\langle 0|_N \neq 0. \end{aligned} \tag{D.21}$$

This result also implies that the associated bit-flipped state:

$$(\hat{X}^{(N)}\,|0...0_{j-1}1_j0_{j+1}...0\rangle\langle 0...0_{j-1}1_j0_{j+1}...0|\,\hat{X}^{(N)} = |1...1_{j-1}0_j1_{j+1}...1\rangle\langle 1...1_{j-1}0_j1_{j+1}...1| \tag{D.22}$$

with $\hat{X}^{(N)} := \hat{X}_1 \otimes ... \otimes \hat{X}_N$, where N is the number of qubits) is neither a steady state,

$$\hat{\mathcal{L}}^{(\text{Fuks})}[|1...1_{j-1}0_j1_{j+1}...1\rangle\langle 1...1_{j-1}0_j1_{j+1}...1|] = \hat{X}^{(N)}\hat{\mathcal{L}}^{(\text{Fuks})}[|0...0_{j-1}1_j0_{j+1}...0\rangle\langle 0...0_{j-1}1_j0_{j+1}...0|]\hat{X}^{(N)} \neq 0 \tag{D.23}$$

because of the symmetric definition of the jump operators with $\hat{X}^{(3)}\hat{L}_1\hat{X}^{(3)} = \hat{L}_6$, $\hat{X}^{(3)}\hat{L}_2\hat{X}^{(3)} = \hat{L}_3$, and $\hat{X}^{(3)}\hat{L}_4\hat{X}^{(3)} = \hat{L}_5$, where $\hat{X}^{(3)} := (\hat{X} \otimes \hat{X} \otimes \hat{X})$, see Eq. (5.13).

Next, the off-diagonal density matrix elements in Eq. (D.18) are taken into account. The first one reads

$$\hat{\mathcal{L}}^{(\text{Fuks})}[|0...0\rangle\langle 0...0_{j-1}1_j0_{j+1}...0|] = \hat{\mathcal{L}}_{j-1}[|000\rangle\langle 001|_{j-1}] + \hat{\mathcal{L}}_j[|000\rangle\langle 010|_j] + \hat{\mathcal{L}}_{j+1}[|000\rangle\langle 100|_{j+1}], \tag{D.24}$$

where, analogous to the derivation in Eq. (D.20):

$$\begin{aligned}
\hat{\mathcal{L}}^{(\text{Fuks})}_{j-1}\Big[|000\rangle\langle 001|_{j-1}\Big] &= \hat{L}_{3_{j-1}}|000\rangle\langle 001|_{j-1}\hat{L}^\dagger_{3_{j-1}} - \frac{1}{2}\Big(|000\rangle\langle 001|_{j-1}\hat{L}^\dagger_{3_{j-1}}\hat{L}_{3_{j-1}} + \hat{L}^\dagger_{3_{j-1}}\hat{L}_{3_{j-1}}|000\rangle\langle 001|_{j-1}\Big) \\
&= \frac{\gamma}{2}|0\rangle\langle 0|_{j-2}\otimes\Big(|1\rangle\langle 0|\,|0\rangle\langle 0|\,|0\rangle\langle 1|_{j-1}\otimes|1\rangle\langle 1|\,|0\rangle\langle 1|\,|1\rangle\langle 1|_j - \\
&\quad - \frac{1}{2}(|0\rangle\langle 0|\,|0\rangle\langle 1|\,|1\rangle\langle 0|_{j-1}\otimes|0\rangle\langle 1|\,|1\rangle\langle 1|_j + |0\rangle\langle 1|\,|1\rangle\langle 0|\,|0\rangle\langle 0|_{j-1}\otimes|1\rangle\langle 1|\,|0\rangle\langle 1|_j)\Big) = \\
&= -\frac{\gamma}{4}|0\rangle\langle 0|_{j-2}\otimes|0\rangle\langle 0|_{j-1}\otimes|0\rangle\langle 1|_j\,,
\end{aligned} \tag{D.25a}$$

$$\begin{aligned}
\hat{\mathcal{L}}^{(\text{Fuks})}_{j}\Big[|000\rangle\langle 010|_{j}\Big] &= \hat{L}_{1_j}|000\rangle\langle 010|_j\hat{L}^\dagger_{1_j} - \frac{1}{2}\Big(|000\rangle\langle 010|_j\hat{L}^\dagger_{1_j}\hat{L}_{1_j} + \hat{L}^\dagger_{1_j}\hat{L}_{1_j}|000\rangle\langle 010|_j\Big) \\
&= \gamma|0\rangle\langle 0|_{j-1}\otimes\Big(|0\rangle\langle 1|\,|0\rangle\langle 1|\,|1\rangle\langle 0| - \frac{1}{2}(|0\rangle\langle 1|\,|1\rangle\langle 0|\,|0\rangle\langle 1| + |1\rangle\langle 0|\,|0\rangle\langle 1|\,|0\rangle\langle 1|)\Big)_j\otimes|0\rangle\langle 0|_{j+1} \\
&= -\frac{\gamma}{2}|0\rangle\langle 0|_{j-1}\otimes|0\rangle\langle 1|_j\otimes|0\rangle\langle 0|_{j+1}\,,
\end{aligned} \tag{D.25b}$$

$$\begin{aligned}
\hat{\mathcal{L}}^{(\text{Fuks})}_{j+1}\Big[|000\rangle\langle 100|_{j+1}\Big] &= \hat{L}_{5_{j+1}}|000\rangle\langle 100|_{j+1}\hat{L}^\dagger_{5_{j+1}} - \frac{1}{2}\Big(|000\rangle\langle 100|_{j+1}\hat{L}^\dagger_{5_{j+1}}\hat{L}_{5_{j+1}} + \hat{L}^\dagger_{5_{j+1}}\hat{L}_{5_{j+1}}|000\rangle\langle 100|_{j+1}\Big) \\
&= \frac{\gamma}{2}\Big(|1\rangle\langle 1|\,|0\rangle\langle 1|\,|1\rangle\langle 1|_j\otimes|1\rangle\langle 0|\,|0\rangle\langle 0|\,|0\rangle\langle 1|_{j+1} - \\
&- \frac{1}{2}(|0\rangle\langle 1|\,|1\rangle\langle 1|_j\otimes|0\rangle\langle 0|\,|0\rangle\langle 1|\,|1\rangle\langle 0|_{j+1} + |1\rangle\langle 1|\,|0\rangle\langle 1|_j\otimes|0\rangle\langle 1|\,|1\rangle\langle 0|\,|0\rangle\langle 0|_{j+1})\Big)\otimes|0\rangle\langle 0|_{j+2} \\
&= -\frac{\gamma}{4}|0\rangle\langle 1|_j\otimes|0\rangle\langle 0|_{j+1}\otimes|0\rangle\langle 0|_{j+2}\,,
\end{aligned} \tag{D.25c}$$

such that

$$\hat{\mathcal{L}}^{(\text{Fuks})}[|0...0\rangle\langle 0...0_{j-1}1_j0_{j+1}...0|] = -\gamma\,|0...0\rangle\langle 0...0_{j-1}1_j0_{j+1}...0| \neq 0. \tag{D.26}$$

Analogously, due to the symmetry of the Lindbladian, the action of the Lindbladian on the associate hermitian conjugate state as well as the corresponding bit-flipped states and its hermitian conjugate are all non-zero — specifically,

$$\begin{aligned}
\hat{\mathcal{L}}^{(\text{Fuks})}\big[\,|0...0_{j-1}1_j0_{j+1}...0\rangle\langle 0...0|\,\big] &= \Big(\hat{\mathcal{L}}^{(\text{Fuks})}\big[\,|0...0\rangle\langle 0...0_{j-1}1_j0_{j+1}...0|\,\big]\Big)^\dagger = |0...0_{j-1}1_j0_{j+1}...0\rangle\langle 0...0|, \\
\hat{\mathcal{L}}^{(\text{Fuks})}\big[\,|1...1\rangle\langle 1...1_{j-1}0_j1_{j+1}...1|\,\big] &= \hat{X}^{(N)}\hat{\mathcal{L}}\big[\,|0...0\rangle\langle 0...0_{j-1}1_j0_{j+1}...0|\,\big]\hat{X}^{(N)} = |1...1\rangle\langle 1...1_{j-1}0_j1_{j+1}...1|, \\
\hat{\mathcal{L}}^{(\text{Fuks})}\big[\,|1...1_{j-1}0_j1_{j+1}...1\rangle\langle 1...1|\,\big] &= \Big(\hat{X}^{(N)}\hat{\mathcal{L}}\big[\,|0...0\rangle\langle 0...0_{j-1}1_j0_{j+1}...0|\,\big]\hat{X}^{(N)}\Big)^\dagger = |1...1_{j-1}0_j1_{j+1}...1\rangle\langle 1...1|.
\end{aligned} \tag{D.27}$$

Overall, it has been shown that $\hat{\mathcal{L}}^{(\text{Fuks})}[\hat{\rho}] \neq 0$, see Eq. (D.18), such that the state $\hat{\rho}$ in Eq. (D.17) is not a steady state of the QCA — all steady states are of the form (D.6).

Appendix E

Proof that Dephasing QCA solves the DC task

The proof of the conservation of the number density in the Dephasing QCA (see Sec. 5.4.2) follows in an analogous manner to the proof for the Fukś QCA (see Sec. 5.4.1), by showing the conversation of the expectation value of $\hat{S}_z = \frac{1}{2}\sum_i \hat{Z}_i$ as outlined in Appendix. C. In contrast, the Dephasing Lindbladian acts on only two instead of three neighboring sides, j and $j+1$, such that Eq. (C.2) becomes

$$\left(\hat{\mathcal{L}}^{(\text{Dephasing})}\right)^{\dagger}\left[\hat{S}_z\right] = \frac{1}{2}\sum_j \left(\left(\hat{\mathcal{L}}^{(\text{Dephasing})}_{j,j+1}\right)^{\dagger}\left[\hat{Z}_j\right] + \left(\hat{\mathcal{L}}^{(\text{Dephasing})}_{j,j+1}\right)^{\dagger}\left[\hat{Z}_{j+1}\right]\right). \tag{E.1}$$

Plugging in the definition of the Dephasing Lindbladian in Eqs. (5.15) and (5.16) leads to:

$$\begin{aligned}\left(\hat{\mathcal{L}}^{(\text{Dephasing})}_{j,j+1}\right)^{\dagger}\left[\hat{Z}_j\right] + \left(\hat{\mathcal{L}}^{(\text{Dephasing})}_{j,j+1}\right)^{\dagger}\left[\hat{Z}_{j+1}\right] &= -i\,\Omega\,\left[\hat{X}_j\hat{X}_{j+1} + \hat{Y}_j\hat{Y}_{j+1}, \hat{Z}_j + \hat{Z}_{j+1}\right] + \\ + \sum_{k=1}^{4}\left(L^{\dagger}_{k_{j,j+1}}(\hat{Z}_j + \hat{Z}_{j+1})\hat{L}_{k_{j,j+1}} - \frac{1}{2}\Big((\hat{Z}_j + \hat{Z}_{j+1})\hat{L}^{\dagger}_{k_{j,j+1}}\hat{L}_{k_{j,j+1}} + \hat{L}^{\dagger}_{k_{j,j+1}}\hat{L}_{k_{j,j+1}}(\hat{Z}_j + \hat{Z}_{j+1})\Big)\right).\end{aligned} \tag{E.2}$$

The Hamiltonian term is vanishing $\forall j$ as

$$\begin{aligned}\left[\hat{X}_j\hat{X}_{j+1} + \hat{Y}_j\hat{Y}_{j+1}\ ,\ \hat{Z}_j + \hat{Z}_{j+1}\right] &= \left[\hat{X}_j, \hat{Z}_j\right]\hat{X}_{j+1} + \left[\hat{Y}_j, \hat{Z}_j\right]\hat{Y}_{j+1} + \hat{X}_j\left[\hat{X}_{j+1}, \hat{Z}_{j+1}\right] + \hat{Y}_j\left[\hat{Y}_{j+1}, \hat{Z}_{j+1}\right] \\ &= -2i\hat{Y}_j\hat{X}_{j+1} + 2i\hat{X}_j\hat{Y}_{j+1} - 2i\hat{X}_j\hat{Y}_{j+1} + 2i\hat{Y}_j\hat{X}_{j+1} \\ &= -2i\Big(\hat{Y}_j\hat{X}_{j+1} - \hat{X}_j\hat{Y}_{j+1} + \hat{X}_j\hat{Y}_{j+1} - \hat{Y}_j\hat{X}_{j+1}\Big) \\ &= 0,\end{aligned} \tag{E.3}$$

due to the commutation relations of the Pauli operators, $\left[\hat{\sigma}^i, \hat{\sigma}^j\right] = 2i\varepsilon^{ijk}\hat{\sigma}^k\ \forall\ \hat{\sigma}^l \in \left\{\hat{X}, \hat{Y}, \hat{Z}\right\}$ with $l \in \{i, j, k\}$ where ε^{ijk} the Levi-Civita symbol.

Next, the dissipator is vanishing too, because the summands for all four jump operators in

Eq. (5.17) are zero $\forall j$. That is, the first jump operator $\hat{L}_{1_{j,j+1}} = \hat{P}_{0_j}\hat{P}_{0_{j+1}}$ yields:

$$\begin{aligned}
&\hat{L}^\dagger_{1_{j,j+1}}\Big(\hat{Z}_j + \hat{Z}_{j+1}\Big)\hat{L}_{1_{j,j+1}} - \frac{1}{2}\Big(\Big(\hat{Z}_j + \hat{Z}_{j+1}\Big)\hat{L}^\dagger_{1_{j,j+1}}\hat{L}_{1_{j,j+1}} + \hat{L}^\dagger_{1_{j,j+1}}\hat{L}_{1_{j,j+1}}\Big(\hat{Z}_j + \hat{Z}_{j+1}\Big)\Big)\\
&= \hat{P}_{0_j}\hat{P}_{0_{j+1}}\Big(\hat{Z}_j + \hat{Z}_{j+1}\Big)\hat{P}_{0_j}\hat{P}_{0_{j+1}} - \frac{1}{2}\Big(\Big(\hat{Z}_j + \hat{Z}_{j+1}\Big)\hat{P}_{0_j}\hat{P}_{0_{j+1}} + \hat{P}_{0_j}\hat{P}_{0_{j+1}}\Big(\hat{Z}_j + \hat{Z}_{j+1}\Big)\Big)\\
&= \hat{P}_{0_j}\hat{P}_{0_{j+1}} - \frac{1}{2}\Big(\hat{P}_{0_j}\hat{P}_{0_{j+1}} + \hat{P}_{0_j}\hat{P}_{0_{j+1}}\Big)\\
&= 0
\end{aligned} \tag{E.4}$$

with $\hat{P}_0 = |0\rangle\langle 0|$ and $\hat{P}_0\hat{Z} = \hat{Z}\hat{P}_0 = \hat{P}_0\hat{Z}\hat{P}_0 = \hat{P}_0$; and analogously, the term of the fourth jump operator $\hat{L}_{4_{j,j+1}} = \hat{P}_{1_j}\hat{P}_{1_{j+1}}$ leads to:

$$\begin{aligned}
&\hat{L}^\dagger_{4_{j,j+1}}(\hat{Z}_j + \hat{Z}_{j+1})\hat{L}_{4_{j,j+1}} - \frac{1}{2}\Big((\hat{Z}_j + \hat{Z}_{j+1})\hat{L}^\dagger_{4_{j,j+1}}\hat{L}_{4_{j,j+1}} + \hat{L}^\dagger_{4_{j,j+1}}\hat{L}_{4_{j,j+1}}(\hat{Z}_j + \hat{Z}_{j+1})\Big)\\
&= -\hat{P}_{1_j}\hat{P}_{1_{j+1}} - \frac{1}{2}\Big(-\hat{P}_{1_j}\hat{P}_{1_{j+1}} - \hat{P}_{1_j}\hat{P}_{1_{j+1}}\Big)\\
&= 0
\end{aligned} \tag{E.5}$$

with $\hat{P}_1 = |1\rangle\langle 1|$ and $\hat{P}_1\hat{Z} = \hat{Z}\hat{P}_1 = \hat{P}_1\hat{Z}\hat{P}_1 = -\hat{P}_1$. Last, the summands of the second and third jump operators $\hat{L}_{2_{j,j+1}} = |\psi^+\rangle\langle\psi^+|_{j,j+1}$ and $\hat{L}_{3_{j,j+1}} = |\psi^-\rangle\langle\psi^-|_{j,j+1}$ are vanishing as

$$\begin{aligned}
&\hat{L}^\dagger_{2,3_{j,j+1}}(\hat{Z}_j + \hat{Z}_{j+1})\hat{L}_{2,3_{j,j+1}} - \frac{1}{2}\Big((\hat{Z}_j + \hat{Z}_{j+1})\hat{L}^\dagger_{2,3_{j,j+1}}\hat{L}_{2,3_{j,j+1}} + \hat{L}^\dagger_{2,3_{j,j+1}}\hat{L}_{2,3_{j,j+1}}(\hat{Z}_j + \hat{Z}_{j+1})\Big)\\
&= 0 - \frac{1}{2}(0+0) = 0.
\end{aligned} \tag{E.6}$$

All in all, it has thus been shown that $\Big(\hat{\mathcal{L}}^{(\text{Dephasing})}\Big)^\dagger\Big[\hat{S}_z\Big] = 0$ according to Eq. (E.1), such that the expectation value of $\hat{S}_z$ is conserved:

$$\frac{\mathrm{d}}{\mathrm{d}t}\Big\langle \hat{S}_z(t)\Big\rangle = 0. \tag{E.7}$$

Next, it is shown that the Dephasing QCA is therefore a density classifier due to its translation invariance. Let $|\hat{\rho}_{\text{ss}}\rangle$ with $\hat{\mathbb{L}}\,|\hat{\rho}_{\text{ss}}\rangle = 0$ be a vectorized steady state of a system defined by a translationally invariant Lindbladian $\hat{\mathbb{L}}$, then $\hat{T}\hat{\rho}_{\text{ss}}\hat{T}^\dagger \to \hat{T}\otimes\hat{T}^*\,|\hat{\rho}_{\text{ss}}\rangle$, with translation operator $\hat{T}$, must also be a steady state of the same system as

$$\begin{aligned}
\hat{\mathbb{L}}\left(\hat{T}\otimes\hat{T}^*\right)|\hat{\rho}_{\text{ss}}\rangle &= \left(\hat{T}\otimes\hat{T}^*\right)\underbrace{\left(\hat{T}\otimes\hat{T}^*\right)^\dagger\hat{\mathbb{L}}\left(\hat{T}\otimes\hat{T}^*\right)}_{=\hat{\mathbb{L}}}|\hat{\rho}_{\text{ss}}\rangle\\
&= \left(\hat{T}\otimes\hat{T}^*\right)\hat{\mathbb{L}}\,|\hat{\rho}_{\text{ss}}\rangle\\
&= 0,
\end{aligned} \tag{E.8}$$

such that any single site translation of a steady state is also a steady state.

Thus, given the Dephasing QCA conserves $\hat{S}_z$ and is translationally invariant, it is shown be a density classifier and solve the DC task.

Appendix F

Fatès QCA

Analogous to the Fukś CA, the Fatès rule is also a radius-one probabilistic CA. It is given by the traffic-majority (TM) rule studied in [162] and consists of a linear combination of the traffic rule 184 with probability $p \in [0,1]$ and the majority rule 232 with probability $1-p$:

$$\hat{\mathbb{S}}^{(\text{Fatès})} = p \underbrace{\hat{\mathbb{S}}^{(184)}}_{\text{traffic rule}} + (1-p) \underbrace{\hat{\mathbb{S}}^{(232)}}_{\text{majority rule}} , \tag{F.1}$$

That is, the same map, either $\hat{\mathbb{S}}^{(184)}$ or $\hat{\mathbb{S}}^{(232)}$ is applied to all cells in one time step, see Fig. F.1, with the corresponding transition probabilities shown in Tab. F.1. The map's fixed point is the all

	CA 184		CA 232	
neighborhood	probability	Kraus operators	probability	Kraus operators
00	$p_{000}=0$ $p_{010}=0$	amp. damping $\{\hat{P}_0, \hat{\sigma}^-\}$	$p_{000}=0$ $p_{010}=0$	amp. damping $\{\hat{P}_0, \hat{\sigma}^-\}$
01	$p_{001}=0$ $p_{011}=1$	identity channel $\{\hat{\mathbb{1}}\}$	$p_{001}=0$ $p_{011}=1$	identity channel $\{\hat{\mathbb{1}}\}$
10	$p_{100}=1$ $p_{110}=0$	bit-flip $\{\hat{X}\}$	$p_{100}=0$ $p_{110}=1$	identity channel $\{\hat{\mathbb{1}}\}$
11	$p_{101}=1$ $p_{111}=1$	amp. pumping $\{\hat{P}_1, \hat{\sigma}^+\}$	$p_{101}=1$ $p_{111}=1$	amp. pumping $\{\hat{P}_1, \hat{\sigma}^+\}$

Table F.1: Fatès QCA. Second and fourth column: transition probabilities p_{acb} representing the likelihood of the state transition $|acb\rangle \to |a1b\rangle$, with $a,b,c \in \{0,1\}\ \forall\ p \in [0,1]$. Third and fifth column: set of Kraus operators of the associated quantum channels acting on the center site j.

zero state if the initial state exhibits a number density less than $\frac{1}{2}$, the all one state if the initial number density is greater than $\frac{1}{2}$, or random for an equal initial number of zero and one states. However, the desired fixed point is reached only within a certain error threshold depending on the probability p and the structure of the input state, and does not solve the majority voting problem with complete accuracy, see discussion in [162].

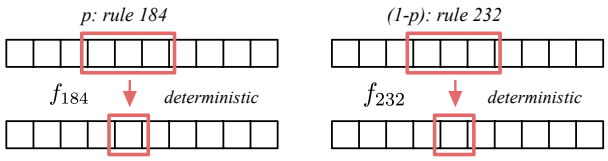

Figure F.1: Illustration of the dynamics of the Fatès QCA, which applies a stochastic combination of the deterministic elementary CA rules 184 and 232 with probability p or $1-p$, respectively.

Translating the CA rule in Tab. F.1 in the Kraus operator formalism, one would, analogous to the Fukś QCA, implement a complete amplitude damping (pumping) channel for the $|0\rangle\langle 0|_{j-1} \otimes |0\rangle\langle 0|_{j+1}$ ($|1\rangle\langle 1|_{j-1} \otimes |1\rangle\langle 1|_{j+1}$) neighborhood, apply the identity operation in case of the $|0\rangle\langle 0|_{j-1} \otimes |1\rangle\langle 1|_{j+1}$ state, and a stochastic bit-flip in case of the $|1\rangle\langle 1|_{j-1} \otimes |0\rangle\langle 0|_{j+1}$ neighborhood, as this is the only neighborhood that differentiates between the CA rules 184 and 232. The corresponding sets of Kraus operators are the same for both rules, except in case of the 10 neighborhood:

$$\hat{K}_0^{(00)} = |0\rangle\langle 0|\,, \qquad \hat{K}_1^{(00)} = \hat{\sigma}^-, \tag{F.2a}$$

$$\hat{K}_0^{(01)} = \hat{\mathbb{1}}, \tag{F.2b}$$

$$\hat{K}_0^{(10)} = \begin{cases} \hat{X} & \text{for rule 184} \\ \hat{\mathbb{1}} & \text{for rule 232} \end{cases}, \tag{F.2c}$$

$$\hat{K}_0^{(11)} = |1\rangle\langle 1|\,, \qquad \hat{K}_1^{(11)} = \hat{\sigma}^+, \tag{F.2d}$$

These define the superoperator in Eq. (5.7) according to Eq. (5.3). However, this map does not lead to the desired steady state $|0...0\rangle\langle 0...0|$ ($|1...1\rangle\langle 1...1|$) for an initial number density less (greater) than $\frac{1}{2}$, and is therefore not further inspected. Fig. F.2 shows an example in which the mapping fails, using even-odd partitioning scheme for each rule with $p = \frac{1}{2}$. Changing the value of p does not improve reaching the correct steady state; rather, it affects the speeding up or slowing down of convergence.

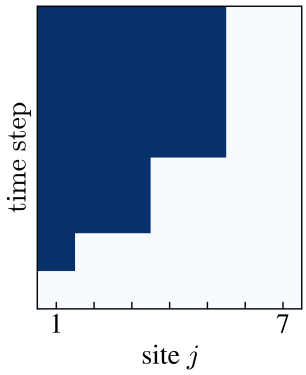

Figure F.2: Application of the Fatès rule using an even-odd partitioning scheme with $p = \frac{1}{2}$. Starting from the state $|1111100\rangle$ with $N = 7$, the system does not evolve into the desired majority steady state $|1\rangle^{\otimes N}$. One time step corresponds to one update of the QCA, i.e. updating all even and all odd lattice sites sequentially.

Appendix G

Proof of the properties of $\hat{\mathbb{A}}$ and the dynamics of the Majority Voting Lindbladian

G.1 Proof of the properties of $\hat{\mathbb{A}}$

In the following, the properties of $\hat{\mathbb{A}}$ are proved, see Sec. 5.4.3. The first property is easily demonstrated by applying operator $\mathbb{A}$ to a state featuring a cluster of $|1\rangle$s, observing that the action of $\hat{\mathbb{A}}^{m_a}$ spreads the $|1\rangle$ states out along the chain, see below example:

$$\begin{aligned}|000011111110000\rangle &\xrightarrow{\hat{\mathbb{A}}} |000010111111000\rangle \\ &\xrightarrow{\hat{\mathbb{A}}^2} |000010101111100\rangle \\ &\xrightarrow{\hat{\mathbb{A}}^3} |000010101011110\rangle \\ &\xrightarrow{\hat{\mathbb{A}}^4} |000010101010111\rangle \\ &\xrightarrow{\hat{\mathbb{A}}^5} |010010101010101\rangle.\end{aligned}$$

Next, $\left[\hat{\mathbb{S}}_z, \hat{\mathbb{A}}\right] = 0$ is derived, where $\hat{\mathbb{S}}_z$ is the vectorized form of $\hat{S}_z = \frac{1}{2}\sum_j \hat{Z}_j$. Defining $\hat{\mathbb{A}} = \prod_j \hat{\mathbb{A}}_j$ with $\hat{\mathbb{A}}_j = \hat{\mathbb{K}}_{0_j} + \hat{\mathbb{K}}_{1_j}$ and $\hat{\mathbb{K}}_{\mu_j} = \hat{K}_{\mu_j} \otimes \hat{K}^*_{\mu_j}$ $\forall \mu \in \{0,1\}$ yields:

$$\begin{aligned}\left[\hat{\mathbb{S}}_z, \hat{\mathbb{A}}_j\right] &= \frac{1}{2}\left[\hat{\mathbb{Z}}_{j-1} + \hat{\mathbb{Z}}_j + \hat{\mathbb{Z}}_{j+1}, \hat{\mathbb{K}}_{0_j} + \hat{\mathbb{K}}_{1_j}\right] \\ &= \left[\hat{Z}_{j-1}, \hat{K}_{1_j}\right] + \left[\hat{Z}_j, \hat{K}_{1_j}\right] + [Z_{j+1}, \hat{K}_{1_j}] + \left[\hat{Z}_{j-1}, \hat{K}_{0_j}\right] + \left[Z_j, \hat{K}_{0_j}\right] + \left[\hat{Z}_{j+1}, \hat{K}_{0_j}\right] = 0,\end{aligned} \tag{G.1}$$

where, in the first step, we have exploited the commutativity of operators on different sites and the property $[A \otimes B, C \otimes D] = (AC) \otimes (BD) - (CA) \otimes (DB)$ is used abandoning the vectorized form.

In the second step, the first four summands are vanishing since $\left[\hat{Z}, |0\rangle\langle 0|\right] = 0 = \left[\hat{Z}, |1\rangle\langle 1|\right]$, and the last two summands cancel each other out as $\left[\hat{Z}_j, \hat{K}_{0_j}\right] = -\left[\hat{Z}_{j+1}, \hat{K}_{0_j}\right] = 2\hat{K}_{0_j}$. Thus, taking the product over all lattice sites j into account, $\hat{\mathbb{A}} = \prod_j \hat{\mathbb{A}}_j$:

$$\left[\hat{\mathbb{S}}_z, \hat{\mathbb{A}}\right] = \underbrace{\left[\hat{\mathbb{S}}_z, \hat{\mathbb{A}}_1\right]}_{=0} \prod_{j=2}^{N} \hat{\mathbb{A}}_j + \sum_{i=1}^{N-2} \left(\prod_{j=1}^{i} \hat{\mathbb{A}}_j\right) \underbrace{\left[\hat{\mathbb{S}}_z, \hat{\mathbb{A}}_{i+1}\right]}_{=0} \left(\prod_{l=i+2}^{N} \hat{\mathbb{A}}_l\right) + \left(\prod_{j=1}^{N-1} \hat{\mathbb{A}}_j\right) \underbrace{\left[\hat{\mathbb{S}}_z, \hat{\mathbb{A}}_N\right]}_{=0} = 0 \quad \text{(G.2)}$$

using the property $[C, A \cdot B] = [C, A] \cdot B + A \cdot [C, B]$, where each individual commutator is vanishing due to Eq. (G.1).

G.2 Majority Voting Lindbladian $\hat{\mathbb{L}}^{(\mathrm{ML})}$ by using a Machine Learning approach

The supervised machine learning approach is used to find an appropriate Lindbladian evolution exhibiting steady states $|0\rangle^{\otimes N}$ and $|1\rangle^{\otimes N}$ that represent the corresponding majority state of the initial state. The ansatz for the set of jump operators is to take into account all four possible neighboring state combinations $|\alpha\rangle\langle\alpha|_{j-1} \otimes |\beta\rangle\langle\beta|_{j+1}$, and both, the amplitude raising and lowering operators, $\hat{\sigma}_j^+$ and $\hat{\sigma}_j^-$ acting on the center site. That is, given the Lindbladian in vectorized form

$$\hat{\mathbb{L}}^{(\mathrm{ML})}(\vec{w}) = \sum_{j=1}^{N} \sum_{k=1}^{8} \left(\hat{L}_{k_j} \otimes \hat{L}_{k_j}^* - \frac{1}{2}\left(\hat{L}_{k_j}^\dagger \hat{L}_{k_j} \otimes \hat{\mathbb{1}} + \hat{\mathbb{1}} \otimes \hat{L}_{k_j}^\dagger \hat{L}_{k_j} \right) \right), \quad \text{(G.3)}$$

where $\vec{w} = (w_1, ..., w_8)$ and the eight considered jump operators are:

$$\hat{L}_{1_j} = \sqrt{w_1}\, |0\rangle\langle 0|_{j-1} \otimes \hat{\sigma}_j^+ \otimes |0\rangle\langle 0|_{j+1}\,, \quad \text{(G.4a)}$$
$$\hat{L}_{2_j} = \sqrt{w_2}\, |0\rangle\langle 0|_{j-1} \otimes \hat{\sigma}_j^- \otimes |0\rangle\langle 0|_{j+1}\,, \quad \text{(G.4b)}$$
$$\hat{L}_{3_j} = \sqrt{w_3}\, |0\rangle\langle 0|_{j-1} \otimes \hat{\sigma}_j^+ \otimes |1\rangle\langle 1|_{j+1}\,, \quad \text{(G.4c)}$$
$$\hat{L}_{4_j} = \sqrt{w_4}\, |0\rangle\langle 0|_{j-1} \otimes \hat{\sigma}_j^- \otimes |1\rangle\langle 1|_{j+1}\,, \quad \text{(G.4d)}$$
$$\hat{L}_{5_j} = \sqrt{w_5}\, |1\rangle\langle 1|_{j-1} \otimes \hat{\sigma}_j^+ \otimes |0\rangle\langle 0|_{j+1}\,, \quad \text{(G.4e)}$$
$$\hat{L}_{6_j} = \sqrt{w_6}\, |1\rangle\langle 1|_{j-1} \otimes \hat{\sigma}_j^- \otimes |0\rangle\langle 0|_{j+1}\,, \quad \text{(G.4f)}$$
$$\hat{L}_{7_j} = \sqrt{w_7}\, |1\rangle\langle 1|_{j-1} \otimes \hat{\sigma}_j^+ \otimes |1\rangle\langle 1|_{j+1}\,, \quad \text{(G.4g)}$$
$$\hat{L}_{8_j} = \sqrt{w_8}\, |1\rangle\langle 1|_{j-1} \otimes \hat{\sigma}_j^- \otimes |1\rangle\langle 1|_{j+1}\,. \quad \text{(G.4h)}$$

Since the states $|0\rangle^{\otimes N}$ and $|1\rangle^{\otimes N}$ are the desired steady states, the weights w_1 and w_8 are set to zero because their corresponding jump operators would transform the state $|0_{j-1}0_j0_{j+1}\rangle$ into the state $|0_{j-1}1_j0_{j+1}\rangle$, and $|1_{j-1}1_j1_{j+1}\rangle$ into $|1_{j-1}0_j1_{j+1}\rangle$, respectively. The remaining decay rates

$(w_2, ..., w_7)$ are determined by the ML algorithm using the following training set:

$$\begin{aligned}
\vec{x}_1 &= [0,0,0,0] \longrightarrow y_1 = 0, & \vec{x}_7 &= [1,1,0,1,1] \longrightarrow y_7 = 1,\\
\vec{x}_2 &= [1,0,0,0] \longrightarrow y_2 = 0, & \vec{x}_8 &= [1,1,1,0,0] \longrightarrow y_8 = 1,\\
\vec{x}_3 &= [1,0,1,1] \longrightarrow y_3 = 1, & \vec{x}_9 &= [1,0,1,1,0] \longrightarrow y_9 = 1,\\
\vec{x}_4 &= [1,0,0,0,0] \longrightarrow y_4 = 0, & \vec{x}_{10} &= [1,0,1,0,1] \longrightarrow y_{10} = 1,\\
\vec{x}_5 &= [1,1,0,0,0] \longrightarrow y_5 = 0, & \vec{x}_{11} &= [1,1,1,1,1] \longrightarrow y_{11} = 1,\\
\vec{x}_6 &= [1,0,1,0,0] \longrightarrow y_6 = 0,
\end{aligned}$$

for system sizes $N \in \{4, 5\}$, where $X_{\text{train}} = \{\vec{x}_1, ..., \vec{x}_{11}\}$, $Y_{\text{train}} = \{y_1, ..., y_{11}\}$, and y_i is the density classification output of the state described by $\vec{x}_i$. The cost function is defined by

$$C(\vec{w}) = \sum_{i=0}^{11} (-1)^{1-y_i} f_0(\vec{w}, \vec{x}_i) + (-1)^{y_i} f_1(\vec{w}, \vec{x}_i), \tag{G.5}$$

where

$$f_0(\vec{w}, \vec{x}_i) = \left\langle \vec{0} \middle| e^{\hat{\mathbb{L}}(\vec{w})\tau} \middle| \vec{x}_i \right\rangle, \tag{G.6a}$$

$$f_1(\vec{w}, \vec{x}_i) = \left\langle \vec{1} \middle| e^{\hat{\mathbb{L}}(\vec{w})\tau} \middle| \vec{x}_i \right\rangle, \tag{G.6b}$$

with $|\vec{0}\rangle$ and $|\vec{1}\rangle$ labeling the vectorized forms of the states $|0\rangle^{\otimes N}$ and $|1\rangle^{\otimes N}$, respectively. Note that each summand of the cost function in Eq. (G.5) equals -1 for every state well-classified, such that $C(\vec{w}) = -11$ if the system solves the majority voting problem for every initial state. The goal is to minimize the cost function $C(\vec{w})$ over $\vec{w}$ setting the parameter $\tau = 10\,N^2$ and letting the weights vary in the range $[0, 1]$. For finding the global minimum, the basin-hopping algorithm [223, 224] with the L-BFGS-B local minimizer is used as implemented in the Python library SciPy [225]. Once a solution is found, it is possible to achieve an improvement in convergence time by appropriately scaling the weights $\vec{w}$. However, none of the solutions $\vec{w}$ of the cost function reaches the expected value of -11 if all the states present in the training set were well classified. This numerical evidence seems to suggest that a global solution capable of classifying every initial state and using a Lindbladian of the form (G.3) does not exist. Furthermore, for many of the found solutions the cost function reaches a value close to -9 with only one state misclassified, namely $\vec{x}_5$. Therefore, testing the solution on the set of states X_{test} randomly generated of size $N \in \{4, 5, 6, 7\}$, it is observed that the misclassified states belong to a specific set R. Given the system size N, R is the set of states with a majority of $|0\rangle$ states, where there exist at least two neighboring $|1\rangle$ states.

A numerical solution for the non-zero weights is $w_2 = 1.000$, $w_3 = 0.043$, $w_5 = 0.040$, and $w_7 = 0.075$, where the first three decimal digits are taken into account to ensure that the expectation value of $\hat{n}/N$ exceeds 0.99 which corresponds to having an average value of $\delta = 0.99 - 0.5 = 0.49$ for each site (see Def. 6). Analyzing how the Lindbladian evolves states not belonging to R enables understanding its action and thus comprehending its effectiveness. As observable in illustrative examples below (see Fig. G.2), the action of $\hat{\mathbb{L}}^{(\text{ML})}$ can be summarized by two contributions:

i) it transforms every part of the string containing an alternation of zeros and ones into all zeros: $|...010101...\rangle \to |...00000...\rangle$;

ii) it transforms every cluster of ones into a larger cluster by progressively adding ones both to the right and to the left across the entire chain: $|...000111000...\rangle \to |...001111100...\rangle \to |...011111110...\rangle$.

From this, we come to realize that what we have uncovered throug the ML approach is essentially equivalent to the Lindbladian in Eq. (5.25) employing the conventional rule of updating the central cell. However, evolving with this Lindbladian, the times needed to reach the final state in the worst-case scenario, are extremely higher (as it is shown in Fig. G.1) so that this solution has not been further explored. A usual, we considered the steady state reached when n/N exceeds 0.99

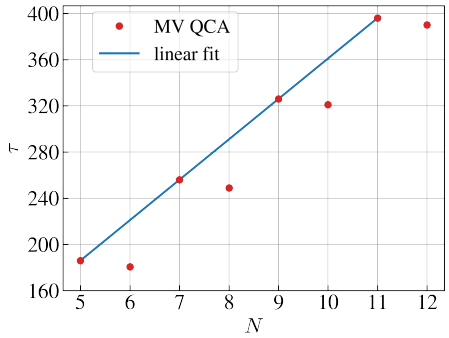

Figure G.1: Time τ needed to reach the steady state of the Majority Voting (MV) (in the worst-case scenarios and in the sector $n > N/2$) as function of the system size $N \in [5, 12]$, computed using the QuTiP library in Python [226]. The linear regression fit corresponds to the data of τ associated with the odd lattice site, yielding $\tau(N) = c \cdot N + d$ with the parameters $c = 34.992 \pm 0.005$ and $d = 11.03 \pm 0.04$.

which corresponds to having an average value of $\delta = 0.99 - 0.5 = 0.49$ for each site (see Def. 6).

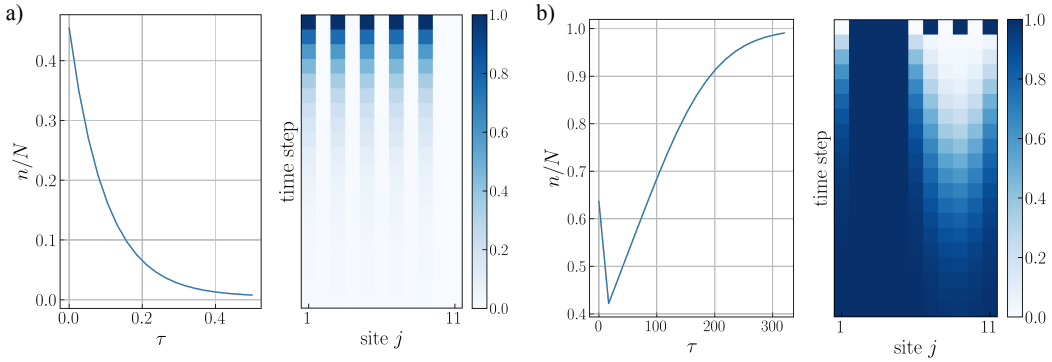

Figure G.2: Time evolution according to the Lindbladian (G.3) of the initial states a) $|10101010100\rangle$ and b) $|01111010101\rangle$ with $N = 11$. On the left of each image, the normalized density n/N is shown as a function of time τ; on the right one can see the time evolution of the state, reaching the state a) $|0\rangle^{\otimes 11}$ and b) $|1\rangle^{\otimes 11}$, where each time step is equal to a) $0.025\,\tau$ and b) $20\,\tau$. Note that in b) the density is decreasing for small τ and then monotonically increasing as observed in the plot on the right showing the time evolution of the state.

Appendix H

Proof of the scaling of τ with system size N in discrete-time evolution

As described in the body of the Chapter 5, the goal of transformation $\hat{\mathbb{A}}$ is to separate the clusters of $|1\rangle$s and spread them throughout the chain. When $\hat{\mathbb{A}}$ operates in the sector $n > N/2$ (where n is the expectation value of $\hat{n} = \sum_j \hat{P}_{1j}$ as usual), it will never manage to completely separate the $|1\rangle$s, and a cluster will always survive. It will be thanks to the survival of this cluster that $\hat{\mathbb{B}}$ will be able to bring the resulting state to $|1\rangle^{\otimes N}$ (the action of $\hat{\mathbb{A}}$ in this sector would not be necessary). Conversely, when $\hat{\mathbb{A}}$ acts on a state with $n \leq N/2$, it will be able to completely separate the $|1\rangle$s, and $\hat{\mathbb{B}}$ will bring the state to $|0\rangle^{\otimes N}$.

In this appendix, we aim to address the following questions: using the partition scheme depicted in Fig. 5.1 for $\hat{\mathbb{A}}$, what is the minimum number of time steps τ required to ensure that, beginning from any initial state with $n \leq N/2$, the resultant state does not contain any consecutive $|1\rangle$s? Using the partition scheme depicted in Fig. 5.1 for $\hat{\mathbb{B}}$, what is the minimum number of time steps τ required to ensure that, after applying $\hat{\mathbb{A}}$, the resultant state is correctly classified?

To address the first question, we must first identify the worst-case scenario, which is the one requiring the greatest number of steps. Then, we need to understand how $\hat{\mathbb{A}}$, using a partition scheme, reaches the solution.

We will start by understanding how $\hat{\mathbb{A}}$ (without any partition scheme) acts on a state having a cluster of d states $|1\rangle$s:

$$
\begin{aligned}
&|\cdots 00\overbrace{1_j 1_{j+1} 1_{j+2} \cdots 1_{j+d}}^{d} 00000\cdots\rangle \\
&|\ldots 001_j 0_{j+1}\overbrace{1_{j+2}\cdots 1_{j+d+1}}^{d-1} 0000\cdots\rangle \\
&|\ldots 001_j 0_{j+1} 1_{j+2} 0_{j+3}\overbrace{1_{j+4}\cdots 1_{j+d+2}}^{d-2} 000\cdots\rangle \\
&\cdots \\
&|\ldots 001_j 0_{j+1} 1_{j+2} 0_{j+3} 1_{j+4}\cdots 1_{j+2d-1}\cdots\rangle
\end{aligned}
$$

So the first application of $\hat{\mathbb{A}}$, splits the cluster by inserting a 0 after the leftmost 1 and shifting the remaining 1s by one site. It is evident, therefore, that the number of times $\hat{\mathbb{A}}$ needs to be applied is equal to the number of zeros required to completely split the cluster, which is $d-1$.

We now demonstrate that the worst-case scenario is equivalent to splitting a single cluster with $\frac{N}{2}$ ones. Indeed, let us consider two clusters, each having d_1 and d_2 ones respectively, with d_1 to the left of d_2, separated by l zeros. If $l > d_1$, then the two clusters will be divided independently without ever interfering with each other and will be completely separated in a number of steps equal to $\max(d_1, d_2) - 1$.

$$
\begin{aligned}
&|\cdots 0 \overbrace{1_j 1_{j+1} 1_{j+2} \cdots 1_{j+d_1}}^{d_1} \overbrace{0000\cdots 0}^{l} \overbrace{1_k 1_{k+1} 1_{k+2} \cdots 1_{k+d_2}}^{d_2} 00000\cdots\rangle \\
&|\cdots 01_j 0_{j+1} \overbrace{1_{j+2} \cdots 1_{j+d_1+1}}^{d_1-1} \overbrace{000\cdots 0}^{l-1} 1_k 0_{k+1} \overbrace{1_{k+2} \cdots 1_{k+d_2+1}}^{d_2-1} 0000\cdots\rangle \\
&|\cdots 01_j 0_{j+1} 1_{j+2} 0_{j+3} \overbrace{\cdots 1_{j+d_1+2}}^{d_1-2} \overbrace{0\cdots 0}^{l-2} 1_k 0_{k+1} 1_{k+2} 0_{k+3} \overbrace{\cdots 1_{k+d_2+2}}^{d_2-2} 0\cdots\rangle \\
&\cdots \\
&|\cdots 01_j 0_{j+1} 1_{j+2} 0_{j+3} \cdots 1_{j+2d_1-1} \overbrace{\cdots 0}^{l-d_1+1} \; 1_k 0_{k+1} 1_{k+2} 0_{k+3} \cdots 1_{k+2d_2-1} \cdots\rangle
\end{aligned}
$$

with the index $k = j + l$.
If $l < d_1$, then at some point the first cluster will encounter the second one after l steps, with a number of remaining ones to divide equal to $d_1 - l$, which will be added to d_2. Therefore, overall, the cluster will need a number of steps equal to $l + d_1 - l + d_2 - 1 = d_1 + d_2 - 1$, which is the same number required if the initial state had been composed of a single cluster with $d = d_1 + d_2$ ones, as you can see in the following example:

$$
\begin{array}{rll}
 & |\cdots 00 \overbrace{111111}^{d=6} 000000\cdots\rangle & |\cdots 00 \overbrace{111}^{d_1=3} 00 \overbrace{111}^{d_2=3} 00000\cdots\rangle \\
\hat{\mathbb{A}}^1 \longrightarrow & |\cdots 0010111110000000\cdots\rangle & |\cdots 0010110101100000\cdots\rangle \\
\hat{\mathbb{A}}^2 \longrightarrow & |\cdots 0010101111000000\cdots\rangle & |\cdots 0010101101010000\cdots\rangle \\
\hat{\mathbb{A}}^3 \longrightarrow & |\cdots 0010101011100000\cdots\rangle & |\cdots 0010101011010000\cdots\rangle \\
\hat{\mathbb{A}}^4 \longrightarrow & |\cdots 0010101010110000\cdots\rangle & |\cdots 0010101010110000\cdots\rangle \\
\hat{\mathbb{A}}^5 \longrightarrow & |\cdots 0010101010101000\cdots\rangle & |\cdots 0010101010101000\cdots\rangle
\end{array}
$$

Generalizing to multiple clusters d_i and knowing that we are in the sector $n \leq \lfloor \frac{N}{2} \rfloor$, we have $d = \sum_i d_i \leq \lfloor \frac{N}{2} \rfloor$, with the worst-case scenario resulting from the saturation of the inequality.

It is important to stress that all these arguments remain valid when adopting the partition scheme for $\hat{\mathbb{A}}$: indeed, through direct examination, it is evident that what changes is the way in which the cluster is divided, but not the number of $|0\rangle$ to the right of the cluster required to complete the spreading of the $|1\rangle$s.

Having identified the worst-case scenario, we continue our analysis by determining how many time steps $\hat{\mathbb{A}}$, using our partition scheme, needs to reach the goal. Considering Figure H.1 showing an example with $N = 12$ in the case $N \bmod 3 = 0$, it can be easily observed that, once the process

of splitting begins, a zero separator is added every four layers so that the desired state is reached after $4(\lfloor \frac{N}{2} \rfloor - 2) + 1$. Therefore, considering that this process can, at worst, start at the third layer, we have

$$\tau_A = 4\left(\left\lfloor \frac{N}{2} \right\rfloor - 2\right) + 1 + 2 = 4\left\lfloor \frac{N}{2} \right\rfloor - 5. \tag{H.1}$$

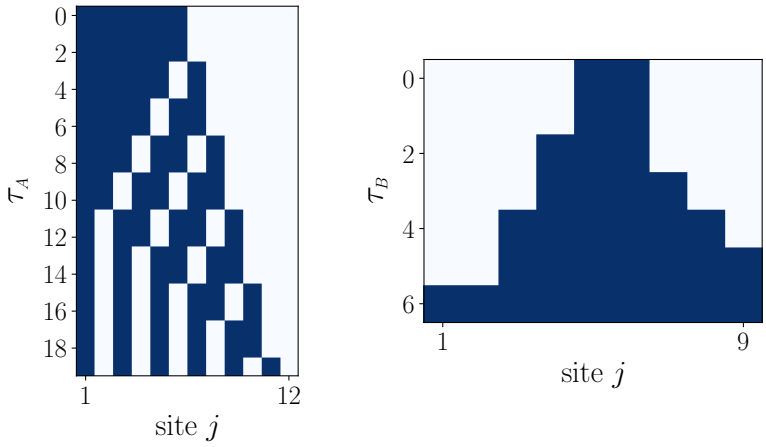

Figure H.1: On the left, discrete evolution of the state $|111111000000\rangle$ by using the partitioned version of $\hat{\mathbb{A}}$. On the right, discrete evolution of the state $|000011000\rangle$ by using the partitioned version of $\hat{\mathbb{B}}$.

Now, we can address the second question regarding $\hat{\mathbb{B}}$. It is evident that the worst-case scenario occurs when the smallest possible cluster (which, for $N \mathrm{mod} 3 = 0$ and N odd, consists of two consecutive ones) needs to be expanded along the chain. In Figure H.1, it is illustrated how $\hat{\mathbb{B}}$, when partitioned, enlarges a cluster of three ones: once the process starts, two zeros are converted to ones every two time steps. Therefore, considering that this process can, at worst, begin at the second layer, we have

$$\tau_B = 2\left(\frac{N-3}{3}\right) + 1 + 1 = \frac{2}{3}N. \tag{H.2}$$

Finally, we obtain

$$\tau = \tau_A + \tau_B = 4\left\lfloor \frac{N}{2} \right\rfloor + \frac{2}{3}N - 5. \tag{H.3}$$

Acknowledgements

For the completion of this thesis, I would like to express my gratitude to the reviewers, Professor Mario Collura and Professor Salvatore Marco Giampaolo, for their kind words about this work and for the insightful comments and suggestions that have contributed to its improvement.

I am also grateful to Professor Gavin Brenner and all my colleagues at Macquarie University for their valuable collaboration, from which I have learned so much.

I would like to extend my heartfelt thanks to my supervisor, Elisa Ercolessi, for her dedicated work over these years, as well as for the trust and encouragement she has always given me.

I am deeply thankful to my family for their support and to my friends in Bologna for always being there for me.

I would also like to thank all my friends and colleagues, especially Sunny, Simone, Rafael and Riccardo, who have shared much of this journey with me and have made it a more enjoyable experience.

Finally, last but not least, I want to thank Jack, who, throughout these years far from home, has managed to care for me despite myself. In him, I have found an intimate and safe place that I can truly call home, a place to which I can always return.

Federico